Tensile Strength and Fracture Mechanics of Cohesive Dry Snow Related to Slab Avalanches

by

Christopher P. Borstad

B.Sc. Physics, Colorado State University, 2002

M.A.Sc. Civil Engineering, University of British Columbia, 2005

A THESIS SUBMITTED IN PARTIAL FULFILLMENT
OF THE REQUIREMENTS FOR THE DEGREE OF

Doctor of Philosophy

in

THE FACULTY OF GRADUATE STUDIES
(Civil Engineering)

The University Of British Columbia
(Vancouver)

August 2011

© Christopher P. Borstad, 2011

Abstract

Fracture mechanics has been applied for over 30 years to explain the release of slab avalanches, but most studies have focused on the initial shear fracture which governs the loss of slab stability rather than the ultimate tensile fracture which releases the avalanche. The application of continuum fracture mechanics to snow—a porous material near the melting temperature—requires a homogenization scheme which accounts for the characteristic length scales associated with the diffuse nature of cracking in snow. An experimental campaign was conducted to measure the strength, fracture mechanical properties, and length scales in the tensile fracture of cohesive dry snow related to slab avalanches. Over 1000 natural snow samples were fractured in beam bending tests in a cold laboratory. Significant rate and size effects were observed in the experiments, though the loading rates were sufficiently high to justify an effective elastic analysis of the data.

Using beam theory, the tensile strength was calculated from hundreds of unnotched bending tests and compared with over 2000 synthesized tensile strength measurements from the literature. From the results of three different types of fracture experiments, the fracture toughness and effective fracture process zone length were calculated using equivalent elastic fracture mechanics, which approximately accounts for the nonlinearity engendered by the distributed nature of microcracking in snow. A thin-blade penetration resistance gauge was developed which characterizes structural variations in cohesive snow. The maximum force of penetration was the best index variable for correlating with tensile strength and fracture toughness. A nonlocal damage mechanics model, implemented in a finite element code, was calibrated using the results of ten series of experiments, providing a foundation for future predictive modeling applications related to slab avalanches. The tensile strength and fracture toughness of cohesive snow are now well constrained as functions of the snow density, penetration resistance, grain size, strain rate and sample size. The tensile fracture process zone was determined to be about 10-20 times the grain size, a length scale which necessitates the use of nonlinear fracture mechanics in the analysis of all but the very largest slab avalanches.

Preface

Chapter 3 contains published material. The bibliographic citation is:

> Borstad, C.P. and D.M. McClung (2011), Thin-blade penetration resistance and snow strength, *Journal of Glaciology*, Vol. 57, No. 202, pp. 325–336.

All of the research, analysis and writing of the paper was carried out by myself as first author. Copyright for all material is jointly vested between myself and the International Glaciological Society (IGS).

Section 5.3 of Chapter 5 contains published material. The bibliographic citation is:

> Borstad, C.P. and D.M. McClung (2009), Size effect in dry snow slab tensile fracture, *Proceedings of the 12$^{\text{th}}$ International Conference on Fracture*, Ottawa, Canada, 12-17 July 2009, 10 pp.

David McClung, as second author, contributed a statistical analysis of a published data set and approximately 5% of the writing. The remainder of the research, analysis and writing was carried out by myself as first author. Copyright over all material from this publication was retained by the authors.

Chapter 6 contains material submitted for publication. All of the research, analysis and writing of the manuscript was carried out by myself as first author.

Table of Contents

List of Tables

List of Figures

List of Symbols

Latin

A	Area
a_e	Equivalent elastic crack length
$a_\circ$	Original crack or notch length
b	Beam width
B	Blade hardness index
$\mathtt{B}$	Geometric function in Bažant's notched size effect law
c_f	Critical equivalent elastic crack extension or effective fracture process zone length
D	Characteristic specimen dimension, here typically the beam depth
D_b	Length scale characterizing the boundary layer of microcracking prior to crack coalescence
$D_\circ$	Notched size effect transitional size
D^e	Elastic stiffness tensor
E	Grain size
E	Young's modulus
E_t	Post-peak strain softening tangent modulus
f	Frequency in revolutions per second
f_r	Modulus of rupture (flexural strength)
$f_{r\infty}$	Asymptotic large-size limit of the modulus of rupture
f_t	Tensile strength
F	Force
g	Dimensionless linear elastic fracture mechanics geometry function ($g = k^2$)
$g_\circ$	Shorthand notation for $g(\alpha_\circ)$
G_F	Fracture energy
k	Dimensionless linear elastic fracture mechanics geometry function
$k_\circ$	Shorthand notation for $k(\alpha_\circ)$
$\mathtt{k}$	Scaling factor relating c_f between notched and unnotched tests
K_I	Mode I stress intensity factor
K_{Ic}	Mode I fracture toughness
K_{INu}	Mode I apparent fracture toughness
K_{tn}	Net stress concentration factor
l	Length
m	Weibull modulus
M	Bending moment
n_d	Similitude dimension
P	Applied load

r	Radius
r^2	Coefficient of determination for linear regression models
r_s	Spearman's correlation coefficient
R	Snow hardness, here denotes hand hardness index unless otherwise specified
R	Nonlocal interaction radius
R^2	Coefficient of determination for nonlinear regression models
R_{ram}	Ram hardness
$\mathbb{R}$	Radius of cylindrical tensile strength sample
S	Beam support span
t	Time
T	Temperature
V	Crosshead speed

Greek

α	Nondimensional crack length $(a_\circ/D)$
β	Brittleness number $(D/D_\circ)$
γ	Quasi-brittle multiplier for Irwin's plastic zone radius estimate
ε	Strain
$\varepsilon_\circ$	Limit elastic strain under uniaxial tension
ε_f	Post-peak strain softening (ductility) parameter
$\dot{\varepsilon}$	Strain rate
$\dot{\varepsilon}_N$	Nominal strain rate predicted by beam theory
$\bar{\varepsilon}$	Nonlocal scalar equivalent strain
$\tilde{\varepsilon}$	Local strain
η	Multiplier for D_b in the limit for $D \to 0$ in Bažant's "universal" size effect law
κ	Internal history variable representing maximum previous level of equivalent strain
ν	Poisson's ratio
ρ	Density
σ	Stress
σ_x	Tensile stress
σ_N	Nominal stress
σ_{Nu}	Nominal strength, defined as maximum nominal stress at failure
$\dot{\sigma}$	Stress rate
ϕ	Nondimensional measure of ductility in nonlocal isotropic damage model
χ	Nonlinear term in the regression analysis of the "universal" size effect law
ω	Scalar damage parameter
Ω	Angular frequency

Glossary

COV Coefficient of Variation

FPZ Fracture Process Zone, the spatially distributed zone of softening damage ahead of a crack tip in a quasi-brittle material such as snow. Different in size and behaviour from the hardening crack-tip plastic zone in ductile materials.

LCD Liquid Crystal Display

LEFM Linear Elastic Fracture Mechanics

LVDT Linear Variable Differential Transformer, used for accurate measurements of linear displacement.

RVE Representative Volume Element, typically the minimum volume size over which continuum physical relations are applicable for a heterogeneous material.

SMP SnowMicroPenetrometer, a motor-driven cone penetrometer that records snow hardness at sub-millimeter resolution.

Acknowledgements

I would like to thank my supervisor David McClung for supporting me, challenging me, and allowing me the space to develop into an independent scientist. Thanks also to the rest of my committee members, Sid Mindess, Reza Vaziri and Erik Eberhardt for many interesting discussions, insightful comments and sage advice over the years. A special thanks to the Natural Sciences and Engineering Research Council of Canada, the University of British Columbia, and Canadian Mountain Holidays for financial support.

This research would not have been possible without the generous in-kind support of Parks Canada and the staff of the Avalanche Control Section at Rogers Pass. Thanks to Bruce McMahon and Jeff Goodrich for defending the cold lab space over the years against cubicle expansion and for allowing researchers to interact with the forecasting operation on a daily basis. The support and front-line contact were invaluable. Thanks to the rest of the forecasting staff and wardens for the engaging discussions, the rides to Mt. Fidelity, and the opportunity to work in such a beautiful and dynamic natural environment.

A special thanks to Steve Conger for introducing me to many different facets of the avalanche industry, for assistance with field and lab work, and for many useful discussions and challenging questions over the years. Thanks to Eirik Ainer Sharp and Andrea McLeod for assistance with the field and lab work and for taking great care with the delicate snow samples.

To my family, I owe you an undying gratitude for your unwavering love and support as I followed my passions. Thank you Jed for your unconditional love and companionship and for never failing to lift my spirits.

To Beth, I cannot summon the words to express my thanks for your patience, support, encouragement, forgiveness and love during this time. I could not have achieved this without you.

Chapter 1

Introduction

The scientist studying snow and ice is not to be envied. It may be wonderful to work on glaciers and snowy slopes. On the other hand, ice and snow are probably the most complex bodies ever considered in continuum mechanics.

–Hans Ziegler

Snow avalanches are a hazard to people and structures in most mountainous areas of the world. Avalanches have caused human fatalities and captured the imagination of people inhabiting mountainous terrain for thousands of years. In recorded history, the largest losses of life to avalanches have been in great military expeditions in Europe (*Bader and Kuriowa*, 1962; *Voight et al.*, 1990). During Hannibal's crossing of the Alps in 218 B.C., thousands of men and a great many of the horses who died were likely consumed by avalanches. During World War I, between 40,000 and 80,000 troops died in avalanches in the mountains of Tyrol, with as many as 10,000 dying in the course of just one to two days on the Austro-Italian front in 1916. In North America, most avalanche accidents prior to the late 1900s were related to mining or railroad operations in mountainous terrain (*Voight et al.*, 1990; *Jamieson and Stethem*, 2002). In more recent times, most fatalities involve recreationists who were voluntarily exposed to the avalanche hazard (*Voight et al.*, 1990; *Jamieson and Stethem*, 2002; *McClung and Schaerer*, 2006).

In addition to causing human fatalities, avalanches have direct and indirect economic costs to the construction, transportation and tourism sectors every winter in regions with sufficient snowfall and slopes greater than about 25 degrees (*McClung and Schaerer*, 2006). In Canada, the direct economic costs related to avalanches exceed $10 million per year (*McClung and Schaerer*, 2006), and in the U.S. the number is probably an order of magnitude greater (*Voight et al.*, 1990).

Climate change is likely to influence the global distribution and extent of avalanches, though predicting these effects will be very difficult. Climate change will alter the distribution and variability of temperature and precipitation (*IPCC*, 2007), both of which influence avalanche activity (*Stethem et al.*, 2003). In Europe, the seasonal timing of the most destructive avalanches may shift toward spring, and the relative proportion of wet slab avalanches compared to dry slab avalanches may increase (*Martin et al.*, 2001). Changing weather and temperature patterns may shift avalanche activity away from regions where it is currently common toward regions where it is currently more rare (*Glazovskaya*, 1998). The link between climate change and avalanche activity is very tenuous, and more research will be needed to address these questions, but it appears that the avalanche problem will persist well into the future even in a warming climate.

Overview

An investigation was conducted into the tensile fracture properties of cohesive snow related to slab avalanches. In a slab avalanche, a large volume of cohesive snow is released all at once following the propagation of fractures. The first fracture is beneath a cohesive snow slab in a layer or interface which is weak in shear. This initial fracture propagates widely before a tensile fracture ultimately releases the avalanche (*McClung and Schaerer*, 2006). Though the shear fracture is the initial instability, this mode of fracture has been studied more widely and was not considered in the present study. However, the shear fracture is only possible if the snow is sufficiently cohesive to support tensile stresses (*Mellor*, 1968). The tensile fracture properties of the snow slab also determine the distance over which the shear fracture must propagate before the strength or fracture toughness of the slab is overcome. Thus the tensile properties of cohesive snow both enable a slab avalanche and influence its dimensions and destructive potential (*McClung and Schweizer*, 2006).

The majority of the present study involved experimental methods to *understand* the response of snow to tensile stresses applied at sufficiently high rates to minimize creep effects and cause fast fracture, as in slab avalanches. Natural snow was sampled over a wide range of conditions for the experiments, and the results were correlated with a variety of fundamental snow properties and testing conditions to enable comparison with the state of snow in a slab avalanche and to facilitate the in-situ estimation of fracture properties using index measurements. Equivalent elastic theories, which treated the snow as an elastic continuous material and approximately accounted for the observed nonlinearities, were applied to *explain* the experimental results and calculate properties such as tensile strength, fracture toughness, and effective fracture process zone size. These calculated properties were used in a continuum damage mechanics model to simulate a variety of the experiments, a first step toward the refined calibration of models that can *predict* the response of snow to the types of loading relevant to slab avalanches.

A general and more thorough description of the avalanche phenomenon is given here first, followed by a review of applications of fracture mechanics to explain avalanche triggering and release. A newly developed conceptual framework is presented to orient and contextualize the research, followed by the guiding principles and hypotheses of the research project. Finally, the chapter structure of the thesis is delineated.

1.1 Description of Snow and Avalanches

1.1.1 Alpine snow from a material science perspective

Snow is a particularly difficult material to study and analyze using common experimental methods and physical theories. One of the characteristic properties of alpine snow is its inherent thermodynamic instability (*Bader and Kuriowa*, 1962), a result of the proximity of snow to its melting temperature. Alpine snow in which avalanches form is usually within 90% of its melting temperature on an absolute scale (*McClung and Schaerer*, 2006). Other than solid ice, no other common natural or engineering material exists so close to its melting temperature (one exception may be magmatic structures in the asthenosphere). Consequently, in some regards, snow and ice may be considered model "high temperature" materials. However, relative to other common engineering materials such as metals, ice has a very low melting point diffusivity, which allows it to fracture right up to the melting temperature (*Schulson et al.*, 1984).

In addition to its proximity to the melting temperature, alpine snow is also characterized by a very high porosity, or, equivalently, a low solid volume fraction. For most slab avalanches, the density of the snow slab is between 100–350 kg m^{-3} (*Perla*, 1977). Given the density of solid freshwater ice (917 kg m^{-3}), this snow density range corresponds to a volume fraction filled by solids of about 0.1–0.4. Therefore most of the volume of snow is filled by air. The large pore space can allow for grain rearrangement and shearing of grain contact areas without appreciable deformation of the grains themselves (*Bader and Kuriowa*, 1962), leading to different bulk properties under different modes of loading (e.g. *Butkovich*, 1956; *Mellor*, 1975).

The material properties of snow have important temperature-dependent and rate-dependent characteristics (e.g. *Mellor and Smith*, 1966; *McClung*, 1977; *Narita*, 1980; *McClung*, 1981; *Schweizer*, 1998). Creep effects in snow are important for all but the fastest rates of loading (*Bader and Kuriowa*, 1962), and the same can be said for solid ice (*Schulson and Duval*, 2009). In fact, snow slabs may not ever respond fully elastically for relevant rates of loading in avalanches.

The highly irregular alpine snow cover is built up over the course of a winter by varying environmental conditions and successive storm and wind events, each of which produce snow of different types. The result is a layered and heterogeneous snow structure with spatial variability in properties over a number of length scales relevant to the triggering of avalanches. Spatial variability is the result of environmental processes such as wind and radiation and their interaction with the snow as a function of the local terrain and ground cover (e.g. *Schweizer et al.*, 2008). Metamorphism of snow on the ground, caused by changes in liquid water content, temperature, or a temperature gradient, gives rise to significant changes in the grain size, shape, and internal cohesion of the snow (*Colbeck*, 1982).

The above-mentioned effects combine to complicate the comparison of experimental results from different snow studies which typically involve different loading rates, temperatures, specimen geometries and sizes, and snow from different sources with different thermodynamic histories. These effects also make experimental design difficult in the study of avalanches, for the experimental conditions in situ or in a lab may not replicate to the conditions at the point where an avalanche is triggered. In situ snow studies give better indications of the properties of snow in its natural state (*Perla*, 1969; *McClung*, 1979a; *Jamieson*, 1988; *Conway and Abrahamson*, 1984), though laboratory tests measuring similar properties can give quite different results (*Martinelli*, 1971; *Narita*, 1980; *Sigrist*, 2006). In either case, small-scale measurements are complicated by statistical and deterministic size effects when attempting to relate experimental results to the avalanche scale (*Sommerfeld*, 1974; *Perla and Beck*, 1983; *Bažant et al.*, 2003; *McClung*, 2003; *Sigrist et al.*, 2005b; *Sigrist*, 2006).

1.1.2 Classification of avalanches

Snow avalanches can be classified into two types. The first are *loose avalanches*, which initiate with the failure of a very small volume of cohesionless surface snow. Below the initiation point, loose avalanches fan out and gain mass as they slide downslope. This type of slide more closely resembles the commonly-held notion of an avalanche as "snowball effect" involving a continuously growing mass of loose snow. Loose avalanches are typically small in volume, flow relatively slowly, and have limited destructive effects (e.g. *McClung*, 2003; *McClung and Schaerer*, 2006). For these reasons loose avalanches have relatively little practical importance or emphasis in academic studies, and will not be considered here.

The second and more important type of avalanche is a *slab avalanche*, which occurs when the snow is sufficiently cohesive to transmit tensile stresses and thereby permit fracture propagation (*Mellor*, 1968). Slab avalanches are released by fractures that propagate long distances and isolate a large volume of snow (Figure 1.1) which then flows rapidly downslope with sometimes great destructive effects (*Perla and LaChapelle*, 1970; *Perla*, 1977; *McClung*, 1979b, 1981, 1987, 1996; *Bažant et al.*, 2003; *Schweizer et al.*, 2003). The slope-normal slab thickness is typically less than 1 meter in slab avalanches (*Perla*, 1977), and the ratios of width-to-depth and length-to-depth of the slab are on the order of 10–10^3 with a median for both ratios around 100 (*McClung*, 2009a). The mean slope angle at which slab avalanches are released is $38°$, with nearly all recorded observations falling between $30°$ and $45°$ (*Perla*, 1977). Most slab avalanches which involve humans are caused by humans (e.g. *Jamieson and Johnston*, 1992), whereas natural slab avalanches, caused primarily by storm snow loading (*McClung and Schaerer*, 2006) are the primary threat to civil infrastructure (*Schweizer et al.*, 2003).

Slab avalanches can be further classified according to the moisture content of the snow, the hardness of the slab, the location of the sliding surface or weak layer, topographic features of the slope, or triggering factor (*Mellor*, 1968; *Martinelli*, 1971). In most alpine areas, most avalanches over the course of a winter occur in *dry snow*, that is, snow with no liquid water content (*McClung and Schaerer*, 2006). Slab avalanches in dry snow cause more destruction and fatalities than other types of avalanches in most mountainous regions (*McClung and Schaerer*, 2006). Moist or wet slab avalanches, which occur in snow with a limited amount of free water ($< 3\%$ water content by volume for moist snow, 3–8% for wet snow), are typically of less concern over the course of a winter, other than a punctuated period at the end of the season as temperatures

Figure 1.1: *Photograph of the fracture boundaries of a large slab avalanche. The exposed bed surface—the weak stratigraphic layer that was the first to fail—is denoted "A." The tensile fracture surface at the upslope boundary (the crown), which ultimately released the slab, is labeled "B." The lateral fracture boundaries (flanks), only one of which is visible in this image (labeled "C"), can fail by a combination of shear and tensile fractures in the slab. The downslope fracture boundary, or stauchwall, is often not visible after the slab overruns it. A secondary step-down tensile fracture surface is visible at "D," caused by the force of the flowing snow from upslope.*

increase. Moist or wet slabs also have very different mechanical properties from dry slabs, and it would be difficult to handle and maintain wet snow in a stable state in a cold lab. For these reasons, the focus of the present investigation was limited to dry snow.

1.1.3 Requisite components of a slab avalanche

There are three necessary components for a slab avalanche to occur. The first, as mentioned above, is a sufficiently cohesive snow slab to support the propagation of fractures. The second is a weak layer or weak interface beneath the slab. Finally, a slab avalanche requires some kind of trigger to cause the initial unstable shear fracture.

The initial cohesion of newly fallen storm snow is usually low, with any cohesive strength due primarily to interlocking of the snow crystals (*Fukue*, 1977). Instabilities during a storm are often limited to loose avalanches, unless the new snow is loading a pre-existing slab and weak layer which are near critical. Depending on the temperature, humidity, and wind during and after a storm, bond formation (sintering) in the newly fallen snow may proceed rapidly. Sintering occurs as a function of time, temperature, and the temperature gradient within a snow layer (e.g. *McClung and Schaerer*, 2006). Bond formation and growth during the sintering process promotes bulk cohesion of the snow, and, once a threshold in cohesion is reached, the snow may first begin to transmit tensile stresses. Estimating the timing at which this cohesion threshold is reached—either in slab snow losing cohesion or loose snow gaining cohesion—is important for forecasting avalanches.

Weak layers involved in slab avalanches are often snow surfaces that were exposed for long periods of time before burial. Specific types of weak crystals form or metamorphose at or near the surface of the snow pack depending on the environmental conditions. Weak layer crystals which are commonly responsible for slab avalanche activity, such as *surface hoar* and *near-surface facets*, form under a large temperature or vapour pressure gradient at or near the snow surface caused by a strong radiation imbalance (*Schweizer et al.*, 2003). Buried layers composed of these crystal forms have been termed "persistent" weak layers, as the crystals have a tendency to resist bond formation and persist for long periods of time in a weak state (*Jamieson and Johnston*, 1992). Sun crusts, rain crusts, or other weathered surfaces may also be formed during long spells between storms, and these surfaces may also be failure layers once buried (*Schweizer et al.*, 2003; *McClung and Schaerer*, 2006). Figure 1.2 is a photograph of a layer of surface hoar crystals developing on the snow surface prior to burial. Persistent forms such as surface hoar and facets tend to be anisotropic, behaving much weaker in shear than in slope-normal compression. This anisotropy is an important characteristic in the mechanics of slab avalanches (e.g. *McClung*, 2003; *McClung and Schaerer*, 2006; *Reiweger and Schweizer*, 2010).

The third necessary component for a slab avalanche is a trigger that causes the initial unstable fracture in the weak layer. Most slab avalanches are triggered naturally by precipitation or wind loading (*McClung and Schaerer*, 2006). Rapid artificial loading by explosives, snow machines or people can also trigger a slab avalanche. Most avalanches (greater than 80%) in which humans are partially or fully buried or killed were triggered by the victims themselves (*McClung and Schaerer*, 2006). In the absence of an increase in load, a change in snowpack properties caused by a sudden change in temperature (*McClung*, 1996; *Schweizer et al.*, 2003) may also render a slab unstable.

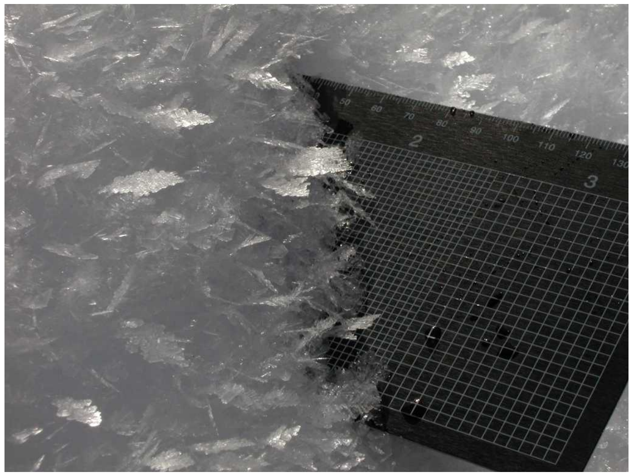

Figure 1.2: *Photograph of exposed surface hoar crystals, a common weak layer responsible for slab avalanches once buried. Grid units are in mm.*

1.2 Historical Analysis of Slab Avalanches

1.2.1 Predicting avalanches using a stability index

An early and still common method for analyzing the stability of a snow slab and thereby predicting avalanches is to calculate a stability index, or ratio of stress to strength (or vice-versa) of the snow. *Bucher* (1948) proposed as a stability index the ratio of shear stress to shear strength within a weak layer. *Bradley* (1966) proposed a ratio of compressive strength of a weak basal layer (such as depth hoar) to the normal load of the entire snowpack. *Mellor* (1968) assumed that slab avalanches initiate when shear stress exceeds shear strength "over a significant area of the snow cover." Applying these ratios implicitly assumes that strength is the governing factor for slab stability, a classic strength of materials approach.

Calculating the stress component of a simple stability index is relatively straightforward; the mean slab density, slope-normal slab thickness, and slope angle are the only requirements. These terms are known or can be estimated with relative confidence in most cases. The more uncertain term is the snow strength, which is typically calculated from the results of in situ testing that directly measures the layer of interest (most commonly in shear). However, due to the spatial variability of snow properties, approximate nature of the strength calculation, and small volume of snow sampled relative to the avalanche scale, these strength values likely contain most of the overall uncertainty in a calculated stability index.

Sommerfeld (1969) emphasized a problem with this type of stability factor analysis, namely that a great many large avalanches involve slabs with stability indices (ratios of strength to stress) greater than 1. *Perla* (1977) reported a mean stability index, calculated after the fact for 80 avalanches, of 1.7 ± 1. This value suggested that the index would not have, on average, predicted the observed avalanches. The large variability of the calculated indices also cast doubt on the applicability of such a technique for predictive purposes.

A number of subsequent refinements to simple stability indices were introduced that attempted to account for size effects, the load produced by a skier, or other contributing factors (e.g. *Sommerfeld and King*, 1979; *Conway and Abrahamson*, 1984; *Föhn*, 1987; *Jamieson*, 1995). These modified indices still neglected the effects of slab temperature and hardness, which hampers their applicability and accuracy in forecasting avalanches (*McClung and Schweizer*, 1999). Stability indices do not (and for all practical purposes cannot) take into account the size and distribution of imperfections within the weak layer, which are commonly believed to be the fundamental source of slab avalanche instability (*McClung and Schaerer*, 2006). A fracture mechanical slope stability index would take the form of a ratio between the shear stress intensity factor and the shear fracture toughness of a weak layer (*McClung*, 2003), though the shear fracture toughness of the *weakest* portion of the weak layer, that which governs the loss of stability, can never be measured in the field prior to avalanche release because its size and location are unknown. Though some field studies have found direct evidence for such "shear deficit zones" (e.g. *Conway and Abrahamson*, 1988), many extensive studies have not (*Schweizer*, 1999). For these reasons, and for relative simplicity, stability indices as a function of stress and strength have remained in favor in some applications despite their drawbacks.

1.2.2 Fracture sequence in slab avalanches

Observations of the geometry and inclination of the fracture surfaces in slab avalanches provided an early benchmark for models of avalanche release. In slab avalanches, the uppermost tensile fracture surface through the slab, or crown (labeled "B" in Figure 1.1), is nearly always oriented perpendicular to the bed surface, plus or minus ten degrees (*Perla and LaChapelle*, 1970). This indicates that the maximum principal stress in the slab is oriented parallel to the weak layer when it fails, an important observation that informed an early debate over the fracture sequence in slab avalanches.

Many investigators assumed that shear failure of the weak layer was the primary failure which governed the instability of a slab (*Bucher*, 1948; *Jaccard*, 1966). Others held that the tensile fracture through the slab was the initial failure which led to slab avalanche release (*Haefeli*, 1963; *Roch*, 1966; *Sommerfeld*, 1969;

Perla, 1975). Following this initial tensile failure of the slab, it was postulated that the weak layer beneath the slab would be overstressed and subsequently fail, releasing the avalanche.

Many of the early tensile failure models for slab release were incompatible with the observed angle of the crown surface with respect to the weak layer. A static tensile failure model for an inclined slab, independent of the action of an underlying weak layer, would have a slope angle dependence in the orientation of the principal tensile stress. The discrepancy between observed and predicted angles of intersection of the crown and bed surface was explained by some as a result of slope geometry. The influence of a weak basal layer undergoing large-scale shear slip was later postulated as an explanation for the rotation of principal stresses, even if the tensile fracture was still thought to be the initial instability (*Perla and LaChapelle*, 1970).

A more consistent explanation of the observed crown fracture angles followed from the introduction of fracture mechanics to explain slab avalanche release. *McClung* (1979b, 1981, 1987) was the first to apply principles of fracture mechanics to the problem of slab avalanche triggering. Based on experimental evidence of strain softening in snow under simple shear (*McClung*, 1977), the pioneering slip surface model of *Palmer and Rice* (1973) was applied by *McClung* (1979b) to explain the release of a slab avalanche following the growth of a strain-softening shear band in a weak layer beneath a snow slab. This model predicted principal tensile stresses in the slab nearly in alignment with the weak layer.

McClung (1981) was the first to introduce the shear stress intensity factor K_{II} and shear fracture toughness K_{IIc} as fundamental parameters governing the stability of a snow slab. *McClung* (1987) outlined further detail on shear fracture propagation conditions and discussed effects such as layered slab stratigraphy, dynamic effects and weak layer anisotropy that would favor tensile fractures oriented perpendicular to the weak layer following an initial shear fracture. The current consensus opinion is that the perpendicularity of the crown fracture surface to the weak layer is the result of an initial failure between the slab and the substratum which propagates widely before tensile failure through the slab releases the avalanche (e.g. *Schweizer et al.*, 2003; *McClung and Schaerer*, 2006).

1.3 Fracture Mechanics of Snow Slab Release

1.3.1 Shear fracture and initial slab instability

The initial shear fracture which governs the loss of slab stability is typically assumed to nucleate from an imperfection or especially weak region within the weak layer (*Bažant et al.*, 2003; *Schweizer et al.*, 2003). The length scale associated with this initial imperfection is expected to be on the order of at least 10 cm (*McClung*, 2005, 2009b). The strain-softening shear fracture process zone in the weak layer is expected to be large, perhaps on the order of the slab depth (*Bažant et al.*, 2003). The nonlinear effects caused by a large fracture process zone can be approximately accounted for using equivalent elastic fracture mechanics, whereby an infinitely-sharp crack tip which obeys linear elastic fracture mechanics (LEFM) is extended into the fracture process zone of the actual crack (*Bažant et al.*, 2003). A similar procedure was applied for the tensile fractures in the present study. Since the fracture in the weak layer beneath the slab is not within the scope of the present research, it will not be discussed further here. A review of slab release models which focus on the initial shear instability can be found in *Schweizer et al.* (2003).

1.3.2 Tensile properties of cohesive snow relevant to avalanche release

The tensile properties of a cohesive snow slab play two fundamentally important roles in slab avalanches. First, the cohesion of the snow supports the transmission of tensile stresses through the slab and thus enables the initial shear fracture to propagate beneath the slab. This particular role of the snow slab is often taken for granted. For example, no common or standard test or index property exists which distinguishes cohesionless snow from snow with sufficient cohesion to support the propagation of fractures. Experienced observers can often make this distinction (*McClung and Schaerer*, 2006), one that is typically based on some measure of snow hardness (penetration resistance). However, prior to this study, an objective and quantifiable classification for slab snow as distinct from loose snow had not been addressed since an early study by *Fukue* (1977).

Previous investigators have considered the cohesive strength of snow as synonymous with tensile strength (*Bader and Kuriowa*, 1962; *Mellor*, 1968). The tensile strength of cohesive dry snow has been measured using a diversity of field and lab techniques (e.g. *de Quervain*, 1951; *Bader et al.*, 1951; *Roch*, 1966; *Sommerfeld and Wolfe*, 1972; *Sommerfeld*, 1974; *McClung*, 1979a; *Narita*, 1980; *Jamieson*, 1988). The most common index variable for the tensile strength is the snow density, though reported values of strength vary by nearly two orders of magnitude at a given density. This is the result of different specimen sizes, loading rates, testing techniques, and important variations in snow structure at a given density. In other words, cohesion is a function of much more than density.

Provided that a snow layer is sufficiently cohesive to support fracture propagation, the second fundamental role that the slab plays is in governing the release dimensions, and therefore indirectly the destructive potential, of a slab avalanche (*McClung and Schweizer*, 2006). The tensile fracture toughness (or fracture energy) governs the distance that the underlying shear fracture will propagate before the slab fails (Figure 1.3a). The tensile fracture is assumed to initiate in a boundary layer at the base of the slab without requiring a stress concentration or initial flaw in the slab (*McClung and Schweizer*, 2006). This boundary layer is characterized by a gradient in stress and strain at the base of the slab, which is caused by the propagating shear fracture beneath the slab and the typical increase in density and hardness of the slab as a function of depth.

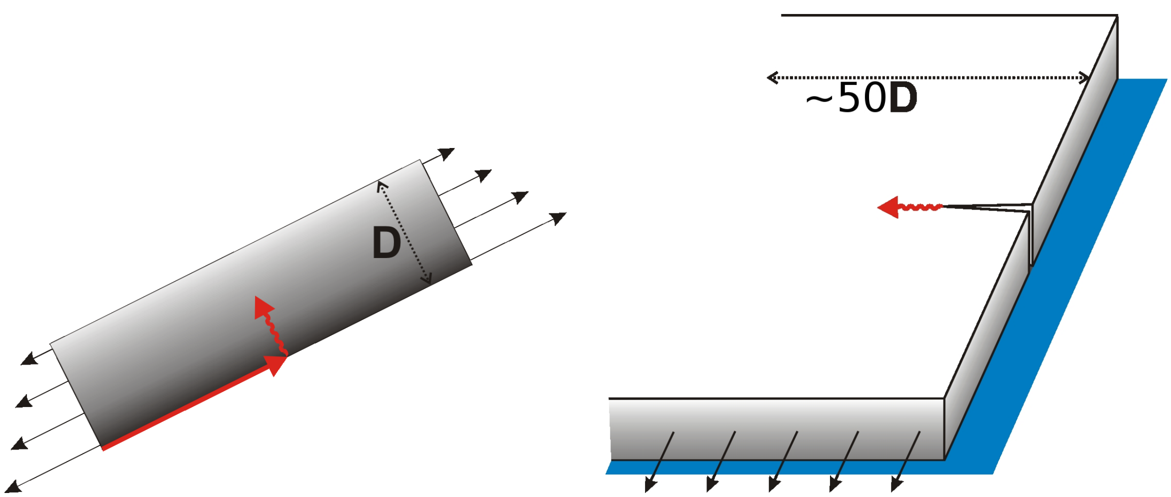

(a) **(b)**

Figure 1.3: *Modes of tensile fracture through a slab. Following shear fracture propagation beneath the slab, the initial tensile fracture is assumed to propagate from the bottom to the top of the slab after coalescence of a tensile crack in a highly stressed boundary layer at the bottom of the slab (a). Once the initial tensile fracture has reached the surface of the slab, the tensile fracture may propagate laterally across the slope as the shear fracture continues to propagate beneath the slab (b). The characteristic length scale for the fracture mechanics of slab avalanches is the slope-normal slab thickness D. From thousands of observations, the median half-width of a released slab is around 50D (McClung, 2009a).*

Once the initial tensile fracture coalesces and propagates to the surface of the slab, the fracture may, in part, proceed laterally across the slope while the weak layer continues to fail in shear or anti-plane shear (Figure 1.3b). This latter mode of tensile fracture, represented in a plane of symmetry in Figure 1.3b, may be conceptualized as a center-cracked panel on a frictional bed. However, the role of side friction in combination with the downslope motion of the slab may combine to produce a curved fracture trajectory (*McClung*, 2009a).

The ratio of fracture energy or fracture toughness in tension to that in shear is important in determining the overall release dimensions of a slab avalanche (*McClung and Schweizer*, 2006). The mean tensile fracture energy of the slab is about 10 times greater than the shear fracture energy of the weak layer (*McClung*, 2007b). However, the surface area of the perimeter fractures that fail in tension is approximately 30 times smaller than the basal shear fracture area (*McClung*, 2009a). Therefore, the total fracture energy consumed in tension is roughly comparable to that in shear, based on median measurements of avalanche dimensions (*McClung*, 2009a).

1.3.3 Measurement and calculation of fracture properties

The tensile fracture toughness of cohesive snow was first calculated from the results of notched cantilever beam tests (*Kirchner et al.*, 2000, 2001, 2002a; *Schweizer et al.*, 2004). These studies used the framework of Linear Elastic Fracture Mechanics (LEFM) to calculate the critical stress intensity factor at which the beam samples failed. In using LEFM, these investigators implicitly assumed that any inelastic nonlinear zone ahead of the notch tip had a negligible size compared to all other specimen dimensions in the experiments (*Bažant and Planas*, 1998). However, for a heterogeneous and porous material such as snow, the specimen size requirements may not have been met for this assumption to be valid.

A further assumption for the use of LEFM or any other continuum mechanical theory for a highly porous material such as snow is that the specimen dimensions are sufficiently large compared to the scale of heterogeneity (in the case of snow, the grain size) to ensure that the specimen is, in bulk, homogeneous. This is a requisite for the approximation of snow as a continuum. For solid ice, the homogeneous limit is on the order of 10–200 times the grain size (*Dempsey et al.*, 1999b; *Schulson and Duval*, 2009). An analogous relation for snow does not exist, but might take into account, in addition to the grain size, the mean grain spacing or pore space in the snow.

The first nonlinear fracture theory applied to tensile fracture data was by *Sigrist et al.* (2005b); *Sigrist* (2006) for the analysis of both notched cantilever beam tests and notched three-point bending tests conducted in a cold laboratory. These studies applied the equivalent elastic crack approach (e.g. *Bažant and Kazemi*, 1990a,b; *Bažant and Planas*, 1998) to account for the presence of a large and distributed fracture process zone ahead of the notch tip. Using the same theoretical approach, *McClung and Schweizer* (2006) calculated both the shear and tensile fracture toughness of dry snow slabs using data from other sources. They estimated the length of the effective fracture process zone in tension on the order of 1–10 cm, though the uncertainty was large and possibly important rate effects were not tested for in the data. However, their results strongly support the assertion that nonlinear fracture mechanics is necessary, and that LEFM is inapplicable, for most length scales of interest in slab avalanche applications. A further critical implication is that the fracture parameters determined from laboratory-scale tests will be inapplicable for full-scale analysis of avalanches unless a proper nonlinear size scaling correction is applied.

As with most cohesive snow properties, the published fracture toughness data has been primarily indexed against the snow density. The reported values of fracture toughness vary by nearly an order of magnitude at a given density (*Kirchner et al.*, 2000, 2002a,b; *Schweizer et al.*, 2004; *Sigrist et al.*, 2005b; *Sigrist*, 2006; *McClung and Schweizer*, 2006), though *Schweizer et al.* (2004) binned data into “hard” and “soft” snow categories (from hand hardness index values) prior to fitting models of tensile strength as a function of density. The variability between studies is due to a number of factors, from variations in the microstructure and grain size of snow at a given density, to rate, size and geometry effects, to the assumption about which fracture theory (linear or nonlinear) on which to base the analysis.

1.4 Theoretical Framework and Guiding Principles of Thesis

Many open questions remain with regard to the tensile properties of snow slabs related to avalanches, and this study addressed many of these. Outlined below is a conceptual classification that was devised for the purpose of framing much of the analysis and discussion in the present study. This classification has two primary divisions: the spatial scale of interest and the amount of internal cohesion of the snow. Both should be addressed with the porous and heterogeneous nature of snow in mind, as shown schematically in Figure 1.4.

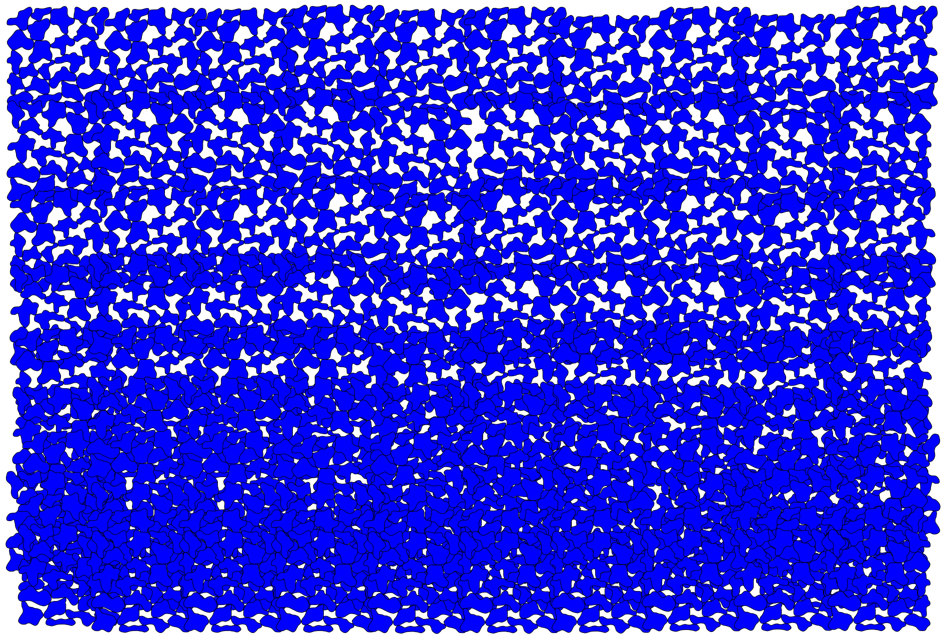

Figure 1.4: *Schematic illustrating the porous and heterogeneous nature of dry seasonal snow. The layering of the snow structure and the densification with depth is represented. Characterization of snow using continuum mechanics is only valid for volume elements much greater than the grain size.*

1.4.1 Cohesion threshold for fracture propagation

As discussed above, slab snow and loose snow are delimited by a cohesion threshold. Above this threshold, the snow is able to support the transmission of tensile stresses and therefore fracture propagation. The ability to quantify this cohesive threshold in-situ would have practical benefits since forecasting the onset of slab avalanche activity in newly fallen snow can be difficult. Similarly, the loss of cohesion in snow undergoing destructive metamorphism or warming to the melting temperature can cause loose avalanches which can also be difficult to predict.

The cohesion threshold also defines the domain for which the response of snow is adequately characterized by *material* properties, for loose snow, versus *structural* properties for slab snow. Material properties may be taken as the bulk snow density, grain size and grain shape as well as inherited properties of the parent material (ice). Structural properties in some way measure or account for the manner in which snow is bonded into a coherent slab structure which gives it specific bulk behaviour. Examples of structural properties include tensile strength, Young's modulus and fracture toughness. These parameters depend on the number and area of bonds per grain or unit volume of the snow and therefore only make sense to define for cohesive snow.

The most well-defined index properties which are sensitive to snow structure are the various measures of penetration resistance or snow hardness (e.g. *Shapiro et al.*, 1997). The most common hardness test is a subjective hand penetration test, but the results from this index test vary across observers and are difficult to use quantitatively. *Fukue* (1977) studied the penetration of a thin blade into snow and related penetration resistance to cohesive strength, though this promising study appears to have been largely overlooked in the last 30 years. Currently, no hardness test or structural index measurement exists which is objective, quantifiable, and widely adopted. Consequently, most studies reporting strength or fracture properties have not reported any hardness measurements or correlations with properties other than density.

Density is thus the most commonly used variable to index cohesive snow properties, even though it is commonly agreed and often stated that density is an inadequate measure of cohesion or snow structure (*Bader and Kuriowa*, 1962; *Ballard and Feldt*, 1966; *Ballard and McGaw*, 1966; *Mellor and Smith*, 1966; *Shapiro et al.*, 1997). Density is, however, a reasonable first approximation for snow structure in the absence of an alternative index property which is more sensitive to structure. Density also has the advantage of being easy to measure, relatively objective, and easily comparable across data sets. However, snow properties such as strength often display large scatter when expressed as a function of the snow density (or porosity), and most of this scatter can be attributed to variations in snow structure at a given density (e.g. *Mellor and Smith*, 1966; *Shapiro et al.*, 1997; *Schweizer et al.*, 2003). For example, the uniaxial tensile strength of snow slabs with rounded grains is about twice that of slabs with angular or faceted grains at the same density (*Jamieson*, 1988; *Jamieson and Johnston*, 1990), and the same is true of other cohesive properties. In most studies, however, the lack of a superior, repeatable and objective index measure for snow structure has left most investigators with no better alternative variable than density for correlating with strength and fracture properties. This need was addressed in the present study by the development of a new penetration resistance gauge, the results of which were consistently correlated with measured tensile properties and compared to density for predictive merit.

1.4.2 Length scales in the analysis of slab avalanches

In the majority of slab avalanches, the slope-normal slab thickness is in the range of 0.1–1 m, with a mean of about 0.7 m (*Perla*, 1977). The slab thickness is the characteristic length scale for analysis of slab avalanches using fracture mechanics. Other important length scales include the continuum limit and the size of the fracture process zone during crack initiation and propagation in snow. These length scales are more uncertain than the slab thickness, which can be directly measured, but are important for scaling analyses of slab strength and fracture properties with changing slab thickness and for relating lab-scale measurements to the slope scale.

Continuum limit

The *continuum limit* defines the length scale above which a mass of snow may be considered, in bulk, to be homogeneous. This distinction allows the use of continuum mechanics for the analysis of the bulk response of a snow slab or specimen (provided that the snow is also above the cohesive threshold). For a material such as snow, which has a highly porous and heterogeneous microstructure, continuum equations do not apply for arbitrarily small volume elements (see e.g. Figure 1.4). For most applications related to avalanches, however, the volume element of interest is much greater than the grain size and likely sufficient for the application of continuum mechanics (*Salm*, 1971). Below the continuum limit, discrete models are necessary to describe the mechanical response of a heterogeneous material (*Bažant and Jirásek*, 2002).

The continuum limit is an important characteristic length scale in the analysis of slab avalanches, one that can be defined in a number of ways. It can be considered as the size of the Representative Volume Element (RVE), the minimum volume for which continuum relations are applicable for the material (e.g. *Bažant and Pang*, 2006). As with polycrystalline ice, the continuum or homogeneity limit may be expressed as a multiple of the grain size. For freshwater and sea ice, this limit has been expressed as a requirement that the initial crack length as well as the unbroken ligament in a fracture test be greater than about 10–100 times the grain size (*Dempsey et al.*, 1999a,b; *Mulmule and Dempsey*, 2000; *Schulson and Duval*, 2009). The homogeneity requirement for snow may be of a similar order of magnitude in terms of a grain scale multiple.

Fracture process zone

Provided that the continuum limit is satisfied, another critical length scale in the fracture of snow is the length of the fracture process zone (FPZ). The FPZ is a zone of softening damage ahead of an existing or coalescing crack in a heterogeneous material (e.g. *Cotterell and Mai*, 1996; *Bažant and Planas*, 1998). For a material such as snow, this inelastic zone is likely characterized by distributed bond breakage ahead of a traction-free crack or notch. The open structure of the ice matrix in porous cohesive snow will necessarily force an advancing fracture to have a distributed or diffuse nature, making an unambiguous definition of a "crack" in snow difficult.

The FPZ may also be defined as the minimum length scale, dependent on the material microstructure, over which strain can localize (*Bažant and Pijaudier-Cabot*, 1988). In this sense, the FPZ may be physically related to the size of the RVE at the continuum limit. Initial estimates of the effective process zone length in both shear and tension are on the order of 50-100 times the grain size (*Bažant et al.*, 2003; *McClung and Schweizer*, 2006; *Sigrist*, 2006).

The length scale of the FPZ is fundamental for any scaling relation for the fracture mechanics of slab avalanches and determines, for example, the structural scale (if any) at which Linear Elastic Fracture Mechanics (LEFM) is applicable for analysis of slab avalanches. In order for LEFM to be applicable, the characteristic length scale(s) in the fracture problem need to be at least an order of magnitude greater than the effective process zone size or more, depending on geometry (*Bažant and Planas*, 1998).

Therefore, careful consideration of several length scales is necessary in the analysis of slab avalanches. No fracture mechanical study to date has addressed explicitly the continuum limit, though the application of continuum mechanics implicitly assumes that this limit is satisfied. If the RVE is of similar size as the FPZ, and if these length scales are on the order of about 100 times the grain size, then specimen sizes on the order of 5-10 cm are necessary for homogeneity and the applicability of continuum mechanics. Specimen sizes on the order of 1 m would be necessary for the direct applicability of LEFM, though sampling and testing natural snow specimens of this size would be impractical, if not impossible. However, the grain size multiple that defines the continuum limit and process zone size are highly uncertain given the sparsity of data currently and the large scatter in the data on which these estimates are based.

The cohesion threshold for fracture propagation and the length scales discussed above are represented schematically in a Cartesian classification scheme in Figure 1.5. The cohesion is represented on the ordinate (y-axis) and the spatial scale on the abscissa (x-axis). The domain of applicability of fracture mechanics for analyzing avalanches is represented as the region above both the continuum limit length scale and the cohesive threshold. The LEFM limit length scale defines the regions for which quasi-brittle (nonlinear) fracture mechanics versus LEFM apply. Below the cohesive threshold, loose snow is adequately characterized by material properties. Above the cohesive threshold, slab snow takes on structural properties that may not be adequately characterized by material properties such as density. The present study constrained the quantitative definition of the cohesive threshold, the LEFM limit, and the effective process zone length.

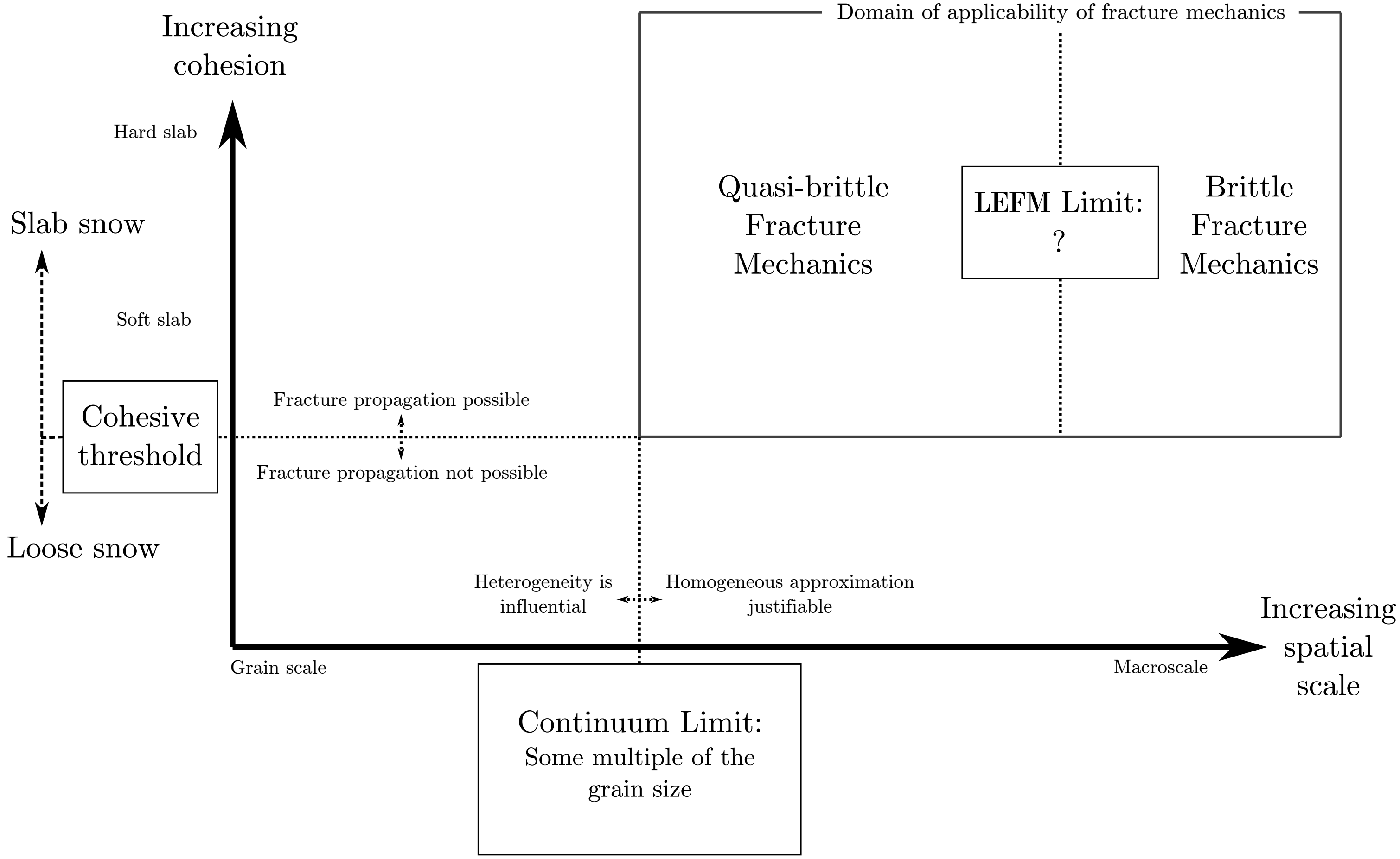

Figure 1.5: *Scale-Cohesion classification of snow for the purpose of analyzing avalanches. The cohesive threshold is defined as the limit at which snow has sufficient internal cohesion (tensile strength) to support the propagation of fractures. Continuum mechanics only applies to snow at length scales above the continuum limit, a length scale which has not been rigorously defined but may be on the order of 10–100 times the grain size. The size of the fracture process zone in slab avalanche fractures may also be on the same order of magnitude. The domain of applicability of fracture mechanics is defined by both the cohesive threshold and the continuum limit length scale. Linear elastic fracture mechanics (*LEFM*) is only valid above a length scale for which the size of the fracture process zone is negligible. This limit is ill-constrained for snow.*

1.4.3 Nonlinear quasi-brittle fracture mechanics

Provided that the continuum limit is satisfied, and that a large fracture process zone is present (a safe assumption), a nonlinear fracture theory is necessary for analysis of fractures in cohesive snow. One approach to accounting for nonlinearity is by defining an elastically equivalent crack system that gives the same global response, such as energy dissipation or the stress-displacement curve, as in the actual specimen (e.g. *Cotterell and Mai*, 1996; *Bažant and Planas*, 1998). This type of approach smears out all of the toughening mechanisms in the process zone using a single parameter that represents the difference in length between the actual and equivalent cracks (*Bažant and Gettu*, 1992). The framework of LEFM is then applied to the equivalent specimen, which is an advantage of this approach since the theoretical foundation of LEFM is well developed. Furthermore, the quasi-brittle fracture mechanical scaling laws of *Bažant and Planas* (1998); *Bažant* (2005) contain LEFM as an asymptotic limit for vanishing process zone size or increasing specimen size, so the safest and most general assumption for the analysis of fractures in heterogeneous materials is that a large fracture process zone is present.

The equivalent elastic crack technique is not designed to explore the micromechanical details of the process zone itself (*Mindess*, 1991). If this was the objective, a variety of direct and indirect techniques are available: acoustic emissions, scanning electron microscopy, stereo imaging, and interferometry, to name just a few (e.g. *Mindess*, 1991; *Cotterell and Mai*, 1996). Alternatively, if the full softening-displacement curve is known or measured for the actual specimen, the elastically-equivalent process zone length can be related to the length of the actual process zone (e.g. *Planas and Elices*, 1989; *Bažant and Kazemi*, 1990b).

For situations in which the nonlinearity is too great to use the equivalent elastic crack approach, a variety of alternative nonlinear techniques are available. Examples include the crack band model, the cohesive crack model, the J-integral, multiple-parameter models, or numerical techniques (e.g. *Cotterell and Mai*, 1996; *Bažant and Planas*, 1998; *Bažant*, 2005).

1.4.4 Rate effects in the fracture of snow

The proximity of snow to its melting temperature and the resulting thermodynamic instability gives rise to important rate effects for most rates of loading (e.g. *Bader and Kuriowa*, 1962; *Mellor and Smith*, 1966; *Narita*, 1980; *Schweizer*, 1998). In solid ice, creep effects are also important in all but the fastest fracture tests (e.g. *Dempsey et al.*, 1999b; *Schulson and Duval*, 2009). Rate-dependent results in experimental data for snow and ice should be expected as a general rule. Accordingly, systematic and thorough testing for rate effects should be part of nearly any experimental study of the mechanical properties of snow.

For laboratory tests on snow, *Bader and Kuriowa* (1962) suggested that loading times to failure of less than 10 seconds are necessary to avoid inelastic effects. Rate effects are present in snow at least up to strain rates of 10^{-3} s^{-1} in uniaxial tension (*Narita*, 1983) and 10^{-2} s^{-1} in unconfined compression (*Mellor and Smith*, 1966). In both studies, the beginning of what appeared to be an asymptotic limit strength for higher strain rates was observed, suggesting an approach to fully elastic response.

A ductile-to-brittle transition has been observed for snow at a critical strain rate of $2.5 \times 10^{-3}\ s^{-1}$ in unconfined compression (*Mellor and Smith*, 1966), $10^{-4}\ s^{-1}$ in uniaxial tension (*Narita*, 1980, 1983), and about $10^{-3}\ s^{-1}$ in shear (*Schweizer*, 1998). A similar transition in solid ice has been observed as a function of strain rate (*Schulson and Duval*, 2009). This transition can be explained as a balance between competing effects of creep and fracture in the material; below the transition, creep leads to crack blunting, while above the transition crack propagation dominates (*Mellor and Smith*, 1966; *Schulson and Duval*, 2009). As such, this transition might be more appropriately labeled a "creep-to-fracture" transition. This terminology was adopted for the present study to avoid confusion between the terms "brittle" and "quasi-brittle" as applied to the linear and nonlinear fracture theories, respectively, discussed above.

The creep-to-fracture transition marks the strain rate at which maximum strength values have been measured as a function of strain rate for a given type of snow (*Mellor and Smith*, 1966; *Narita*, 1980, 1983; *Schweizer*, 1998). The critical transition shifts toward higher strain rates as the snow temperature approaches the melting point (*Narita*, 1983), a similar trend as in solid ice (*Schulson and Duval*, 2009).

These transition strain rates do not define the limits of applicability of elasticity theory, rather the point at which viscous and elastic effects are critically balanced. Strain rates much higher than the critical transition are likely necessary before snow responds fully elastically. However, no consistent and systematic approach for defining a fully elastic strain rate for different types of snow under various loading scenarios has been developed. That said, an equivalent elastic fracture analysis as an approximation to a fully viscoelastic solution is acceptable as long as the creep strain at failure is not too large (*Bažant and Gettu*, 1992). In this type of elastic-viscoelastic correspondence, the elastic modulus is replaced by an appropriate effective modulus, such as the creep compliance for the time to failure or the secant modulus at peak load (e.g. *Schapery*, 1997; *Dempsey and Palmer*, 1999).

The effective size of the fracture process zone in snow is expected to have a rate dependence, as in concrete (*Bažant and Gettu*, 1992). Even above the creep-to-fracture transition, creep effects within the fracture process zone and bulk relaxation away from the FPZ are likely to diminish the effective size of the FPZ (see e.g. Figure 7.2, *Bažant*, 2005). Thus, separate creep effects may need to be considered in the bulk of the material and within the strain-softening fracture process zone (*Cotterell and Mai*, 1996; *Bažant and Li*, 1997). Though rate dependence in tensile strength measurements has been demonstrated (e.g. *Narita*, 1980, 1983), no studies to date have investigated the sensitivity of fracture parameters such as the fracture toughness or process zone length to loading rate.

When speaking of rate effects, distinction should also be made between the rates of loading (or unloading) relevant for an avalanche and analogous rates in lab-scale or in situ tests. For the avalanche case, the dynamic unloading of the slab as the weak layer fractures should occur at a high enough rate that the slab behaviour can be considered mostly elastic (*Bažant et al.*, 2003). Viscous effects may still play a role in some avalanche cases, especially for post-control releases or for cases where progressive strain softening in the weak layer rather than rapid fracture is responsible for avalanche triggering (*McClung*, 1981). Furthermore, humans, snow machines and explosives apply loads to the snow surface at different rates, for which the response of the slab is expected to differ from the perspective of avalanche triggering.

1.4.5 Note on temperature effects

Given the proximity of snow to the melting temperature, one would expect the material and structural properties of snow to display strong temperature dependence. In some cases, this is true. The creep and creep rate of snow are more sensitive to temperature than any other properties (e.g. *Bader and Kuriowa*, 1962). Creep parameters for ice are also highly sensitive to temperature (*Schulson and Duval*, 2009).

However, elastic properties of snow and ice are only weakly dependent on temperature. The strength of snow weakly increases with decreasing temperature (*Roch*, 1966; *Narita*, 1983). The stiffness, or the initial tangent modulus, may be more sensitive to temperature than strength (*McClung*, 1996). For solid ice, the elastic stiffness increases by only 5% as the temperature decreases from $0°C$ to $-50°C$ (*Schulson and Duval*, 2009). The fracture toughness of solid ice is only weakly dependent, if at all, on temperature over the range

$-2°C$ to $-50°C$, and the tensile strength follows a similar trend over a temperature range from $0°C$ to $-30°C$ (*Schulson and Duval*, 2009).

Therefore, strong temperature effects in experimental data are indirect evidence of the presence of creep effects. The present study aimed to measure properties that were mostly elastic in accordance with the expectation of slab behavior in avalanches. In order to achieve this, the loading rates in experiments were chosen to produce nominal strain rates well above the creep-to-fracture (ductile-to-brittle or viscous-to-elastic) transition. Thus, temperature effects were expected to be second-order at most.

1.5 Summary

To summarize and emphasize many of the points raised above, several key principles and hypotheses which guided the present study are reviewed here.

1. The tensile fracture properties of cohesive snow have yet to be systematically correlated with any index properties which represent the *structure* of the snow. The tensile strength has been shown in a few studies to correlate well with penetration resistance, thus parameters such as fracture toughness are likely to be well explained by some quantifiable measure of penetration resistance or other index property which is sensitive to snow structure. Such an index is also likely to help explain some of the observed scatter in properties when expressed as a function of density.

2. If a *continuum* property such as strength or toughness is to be correlated with a hardness measure or other index measure for snow structure, the measure should characterize the snow over a continuum length scale, that is a length scale for which a continuum approximation of snow is justified.

3. Important *length scales* in the fracture of snow, specifically the length of the fracture process zone or length defining the limit of applicability of linear elastic fracture mechanics, remain to be constrained. These length scales are likely to be influenced by rate effects.

4. Systematic testing for *rate effects* needs to be carried out for any fracture experiments on snow. A significant difference in properties calculated from tests at different rates should be expected in most cases. Rate effects and temperature effects may be difficult to separate and easy to confuse.

5. The most appropriate starting assumption for an analysis of snow fracture, which follows from physical reasoning related to the structure of snow, is that a large fracture process zone engenders *nonlinearity in fracture*. This nonlinearity may be accounted for approximately using equivalent elastic fracture mechanics, which in some cases requires only the measurement of peak loads in fracture experiments and allows the general framework of LEFM to be used, but leads to scaling laws which are nonlinear.

6. A *size effect* will be important for relating the results of lab-scale strength or fracture experiments to the avalanche scale. Careful measurement of the size-dependence of test results, over as wide a size range as possible, should to be conducted for fitting results to fracture mechanical scaling relations and for calculating relevant properties for full-scale analysis of avalanches.

1.5.1 Chapter outline

Chapter 2 contains a description of the experimental methods used for the present study. Some methods were adopted from previous snow studies or analogous studies of other heterogeneous materials. Most of the techniques for characterizing the in situ properties and stratigraphy of snow came from industry-adopted standards. Beam bending tests were conducted in a cold lab to measure the tensile (flexural) properties of cohesive snow. The nature of snow compared to other engineering materials necessitated the development of several new tools and techniques for the laboratory testing. Many of the newly-developed experimental methods represent a significant original contribution of the present study.

In Chapter 3, a new thin-blade penetration resistance gauge is introduced that was developed for characterizing snow structure over a length scale (on the order of 10–100 grain contacts) relevant for a continuum description of the fracture of slab avalanches. The blade hardness index, defined as the maximum resistance to penetration, was a highly repeatable measure across observers compared to the common and subjective hand hardness test. This new tool is small, inexpensive, easy to use and is being adopted by several practitioners in the avalanche industry. The blade hardness index was a better variable than density, or any other variable, for correlating with the tensile strength and fracture toughness data from the present study.

Chapter 4 contains a review of the extensive literature on the tensile strength of snow, a re-analysis of much of this data and a contribution of hundreds of new measurements. The literature review synthesized around 2000 measurements from 20 sources, mostly expressed as a function of density. Much of the data was re-analyzed to account for neglected geometric stress concentrations in the experiments. The data from the present study included 245 unnotched beam bending experiments in the cold lab which were used to calculate the tensile (or flexural) strength. The new data was systematically correlated with and analyzed for dependence on density, hardness, grain size, loading rate, and specimen size. General agreement was found between the existing and new strength data when expressed as a function of snow density, though with large scatter. The results of the current study challenge the existing norm of indexing snow properties only against the density, in light of the wide scatter in strength values at a given density and the better correlation of strength with penetration resistance. This chapter now represents the largest collection of data on the tensile strength of dry alpine snow in the literature.

Chapter 5 contains an analysis of 23 different test series, covering nearly 300 experiments, that measured the nominal strength of beam samples in three and four point bending over different specimen sizes and relative notch depths. The data were analyzed using Bažant's equivalent elastic crack (quasi-brittle) theories for the size effect. Fitting of these theories through the experimental data led to a collection of fracture parameters such as the fracture toughness, effective process zone length, transitional size bridging plasticity and LEFM in notched tests, and boundary layer thickness over which cracks initiate in unnotched tests. These properties were related to density, penetration resistance and loading rate. As with the tensile strength data, the fracture toughness was better correlated with thin-blade penetration resistance than density. The fracture toughness and effective fracture process zone length both showed rate dependence. Best estimates for the length of the fracture process zone in snow slab tensile fractures, at rates sufficiently high to minimize creep strains, are given as a function of the grain size.

A numerical modeling approach based on continuum damage mechanics and some results of simulations of the laboratory experiments are given in Chapter 6. The nonlocal isotropic damage model was applied for the first time to simulate the initiation and propagation of tensile fractures in snow. The length scale over which nonlocal averaging was conducted in the simulations was related to the critical equivalent crack extension from the experimental data. A sensitivity analysis was conducted to explore the dependence of the numerical results on the most uncertain model parameters. Subsequently, a prescriptive algorithm was developed for determining numerical parameters based on the results of experimental bending tests. This algorithm was tested against the results of 10 different experimental series, and generally good agreement was found between the simulations and experiments. The model was able to reproduce key features of the experimental load-displacement curves, such as the mean peak load, rounding of the curve near peak load, and strain softening following peak load, that are consistent with a quasi-brittle fracture mechanical interpretation of the failure process. Since no additional tuning of numerical parameters was conducted to improve the fits, these results are promising for future predictive applications of the numerical model to simulate full-scale avalanche fractures for which no experimental data is (or ever will be) available.

Chapter 7 contains overall conclusions of the present study and a discussion of the results with respect to the hypotheses, guiding principles and general themes laid out here in the introduction. A number of recommendations for future research are discussed, building on and refining the methods and results of the present study. The implications of the present study and their link with the larger field of snow and avalanche mechanics are given.

Three appendices are include for reference. Appendix A contains images and analysis of the fracture morphology from the bending experiments, demonstrating that the experiments indeed failed by the propagation of single tensile fractures. Appendix B contains background related to the goodness of fit of the nonlinear regression models used to fit much of the experimental data. Appendix C contains equations for the order-of-magnitude calculations of the creep strains in the experiments given the observed times to failure.

Chapter 2

Methods

The experiments in the present study were carried out at Rogers Pass in the Selkirk range of the Columbia mountains of British Columbia, Canada. The TransCanada highway travels through Rogers Pass, which lies within Glacier National Park of Canada. The pass sits at an elevation of 1320 m.a.s.l., and the cold lab and primary study plot are located in a compound (Figure 2.1) of several buildings operated by Parks Canada as part of the service of road maintenance, avalanche forecasting and control, and parks operations.

The natural setting of the Rogers Pass area is a great location for snow and avalanche research. It was possible to sample natural snow of a variety of types from multiple elevations. Natural snow samples were used entirely for the present research. Avalanche activity is frequent along the highway through Rogers Pass in the winter, which allows researchers to gain a close (though hopefully not too close) appreciation for the phenomena at hand. Living quarters were provided by Parks Canada for me and field assistant(s) for each of the three winters of research conducted for this study. This was a tremendous benefit, as the cold lab and primary study plot were both within walking distance from the apartment building. It would not have been possible to carry out such a large number of experiments without this kind of institutional support for avalanche research.

This chapter contains descriptions of the principal experimental methods of the present study. Only one previous experimental study of a similar kind had been conducted on which to build (*Sigrist*, 2006), but much of the detail related to experimental methods was omitted. Some similar methods were adopted, however, as will become apparent. The chapter sections are organized around the primary locations where each

Figure 2.1: *Overview of Rogers Pass and the Parks Canada compound where the cold lab is located.*

technique was utilized, starting with in situ characterization of snow properties, followed by the methods of snow sample extraction, transport and storage in the cold lab. Finally, detailed summaries are given of cold lab testing equipment, methods, and a few results related to the unique experimental design considerations for a material such as snow.

2.1 In Situ Snow Stratigraphy Characterization

At the start of each field day, a standard snow profile observation was conducted, following avalanche industry guidelines (*Canadian Avalanche Association (CAA)*, 2007). This profile included the observation and description of the stratigraphic layering of the snowpack and the demarcation of the snow into a discrete set of layers, each with approximately homogeneous properties. For each identified layer, measurements or descriptions of the hand hardness index, size and form of the snow crystals (grains), density, temperature, and the wetness of the snow (only dry snow was considered in the present study). Additionally, meteorological and site characteristics were recorded such as the slope angle, aspect, elevation, sky cover, wind speed and direction, air temperature, type and rate of precipitation, and depth of foot penetration into undisturbed snow. Detailed descriptions of the observations and measurements most important to this study are given below.

2.1.1 Study plots

Snow was extracted from two primary sources in the present study. The most common source of snow was from a sheltered study plot within the Rogers Pass compound, a short walk from the cold lab at an elevation of 1320 m (Figure 2.2a). This plot was on mostly flat ground, surrounded on three sides by trees and on the fourth by two apartment buildings. The plot was therefore mostly sheltered from wind effects. The area of the study plot was approximately 10 m by 50 m. All snow sampled from this study plot was taken a distance of, at minimum, 1.5–2 m away from any previous snow pit location. This was to ensure that previously exposed snow surfaces did not alter the natural state of the sampled snow, at least no more than would be detectable above other environmental drivers of snow metamorphism.

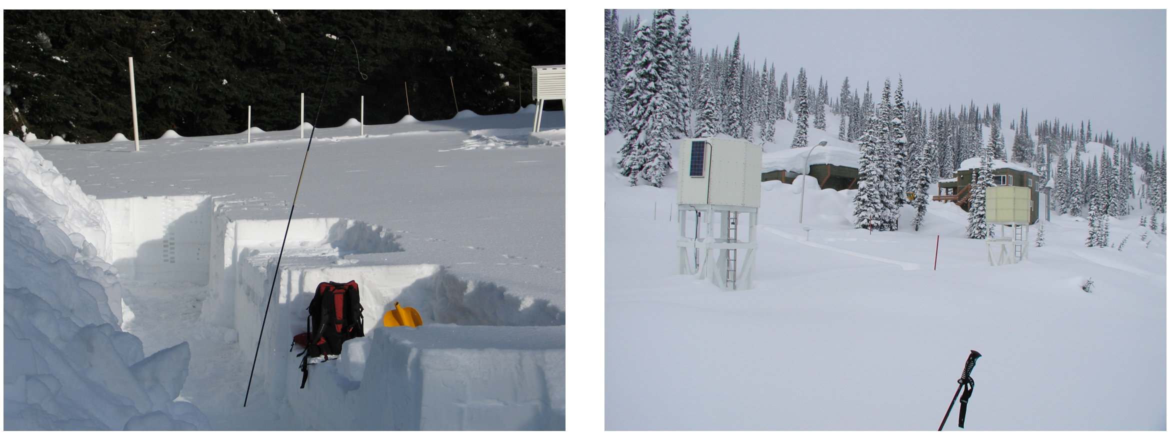

(a) **(b)**

Figure 2.2: *Primary study plot at Rogers Pass, showing the remnant holes of previous snow pits (a); secondary study plot at Mt. Fidelity research station, accessed by snow machines (b).*

Occasionally, when snowmobile or snowcat transportation was available, snow was sampled from a study plot near treeline at an elevation of 1900 m on Mt. Fidelity (Figure 2.2b). This mountain is a short drive west from Rogers Pass and is the location of a permanent research station used by the Avalanche Control Section of Parks Canada for monitoring snow and weather conditions. Snow was typically sampled from flat terrain near the research station. Snow samples were packed into insulated boxes for transportation back to the cold lab. The samples were first transported on a snow cat back down to the highway and were then driven to Rogers Pass and carried into the cold lab.

2.1.2 Snow pit preparation

Once a study site was chosen for a particular day, a snow pit was dug in an area free of disturbances with as uniform a shape as possible. The dimensions of the pit were typically around 2 m by 4 m, with a depth that depended on the particular layer of interest that day. The pit was typically dug to a depth of at least 50 cm below the layer of interest to facilitate more ergonomic sample extraction. Figure 2.3 shows a sharp corner being prepared in a new snow pit. One such sharp corner, the principal location for making stratigraphic observations, was prepared in every pit. The walls of the snowpit were shaved such that the 90° corner was fully shaded to prevent solar radiation from changing the exposed snow crystals before or during the observations. The axis of the corner was oriented vertically regardless of slope angle. All standard stratigraphic observations prior to sample extraction were made from these corners.

Figure 2.3: *Preparing the observation corner of a snow pit. Photograph by Elisabeth Hicks.*

2.1.3 Identification of layering and distinct stratigraphic boundaries

Once the snowpit was finished, the major stratigraphic boundaries were identified. The primary indicator of a major stratigraphic boundary was a distinct change in the snow hardness, as measured using the force required to penetrate the snow by hand or using a thin plate or card. Many interfaces could also be identified visually from a change in the size or type of snow crystals. Often, one or more layers within the snowpack could be identified by the presence of dirt or dust which was deposited on the snow surface earlier in the season and then buried by subsequent snowfall. These “dirty” layers could be dated and used to more easily locate and reference other layers within the snowpack. A common paint brush was typically used to brush out layering detail on an exposed pit wall. This technique often helped to locate thin and weak layers within the snowpack.

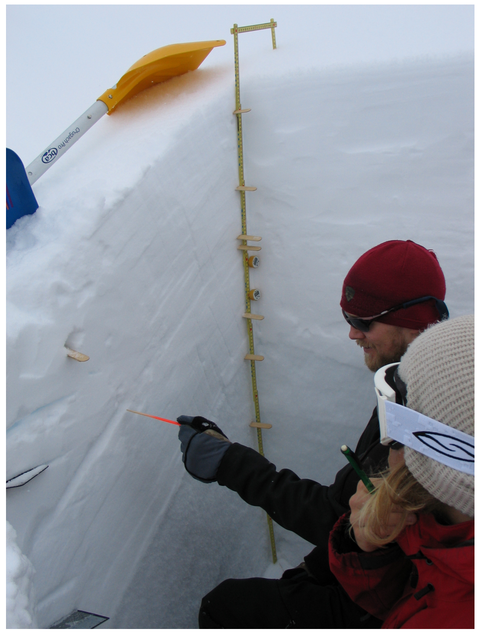

Figure 2.4: *Photograph showing observation corner of a snowpit, with the author and field assistant discussing a weak layer. Markers next to the meter stick in the corner indicate major stratigraphic boundaries within the snowpack. Photograph by Elisabeth Hicks.*

Layer boundaries were identified using markers placed next to a meter stick in the observation corner, as in Figure 2.4. Note also the presence of two digital thermometers in the observation corner. The shovel on the snow surface was used to shade the measurement of the snow surface temperature and the temperature within the first 30 cm below the surface. The stratigraphic boundaries were recorded using the distance of the boundary from either the snow surface or the ground.

2.1.4 Snow crystal identification and classification

Once the stratigraphic boundaries were located and recorded, the type and size of snow crystals (the terms *snow crystals, crystals* and *grains* are used synonymously throughout this text) were determined and recorded. Crystals were sampled from the exposed snowpit wall by lightly scraping the wall with a metal or plastic card. The crystals were then gently disaggregated by tapping the card, allowing individual crystals or small clusters of crystals to spread out on the card. The surface of the card had several painted grids, varying in size from typically 0.5 mm to 2 mm or more in spacing. This grid aided in the determination of the grain size, defined as the *average maximum linear extension* of the grains (*Canadian Avalanche Association (CAA)*, 2007). Note that this procedure and definition of grain size is highly subjective. Crystals were viewed using a hand lens with a magnification of typically 8-12 times (Figure 2.5). Care was taken to ensure that the snow crystals were not exposed to sunlight or heat from hands or gloves. Often, several samples of crystals were taken from within a layer to add confidence to the observations.

(a) **(b)**

Figure 2.5: *Photographs showing the procedure for observing and classifying snow crystals. Photographs by Steve Conger (a) and Elisabeth Hicks (b).*

The crystals within each layer were classified and recorded using the International Classification for Seasonal Snow on the Ground (*Colbeck et al.*, 1990; *Fierz et al.*, 2009). Note that during the course of this investigation the old standards (*Colbeck et al.*, 1990) were updated, and several changes to the grain form classification were made in the updated standards (*Fierz et al.*, 2009). For reporting the grain forms in this text, all grain form classes have been converted, where possible, to the new (2009) standard.

2.1.5 Density and hardness

The density and hardness of the snow were measured in a wall of the snow pit adjacent to the observation corner, parallel to the snow layering. The density was measured by extracting a sample of snow using a stainless steel rectangular cutter and then weighing the snow sample. The most common density sampler had a volume of 100 cm^3. Since the density sampler was 3 cm thick, the density was typically recorded every 3 cm of depth from the surface of the snow to the bottom of the snowpit (often the ground). This produced a stepwise continuous profile of density as a function of depth.

The hand hardness index of each layer was recorded by pushing a gloved hand into the snow. The objective of the hand test is to record the object (gloved hand in various cross-sectional shapes, pencil or knife) that can be pushed into the snow using the given 10–15 N force. For example, if the snow was too hard to insert a gloved finger using no more than 10–15 N of force, then the blunt end of a pencil or a knife was used to penetrate the snow. The hardness was recorded as the object which most closely required the given (10–15 N) force to penetrate. Variations in hardness were recorded using "+" and "-" qualifiers, representing approximately one-third level deviations above and below the given index value, respectively.

A new thin-blade penetration resistance gauge was developed for measuring an alternative and more objective value of hardness for each snow layer (*Borstad and McClung*, 2011). A 10 cm wide blade with a 0.6 mm blunt leading edge was attached to a digital push-pull gauge. The blade was inserted into the snow at a penetration rate slightly faster than the hand hardness test, and the maximum force of penetration was recorded as the blade hardness index. Chapter 3 is devoted to the design, use and analysis of data obtained using this new gauge.

Figure 2.6 shows an overview of a snowpit after the stratigraphic profiling and sample extraction were completed. The meter stick is still present in the observation corner. The small round holes to the left of the meter stick are finger holes left by the hand hardness test. Further to the left, the regular array of holes are remnants of the density sampling. Next to each density sample, the blade hardness index was measured. Repeated measurements of the blade hardness index were also conducted within the layer from which samples were extracted.

Figure 2.6: *Photograph of a snowpit following stratigraphic profiling and snow sample extraction.*

2.2 Snow Sample Extraction, Transport and Storage

All snow samples in the present study were extracted from layers of natural snow which were approximately homogeneous in snow properties with depth. Following the standard stratigraphic profile, a specific layer was selected from which to extract samples for lab testing. This selection was based on a number of criteria. First, the layer needed to be reasonably homogeneous in properties such as density and hardness with depth. The standard stratigraphic profiling technique, which separated the snowpack as best as possible into individual layers with approximately homogeneous properties, ensured that this criterion was met. However, even snow layers which were considered homogeneous in the field typically had a layered structure, even if properties such as density and hardness did not change appreciably (Figure 2.7).

Second, the snow layer needed to be at least 10 cm thick to allow the insertion of the beam-shaped

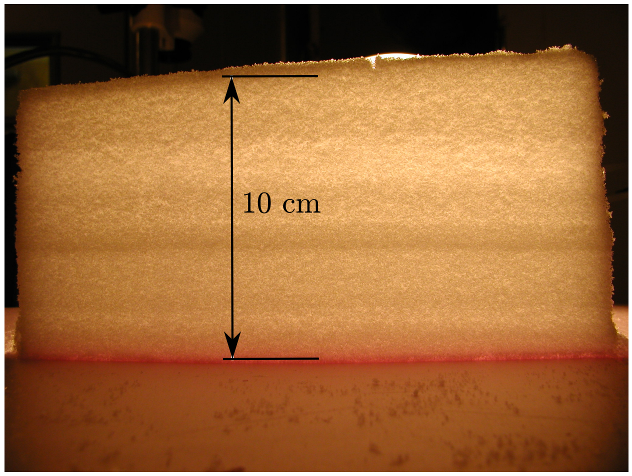

Figure 2.7: *Thin-shaved snow sample, lit from behind, showing the layered structure of the snow. This sample was taken from a layer judged to be homogeneous in the field. Common hand tests for determining stratigraphic layer boundaries often miss subtle changes in layering such as this. For this reason, fracture specimens were oriented such that tensile fracture propagated parallel to the layering (into or out of the page) rather than across the layering (up or down through the layering).*

sample cutters, all of which had a width of 10 cm. The width of the beam was always oriented normal to the slope, which allowed beams of different depth and span to be extracted from any layer at least 10 cm thick. Layers of 15 cm or more thickness were preferred in order to guarantee that the sample cutters did not deviate from the layer during insertion.

If multiple layers were available that met the criteria of homogeneity and thickness, then selection was based on the particular type of test series that was being conducted on that day. As much as possible, a wide variety in types of natural snow were sought for study. If a particular test series had been conducted previously using high-density or high-hardness snow, then lower density and hardness snow would be given preference if available.

2.2.1 Sample extraction and transportation

The samples were excised using stainless steel rectangular boxes, open on both ends. Table 2.1 shows the dimensions of the five different sample cutters used in this study. Note that the free ends of the beam-shaped samples often needed to be trimmed off to ensure consistency across all samples within a data set, so the values of L represent the maximum possible length of the samples. In the lab, the actual length of the prepared sample prior to testing was recorded in place of the value of L in Table 2.1.

The width W of the cutters was always oriented slope-normal during extraction. This forces the tensile fracture in the laboratory bending test to be oriented parallel to the stratigraphic layering of the snow, as in Figure 2.8 (also Figure 1.3b). This orientation provides an average measure of the fracture properties of the layer, as the tensile crack initiates across all layers simultaneously and propagates parallel to the layering. The chosen orientation was judged to allow the most consistent sampling technique for repeatability. The alternative would be to orient the samples and resulting tensile fracture perpendicular to the layering. Although this orientation would correspond to the initial tensile fracture in a slab avalanche (Figure 1.3a), homogeneous layers that are 20 cm thick or more, which would be necessary to test for size effects, are rare in an alpine snowpack. Even 10 cm-thick layers can be difficult to find at times over the course of a winter.

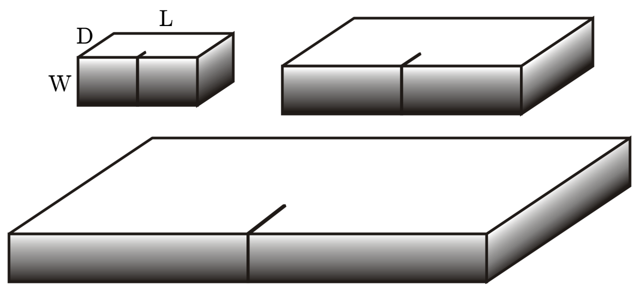

Figure 2.8: *Schematic showing orientation of notched beams of different sizes taken from the same layer (not to scale). The width of the beams was oriented normal to the slope so that the fracture propagated parallel to the layering and across all layers simultaneously.*

D (cm)	L (cm)	W (cm)
2.5	12.5	10
5	25	10
10	50	10
15	75	10
20	100	10

Table 2.1: *Dimensions of beam-shaped snow sample cutters.*

Prior to sample extraction, either the top or bottom of the snow layer of interest was marked along the snowpit wall adjacent to the observation corner (Figure 2.9). All but approximately 30 cm of snow above the layer of interest was removed in order to facilitate cutting the back of the samples once the cutter was inserted. The saw used to cut the back of the samples is just sticking out of the snow in the right of Figure 2.6. Figure 2.9a shows a layer from which all samples extracted had the same dimensions (10 cm by 50 cm by 10 cm), whereas figure 2.9b shows a layer from which samples of a variety of sizes were extracted.

(a) **(b)**

Figure 2.9: *Photographs of snow pits showing holes left by snow sample extraction from the study plot at Rogers Pass (a) and at Mt. Fidelity (b). Note the coloured markers placed along the boundary of the extraction layer for reference.*

The cutter for the most common sample size used in the present study (with D = 10 cm) is shown in the lower right of Figure 2.6. Next to the cutter is a plunger used to gently push the sample out of the cutter. Samples were pushed onto a large, thick styrofoam sheet on the snow surface. Once the sheet was full of samples, it was either carried directly to the cold lab (if using the study plot near the lab) or, if using the Mt. Fidelity study plot, packed into a large insulated box for transport back to the lab (this box is just visible to the right of the person in Figure 2.9b).

2.2.2 Sample storage prior to testing

Once in the cold lab, the samples were stored in the open (Figure 2.10) for as short a period of time as possible prior to testing. This was to ensure that the snow changed as little as possible, compared to the state it was in at the time of extraction, due to the different thermodynamic environment of the lab. Though the temperature of the lab was usually set to mimic the temperature of the snow layer from which the samples originated, the humidity of the lab was lower than that of the pore air in the snowpack, which is typically at 100% (*McClung and Schaerer*, 2006). Small changes in the snow crystals were observed within just a couple hours after arrival in the lab. As a result, testing of the samples commenced within typically 2 hours after all samples were in the lab. Most test series in the lab lasted 2-4 hours, so the maximum time that a sample was exposed in the lab prior to testing was about 6 hours.

Figure 2.10: *Photograph of specimens of different sizes stored in the cold lab prior to testing.*

2.3 Laboratory Testing

The experiments were carried out in a cold laboratory located in the Parks Canada compound at Rogers Pass. The floor plan of the lab is 3.3 m by 3.3 m with a ceiling height of 2.2 m. This small size limits the space available for storage of samples amid the other testing equipment and space for two people to move about and work. The temperature of the lab can be controlled down to about -20°C. The air temperature within the lab fluctuates within about 2 degrees of the set temperature. The lab was always kept colder than about -5°C to avoid any melting of the snow samples during preparation or handling, as the heat generated by some of the instruments in the lab melted snow crystals at higher ambient air temperatures. Humidity control was unavailable in the lab.

The lab contained a microscope, a digital scale, table top space for sample storage and preparation, miscellaneous tools and instruments related to sample preparation and handling, and a universal testing machine. Details and photographs of key experimental procedures are given below.

2.3.1 Universal testing machine

A bench-top universal testing machine supplied by Adelaide Testing Machines (model SO-200) was used for the bending experiments (Figure 2.11). A number of custom modifications were made to the machine to ensure reliable and repeatable operation at sub-freezing temperatures. Most importantly, the motor and electrical housing of the machine was heated by a custom-built internal heater with a programmable thermostat, which allowed the internal temperature of the machine to remain above freezing. Additionally, the ball-screw on which the actuator travelled was lubricated with a silicone-based lubricant for better operation at low temperatures. The entire base of the machine was insulated with styrofoam sheets. Finally, legs were constructed on the back of the machine to allow it to be placed on its back for horizontally-oriented tests. This manner of testing will be discussed further below.

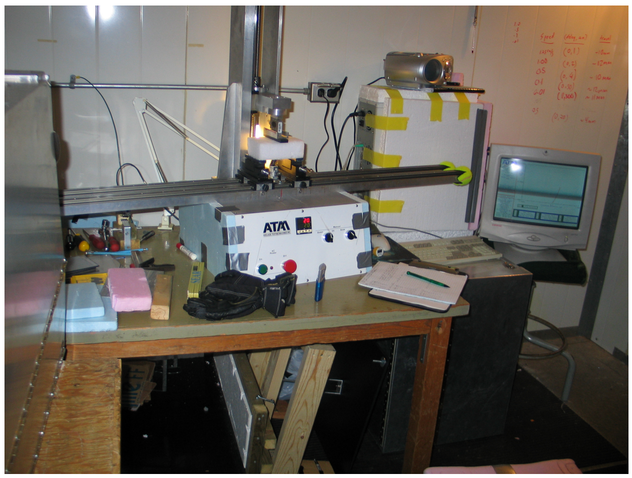

Figure 2.11: *Photograph of bench-top testing machine set up for a bending test in the cold lab. The computer which controlled the machine is to the right.*

The testing machine was operated by a PC running Windows 98 software. The CPU of the computer was insulated with thick styrofoam sheets to buffer the electronics from temperature changes which might promote condensation on the internal circuitry. Surprisingly, no computer problems related to operation at low temperatures were encountered. The control software allowed only basic open-loop displacement control of the machine crosshead. No cyclical or load-control experiments were possible, nor was closed-loop servo control. This software limitation was related to the design specification for as high a crosshead speed as possible. Fast loading rates to minimize viscous effects were one of the most important design considerations in the present study, and this required a simplified software routine given the chosen testing machine and budget constraints.

The control software was only capable of recording 1200 data points per test. It was necessary to adjust two control parameters to achieve the desired sampling frequency without going over this limit. One parameter determined the time delay between recorded points relative to the processor speed of the CPU.

This parameter was therefore a sort of sampling period. The second parameter determined an averaging interval for curve smoothing. In nearly every test in the present study the average interval was set to 1, that is no averaging was performed and the raw curve was recorded. The sampling period was empirically adjusted in order to maximize the sampling frequency without hitting the 1200 point limit in the duration of a test. If this limit was reached, the test was aborted. In tests performed at the fastest crosshead speed possible, this limit was never reached. However, tests at slower crosshead speed were sometimes recorded with low sampling frequencies if the sampling period parameter was not set correctly.

The crosshead displacement and load indicated by the load cell were recorded for every test. An encoder on the DC servo motor drive shaft was used for the crosshead displacement and speed calculations and control. The sampling frequency was adjustable using the control software, as described above. For the fastest loading rates (1.25 cm s^{-1}), the sampling frequency was in the range of 500–1400 Hz, depending on the averaging interval.

The actuator (crosshead) of the testing machine was mounted with an HBM RSC load cell. During the winter of 2006–2007, a load cell with 250 N capacity was used. This initial load cell was selected based on estimated values of nominal strength calculated using beam theory compared to published values of the tensile strength of snow (*Jamieson and Johnston*, 1990). However, many tests during this first season had peak loads which exceeded 200 N, the chosen safety cutoff load at which the test was aborted to avoid damage to the load cell. Subsequently, a 1000 N load cell with a 0.5 N resolution (model RSC-200, calibrated with dead weights) was purchased for the following two winters of research. The data obtained from this load cell comprises the majority of the data analyzed in this study.

Two Sentech Linear Variable Differential Transformers (LVDTs) were attached to the testing machine for the measurement of beam deflection at various points. These LVDTs were calibrated to an accuracy of $\pm$0.025 mm using digital calipers. The most common deflection measurements were made at the midspan below the beam. In some experiments, the second LVDT was mounted on top of the beam directly above one of the rocker supports. Deflections measured by this LVDT indicated the level of deformation or crushing of snow at the supports.

Overall, the testing machine performed in a very satisfactory and consistent manner given the long periods of operation at sub-freezing temperatures.

2.3.2 Bending test apparatus

The testing machine was outfitted with a set of rails upon which rocker supports were mounted. These rails are visible in Figure 2.11 extending laterally below the snow sample and supports. Figure 2.12a shows a close-up of a rocker support, constructed of thick pieces of polycarbonate. The top support plate was interchangeable with plates of different width, such that wider plates could be used for softer snow to prevent excessive crushing at the supports during testing.

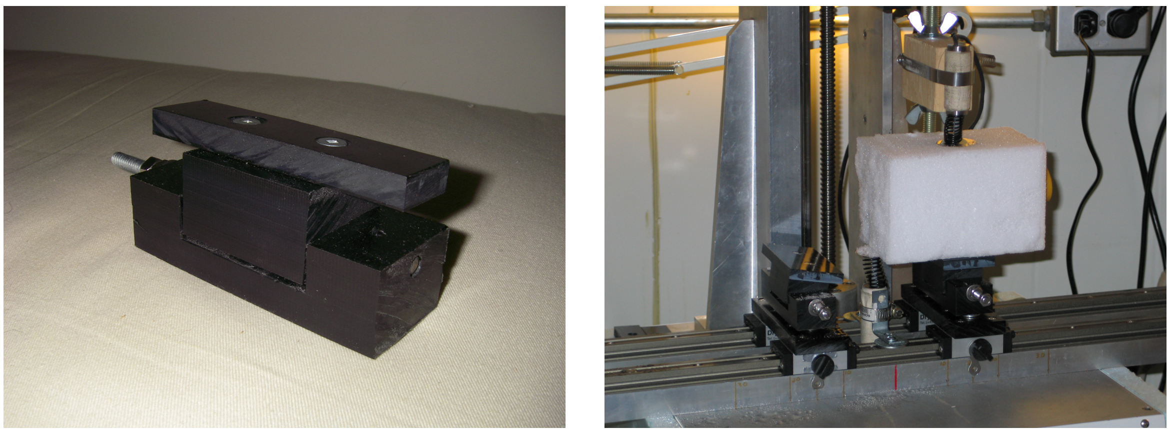

(a) (b)

Figure 2.12: *Photograph of rocker support, constructed of thick pieces of polycarbonate (a) and photograph of testing machine and half of a broken sample following a bending test, showing both rocker supports and two* LVDTs *for measuring deflection (b).*

The rails were designed with the objective of allowing low-friction lateral deflection of the rocker supports during testing, such that the boundary conditions during testing approximated a bending beam on rollers. However, operationally the friction of the rail-support system was too large to permit free lateral sliding during testing. For this reason, the supports were locked into place for each test series to ensure the support span was exactly the same for each test (given the same specimen size). As a result, some frictional sliding between the snow sample and the rocker support during testing was unavoidable.

Figure 2.12b shows half of a broken sample after a bending test. At the midspan below the sample, one of the LVDTs is mounted for measuring the midspan deflection. The second LVDT is mounted on top of the sample above the right support. The deflection measured by this second LVDT indicated the amount of crushing at the supports. The arms of the LVDTs had flat, round faces that were lightly pressed against the snow using plastic springs. The force applied by these springs at their typical level of deflection was on the order of 1 N, and was judged small enough not to affect the bending test results for all but a few tests involving the weakest snow in the present study. The LVDTs were not used during the first winter of research (2006–2007). Additionally, some of the smallest bending specimens tested did not permit the mounting of LVDTs for lack of physical space between the supports.

For three-point bending tests (central loading), a polycarbonate loading plate of the same size and shape as the support plates (Figure 2.12) was bolted to the load cell along with a wide aluminum stiffener. Four-point bending tests (third-point loading) were also conducted. These were achieved by first mounting an aluminum plate to the load cell. Onto this plate two rocker supports (of the same type as in Figure 2.12a) were mounted for load application on the top of the sample.

2.3.3 Horizontal weight compensation

An important aspect of the bending tests was weight compensation. The weak nature of snow and the propensity for viscous effects could contribute to a large amount of experimental scatter if the samples were mounted such that a gravitational bending moment contributed significantly to the fracture. In uncompensated bending tests on snow, *Sigrist* (2006) found that the effects of self weight could account for more than 50% of the bending moment required to fail the sample.

The first technique devised to eliminate gravitational effects was to orient the testing machine horizontally. The snow samples were then supported from below on a smooth piece of polycarbonate, which itself was supported on sturdy polycarbonate tables that sat on either side of the crosshead housing. Figure 2.13 shows the testing machine set up for this type of testing. Clear pieces of polycarbonate, as shown, were cut for each specimen size. The indentation in the clear polycarbonate closest to the crosshead was to allow a sufficient amount of crosshead displacement to fracture the sample before contact was made between the loading plate and the polycarbonate. In some early tests, the clear piece of polycarbonate shown was not used, and the samples were simply cantilevered over the gap between the two tables. In all cases, the polycarbonate surfaces were sprayed with a silicone lubricant which reduced the friction between the snow and the polycarbonate.

Figure 2.14 shows a small sample being prepared for testing in this horizontal configuration. Figure 2.14a shows the manner in which samples were manipulated into place using styrofoam. Small pieces of styrofoam were always used to grip and move snow specimens so that contact with the snow was never made

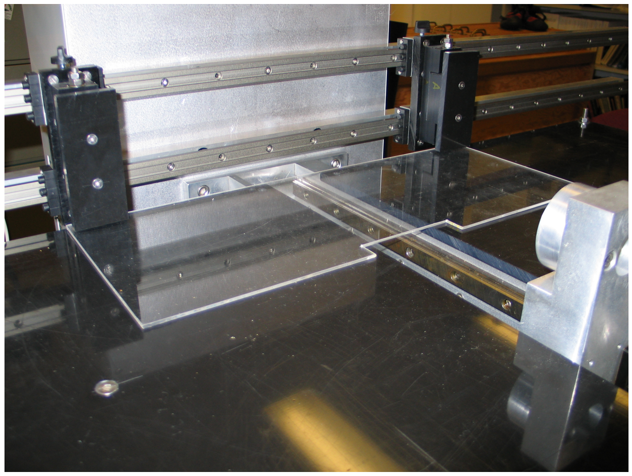

Figure 2.13: *Photograph showing testing machine set up for horizontal weight compensation. The load cell and polycarbonate loading plate are not mounted to the crosshead in this photo.*

directly using a gloved hand. Figure 2.14b shows the same small sample (D = 5 cm) ready for testing, with the load cell/load plate lightly pressed against the sample. The typical pre-load value used to hold samples in place prior to testing was around 1–2 N.

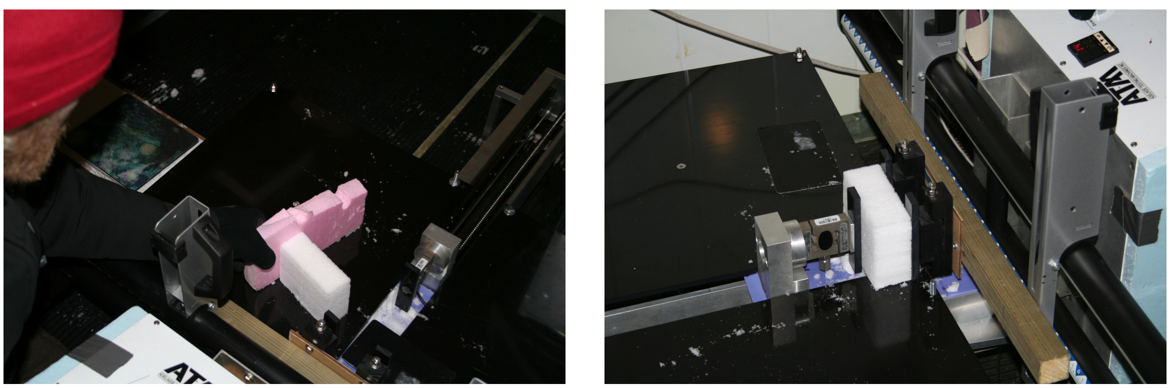

(a) **(b)**

Figure 2.14: *Photograph of a small sample being moved into place for testing in the horizontal configuration (a); the sample mounted in place and ready for the test signal from the PC (b). Photographs by Steve Conger.*

2.3.4 Vertical weight compensation

The second technique for achieving weight compensation was placing the testing machine in the common bench-top vertical orientation and moving the rocker supports to the quarter points of the beam. This placement of the supports cancels the bending moment due to self weight in the central cross section where the failure occurs. Figure 2.15 shows the testing machine oriented in this manner, with a large sample (D = 20 cm) mounted and ready for testing.

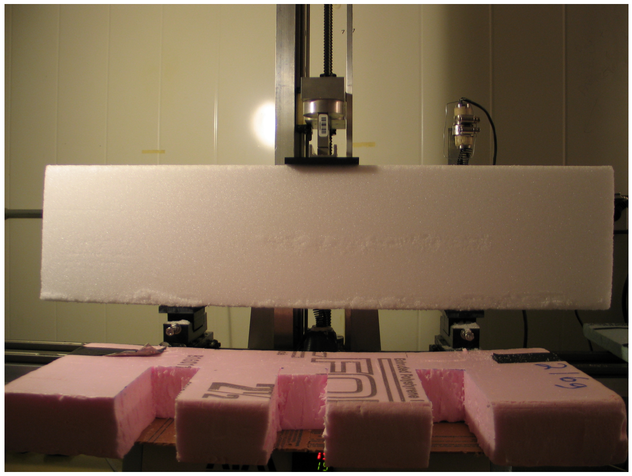

Figure 2.15: *Photograph of the testing machine oriented vertically, with a large sample mounted in a weight-compensated fashion.*

The styrofoam piece in the foreground of Figure 2.15 was used to carry the snow samples from the prep bench to the testing machine. The three notches in the styrofoam are spaced to fit around the rocker supports and the midspan LVDT. The snow sample, sitting atop the styrofoam, would be carefully lifted into place such that the supports and LVDT fit between the notches. The styrofoam was then withdrawn from below and the sample then sat upon the supports, ready for testing.

2.3.5 Specimen notching

For many tests, the snow specimens were notched at the bottom of the central cross section. The notch was cut using a paint scraper blade, the same kind of blade as used in the blade hardness gauge. Lines were painted on the blade at 1 cm intervals relative to the leading edge (Figure 2.16). The blade was mounted to a right-angle device which kept the leading edge of the blade vertical and square to the sample. The blade was carefully pushed into the snow specimen by hand to the desired depth, with the notch tool pressed against a framing square which itself was aligned against the bottom of the sample. Given the rough nature of the notching technique, the uncertainty in the notch depth was judged to be around ± 2 mm.

Figure 2.16: *Photograph of tool used to cut notches into snow samples.*

2.3.6 Density calculation

For small and medium sized specimens, the entire specimen was weighed prior to testing for the calculation of the bulk snow density. Figure 2.17 shows a sample on the digital scale prior to notching and testing. The dimensions of every sample were also measured and recorded prior to testing. For larger specimens that could not be weighed on the scale, 1000 cm^3 samples were cut from the specimens following the bending test and weighed.

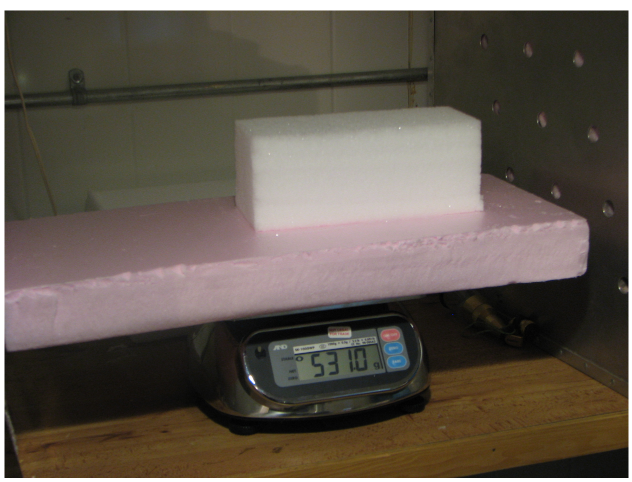

Figure 2.17: *Photograph showing a snow sample being weighed for the calculation of bulk density.*

2.3.7 Temperature measurement

Following each test, a thermometer was inserted into one of the broken halves of the specimen to record the temperature as close to the time of testing as possible. When using a dial-stem thermometer, as in Figure 2.18, the temperature was recorded to the nearest 0.5°C. More often, digital thermometers were used, and the temperature using these gauges was recorded to the nearest 0.1°C. Periodically, all thermometers were calibrated in a slush bath.

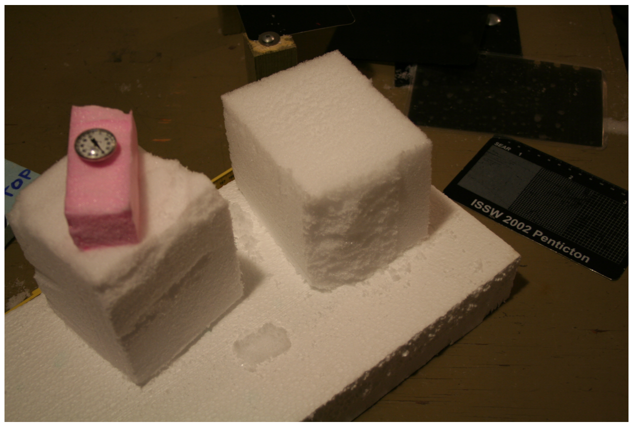

Figure 2.18: *Photograph showing the measurement of temperature of a sample after a bending test.*

2.3.8 Crystal identification

The snow crystals were classified in the lab by observing them under a microscope at a magnification of up to 50×. This was typically done only a couple times during the course of a test series in the lab, as time did not permit the sampling and studying of crystals after each test. Typically, the classification made using the microscope agreed with that made in the field using a hand lens. However, observation of crystals under greater magnification in the lab led to a tendency to classify the crystals as having more angular or faceted forms than visible under low magnification. *McClung and Schaerer* (2006) mention this tendency to focus too much on small-scale detail when observing crystals under high magnification, and for this reason lower magnification was preferred when making the initial classification.

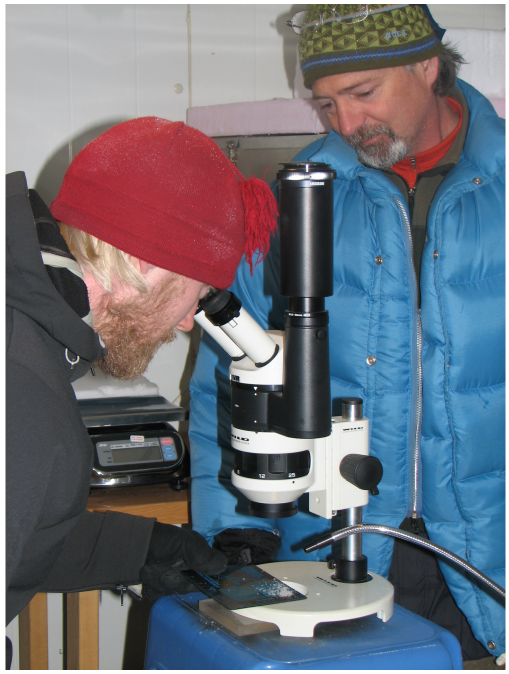

Figure 2.19: *Photograph of the author studying snow crystals under a microscope for classification.*

2.3.9 Practical limitations

Given the limitations of time, area available within a given snow pit, and storage area in the lab, the number of samples that could be successfully tested in a day was limited. For test series using specimens of different sizes, the maximum number of possible tests was in the range of about 10-20. Many of the test series used specimens of all the same moderate size, and for these series up to 30 tests in a day could be conducted. More tests would have been possible if samples had been stored in the lab for extended periods of time, but this was deemed undesirable given the metamorphic change of the snow that would take place.

The largest samples that were successfully extracted from the natural snowpack, transported to the lab, and successfully tested had a beam depth D = 20 cm. Figure 2.20 shows a sample of this size, with length L = 80 cm and support span S = 40 cm, mounted for an unnotched bending test. It was not deemed possible or practical to attempt the extraction of any larger sizes. Only about one in four of the largest specimens which were extracted successfully resulted in successful tests in the lab. Most large samples broke in some stage of removing the sample from the sample cutter, transportation to the lab, or manipulation in the lab prior to testing. Additionally, the largest samples that were successfully tested may have undergone some weakening or damage prior to testing, but to a degree that was not sufficient to cause a failure or be noticed. For this reason medium sized samples were preferred as standard for many of the test series in this study.

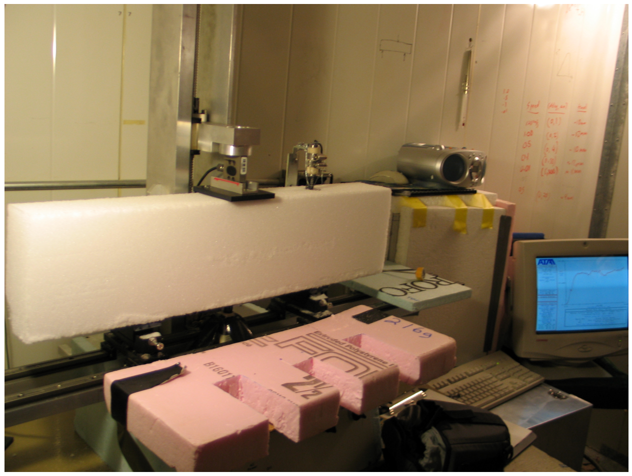

Figure 2.20: *Photograph showing largest specimen size used in the present study, mounted for a bending test.*

The smallest samples successfully tested (D = 2.5 cm) were equally difficult to extract, handle and test. The most difficult component was sample extraction in situ. The stainless steel sample cutters created enough grain-scale disturbance during insertion into the snow that the small samples typically came out irregular and unfit for testing. This practical limitation may be considered as related to a minimum length scale over which cohesive snow behaves as a continuum (recall the continuum limit in the scale-cohesion classification introduced in Figure 1.5).

Figure 2.21 shows the smallest sized specimen tested. Wooden dowels were used as roller supports and for the central loading device attached to the load cell. The different boundary conditions that were required for testing with these small specimens complicated the comparison of results with those from larger specimens. Very little data from samples of this size were conducted or included in the analysis in this study.

The large and flat support and loading plates used to prevent localized crushing in the bending tests occasionally led to adverse effects, especially for unnotched bending tests. In Figure 2.22, a shear failure between one edge of the large loading plate and the adjacent support plate is evident. In this particular case, the loading plate was too wide. Based on experience, the loading and support plates were initially chosen to have a width of $0.25D$ or less, and only increased in width if the snow was soft enough that excessive

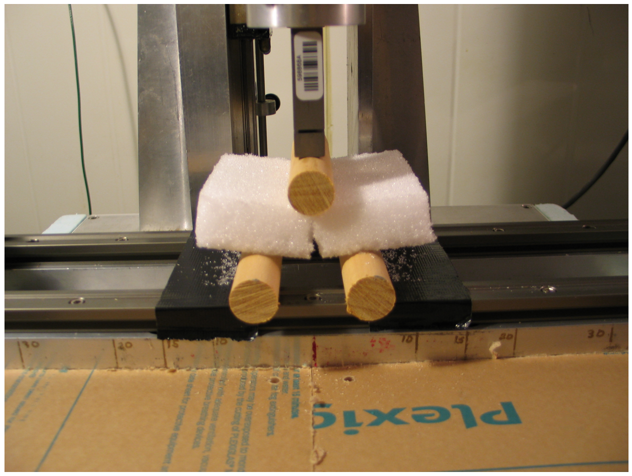

Figure 2.21: *Photograph showing the smallest sample size used in the present study, just after failure in a bending test.*

crushing was observed. Note that the shear failure in Figure 2.22 was the exception rather than the norm, and is shown here simply to reflect one of the experimental challenges in working with a material such as snow. See Appendix 7.5 for a description and images of the tensile fracture morphology that was the norm in this study.

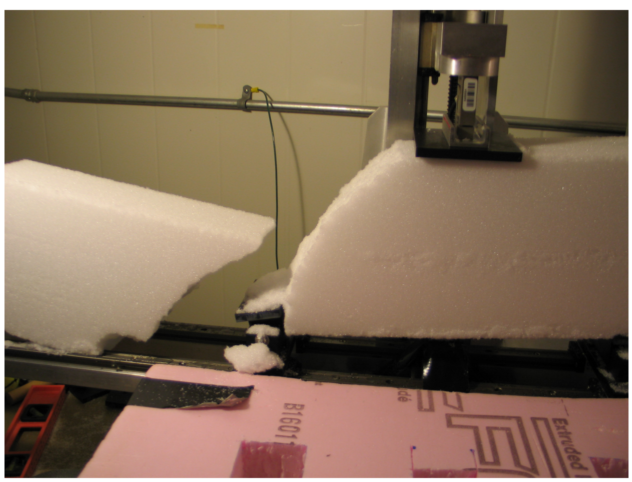

Figure 2.22: *Photograph of a shear failure in a large sample following an attempted unnotched bending test.*

2.3.10 Post-peak behaviour and apparent softening displacement

The measurement of strain-softening displacement was initially desired in the experimental design. This proved to be beyond the capability of the testing machine and bending test apparatus, however. This was in part related to the compliance of the testing machine, which is known to be related to the stability of fracture experiments (*Bažant and Becq-Giraudon*, 1999). Loading apparatus compliance is known to complicate the measurement of post-peak behaviour in ice (*Dempsey et al.*, 1999b). Though no direct measurements of the compliance of the overall loading apparatus were made in the present study, it was estimated that the combined compliance of the testing machine (rated 2 kN frame) plus the bending apparatus (mostly polycarbonate) was high enough to affect experimental stability.

The bending experiments may have been inherently unstable themselves. In a series of fracture experiments on Antarctic shelf ice, *Rist et al.* (1999) could not achieve stable crack growth using three point bending tests. The absence of stable crack growth complicates the measurement of post-peak behaviour in solid ice (*Dempsey et al.*, 1999b). Stable crack growth was never observed in the experiments in the present study; crack growth initiation always appeared unstable. This may have been in part a consequence of the use of open-loop displacement control in the experiments.

The instability observed in the experiments was also linked to the rapid loading rates, which were selected to minimize viscous effects. The high rates of crosshead displacement led to an apparent post-peak deflection curve which was mostly due to the elastic rebound of the load cell and the continued crosshead travel after receiving the signal to stop when the post-peak load dropped below a threshold value (typically about 5 N).

Figure 2.23 shows the post-peak curves from a series of three point bending experiments conducted in the horizontal orientation. The beam depth was 10 cm, the loading span was 20 cm, and all samples were notched to a relative depth of 0.3. Only the crosshead speed was varied between tests. The apparent softening curves are conspicuously consistent for a given crosshead speed. The highest crosshead speed of 1 cm s^{-1} led to a post-peak displacement of around 0.5 mm. Only when the crosshead speed was reduced by an order of magnitude or more did the softening curves begin to converge. However, at these lower speeds viscous effects during loading would be more significant. Therefore, even though the lower speeds may have suggested a more physically realistic softening displacement (at least for the initial post-peak tangent slope, which is important in governing the fracture energy in Bažant's size effect laws), the desire to minimize viscous effects was deemed more important than eliminating this spurious post-peak deflection.

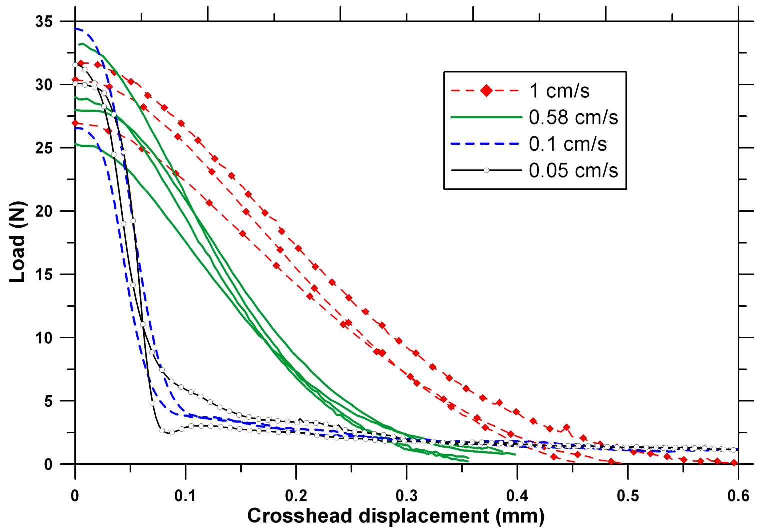

Figure 2.23: *Post-peak curves measured in bending experiments at different loading rates.*

A further investigation of the post-peak rebound behaviour of the load cell was conducted by breaking thin strips of glass in three point bending at different rates. These tests were assumed to produce fully brittle behaviour, but again an apparent softening displacement was measured as a function of loading rate (Figure 2.24). The excellent fit of the regression through the data in Figure 2.24 is confirmation that the observed, apparent softening displacement was due to the consistent elastic rebound of the load cell. Consequently, due to the combined factors of initial crack growth instability, testing machine compliance, and elastic load cell rebound, no reliable post-peak behaviour was measured for the bending experiments in the present study.

2.3.11 Friction between snow and polycarbonate

Approximate values of the friction coefficient between snow and polycarbonate were calculated from a series of experiments which involved simply pushing snow samples along the polycarbonate support tables using the crosshead. A total of ten experiments were conducted with the same sample of snow, each time pushed slightly further along the polycarbonate table at the same constant crosshead speed (1 cm s^{-1}). Figure 2.25 shows the results of two of these experiments, with the static and kinetic friction coefficients calculated using a simple ratio between normal gravitational force and tangential applied force.

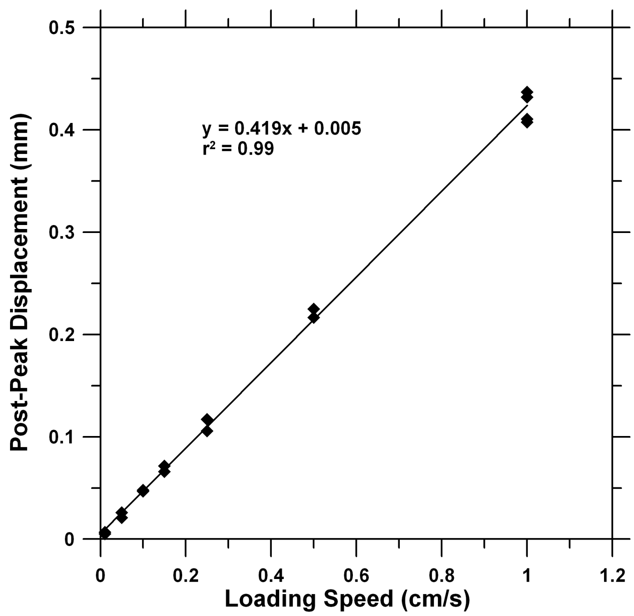

Figure 2.24: *Post-peak load-displacement curves measured in flexural tests of thin glass strips.*

The mean and median static friction coefficient values in this series of experiments was 0.4, with individual values ranging from 0.14 to 0.6. The kinetic friction values were somewhat more repeatable, typically falling between 0.1 and 0.25. These values are higher than reported by *Mellor* (1975) for kinetic friction between snow and polycarbonate, though adhesion may have played a role in the present experiments in addition to simple friction. This adhesion may have even been enhanced by the silicone lubricant which was sprayed on the polycarbonate and wiped to a thin film prior to testing (and repeated periodically for all horizontally-oriented tests). *Mellor* (1975) reported the difficulty in separating the effects of friction and adhesion in experiments.

In the friction experiments, the initial peak and then drop in force occurred over the first 1 mm of displacement (Figure 2.25). Most bending tests required at least this amount of crosshead displacement to fracture the sample. Figure 2.26 shows a typical load-displacement curve for a horizontally-oriented test. The circled region represents a commonly-observed shape in the early part of the loading curve for this type of test. This shape is consistent with an interpretation of the snow overcoming the initial peak static friction value at a displacement of about 0.5 mm, dropping thereafter to the kinetic value for the remainder of the test (Figure 2.25). This behaviour was consistent enough to give confidence in the following frictional-correction to the loading curves for horizontally-oriented tests: when processing the load-displacement

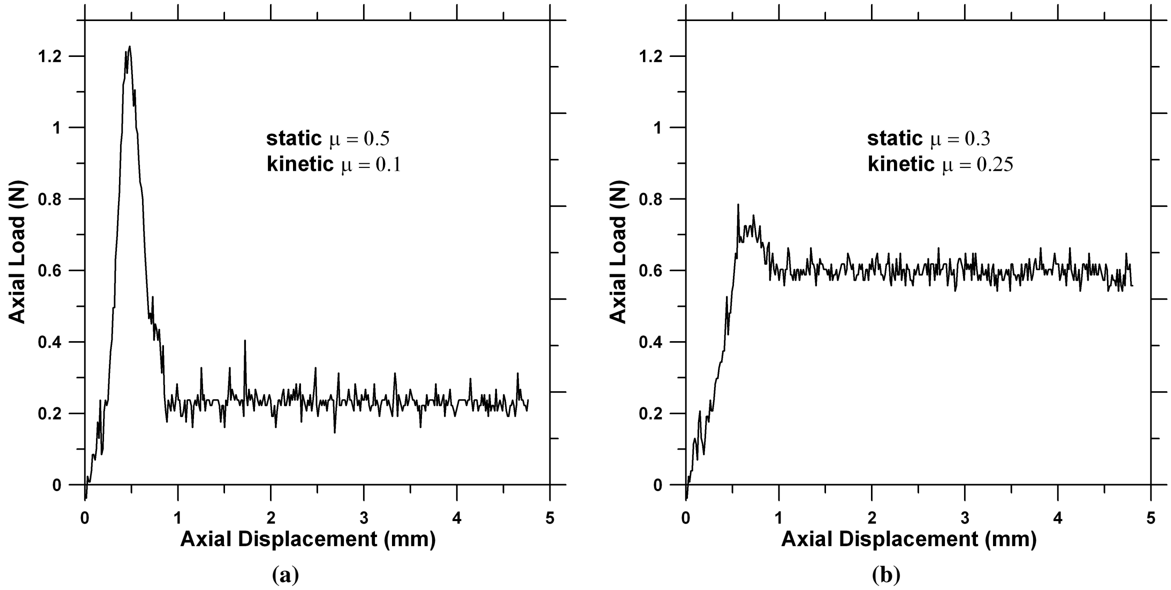

Figure 2.25: *Experimental curves used to measure the friction coefficient between snow and polycarbonate*

curves for analysis, a constant force equivalent to the kinetic friction coefficient times the normal force (weight of the sample) was subtracted from the measured force. This typically amounted to a correction of around a few percent to the peak load.

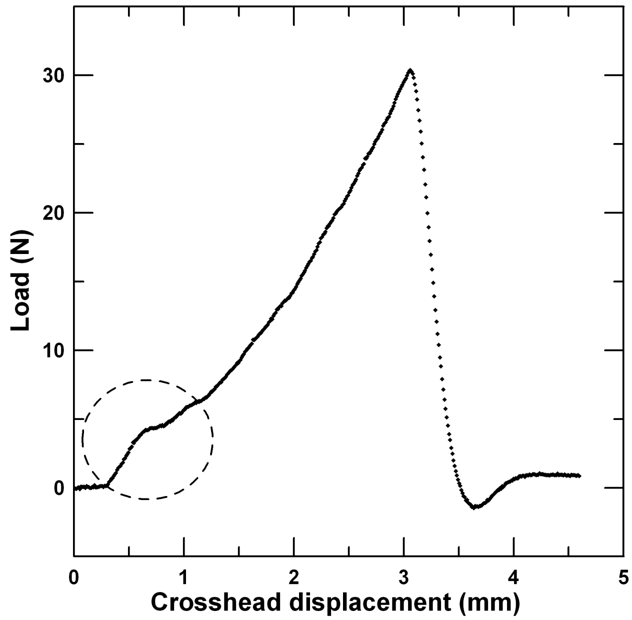

Figure 2.26: *Example load-displacement curve showing the possible influence of friction between snow and polycarbonate support table. From the shape of the loading curves measured in friction experiments (Figure 2.25), the circled region was interpreted as the snow sample overcoming the initial high static friction (plus perhaps adhesion), thereafter dropping to the kinetic friction value. The characteristic shape of the load-displacement curve in the circled region was common enough in the horizontally-oriented tests to give confidence to this physical interpretation.*

Summary

Much of the first of three seasons of research in the cold lab was devoted to development and adaptation of tools and techniques for the unique challenges posed by testing a material such as snow. This was a significant investment in time, resources and patience to get to a point where consistent and confident results could be obtained to meet the objectives of this study. In some cases, special adaptation of existing experimental fracture test methods was possible, and in others the development of entirely new approaches was required. After the first season of development, two full seasons of productive field and laboratory research were conducted using the methods described above. The methods were described here in as much detail as was deemed appropriate to facilitate any future research along the same lines. As challenging a material as snow is to work with, and as challenging as the slab avalanche problem is to analyze, much more data in future studies will surely be welcome.

Chapter 3

Thin-Blade Penetration Resistance and Snow Strength

3.1 Introduction

Snow hardness is defined as the resistance to penetration of an object into snow (*Fierz et al.*, 2009) and is measured using penetrating devices of various shapes and sizes. The resisting force in any hardness measure comes from a combination of bending and rupture of grain bonds and grain structures, compaction of loose grains and friction between snow and the penetrating object. The relative contribution of each resistance component to the total penetration force is unknown. However, bonding is the critical variable in determining the mechanical properties of snow such as strength (*Shapiro et al.*, 1997).

Despite the recognition of the relationship between hardness and the strength or bonding in snow, the bulk density of snow continues to be the most commonly used index variable for mechanical properties of snow. Examples of properties represented as functions of density include strength and Young's modulus (e.g. *Nakamura et al.*, 2010; *Marshall and Johnson*, 2009; *Shapiro et al.*, 1997), fracture toughness (*Sigrist et al.*, 2005b), fracture speeds and fracture energy (*McClung*, 2007a,b), and viscoelastic properties (*Camponovo and Schweizer*, 2001). The scatter in properties at a given density is typically attributed to differences in snow microstructure (*Schweizer et al.*, 2003), differences which might be captured by a

This chapter contains material published as *Borstad and McClung* (2011). Additional information on this publication is described in the Preface. Minor modifications were made here for clarity and flow within the overall structure of the dissertation.

hardness measure.

Several factors explain the widespread use of density in these contexts, when a hardness measure or other parameter representing bonding is theoretically more appropriate. Density is easy to measure and relatively objective, though different density samplers can give rise to inconsistent results with different errors (*Conger and McClung*, 2009). More importantly, no objective standard for hardness has been adopted to supplement or replace the density as a proxy variable in snow mechanics.

A thin blade snow hardness gauge was developed to establish an objective index measure of hardness for direct comparison with strength and other mechanical properties of snow. In order to minimize compaction and displacement of snow ahead of the penetrating tip, the thickness of the blade (0.6 mm at the leading edge) was chosen to be comparable to the grain sizes commonly encountered in alpine snow. The width of the blade (10 cm) was chosen so that around 10–100 grains would be simultaneously in contact with the blade, resulting in an average resistance measure over a length scale that corresponds to the structural scale of interest in most avalanche applications. Examples of relevant length scales in fracture of snow include the critical length of weak layer fractures (often called sweet spots or hot spots) prior to unstable propagation, which are on the order of the slab depth (*Bažant et al.*, 2003) and the scale of distributed damage prior to tensile crack coalescence, which is on the order of 10–100 times the grain size (*Borstad and McClung*, 2009).

The blade hardness gauge consists of an adapted stainless steel paint scraper blade attached to a hand held push-pull gauge. The peak resistance to penetration of the blade into layers or samples of snow was defined as the blade hardness index and was the single quantitative output. Blade hardness measurements were made horizontally in the walls of excavated snow pits. The results were compared against hundreds of density and hand hardness tests. The effects of penetration rate, blade orientation and blade width were explored. The blade hardness index was a consistent measure across observers, overcoming a drawback of the common hand hardness test. The tensile strength of snow samples was measured in a cold lab and the strength correlated better with the blade hardness index than with the density. A threshold in penetration resistance was identified that separated cohesive from cohesionless snow, confirming previous results using a thin blade gauge (*Fukue*, 1977).

This chapter is limited to an exploration of the blade hardness gauge with respect to its response in different types of snow and environmental conditions, sensitivity to various testing conditions and usefulness in providing a single quantitative output for correlation with strength and other mechanical properties of snow related to avalanches. Correlation and comparison with common instability evaluation tests in avalanche work was beyond the scope of the analysis but will be an important area of future research.

We begin with a brief review of relevant snow hardness literature. Emphasis is given to results related to thin blade penetration, compaction of snow in hardness measures and comparisons between direct measurements of strength and hardness. Details on the design and use of the thin blade gauge follow. Tests involving the gauge in excavated snow pits and in the cold lab are described, followed by the results of these tests and discussion. Potential applications of the gauge and limitations of the present study are discussed and conclusions drawn.

3.2 Hardness Measures

3.2.1 Thin blade hardness

Bradley (1966) developed a resistograph that recorded hardness using two blades mounted on either side of a probe. The probe was inserted to the base of the snow, rotated by 90°, and then withdrawn. The resisting force met by the blades during withdrawal was transferred via a spring in the shaft to a scribe that recorded the force on a spool of paper. This design was later modified so that the resistance was met by two upward-pointing cones rather than blades (*Bradley*, 1968). This change may have been the result of difficulty in turning the blades prior to withdrawal in some types of snow (*Floyer*, 2008). Bradley's resistograph was never widely adopted.

Fukue (1977) carried out thin blade penetration measurements that met four primary objectives. Namely, the measure was simple to carry out (1), minimized sensitivity to penetration rate (2), minimized densification of snow around the penetrating object (3) and minimized changes in intergranular bonding between adjacent snow grains (4). The third point has been emphasized as a drawback of many common hardness measures (*Shapiro et al.*, 1997). The last two points may be especially important in any hardness measure with a large compaction zone since ice grains form bonds which gain strength within a fraction of a second after contact (*Szabo and Schneebeli*, 2007).

The blade used by *Fukue* (1977) was 12 mm wide by 0.6 mm thick with a blunt leading edge. It was mounted to an actuator and driven into snow samples in a cold lab and the penetrating force was measured using a transducer. The individual peaks in the force-depth signal were roughly constant within the first 3 cm of penetration depth and slightly increased with further penetration due to friction between the sides of the blade and the snow grains. A ductile-to-brittle transition in penetration speed of 0.2 mm s^{-1} was observed. At penetration speeds below this transition the response of the snow was ductile, characterized by penetrating force which increased without bound. At speeds above this transition, brittle bond failures were evident from the spiked shape of the force displacement signal (Figure 3.1). A slight rate dependence in the brittle range, with decreasing peak penetration force with increasing penetration speed, was observed between 0.2-0.6 mm s^{-1}. Above 0.6 mm s^{-1} the peak force was independent of penetration speed.

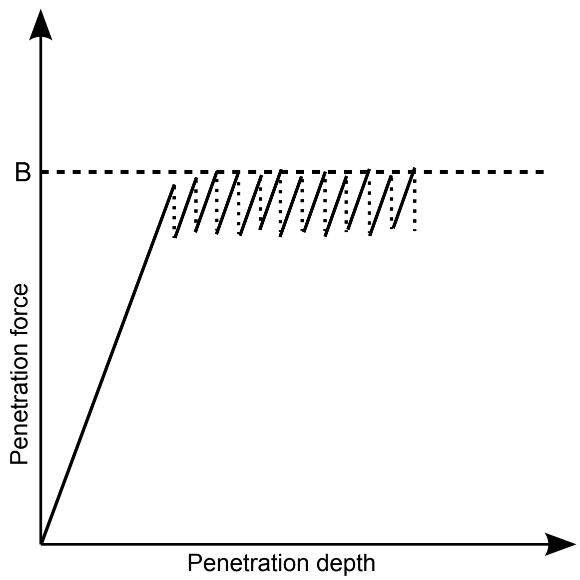

Figure 3.1: *Conceptual schematic (not to scale) of blade penetration force versus penetration distance for brittle penetration rates, based on measurements made by Fukue (1977). In Fukue's study, the minima following individual peaks in force were located at less than half of the peak force. The wider blade in this study should lead to higher minima with respect to individual peaks due to more structural elements in contact with the blade. The blade hardness index (B) is represented by the dashed line.*

Similar trends in the vicinity of the ductile-to-brittle transition were also observed in the uniaxial tensile strength tests, expressed as a function of strain rate, reported by *Narita* (1980). The maximum blade penetration force in Fukue's data and the maximum tensile strength in Narita's data, both as functions of rate (penetration rate and strain rate, respectively), were observed at the ductile-to-brittle transition. This suggests that Fukue's ductile-to-brittle transition at a penetration speed of 0.2 mm s^{-1} corresponds to a nominal bond-scale strain rate on the order of 10^{-4} s^{-1}.

3.2.2 Hand hardness

The hand hardness test (*de Quervain*, 1951) is perhaps the most common hardness test in avalanche forecasting work (*McClung and Schaerer*, 2006) and is, consequently, commonly cited in analysis of avalanche and snow stability data (e.g. *Schweizer and Jamieson*, 2001, 2007). The basic premise of the hand hardness test is to penetrate the snow using a standard force. Achieving this standard force requires selecting penetrating objects of different cross sectional area. Five hand hardness categories (excluding solid ice) are defined corresponding to different cross sectional areas that can be driven into the snow layer without exceeding the given force (*Fierz et al.*, 2009). Operationally, half-scale or $\pm$ qualifiers are often appended to the categorical result to refine the coarse scale.

The current international standard penetration force in the hand hardness test is 10–15 N (*Fierz et al.*, 2009). The previous version of the hardness standard (*Colbeck et al.*, 1990) specified a force of 50 N. However, the North American standard has been 10–15 N for many years (*McClung and Schaerer*, 2006). When comparing different hand hardness indices from different observers, countries or years, therefore, the difference in the applied force may vary by up to a factor of five. This makes any quantitative analysis using the hand hardness index difficult.

Höller and Fromm (2010) measured actual force values associated with the hand hardness test using a push-pull gauge and flat plates with standard cross sectional areas. Their results showed high scatter and overlap between penetration resistance values for adjacent hand hardness categories. Overall, the maximum force values agreed better with the old 50 N force standard (*Colbeck et al.*, 1990), though the force gauge was unable to record values below 10 N. These results illustrate the limitations to quantitative analysis using hand hardness data.

3.2.3 Probe hardness

The Swiss rammsonde or ram hardness test (Haefeli (1939), translated in *Bader et al.* (1954)) is a cone penetration test (60° cone tip angle and 40 mm base diameter) adapted from the soil sciences. The ram resistance is defined as the measured amount of force required to drive the rod a given depth into the snow. The large base area and weight of the instrument limit the vertical resolution of the ram hardness to the centimeter scale (*Pielmeier and Schneebeli*, 2003).

The SnowMicroPen (SMP) is a motor-driven cone penetrometer that records hardness at sub-millimeter resolution (*Schneebeli and Johnson*, 1998; *Johnson and Schneebeli*, 1999). The cone angle is the same as the Swiss rammsonde but the cone diameter (5 mm) is much smaller. *Pielmeier and Schneebeli* (2003) compared SMP hardness profiles to hand hardness and ram hardness and found that the SMP most effectively resolved small scale stratigraphy when compared against planar sections of snow layers. No standard algorithm exists for interpreting and processing the SMP resistance signal, making comparison of results from different studies difficult (*Marshall and Johnson*, 2009). The SABRE probe penetrometer (*Mackenzie and Payten*, 2002) is another probe hardness gauge, with a 12 mm diameter rounded tip, that has seen limited use (*Floyer*, 2008).

3.2.4 Compaction of snow in hardness measures

Floyer (2008) attached tips of different shape and size to the SABRE probe, filmed the penetration pattern around each, and analyzed the films using particle tracking velocimetry. *Floyer and Jamieson* (2010) examined in more detail the compaction around the round probe tip specifically. These experiments provide insight into the assumption that compaction around a probe tip can be neglected in the interpretation of the force signal (e.g. *Johnson and Schneebeli*, 1999; *Marshall and Johnson*, 2009). This compaction can be separated into horizontal (or normal to the direction of penetration) and forward (ahead of the probe tip) components.

The most important qualitative conclusion that can be drawn from the work of *Floyer* (2008) from the perspective of this study was that the tapered blade tip led to a much smaller zone of horizontal and forward compaction than either of the larger conical or rounded probe tips. The relative size and shape of the blade tip in the current study (and also that of *Fukue* (1977)) is shown in Figure 3.2a. Since the leading edge of the blade is blunt rather than tapered, it might be more appropriate to consider the full thickness of the blade as the scaling length L rather than half the thickness. However, in either case the length scale is comparable to or smaller than many common grain sizes encountered in seasonal snow (*Fierz et al.*, 2009). This introduces the grain size (or a relationship between the grain size and available pore space for densification) as the dominant scaling parameter for the horizontal deformation around the tip.

The tip of the SMP (Figure 3.2b), for comparison, has a base radius of 2.5 mm and a shallower cone

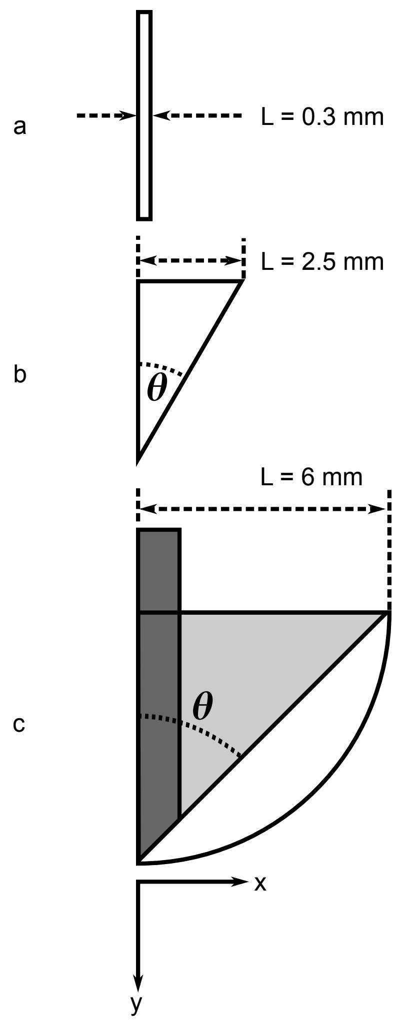

Figure 3.2: *Scaled representation of penetrometer tips, each in a plane of symmetry. Thin blade (a) used by Fukue (1977), with the same leading edge dimensions as the blade in the present study; SnowMicroPen (SMP) dimensions (b), with θ = 30°; tips used by Floyer (2008) (c), with rounded tip (unshaded) and conical tip (light gray, θ = 45°) of the same radius. The blade tip (dark gray) had L = 1 mm, $\theta \approx$ 45°.*

half-angle (30°) than the conical tip used by *Floyer* (2008). This should lead to a relatively smaller zone of compaction around the SMP compared to the SABRE probe. The relative difference between the scaling length L for the SMP and the thin blade in the present study is about the same as the relative size difference between the tapered blade and conical tip used by *Floyer* (2008), though the cone and blade tip angles are different. Though the precise relative shape and size of the compaction zones for the SMP and the thin blade in this study cannot (and need not) be determined, it can be argued based on the results of *Floyer* (2008) and from simple dimensional scaling arguments that the thin blade will horizontally compact less snow as it penetrates compared to any other common hardness measure considered here.

Since the blade tip in the present study is both blunt and thin, the forward compaction may scale disproportionately with *L. Whiteley and Dexter* (1981) found that a 1 mm diameter probe required around 50% more pressure than a 2 mm diameter probe to penetrate sandy soils. The explanation may lie in the development of a passive nose cone being pushed ahead of the probe, similar qualitatively to that observed by *Floyer* (2008). The shape and size of this nose cone does not appear to have a simple scaling relationship with the penetrometer shape and size, especially when the probe tip size is comparable to the grain size. Therefore, comparison of the forward compaction for blunt-tipped thin blades versus other penetrometers is more difficult and uncertain.

3.2.5 Hardness and strength

Bradley (1968) underlined the importance of direct strength measurements for comparison against hardness tests, though few studies have systematically done this. Comparing resistograph measurements to the compressive strength of snow columns containing weak basal layers, *Bradley* (1968) found that the minimum resisting stress from the resistograph roughly correlated with the compressive strength of the basal layer.

Martinelli (1971) reported data relating both ram hardness and density to centrifugal tensile strength. This data was analyzed here to compare the two different proxies for strength. Both the ram hardness and density show very high (and nearly equal) correlations with the nominal centrifugal tensile strength (Table 3.1). The ram hardness and density are also highly correlated with each other. From this data the ram hardness appears no better (nor worse) than density for correlating with strength. Other studies attempting to relate ram hardness to strength have been largely unsuccessful (*Shapiro et al.*, 1997).

Fukue (1977) empirically correlated blade penetration force with cohesive strength in several ways. First, artificial snow samples were allowed to sinter over time at a temperature conducive to bond growth. The unconfined compressive strength of the samples increased with age and therefore bond strength. Thin blade penetration tests were then paired with unconfined compressive strength tests on similar snow samples undergoing sintering. The maximum blade penetration force strongly correlated with unconfined compressive strength, suggesting a link between bonding and blade penetration. Second, confined compression tests were performed at rates both below and above an identified ductile-to-brittle transition in compression rate. Following each test, a thin blade penetration measurement was performed on the sample. Samples that

Table 3.1: *Correlation matrix for data reported by Martinelli (1971). The upper diagonal elements contain Spearman's rank correlation coefficients, r_s*, and the lower diagonal elements are the p-values. Bold face indicates statistically significant correlations at the $\alpha = 0.05$ level. The lower part of the table shows the range of each variable (n=98).*

	f_t	ρ	R_{ram}	T	E
f_t		**0.919**	**0.928**	0.023	0.011
ρ	<**0.001**		**0.940**	0.013	-0.045
R_{ram}	<**0.001**	<**0.001**		-0.054	-0.075
T	0.822	0.899	0.594		0.078
E	0.918	0.662	0.465	0.448	

Nominal tensile strength f_t	$0.4 < f_t < 246.0$ kPa
Density ρ	$68 < \rho < 491$ kg m^{-3}
Ram hardness R_{ram}	$9.81 < R_{ram} < 2207$ N
Temperature T	$-22.4 < T < -1.4$ °C
Grain size E	$0.2 <$ E < 1.5 mm

**Spearman's rank correlations are shown rather than Pearson's product-moment correlations (r) for several reasons. First, Pearson's r is based on the assumption of linear dependence between the two variables. However, associations among the mechanical properties of snow are often nonlinear. Pearson's r also contains the assumption that the underlying parent distributions of the two variables are normal (though violations of this assumption are not severe if the sample size is large). Finally, Pearson's r is much more sensitive to outliers. Spearman's r_s is a non-parametric alternative which tests for any monotonic relationship when the assumptions for using Pearson's r are not met.*

had been compressed at rates above the ductile-to-brittle transition, and therefore had broken bonds, had systematically lower penetration resistance than samples that had been slowly compressed in the ductile range.

Schneebeli and Johnson (1998) directly compared centrifugal tensile strength and average penetration resistance using an early version of the SMP with a cone half-angle of 45° and a 5 mm diameter cone tip. The tensile strength measurements showed a high amount of scatter when expressed either as a function of density or average penetration resistance. However, the uncertain repeatability of the centrifugal tensile tests may have contributed to the large scatter (*Schneebeli and Johnson*, 1998).

No other examples in the literature were found which directly measured snow strength and compared strength with components of SMP resistance signals. Recent studies have analyzed or derived parameters from SMP signals and compared them to either the results of avalanche instability tests, which can provide indices of strength, or to published strength values. *Birkeland et al.* (2004) found that the maximum resistance recorded by the SMP in a weak surface hoar layer increased as a shear strength index increased. Neither the mean nor median resistance in the layer were significantly correlated with the shear strength increase. *Lutz et al.* (2009) used resistance values and drop frequencies from the SMP to calculate a grain-scale strength index and observed changes in this index with artificial load changes in three compression tests. *Marshall and Johnson* (2009) calculated theoretical values of strength from SMP signals and compared these values against tensile, compressive, and shear strength values, expressed as a function of density, from the literature. Around half of the SMP-derived strength values were higher than any published values. This might be explained by the assumption in the calculations that all of the resisting force (less a small amount of friction) was due to the elastic deflection and rupture of bonds (*Marshall and Johnson*, 2009). Accounting for a compaction component in the resistance signal may have brought the derived strength values into better agreement with measurements.

3.3 Methods

The blade hardness measurements were carried out in two settings. The first was in excavated snow pits, alongside standard stratigraphic snow profiling techniques used in avalanche work (*Fierz et al.*, 2009; *Canadian Avalanche Association (CAA)*, 2007). The second was in a cold laboratory, where the blade hardness measurements were paired with tensile strength tests on samples extracted from the natural snow cover. The force gauge, blade attachment and measurement technique are detailed first.

3.3.1 Force gauge and blade attachment

The force gauge used was a Chatillon DFE series with a full bridge strain gauge load cell. Figure 3.3 shows the gauge and blade attachment. The load cell capacity was 250 N with a resolution of 0.1 N. The gauge accuracy was certified to within $\pm 0.25\%$ full scale (± 0.6 N). The gauge was periodically tested for accuracy by hanging dead weights from a hook attached to the gauge. These tests confirmed the accuracy of the gauge in the approximate range of 5–95% of the full scale.

The operating temperature range of the gauge was specified as -1 to +49°C, but the typical testing temperature was in the range -10 to 0°C. When used in the field, the gauge was kept in an insulated container and only brought out just before use. Most tests involving the gauge lasted only a matter of minutes. This

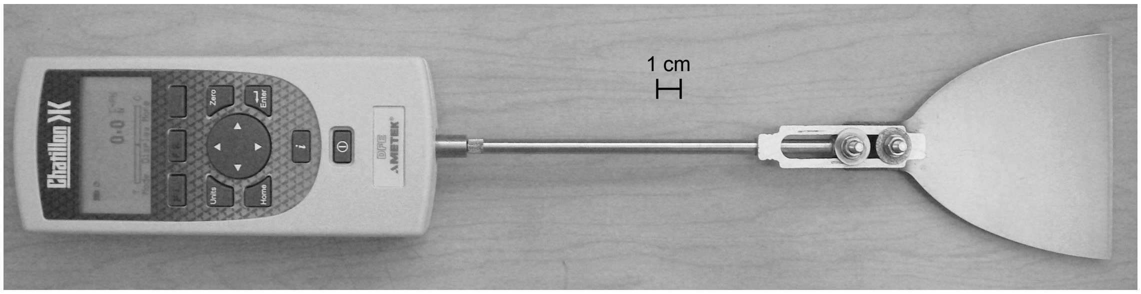

Figure 3.3: *Blade hardness gauge.*

likely limited the actual temperature drop of the load cell in the interior of the gauge relative to the ambient temperature. In the cold lab, however, the gauge was exposed to cold temperatures for longer periods of time and temperature effects might have been more significant. The specified temperature effect on zero load level was 0.09 N/°C relative to the calibration temperature. The median ambient temperature in the lab was about -5°C and the calibration temperature was 23°C, suggesting a possible shift in the zero point of the load cell of up to 2.5 N. However, the actual internal temperature of the load cell was probably slow to change relative to the ambient temperature, buffered by the thick housing of the gauge and the internal circuitry (the gauge manufacturer used 30 minute stabilization times when testing the load cell performance within the range of operating temperatures). The LCD and battery life of the load cell were not affected down to air temperatures as low as -20°C.

The data sampling rate of the force gauge was 5000 Hz. It was possible to record a continuous signal at this rate, which could be sent via a cable to a datalogger or a computer, or simply to record the peak force in tension or compression. For this study only the peak resisting force was recorded. For future studies, high resolution measurements of penetration resistance could be obtained. In particular, the variance of penetration resistance over the length scale of interest (10 cm) could be useful in addition to the peak force. However, this would require a more accurate and sensitive force gauge than used in the present study.

The thin blade used was a 10 cm wide by 0.6 mm thick paint scraper blade with a blunt leading edge. Only the leading 2 mm of the blade was 0.6 mm thick. Behind the leading edge the blade tapered to 0.5 mm thickness. This thickness profile was related to a hardening finish at the tip of the blade. The handle was removed from the original paint scraper, and two bolts were used to clamp the blade to an aluminum turnbuckle (Figure 3.3). One of the bolts also clamped a nut that secured the end of the threaded rod extending from the force gauge. The primary cost of the apparatus was the force gauge, as the paint scraper cost around $10 (USD 2007). The digital force gauge cost around $1250 (USD 2007).

The leading edge of the blade extended about 30 cm from the front of the force gauge. This distance could have been reduced by about 12 cm by using a shorter threaded rod extending from the load cell. The combined weight of the threaded rod and blade assembly was about 100 g. The effect of this cantilevered weight did not cause a load response in the load cell. The assembled blade apparatus was also rigid torsionally, and the load cell was not sensitive to manual twisting of the blade. During penetration tests, twisting, bending or other deflection of the blade was never sensed.

3.3.2 Measurement technique

Blade hardness measurements were carried out by pushing the blade 3–5 cm into the surface of the snow, either into an exposed pit wall or into a snow sample in a cold lab, at an estimated penetration speed of around 10 cm s^{-1} (Figure 3.4). The blade was then withdrawn and the maximum force of penetration was recorded as the blade hardness index.

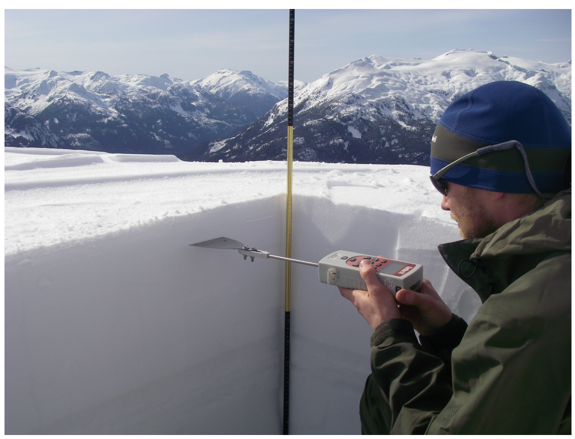

Figure 3.4: *Carrying out a blade hardness measurement with the blade oriented parallel to the stratigraphic layering.*

The adopted notation for recording the blade hardness index was using the symbol '*B*' (Figure 3.1). This distinguished the blade hardness from the commonly used '*R*' for the hand hardness or the ram hardness (*Fierz et al.*, 2009). Unless otherwise noted, the orientation of the blade was parallel to the stratigraphic layering of the snow cover and the blade width was 10 cm. Variations on this notation will be explained as they are introduced below.

The penetration speed was high to ensure that the peak force fell into the rate-independent portion of the brittle range identified by *Fukue* (1977). It was hypothesized that this would maximize the consistency across observers. At this penetration speed, the 5000 Hz data sampling rate of the force gauge records hundreds of samples per centimeter of penetration. This gives high confidence that during rapid penetration of the blade the true peak load was accurately captured.

3.3.3 Standard stratigraphic profiling

In an excavated snow pit, the standard profile measurements included hand hardness of identified stratigraphic layers, temperature measurements every 10 cm of depth from the surface to the ground, grain size and form classification by sampling snow crystals from each layer and examining them on a gridded screen under 10 $\times$ magnification, density measurements, and water content characterization using a hand test. Details of these standard methods can be found in *Fierz et al.* (2009); *Canadian Avalanche Association (CAA)* (2007) and in Chapter 2.

The characterization of hand hardness in this study was consistently done using the 10–15 N force standard. Plus and minus qualifiers were used for finer scale distinctions. For example, a hand hardness index of "2+" was recorded as 2.3 and a "3-" was recorded as 2.7. An approximate uncertainty was then added to reflect the imprecision and subjectivity of the test and to facilitate comparison with results from the old 50 N force standard. It was estimated that the 50 N force standard would result in a hand hardness index of one level lower for characterizing the same snow. For example, if a snow layer was characterized as having hardness index 3, the approximate range for comparison was reported as 2–3. A factor of 5 force difference, representing the maximum difference between the old and new standards, may lead to an even greater difference in reported hand hardness indices, however.

Blade hardness measurements added only a few minutes to standard stratigraphic profiles. Density measurements were typically paired with single blade hardness measurements as a function of depth (Figure 3.5). Often groups of 10 blade hardness measurements were made in manually identified homogeneous snow layers for characterizing the variability of the blade hardness index (Figure 3.6, top). The effects of the blade orientation, width and penetration rate were also investigated in snow pits adjacent to standard profiles.

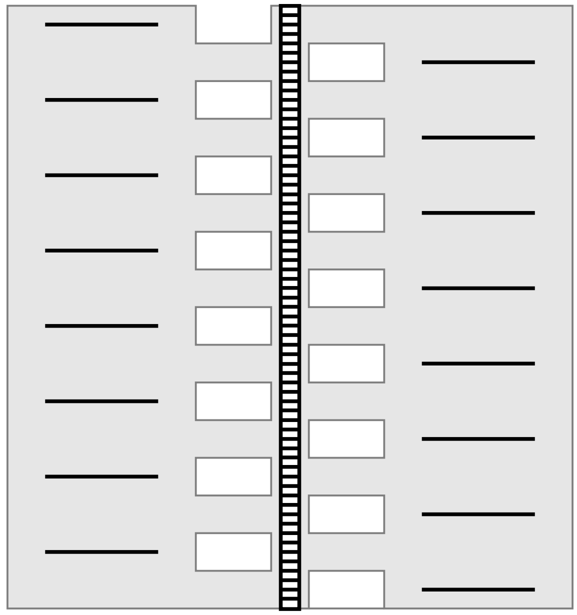

Figure 3.5: *Schematic of paired density and blade hardness measurements, looking at the face of an exposed snow pit wall. The central strip represents a meter stick, the open rectangles are the holes left by the density sampling and the solid black lines are the blade hardness measurements.*

3.3.4 Laboratory strength testing

The blade hardness gauge was also used in a cold laboratory containing a universal testing machine for measuring the tensile (flexural) strength of cohesive snow samples. A blade hardness measurement was paired with each strength test (Figure 3.7). Dry cohesive snow samples were first extracted from homogeneous layers of at least 10 cm thickness in the natural snow cover. The samples were cut out using a stainless steel rectangular cutter with a sharpened leading edge. The most common specimen size had dimensions 50 cm long by 10 cm deep by 10 cm wide.

Once extracted, the samples were transported to a nearby cold laboratory for testing the same day. The samples were weighed in the lab for the calculation of the bulk density. The samples were fractured in unnotched and weight compensated three (or four) point bending tests. The peak force recorded in the test was used to calculate the nominal tensile strength using Timoshenko beam theory (*Timoshenko*, 1940). Immediately after a strength test a blade hardness measurement of the sample was taken, along with the temperature, grain size and grain form classification. The grain size and form were determined by examining a sample of snow crystals under a microscope on a similar crystal screen as that used in the field.

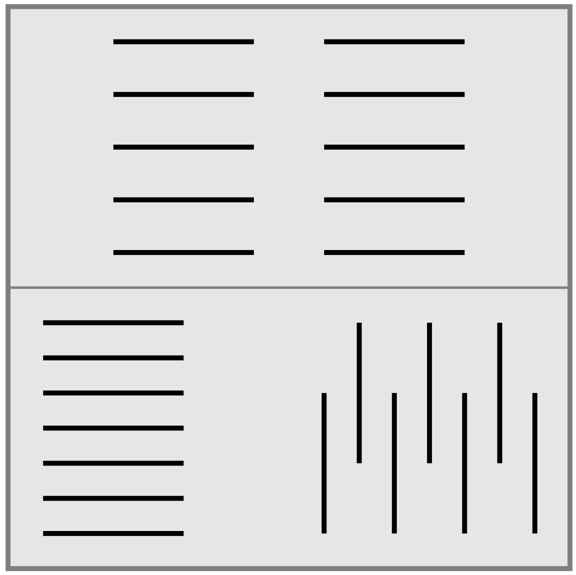

Figure 3.6: *Schematic of blade hardness measurement technique in two different layers, looking at the face of an exposed pit wall. Homogeneous layers are identified manually in a snow pit for this type of test grouping. In the top layer ten measurements are shown, distributed evenly over the thickness of the layer. In the bottom layer an equal number of slope-parallel and slope-normal measurements are shown.*

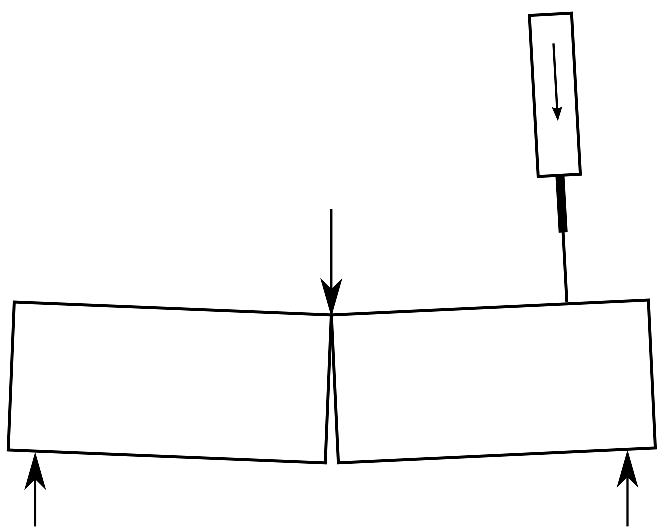

Figure 3.7: *Schematic of paired tests of flexural strength and blade hardness. The snow sample was first broken in three or four point bending (three point bending shown). Next, a blade hardness measurement was taken (upper right of figure) using a part of the sample that experienced low stress during the strength test.*

3.4 Results

3.4.1 Density versus blade hardness index

For a given snow layer, which was typically characterized by a single density, there was wide scatter in blade hardness indices (Figure 3.8). The COV of repeated tests (usually 10 tests) within a layer decreased with increasing layer density, and the slope was statistically significant in a linear regression ($p < 0.001$). Due to the density-hardness correlation, the COV also decreased with increasing mean blade hardness index, and this slope was also statistically significant ($p = 0.02$). Cohesionless snow, hereafter defined as snow with $B = 0$ N, had no clear relation with density. Cohesionless snow was observed with densities ranging from about 30–250 kg m^{-3}.

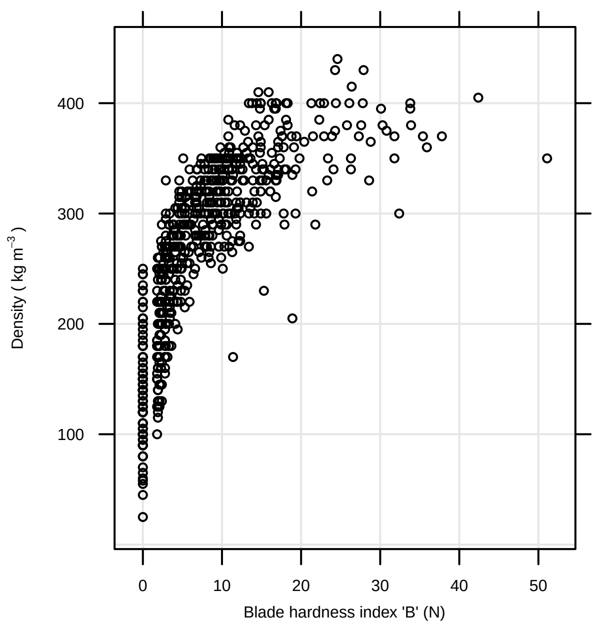

Figure 3.8: *Density versus blade hardness index (B) from 24 snowpit profiles carried out over the winters of 2007/2008 and 2008/2009. The Spearman's rank correlation coefficient is 0.89, p-value <0.001. (n=628)*

In the data set of 628 in situ test pairs, not a single blade hardness index was registered between 0.0 and 1.7 N, indicating a gauge sensitivity problem. More than 90% of the blade hardness index values were less than 20 N, indicating only a small range of the full capacity (250 N) of the load cell was used. A total of 99 values of $B = 0$ N were recorded, many of which were interpreted as legitimate negligible resistance values in cohesionless snow. The true resisting force for some of these tests was likely nonzero, however, but too low to be accurately resolved with the load cell.

3.4.2 Penetration rate effects

Penetration rate effects were considered to be the primary source of possible variability for results obtained with different operators. In one test series, pairs of fast and slow blade hardness measurements were carried out side by side. The same gauge operator was used for all tests in order to isolate the rate effect. The penetration rates were subjectively judged, with the standard 10 cm s^{-1} rate considered fast. For the slow tests, the penetration rate was around a few cm s^{-1}, or approximately one order of magnitude slower. These penetration speeds correspond to bond-scale strain rates on the order of 10^{-3} s^{-1} for the slow tests and 10^{-2} s^{-1} for the fast tests. These rates are both in the rate-independent portion of the brittle range identified by *Fukue* (1977) (as a function of penetration rate) and *Narita* (1983) (as a function of strain rate).

A total of 40 pairs of tests were carried out side by side comparing one fast and one slow measurement at the same depth and within the same layer. All tests were done in a single location, with pairs of tests conducted every 3 cm of depth from near the surface of the snowpack to the ground. This ensured that at least one test pair was conducted within every manually identified layer. The blade was oriented slope-parallel for all tests.

In this test series, there were 8 test pairs in snow of hand hardness index 1–2 in which one of the two tests (fast or slow) had a blade hardness index of 0 N. Given the gauge sensitivity problem near 0 N these test pairs were thrown out of the following analysis. In the 32 pairs of tests for which both the fast and slow results were nonzero, the ratio of fast to slow hardness (B_{fast}/B_{slow}) had a mean and median of 1.1. The ratio of fast to slow hardness did not consistently correlate with any other measured snow property. A Wilcoxon signed rank test was performed on the logarithm of the ratio (the logarithm symmetrizes the ratio about zero) to test whether the fast and slow results were different. The test indicated that the ratio was not significantly different from 1 at the α = 0.05 level (p = 0.07).

A second test series was carried out within a single homogeneous layer (hand hardness index 3–4). A total of 20 tests were carried out, 10 fast and 10 slow. For consistency of speed, the fast measurements were carried out first in a spatial cluster, followed by the slow measurements adjacent to the fast cluster. The blade was again oriented parallel to the layering.

For this test series, the mean hardness was 18.6 N (range 15.0–22.7) for the fast tests and 15.6 N (range 12.5–18.8) for the slow tests. The coefficients of variation of the fast and slow tests were the same at 0.15. Welch's t-test indicated significance in the difference between the means at the $\alpha = 0.05$ level (p = 0.02).

3.4.3 Blade orientation

Paired groups of tests were conducted to explore the effect of the orientation of the blade (Figure 3.6, bottom) on the mean hardness and variability. For these tests, snow layers were first sought that were homogeneous and least 10 cm thick to allow blade penetration perpendicular to the layering. In such layers, 10 tests were carried out in each of two orientations. The first 10 tests were carried out with the width of the blade parallel to the layering ($B_{\|}$) and the next 10 were perpendicular to the layering ($B_{\perp}$). The groups of penetration tests were carried out immediately adjacent to one another to avoid, as much as possible, encountering horizontal changes in layer properties. The mean blade hardness index of each group of 10 tests ($\bar{B}_{\|}$ and $\bar{B}_{\perp}$) as well as the range and standard deviation were recorded. In total, 12 groups of such orientation tests were carried out in different layers. In order to compare the tests across layers with different properties, the ratios of normal to parallel mean blade hardness index ($\bar{B}_{\perp}/\bar{B}_{\|}$) and coefficient of variation ($\overline{CoV}_{\perp}/\overline{CoV}_{\|}$) were calculated for each layer tested.

The mean hardness appeared to be independent of blade orientation (Figure 3.9, top). The bulk of the mean hardness ratios ($\bar{B}_{\perp}/\bar{B}_{\|}$) clustered close to 1, other than two outliers. The majority of layers tested showed lower variability in slope-normal than slope-parallel tests, however. In these cases the COV ratios ($\overline{CoV}_{\perp}/\overline{CoV}_{\|}$) were less than 1. The individual values of the COV ranged from 0.06 to 2.25 for slope-normal tests (mean 0.42, median 0.21) and from 0.13 to 2.0 for the slope-parallel tests (mean 0.35, median 0.16). A Wilcoxon signed rank test indicated that the COV ratio was different from 1 at the $\alpha = 0.05$ level (p = 0.02).

3.4.4 Blade size effect

A wider blade was attached to the gauge in an attempt to bring out more detail than the 10 cm blade, especially in very soft and soft snow (hand hardness indices 1 and 2, respectively). A 20 cm blade with a thickness of 0.48 mm and a blunt leading edge (another off-the-shelf paint scraper blade) was used for comparison. The large blade apparatus weighed about 280 g (compared to 100 g for the 10 cm blade attachment) and had a cantilever length about 3 cm shorter than the 10 cm blade. The additional cantilever

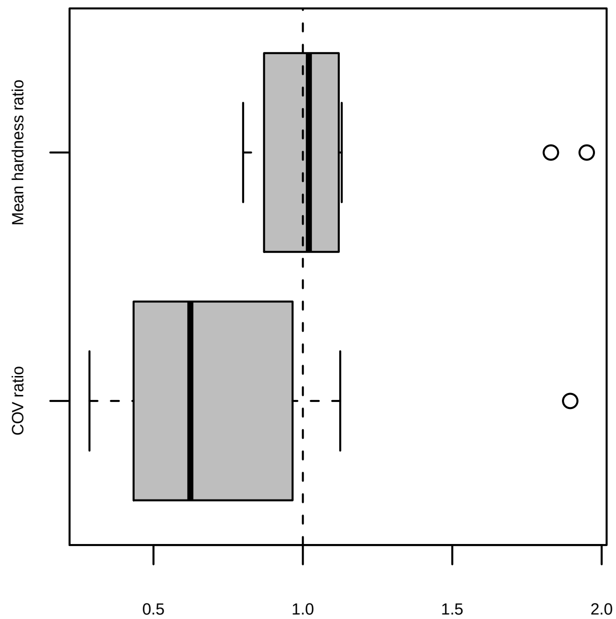

Figure 3.9: *Box plot showing the ratio of mean blade hardness index normal to the layering to mean hardness parallel to the layering ($\bar{B}_{\perp}/\bar{B}_{\parallel}$, top) and mean normal to parallel* COV *($\overline{CoV}_{\perp}/\overline{CoV}_{\parallel}$, bottom). The boxes contain the inner quartile range, the whiskers extend to data points within 1.5 times the inner quartile range from the median, outliers are drawn as individual points, and the thick black line is the median. Each box plot represents 12 group means, with each group containing 10 tests in each orientation. The dashed vertical line is drawn to indicate no difference between orientations.*

weight did not induce an axial load in the load cell.

A total of 55 paired tests were carried out with the 10 cm and 20 cm wide blades. Each test pair was conducted side by side within the same layer. As with the variable penetration rate tests, test pairs were carried out every 3 cm of depth from the surface to the ground.

In the first 10 pairs of size effect tests in very soft snow (hand hardness index 1) near the surface, both blades registered $B = 0$ N. As the hardness increased with increasing depth, however, the 20 cm blade was the first to record values of $B > 0$ N. This was the case in 6 pairs of tests in snow that was transitioning from hand hardness index 2 to 3. In this snow, the 20 cm blade gave nonzero hardness values whereas the 10 cm blade did not register.

Overall, 39 of the 55 pairs of tests had nonzero hardness values for both blades. Among these pairs, the ratio of blade hardness between the 20 and 10 cm blades, normalized by the cross sectional area of the blade tip (0.96 cm^2 and 0.6 cm^2, respectively) ranged from 0.5 to 1.6 with a mean and median of 0.9 and a standard deviation of 0.2.

3.4.5 Blade and hand hardness

The lowest values of the blade hardness index ($B < 5$ N) typically correlated with weakly cohesive snow of hand hardness index 1.7–3.7 (Figure 3.10). There is considerable overlap between blade hardness indices for neighbouring hand hardness categories. The blade hardness data in Figure 3.10 are the group means from 52 different snow layers in which typically 10 blade hardness measurements (parallel to the stratigraphic layering) were taken in each layer. The plotted hand hardness categories are those that correspond to cohesive snow as measured by $B > 0$ N. The blade hardness in layers of hand hardness index 0.7–1.3 was always 0 N. In the context of this study such snow was considered cohesionless. In layers of hand hardness index 1.7–3 some values of $B = 0$ N were recorded, but the mean of repeated tests was always greater than zero.

The variability of repeated blade hardness tests decreased with increasing hand hardness. The COV was highest in any snow that still contained decomposing and fragmented forms, which were most often found in young snow that was in the process of bond formation (and thus had low hand hardness). The next highest COV was found in faceted crystals. The lowest COV's in repeated measures were from rounded grains and mixed rounded and faceted grains.

3.4.6 Blade hardness index as a proxy for strength

Recently deposited snow layers were monitored and sampled for laboratory testing as soon as the snow was cohesive enough to extract, handle and transport. It was not possible to extract any samples characterized by hand hardness index 1 because the snow was too weak. When snow was just cohesive enough to extract, the blade hardness of the snow would, in nearly every case, register above 0 N.

Only 9 of 238 strength tests in the lab were paired with a blade hardness index of 0 N. These nine samples were from the softest and most fragile snow layer that was successfully tested in the lab. The true value of blade hardness index for many (if not all) of these samples was likely between 0 N and 1.7 N. Lack of gauge sensitivity rather than lack of bond strength prevented quantifying the blade hardness index of these samples.

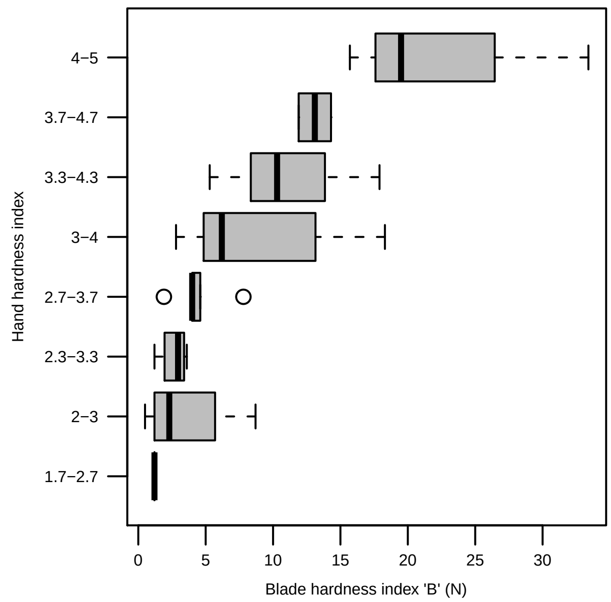

Figure 3.10: *Box plot of hand hardness index versus blade hardness index for cohesive snow. The boxes contain the central 50% of the data points, the whiskers extend to points within 1.5 times the inner quartile range from the median. Outliers are plotted as individual points. Overlap between hand hardness indices is related to the assumed uncertainty and imprecision of the hand test (n=520).*

In our data the tensile strength correlated much better with the blade hardness index than with the density (Table 3.2). The blade hardness index had a nearly equal correlation coefficient with the density as with the tensile strength. This suggests that the blade hardness index could be used to predict both density and strength, equally well, with a single measurement.

A subset of the laboratory strength tests ($n = 143$) also had precise deflection measurements at the bottom of the beam. These measurements allowed for the calculation of the flexural modulus, analogous to an elastic (or linear viscoelastic) modulus. For this subset, the Spearman correlation coefficient between the blade hardness and the flexural modulus was 0.68 and was highly significant ($p < 0.001$).

Table 3.2: *Spearman's rank correlation coefficients (upper diagonal) and p-values (lower diagonal) for the laboratory tensile strength data. Bold face indicates statistical significance at the α = 0.05 level. The lower part of the table shows the range of each variable (n=238).*

	f_t	ρ	B	T	E
f_t		**0.644**	**0.844**	-0.066	**-0.325**
ρ	<**0.001**		**0.819**	0.002	0.085
B	<**0.001**	<**0.001**		-0.046	-0.118
T	0.311	0.972	0.475		-0.099
E	<**0.001**	0.192	0.070	0.126	

Tensile strength f_t	$3.4 < f_t < 66.7$ kPa
Density ρ	$149 < \rho < 364$ kg m^{-3}
Blade hardness index B	$0.0 < B < 17.4$ N
Temperature T	$-12.0 < T < 0.0$ °C
Grain size E	$0.5 < \mathsf{E} < 1.0$ mm

3.5 Discussion

3.5.1 Density and hardness

Tables 3.1 and 3.2 have similar variables which are significantly correlated. The lower correlation between the blade hardness index and density, compared to that between ram hardness and density, may be due to several factors. The ram hardness, which deflects and compacts more snow as the cone tip penetrates, might be expected to correlate better with density than a thin blade measure which minimizes compaction during penetration. The current data set also contained snow with mixed rounded and faceted forms compared to that of *Martinelli* (1971) who did not sample any coarse-grained lower layers in which faceted forms may have been present. At equal densities, snow with faceted forms is weaker than rounded forms (*Jamieson*, 1988). The smaller range of densities tested in the present data may also be a factor in the lower correlation.

The wide variability in mechanical properties of snow at a given density is well known. *Takeuchi et al.* (1998) and *Höller and Fromm* (2010) observed high scatter between density and flat plate hardness measures. *Martinelli* (1971) and *Keeler and Weeks* (1968) reported increasing scatter in ram hardness with increasing density, which is consistent with the blade hardness-density data (Figure 3.8).

3.5.2 Penetration rate effects

Given the high variability in snow properties it was not surprising that no statistically significant rate effect was observed when pairing single blade hardness tests at different penetration rates. The typical COV of repeated measures in the same layer was on the order of 0.1–1. This high level of variability, inherent in snow properties, makes in-situ testing for systematic rate dependence difficult.

In the grouped test series with 10 fast and 10 slow measurements within the same layer, the statistically significant rate effect observed was the opposite of what was expected. The slow tests were weaker than the fast tests, which conflicts with the precise laboratory results of *Fukue* (1977) and *Narita* (1980). The strain rate of the fast blade hardness tests, on the order of 10^{-2} s^{-1}, is higher than any of the previous laboratory results, however.

Horizontal spatial variability cannot be ruled out as a factor in these results, as the fast and slow tests were separated by up to 50 cm within the same layer. *Takeuchi et al.* (1998) and *Höller and Fromm* (2010) demonstrated horizontal variability using push-pull hardness measures at similar length scales. Therefore it cannot be confirmed that the snow properties were the same for the two spatially separated test series. This point could have been addressed by spatially pairing fast and slow tests, alternately. The rate effects could also be influenced by a rate dependence in the development of a nose cone of grains being pushed ahead of the blade tip.

Therefore there is still some uncertainty regarding the dependence of the blade hardness index on penetration rate. Rate effects could be further investigated using a universal testing machine to drive the blade into snow samples at precise speeds. The force gauge used in this study has a mounting backplate which would facilitate integration with a testing machine. The testing machine used for the strength tests in this study had a maximum crosshead speed of 1.25 cm s^{-1}, so it could be used to investigate the slower push speeds. Recording the penetration resistance at 5000 Hz in this sort of testing, rather than just the peak force, would address many of these questions. Such tests would indicate if the schematic interpretation of the blade hardness measure (Figure 3.1), based on the slower penetration speeds of *Fukue* (1977), is appropriate for the fast push speeds used in this study.

When comparing the blade hardness results obtained by different operators, the results varied no more than would be expected given the observed variability in repeated measures using the same operator. The data set was not consistently divided by users to permit formal statistical analysis to confirm this point, however. Three people (the first author and two field assistants) were the primary operators of the gauge for the data contained in this paper and the results from each operator were taken as interchangeable.

Additional tests are necessary using different people pushing the blade hardness gauge into the same layer in order to more conclusively address the consistency across operators. However, given the commonly observed COV of repeated measures (on the order of 0.1–1) in homogeneous snow from the same operator (assuming consistent push speeds for a given operator), it is doubtful that a statistically significant difference in operator results would be found. This result is unique when compared to, for example, the hand hardness test which requires a subjective judgement about penetration force which can vary across observers.

3.5.3 Blade orientation

The lack of dependence of mean hardness on blade orientation in homogeneous layers is likely the result of the careful selection of layers that did not contain thin hard or soft sublayers or noticeable gradients in hardness or other properties from top to bottom. In the presence of stratigraphic changes in layers that were not sensed manually, conditions which were likely present in some cases, the lack of dependence on orientation probably stems from the depth averaging of the slope-parallel measurements. In many cases this technique will capture small hard or thin sublayers.

In most practical in-situ applications, it made the most sense to orient the blade parallel to the layering. The observation that tests conducted normal to the layering had lower variability than parallel oriented tests is important, however. In scenarios where only a single measurement was or could be taken, such as in the lab on snow samples that did not permit multiple measurements, the blade was typically oriented perpendicular to the layering. This is effectively equivalent to saying that, given the choice between sampling from two populations with equal means but different variances, preference was given to sampling from the lower-variance population.

3.5.4 Blade size effect

When normalized by the cross-sectional area of the blade tip, the 20 cm blade gave slightly (but not significantly) lower values of penetration resistance. This could be related to a slightly smaller zone of compaction around the 20 cm blade due to its smaller thickness. The dependence of the results on the width of the blade could further be explored, though the 10 cm length scale was motivated by considerations from the fracture mechanics of slab avalanches. This length scale was also convenient from the perspective of ease of use, especially when compared to the 20 cm blade which was heavier and more awkward to align with the snow.

The original motivation for using a wider blade was to attempt to capture the transition between cohesionless and cohesive snow. It turned out that the force gauge sensitivity problem near zero was the limiting factor in soft snow rather than the blade width, however. The operating range of the gauge was very low compared to the full scale capacity of the gauge. Rather than changing the blade width, a gauge with a lower capacity and higher sensitivity near zero would better identify the threshold penetration resistance that separates cohesive from cohesionless snow.

3.5.5 Hardness and strength

The blade hardness index characterizes an averaged measure of penetration resistance over a length scale of about 100 grains. The index compares favourably side-by-side with tensile strength and flexural modulus measurements in the lab. The tensile strength correlated higher with the blade hardness index than with any other variable in the present data (Table 3.2). Other investigations (e.g. *Martinelli*, 1971) have shown similar correlations with different measures of hardness and tensile strength. The reason that density continues to be used as the primary index variable for strength and other mechanical properties of snow is related to the lack of standardization and adoption of a hardness measure across disciplines interested in snow mechanics and avalanches. The blade hardness gauge in this study is easy to use, inexpensive, and appears promising as a tool for addressing this issue.

The observation that the softest snow that could be physically handled and transported to the laboratory had the lowest (0-2 N) values of the blade hardness index is an independent confirmation that thin blade penetration resistance indicates sufficient bonding between snow crystals to give strength to macroscopic volumes of snow. This is the same conclusion with regard to blade hardness and unconfined compressive strength found by *Fukue* (1977). It is concluded that the blade hardness can be used to classify snow as cohesionless for $B \approx 0$ N and cohesive for higher values of B. Future research will aim to more precisely quantify this threshold.

3.5.6 Applications

The blade hardness gauge developed in this study can be easily adopted by avalanche forecasting and control operations that still rely heavily on snow pit observations. Many operations also cannot afford the cost of a probe penetrometer and are disinclined to adopt technology that requires postprocessing, a steep learning curve, or any subjective judgements. The blade hardness gauge was designed to complement existing observation techniques rather than attempt to eliminate the need to dig a snow pit. The blade hardness is an intuitive measure, analogous to the hand hardness test which is common in avalanche operations. As a research tool, the blade hardness measure shows promise as an objective proxy for macroscopic properties of interest in avalanche applications and snow mechanics generally.

The blade hardness gauge could be used to characterize the strength of thick persistent weak layers that are commonly related to slab avalanches (*McClung and Schaerer*, 2006). For example, the gauge could track the relative hardness of a newly buried weak layer, and the storm snow overlying it, as they both evolve and gain (or lose) strength. The gauge could also be used to track the loss of cohesion in snow during facet formation or as it approaches the melting temperature.

The blade hardness may also be useful for characterizing the strength of snow at higher densities, such as in firn snow. A smaller blade could be used in such a scenario because the rationale for the 10 cm length scale related to avalanches would not apply. This would reduce the potential for blade bending or twisting in stiffer snow. A higher capacity force gauge would be necessary, though, and there would likely be a limiting density beyond which a blade could no longer be pushed into the snow.

3.5.7 Limitations

In principle it would be desirable to have larger sample sizes for many of the hypothesis tests and other comparisons made in this study. Given the destructive sampling technique and the size of the blade, however, this was often not possible. The area that would be taken up by increasing the number of tests would increase the dependence of the results on the spatial variability of snow properties, making conclusions more difficult to draw even if the hypothesis test results appeared more robust. Moreover, part of the motivation in the development of this gauge was to provide a fast, supplemental piece of information related to or dependent on snow microstructure rather than to investigate in detail the microstructure itself.

The types of snow investigated in this study were limited to what was available in the natural snow cover. The range of most properties (Table 3.2) is appropriate for avalanche applications. Most of the tests in this study were done in dry snow. A limited number of tests in moist snow were carried out, but not enough to test for any significant differences with dry snow. Further testing would need to be done to determine how the penetration resistance changes in moist to wet snow.

Additional work also needs to be done to relate the cohesion threshold identified in this study to the cohesion threshold at which slab avalanches first begin to occur in storm snow. Snow avalanches are reported in the hand hardness index range of 1–2 (*Schweizer and Jamieson*, 2001), though a large uncertainty exists in these values. The lowest hand hardness values for samples that could be handled in this study were in the range 1.7–2.7, which suggests that some slab avalanches may occur in snow that is weakly cohesive but too weak to be handled for testing.

There is a potential boundary condition effect associated with measuring hardness in the wall of an excavated snow pit and using the results to characterize the properties of snow in situ where the stress state is different. The observations in the present study, with the COV on the order of 0.1–1 for closely-spaced clusters of resistance values in homogeneous snow, suggest that measuring the influence of internal stress amid the spatial variability of natural snow would be difficult. Moreover, the relative hardness of adjacent layers is often as important a piece of information as actual hardness scores in stability evaluation (e.g. *Schweizer and Jamieson*, 2007).

The capacity of the digital force gauge used in this study did not match the operating range, which likely contributed to the observed sensitivity problems at the bottom 1% of the scale. We did not conduct any calibration tests covering the bottom 5% of the scale, so we can only speculate as to the origin of the observed 1.7 N threshold penetration resistance. Temperature effects on the load cell also likely played a role. Errors introduced by temperature effects were likely larger in the laboratory results than the in situ results. As most of the data was obtained at ambient temperatures between 0 and -10°C, the relative shift in the zero point of the load cell across the data is small (about 0.2 N).

A load cell with a capacity in the range 30–50 N with at least 0.1 N resolution and better than 1% accuracy would be more appropriate for future investigations with a 10 cm blade. Additional calibration procedures should be conducted to more precisely characterize the function of the gauge at low temperature and low load. Comparing the results in the present paper against those obtained with a more appropriate load cell will be the subject of future work.

3.5.8 Conclusions

A thin blade hardness gauge was developed that characterizes an average penetration resistance over a length scale appropriate for the continuum characterization of snow properties relevant to avalanches. Horizontal compaction of snow around the blade is minimized relative to all other common hardness measures. The gauge is an inexpensive, small and lightweight tool that can be used in the field or lab with results that are objective and consistent across observers. The measurement technique is simple and adds little time to other experimental methods. Compared to other standard measurements such as density, temperature and grain size, the blade hardness index was the best variable for correlating with the tensile strength of snow, one of the most important properties in the triggering and release of slab avalanches.

Chapter 4

Tensile Strength of Dry Alpine Snow

The tensile strength of snow has long been viewed as a fundamental property related to the release of slab avalanches. Whether early investigators believed that the initial fracture which triggered an avalanche was in shear beneath the slab or tension through the slab, the coherent properties of slab snow have been viewed as important. This recognition is reflected in the numerous studies of the tensile strength of cohesive alpine snow, beginning as early as the 1930's and continuing through to the present.

In many ways, the measurement of tensile strength has been easier than the characterization of the *structural* factors that influence strength. However, many different types of tests have been conceived and conducted for measuring the strength of snow in tension. These tests span a wide variety of sample volumes, loading geometries, environmental conditions, and strain rates. In most tests only a small portion of the total sample volume is highly stressed and responsible for the failure of the sample. This is typically due to the presence of induced stress concentrations associated with gripping the sample or localizing the failure. The variability in testing conditions associated with the existing strength data, compounded with the microstructural variability both within and across data sets, leads to much difficulty when comparing or synthesizing data from different sources or selecting representative data for a given application.

The first section of this chapter contains a review of published data on the tensile strength of seasonal snow. The most widely used variable which is common across data sets, and often the only reported variable available to address the numerous factors which influence strength, is the density. The data come from uniaxial and bending tests performed in situ and in cold labs. Around 2000 tensile strength tests from 20 sources are synthesized, primarily as a function of density. Where additional information is available, the dependence of strength on hardness, loading rate, sample size and temperature are reviewed.

In the second section of this chapter, new data from the current study is introduced. The data come from three and four point bending tests on unnotched beam samples. A total of 245 tests were conducted over the course of 20 days in the cold lab in the winters of 2007-2008 and 2008-2009. The derivation of the equations for calculating the tensile strength is first presented, followed by an exploratory analysis of the dependence of the strength on the sample density, blade hardness index, grain size, specimen size, loading rate, and beam slenderness.

The third and last section contains univariate models of tensile strength fit through the data from the present study and several other representative studies. A common power-law formulation for the strength as a function of density is used in each case, and several models of strength as a function of hardness are explored where appropriate. Numerous graphical and statistical diagnostics of the model residuals are explored in detail to assess the assumptions inherent in these models, judge the goodness of fit of each model, and choose the best univariate model for representing the data.

4.1 Review and Analysis of Previous Data

As early as the 1930's investigators in Switzerland began to measure the strength properties of snow, adopting many experimental techniques from the soil sciences. The first laboratory uniaxial tensile tests were reported by Haefeli (1939) (translated in *Bader et al.*, 1954). Shortly thereafter, also in Switzerland, the centrifugal tensile testing method was developed (*Bucher*, 1948) which became the predominant method for measuring tensile strength for the next 30 years. Starting in the late 1960's, in situ methods were developed for testing the properties of undisturbed natural snow. These methods allowed for larger specimen sizes which were believed to be more appropriate for relating to avalanche activity than the small specimens typically used in lab tests.

Section 4.1 here is organized first around a discussion of the extensive centrifugal strength data (Section 4.1.1). Next, in Section 4.1.2, the results of in-situ tests are reviewed, followed by strength data from laboratory measurements in Section 4.1.3.

4.1.1 Centrifugal tests

Test description

The 12 data sources reviewed in this section are listed in Table 4.1, which indicates the variables and properties that were reported for each study. The only property which was reported in every study was the strength itself. All but one study reported the density of the snow for each test. Beyond these two properties, one a structural and the other a material property, the types of variables which were reported varied widely.

The general procedure for the centrifugal tensile testing was as follows. Snow samples were first extracted from the snowpack using a cylindrical tube. The primary axis of the tube was typically oriented parallel to the slope (rather than toward the ground). This ensured that the sample was from one distinct stratigraphic layer and did not contain weak layers or interfaces between layers of different properties. The tube was weighed prior to testing in order to calculate the snow density. The sample was then slid into the tester and gripped about the center using clips, as illustrated in Figure 4.1a. This clip system reduced the central cross section of the sample, introducing a volumetric and geometric stress concentration.

Once gripped, the samples were spun about an axis normal to the axis of the cylinder. The spin rate was increased until the sample failed in tension. The location of failure was generally reported as being in the middle of the sample between the clips (due to the stress concentration). Some low density samples were reported to fail at outer points along the cylinder in low density snow, but these points were discarded (e.g. *Keeler*, 1969; *Martinelli*, 1971). In data sets where it was not explicitly stated, I assumed that all samples failed on a plane in the central cross section. It should be emphasized, however, that in most studies no information was given about the location of failure or the exclusion of data points based any criterion.

For calculating the nominal strength, the rotational speed at failure was recorded in some fashion. Early versions of centrifugal testers required the operator to observe a dial and manually record the spin rate at the time of sample failure. An improved tester design (*Sommerfeld and Wolfe*, 1972; *Upadhyay et al.*, 2007) automatically recorded the spin rate at failure. Other investigators may have devised methods to automatically record the spin rate at failure, but very few details of the experimental setup (e.g. acceleration of spin tester, sample storage times, shape of geometric stress concentration) were reported in the sources reviewed here. Typically little more than the calculated nominal tensile strength and the snow density were published (Table 4.1).

Source	σ_{Nu}	ρ	R	T	E	Loading Rate	Permeability	Geometry	n
Bucher (1948)	✓	✓		✓	✓				71
de Quervain (1951)	✓	✓	✓[1]	✓	✓				12
Bader et al. (1951)	✓	✓					✓	✓	9
Butkovich (1956)	✓	✓		✓				✓[4]	6
Roch (1966)	✓	✓		✓					64
Keeler (1969)	✓	✓				✓		✓[4]	150
Keeler and Weeks (1968)	✓	✓				✓		✓[4]	183
Martinelli (1971)	✓	✓	✓[2]	✓	✓	✓	✓	✓[4]	104
Sommerfeld (1974)	✓	✓						✓[5]	158
Gubler (1978)	✓					✓			20
Schneebeli and Johnson (1998)	✓	✓	✓[3]					✓[4]	45
Upadhyay et al. (2007)	✓	✓		✓	✓	✓			153

Table 4.1: *Sources of data and variables reported in published centrifugal tensile experiments on cohesive snow. The nominal tensile strength is given by σ_{Nu} , the density by ρ, the hardness by R, the temperature by T, the grain size by* E.

[1] *Three types of hardness measurements (rammsonde, a small spring-loaded conical tester and the flat plate Canadian hardness gauge) were reported.*

[2] *Ram hardness.*

[3] *Average SnowMicroPen resistance.*

[4] *Only the dimensions of the cylindrical cutter tube or reference to the geometry-specific nomogram developed by Bader et al. (1951) were given.*

[5] *Geometry of samples described in Sommerfeld and Wolfe (1972).*

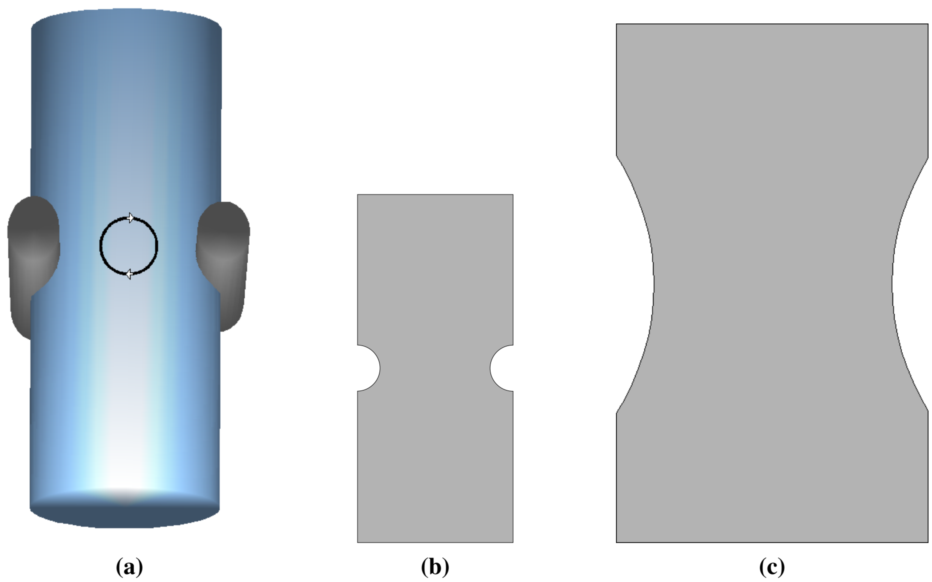

Figure 4.1: *General geometry of centrifugal tensile test specimen with two-pronged clip in the center (a), top view of standard test specimen (b) and relative size and shape of specimens used by Sommerfeld (1974) (c).*

Strength calculation

For a cylindrical sample of radius $\mathbb{R}$ spun about an axis normal to the cylinder axis, the differential centrifugal force acting on a differential disc of mass dm is given by

$$dF = dm\Omega^2 r = \left(\rho\pi\mathbb{R}^2 dr\right)\Omega^2 r \tag{4.1}$$

where Ω is the angular frequency (rad s^{-1}) and r is the radial distance of the disc from the center of the cylinder. This relation is integrated over the half-length $l/2$ of the cylinder to get the total centrifugal force acting on the central cross section of the cylinder:

$$F = \int_{r=0}^{r=l/2} \rho\pi\mathbb{R}^2\Omega^2 r dr = \frac{1}{8}\rho\pi\mathbb{R}^2\Omega^2 l^2 = \frac{1}{2}\rho\pi^3\mathbb{R}^2 f^2 l^2 \tag{4.2}$$

where angular frequency Ω has been expressed as $2\pi f$ where f is the number of revolutions per second. The result was often reported in the literature in terms of the number of revolutions per minute N in relation to the angular frequency Ω via $\Omega = 2\pi N/60$. The nominal tensile strength σ_{Nu} is found by dividing the maximum force in Equation 4.2 (from the value of f at failure) by the effective cross sectional area, which is reduced from the gross area due to the two-pronged clip that holds the sample in the center (Equation 4.1). Expressing the result in terms of frequency f leads to

$$\sigma_{Nu} = \frac{F}{A_e} = \frac{1}{2A_e} \rho \pi^3 \mathbb{R}^2 f^2 l^2. \tag{4.3}$$

Originally reported data

Figure 4.2 shows a summary of nominal centrifugal tensile strength data from the 11 sources in Table 4.1 that reported the snow density (*Gubler* (1978) is the study that did not report density). For a given density, the scatter in strength covers up to two orders of magnitude. This in large part reflects changes in loading rate, snow hardness, temperature, and snow microstructure between and within data sets.

The lowest mean strength values came from *Sommerfeld* (1974), who also had specimen sizes a factor of four larger than the standard sample adopted by the rest of the studies. The data of *Keeler and Weeks* (1968) are systematically higher, by a factor of 2-3, than any other source. This difference could be attributable to differences in hardness or microstructure at the same density compared to the previous studies at different field sites. It could also be due to the presence of some moist or wet snow samples which were subsequently refrozen prior to testing. *Keeler and Weeks* reported that not all of their tests were done before the isothermal transition at the end of the winter season, so some of the samples may have been moist or wet when extracted and then refrozen by the time the tensile test was carried out. A further explanation could be related to a different stress concentration in the central cross section resulting from a differently shaped pronged clip that held the samples into place. The nomogram developed by *Bader et al.* (1951) for relating the spin rate at failure and the mass of the sample to the nominal strength was referenced in the strength calculations of *Keeler and Weeks* (1968), but if any geometric factors were different from those which went into the derivation of that particular nomogram, the results would have been systematically biased. No mention was made of any change in experimental technique, however. A final factor may have been sample storage for long periods of time prior to testing, which would likely promote sintering and an increase in strength at constant density. However, no indication was given on whether samples were stored or, if so, for how long.

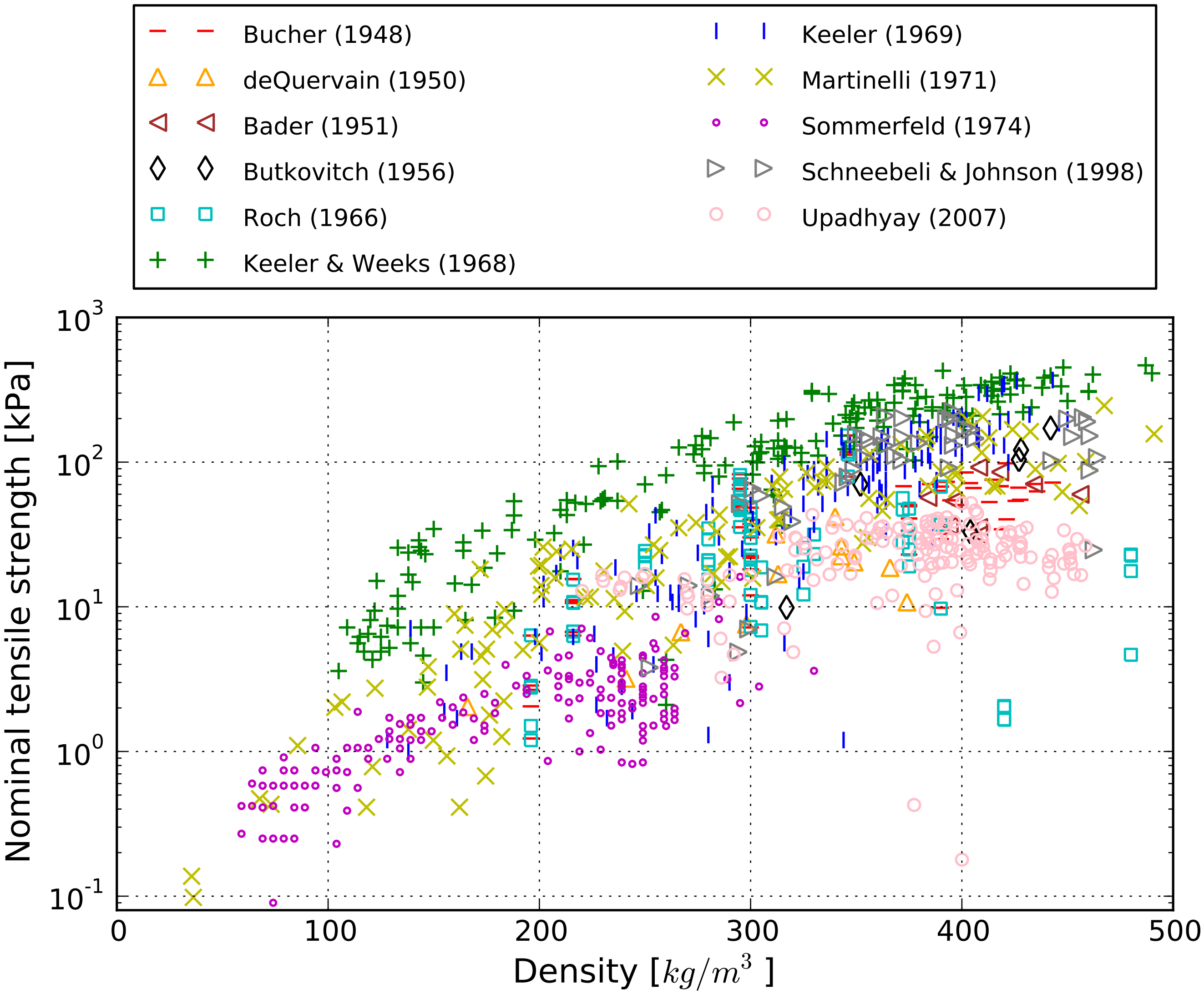

Figure 4.2: *Originally reported centrifugal (nominal) tensile strength as a function of snow density. These data represent the majority of the most commonly cited tensile strength data in avalanche applications.*

Stress concentration in notched samples

The nominal strength values as originally reported in each study were defined using the nominal stress at failure (Equation 4.3). As mentioned above, the notched cross section caused by the two-pronged clip that held and spun the samples in the centrifugal tests introduced a geometric stress concentration. This stress concentration was mentioned by *Sommerfeld and Wolfe* (1972), but was never accounted for in the strength calculations of any of the studies reviewed here.

If the tensile strength was to be equated with the maximum tensile stress at failure, a more consistent definition than using the nominal stress, the data as originally reported in the literature need to be corrected. Otherwise the nominal strength values from tests with different geometries, and therefore different stress concentrations, could not be directly compared. Relations were thus sought for a stress concentration factor to relate the nominal to maximum tensile stress for the geometry of the centrifugal tests.

The stress concentration factor K_{tn} relates the nominal tensile stress σ_N to the maximum stress σ_{max} via

$$K_{tn} = \frac{\sigma_{max}}{\sigma_N}. \tag{4.4}$$

The subscript 'n' in the K_{tn} term indicates that the stress concentration factor uses the net cross sectional area of the specimen for the nominal stress calculation (the gross section can alternately be used). Stress concentration factors were calculated or estimated for the data sources represented in Table 4.1, and the tensile strength f_t was equated with the maximum stress at failure σ_{max}. The key assumption associated with this argument, then, is that the tensile strength f_t should correspond with the maximum stress at failure rather than the nominal stress, which can vary widely depend on the presence and geometry of stress concentrators.

Stress concentration factors for the net cross section were taken from *Pilkey* (1997). The numerical values used to correct the published data were taken as the average of K_{tn} for the flat tension specimen with a U-shaped groove (Figure 4.3a and c) and the round bar with a circumferential groove (Figure 4.3b and d) since the geometry of the actual snow specimens (round sample with straight notches/grooves) was not available. This averaging led to $K_{tn} = 2.25$ for the “standard” data using the sample and notch geometry reported by *Bader et al.* (1951). *Sommerfeld* (1974) improved upon the standard design of the centrifugal testing machine to reduce the stress concentration and increase the size of the sample, leading to $K_{tn} = 1.28$.

Of all the studies listed in Table 4.1, only *Bader et al.* (1951) and *Sommerfeld* (1974) reported the specific shape and dimensions of the notched central cross section. Most other studies in Table 4.1 reported only the diameter and length of the cylindrical sampling tube, neglecting to specify the shape and size of the notch induced by the pronged sample holder and the resulting effective cross sectional area. Five of the sources in Table 4.1, comprising nearly 500 tests, referred to the nominal strength equation reported by *Bader et al.* (1951), which took the form of Equation 4.3 with numerical values for A_e, $\mathbb{R}$, and l already plugged in (as reported: $\sigma_{Nu} = 1.166 \times 10^{-9} MN^2$, where M is the sample mass, N is the number of revolutions per minute at failure and σ_{Nu} is in kg/cm^2). For the present analysis, any literature sources that referenced this equation were given the benefit of the doubt that they indeed used the exact same geometry to justify the use of the published geometry-dependent equation. However, not enough information was typically published to critically evaluate this assumption. For example, it may not be safe to assume that each study used pronged clips of the exact same size and shape to notch and hold the cylindrical samples during testing. There is therefore some uncertainty in the actual value of K_{tn} appropriate for most studies.

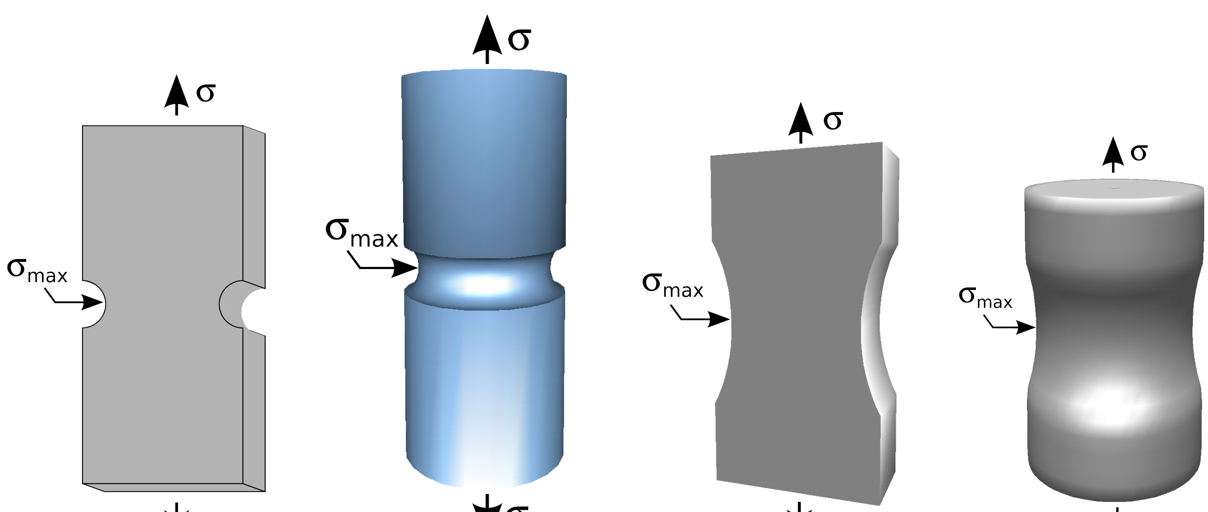

(a) K_{tn}=2.434 **(b)** K_{tn}=2.132 **(c)** K_{tn}=1.321 **(d)** K_{tn}=1.244

Figure 4.3: *Standard geometries used to approximate the stress concentration factor K_{tn}. Geometries in (c) and (d) are for the samples tested by Sommerfeld (1974), (a) and (b) are for all others (not drawn to scale).*

A further complication arises from the nonuniform tensile stress as a function of radius about the center of rotation. The common stress concentration factors referenced from *Pilkey* (1997) are calculated based on the assumption of a uniform, remotely applied load. The total force acting on the central cross section, calculating using Equation 4.2, is appropriate in a nominal or average sense. However, the relationship between locally concentrated stresses and bulk nominal stresses in a nonuniform stress field may be different than characterized by the stress concentration factors considered here. Though from the perspective of obtaining simple estimates, the approach considered here and the resulting values seem reasonable.

The centrifugal tensile strength data, adjusted to account for the stress concentration factor, are shown in Figure 4.4. The data of *Schneebeli and Johnson* (1998) were excluded on the basis of lack of specific information about the shape of the notched cross section. The authors simply describe a "sharp" notch, a description that differed from others regarding the shape of the cross section created by the pronged clip. That authors also did not describe the testing procedure in any detail compared to other studies. These concerns called into question the use of the stress concentration factors considered for the rest of the studies, and it was deemed most appropriate to neglect the data from further analysis.

The adjusted strength values of *Keeler and Weeks* (1968) approach 1 MPa, which is near the tensile strength of pure ice (≈1.5 MPa, *Schulson* (2001)). According to previous compilations of tensile strength data (e.g. *Mellor*, 1975) the tensile strength of snow at a density of around 400 kg/m^3 is still about an order of magnitude lower than that of ice. However, the data reviewed by Mellor are largely contained in this study, so the argument is somewhat circular, though no corrections for the stress concentration were made in previous studies or compilations. Given the large amount of data overlap between other studies, the data of *Keeler and Weeks* (1968) appear questionably high. The mean strength of all the data in Figure 4.4 at a density of about 400 kg/m^3 (including the data of *Keeler and Weeks* (1968)) is around 20–30% of the tensile strength of pure ice, which is physically reasonable.

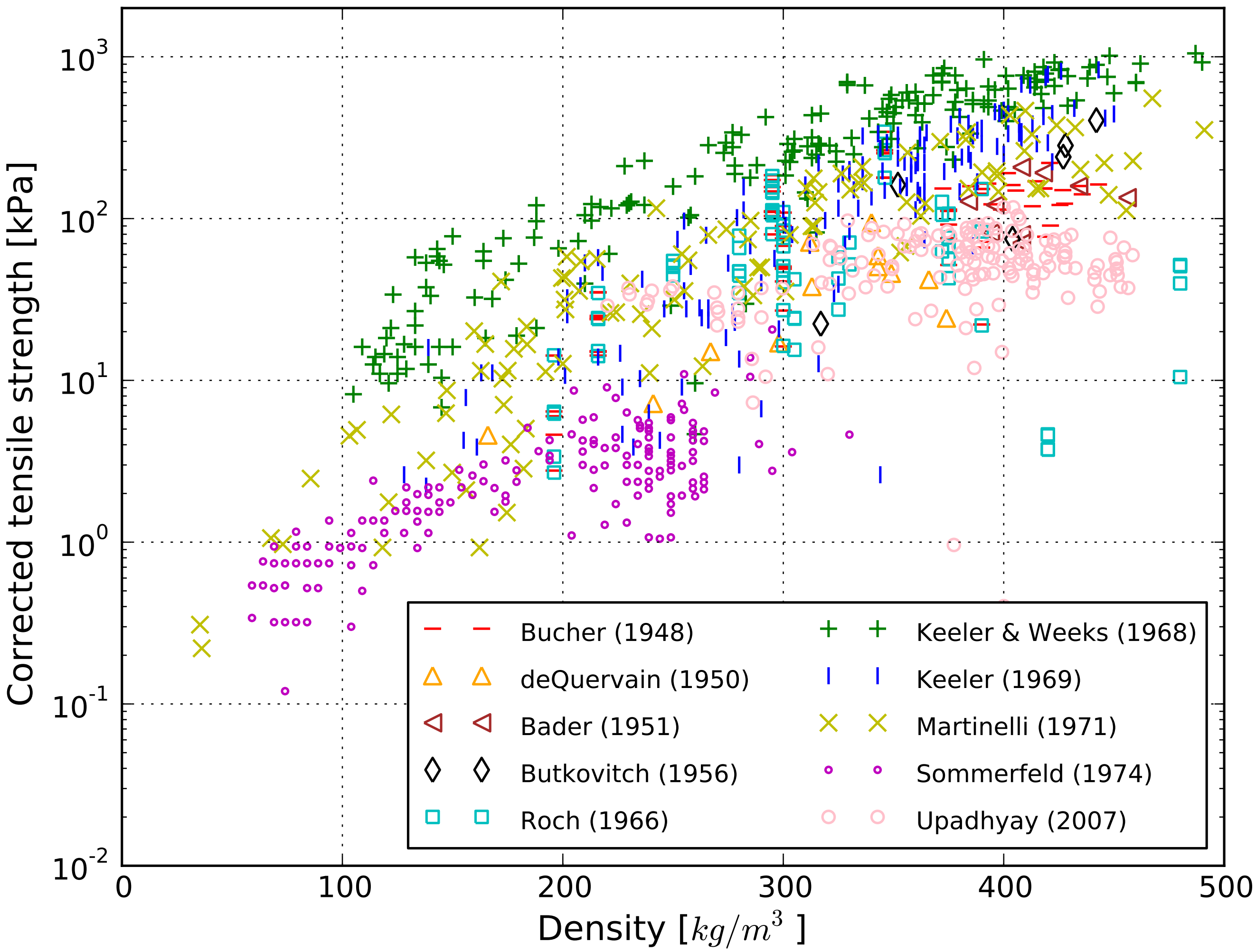

Figure 4.4: *Centrifugal tensile strength versus density, corrected for the stress concentration using Equation 4.4 and the stress concentration factors in Figure 4.3.*

Systematic error associated with reaction time

Early versions of the centrifugal tensile tester had no automatic way to shut off the spinner when the sample failed nor to record the precise spin rate at failure. The operator had to read a dial indicating the spin rate when the failure of the sample was seen or heard. This procedure could have introduced a systematic bias related to the reaction time of the observer. This error can be estimated by calculating what the actual spin rate at failure may have been by using the reported spin rate minus the increase in spin rate associated with the reaction time of the observer:

$$f_{corrected} = f_{recorded} - (\text{reaction time}) \times \frac{df}{dt} \tag{4.5}$$

where df/dt is the acceleration of the spin tester. Table 4.2 shows the acceleration values for the only four studies that reported this information. If the acceleration is known and considered constant for a given data set, and a constant reaction time is assumed, then the recorded strength data can be corrected with Equation 4.5.

Source	df/dt $[rev/s^2]$
Keeler and Weeks (1968)	10
Keeler (1969)	10
Martinelli (1971)	2-3
Upadhyay et al. (2007)	0.13, 0.68

Table 4.2: *Sources that published the rate of acceleration df/dt of the spin tester, allowing calculation of the stress rate and strain rate at failure.*

Equation 4.5 predicts that the systematic error decreases as the recorded value of the spin rate at failure increases (Figure 4.5), since the second term on the right hand side of the equation can be considered constant for a given data set. The slower acceleration rate of the *Martinelli* (1971) data result in a lower systematic error, as evident in Figure 4.5. The systematic error would be the highest in weak snow, which necessarily fails at a lower stress rate (and thus spin rate) at failure. The strength data of *Keeler and Weeks* (1968) are the highest in Figure 4.4 and also come from the highest reported spin tester acceleration (Table 4.2). Equation 4.5 and Figure 4.5 suggest a possible systematic bias of over 50% for the low density (and thus low strength) values of *Keeler and Weeks* (1968). For the strongest samples the bias falls to 5-10%.

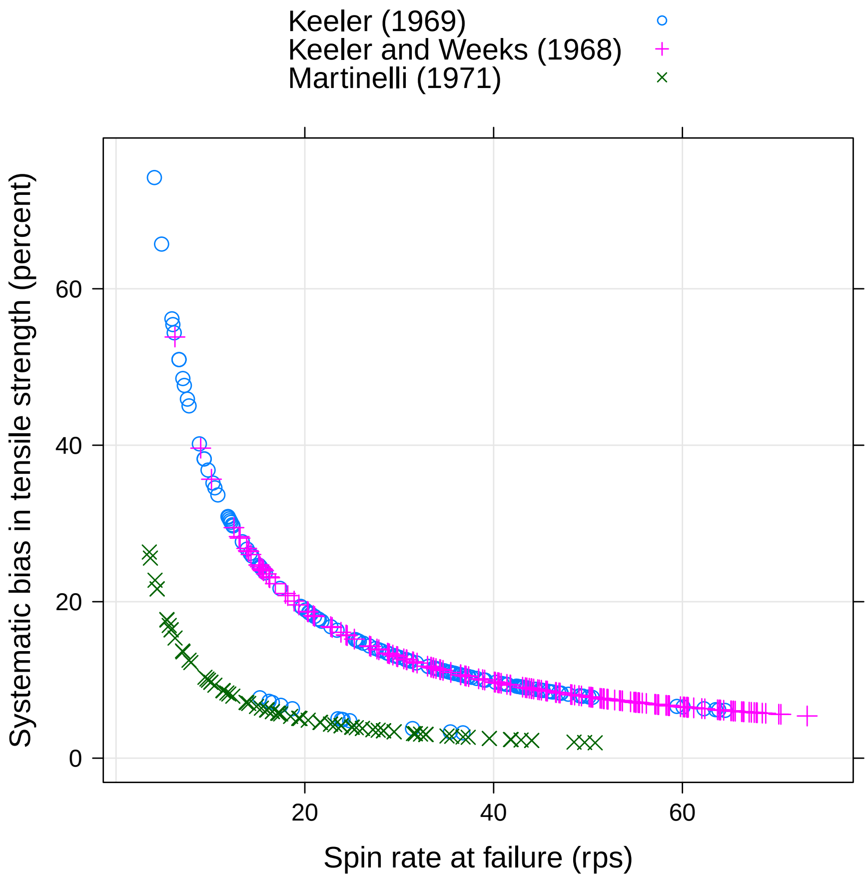

Figure 4.5: *Estimated systematic bias in tensile strength values as a function of the spin rate at failure in revolutions per second. The spin rate is related to the nominal strength via Equation 4.3. A reaction time of 0.2 seconds was assumed.*

No mention is made of the specific technique by which the failure was observed in most of the centrifugal tensile strength literature, whether an automatic shutoff was present, or whether any consideration or compensation for a systematic error associated with reaction time was made. Exceptions are *Sommerfeld* (1974) and *Upadhyay et al.* (2007) who did have optical automatic shutoff mechanisms which recorded the failure spin rate. Serious systematic errors may be present in other centrifugal data but, in the absence of any mention of the rate of acceleration of the tester, no estimate can be made of its importance.

Rate effects

The stress rate at failure can be calculated by differentiating Equation 4.3 with respect to time t:

$$\frac{d\sigma_N}{dt} = \frac{1}{A_e}\rho\pi^3\mathbb{R}^2 l^2 f \frac{df}{dt} \tag{4.6}$$

where df/dt is the rate of acceleration of the spin tester, which was only reported by four studies (Table 4.2). The spin rate at failure can be found from Equation 4.3 given the reported density, nominal tensile strength and dimensions of the snow sample. No information about the diameter of the samples was reported by *Upadhyay et al.* (2007), though the cylinder length was reported. For the following analysis I assumed that the samples of *Upadhyay et al.* had the same diameter as those listed above.

Approximate calculations of the strain rate at failure can be made from the stress rate in Equation 4.6. These approximate calculations can be used to determine where the failure falls with respect to the creep-to-fracture transition strain rate. Below this transition, the strain rate is low enough that creep effects dominate the deformation and clean fractures cannot originate or propagate. Above this transition, elastic effects dominate over creep effects, and clean, fast fractures are observed. For dry snow at the laboratory scale, this transition occurs in tension at $\sim 10^{-4}\,s^{-1}$ (*Narita*, 1980, 1983). The strain rate can be calculated using the stress rate from Equation 4.6 if an assumed stress-strain behaviour is used, such as

$$\dot{\varepsilon} = \frac{\dot{\sigma}}{E} \tag{4.7}$$

where $\dot{\sigma} = d\sigma_N/dt$ from Equation 4.6 and E is an effective Young's elastic (or storage) modulus appropriate for the strain rate and sample properties. This simple linear elastic relation is not necessarily appropriate physically, since the stress rate varies parabolically in time and snow is a strongly rate-dependent material, i.e. $E = E(t)$. This will likely lead to some decaying viscous effects in the deformation of the sample. Therefore, the relation in Equation 4.7 is not appropriate for modeling the stress rate-strain rate behaviour at any arbitrary point in time for the centrifugal tests. However, for order-of-magnitude calculations of the strain rate at failure, the simple relation in Equation 4.7 is a reasonable starting point.

Critical to this calculation is the selection of a representative single value for the elastic modulus E (or effective secant modulus if considering viscous effects) for a test that starts out viscous and ends somewhat less viscous, perhaps only approaching elastic right at failure. From the perspective of evaluating failure strain rates with respect to the creep-to-fracture transition rate, an upper bound estimate for E is more appropriate as it will lead to a lower bound estimate of $\dot{\varepsilon}$. This is important because the slab tensile fracture in an avalanche occurs following the propagation of shear fracture beneath the slab at a speed of around 20 m/s (*McClung*, 2007a). This high speed, combined with observations of clean, planar crown (tensile fracture) surfaces in slab avalanches, suggest that the tensile strain rate in the slab when it fails is above the creep-to-fracture transition. Therefore, lower bound estimates for the failure strain rate allow more conclusive decisions to be made about the applicability of test data for comparing with avalanche conditions.

Cyclical loading tests conducted at a frequency of 100 Hz were reported by *Sigrist* (2006) for the calculation of a dynamic Young's modulus. The strain rate in these tests was on the order of $10^{-3}\ s^{-1}$. Expressed as a function of density, Young's modulus from these data takes the form

$$E = 1.89 \times 10^{-6} \rho^{2.94} \quad [MPa]. \tag{4.8}$$

This equation was used for the calculations of the failure strain rate in Equation 4.7. The modulus values predicted by Equation 4.8 may approximate the true value right at failure but are likely too large for the early portion of the test or even for some kind of average value. They may in fact be too large by an order of magnitude. However, as discussed above, they provide lower bound strain rate estimates.

Figure 4.6 shows the strain rate at failure for data from the four studies that reported the acceleration of their spin testers (Table 4.2). The strain rate at failure is clearly in the brittle range for the data from *Keeler and Weeks* (1968), *Keeler* (1969) and *Martinelli* (1971). In this discussion, "brittle" is taken to mean "above the creep-to-fracture transition" and should not be confused with the distinction between brittle and quasi-brittle fracture, which is primarily a distinction of *relative length scales*, not time or rate scales. Conversely, "ductile" is taken to mean a strain rate below the creep-to-fracture transition.

Upadhyay et al. (2007) varied the acceleration rate between two different test series, as is evident from the bimodal distribution of strain rates in Figure 4.6. In both cases, however, the rate was much lower than used by previous investigators (at least those that reported the rotational acceleration) and the failures clearly fall in the ductile range. Lower modulus values in this case, which would result in higher strain rate estimates, would probably not shift the strain rates above the creep-to-fracture transition. This probably explains the lower values of tensile strength reported by *Upadhyay et al.* (2007) (Figures 4.2 and 4.4) and suggests that the data should be classified separately from the rest of the brittle data.

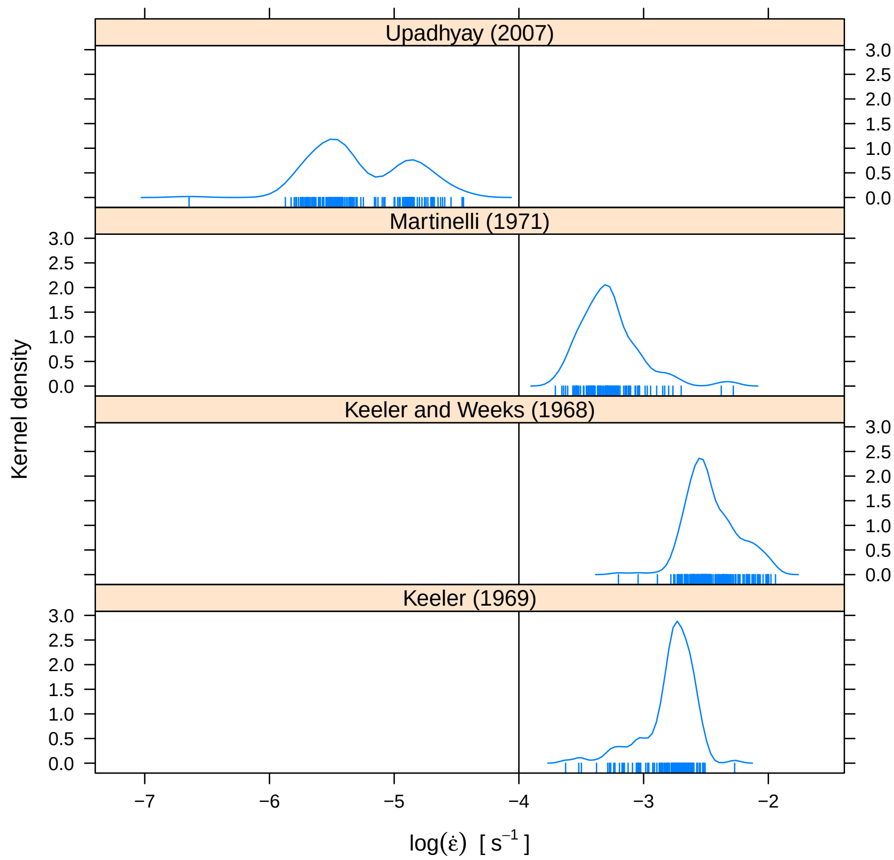

Figure 4.6: *Kernel density plot of the estimated strain rate at failure for sources that reported the rate of acceleration of the spin tester. The vertical line represents the approximate transition between creep rupture for strain rates below* $10^{-4}\,s^{-1}$ *and fast fracture for rates above.*

Temperature effects

Roch (1966) reported the effect of temperature on strength, largely from data originally reported by *Bucher* (1948). Figure 4.7 shows the strength as a function of temperature, plotted as the ratio of the strength at the given temperature divided by the strength at the highest temperature for the given test series. Typically only one strength measurement was made at each temperature.

Most of the data in Figure 4.7a indicate roughly a doubling of the strength as the temperature decreased from $0°C$ to about $-30°C$. For reference, the tensile strength of fresh-water ice increases by just 10% as the temperature is decreased between the same limits (*Schulson and Duval*, 2009). This is an indication that rate-dependent viscous effects in the data of *Roch* (1966) are likely clouding the temperature dependence. An empirical correlation based on the data from *Roch* (1966) has been used by a number of investigators (e.g. *Bader et al.*, 1951; *Butkovich*, 1956) to normalize experimental data to the same temperature, but this may not be appropriate in light of these viscous effects.

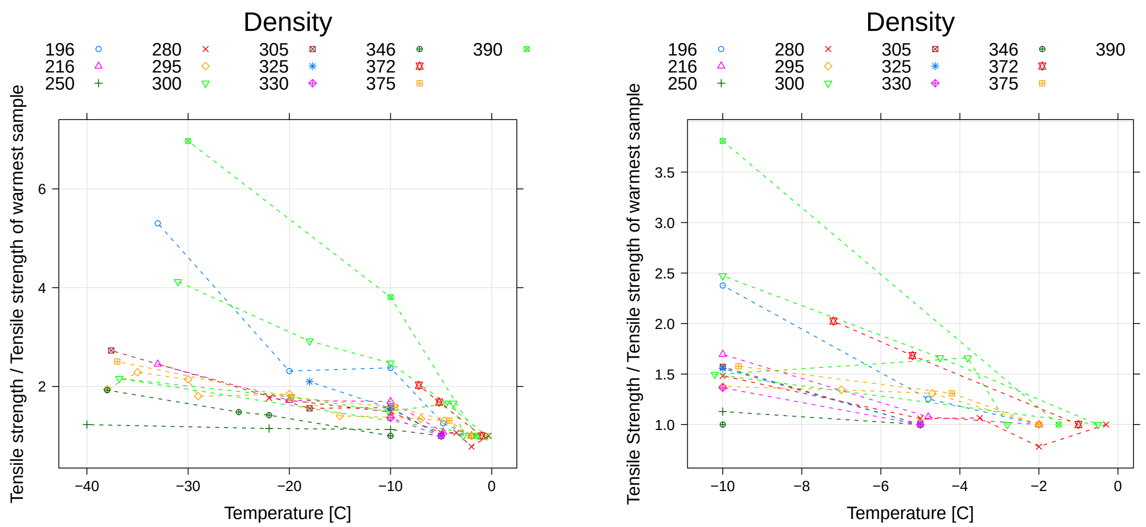

(a) (b)

Figure 4.7: *Ratio of the tensile strength at the given temperature to the strength of the warmest sample of the test series, from data reported by Roch (1966). Both graphs contain the same data, with (b) limited to temperature differences between $-10°C$ and $0°C$.*

Hardness effects

Both *Martinelli* (1971) and *de Quervain* (1951) reported the rammsonde (ram) hardness for the layers in which they also measured the tensile strength. Figure 4.8a shows the nominal tensile strength versus ram hardness. The data show a generally linear trend of increasing strength with increasing hardness, though with large scatter. Figure 4.8b shows the same data plotted against the density, with plot symbols and colors binned according to the associated hardness value. The trends in Figure 4.8 suggest that, for these data, the ram hardness is as good if not better than the density for serving as a single predictor for the tensile strength. Recall from Chapter 3 that the ram hardness and the density had nearly equal and very strong correlations with the nominal tensile strength in the data of *Martinelli* (1971).

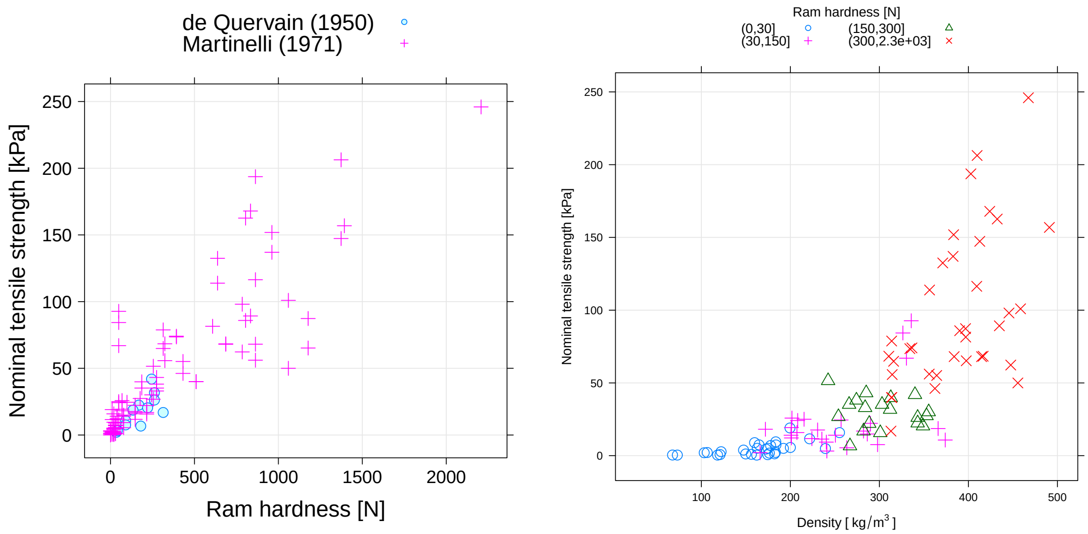

(a) **(b)**

Figure 4.8: *Nominal centrifugal tensile strength versus (a) ram hardness and (b) density for the only two sources that reported any hardness data.*

Size effects

Nearly all of the centrifugal data are from specimens of the same size. The exception is the data of *Sommerfeld* (1974), who used larger specimens of a slightly different shape. The strength values of Sommerfeld's data are on the low end of the centrifugal data. For densities greater than 200 kg/m^3, Sommerfeld's strength values are nearly an order of magnitude lower than much of the rest of the data (Figure 4.4). This difference could be in large part due to the significant size effects between Sommerfeld's specimens and those of the rest of the studies considered here. The size effect could be explained either in statistical or deterministic terms.

According to Weibull statistical theory related to brittle fracture, the mean strength $\bar{\sigma}_N$ for a cross-sectional area A is related to the mean strength $\bar{\sigma}_N^\circ$ at another size A° via

$$\frac{\bar{\sigma}_N}{\bar{\sigma}_N^\circ} = \left(\frac{A^\circ}{A}\right)^{n_d/m} \tag{4.9}$$

where n_d is the similitude dimension and m is the Weibull modulus (*Bažant and Planas*, 1998). Several reasons why Weibull theory is probably not applicable to explain the size effect for snow slab fractures were outlined by *Borstad and McClung* (2009) and will be discussed further in Chapter 5. However, Equation 4.9 was applied here for simplicity and to get a rough idea if the difference between strength values between *Sommerfeld* (1974) and others can be attributable to some kind of size effect.

Sommerfeld (1974) used large samples of effective cross-sectional area 81.6 cm^2 compared to the previous standard of 22.8 cm^2 used by all others in Table 4.1. If Weibull theory was applicable with a modulus $m = 15$ (*Borstad and McClung*, 2009) and we considered the scaling of the cross-sectional area as a case of one-dimensional similitude (which physically corresponds to assuming that the entire cross-section fails simultaneously) then Equation 4.9 predicts a ratio of strengths of

$$\frac{\bar{\sigma}_N}{\bar{\sigma}_N^{\circ}} = \left(\frac{22.8}{81.6}\right)^{1/15} = 0.92 \tag{4.10}$$

for the same snow properties and testing conditions. This is a small decrease (<10%) for the change in area and does not appear to entirely explain the low strength values reported. For low densities (<200 kg/m^3) Sommerfeld's data overlap with those of *Martinelli* (1971) (Figure 4.4). At higher densities, however, there appears to be nearly an order of magnitude or more difference between Sommerfeld's data and those of other studies at similar densities.

Calculated values of the Weibull modulus based on precise laboratory tests are certainly higher than 10 (*Borstad and McClung*, 2009). Lower values based on the coefficient of variation from imprecise in-situ tests are probably not applicable. However, some in situ field data have suggested values closer to $m = 5$. Using this value in Equation 4.10 leads to a prediction of about a 23% decrease in the strength. This still does not make up the observed discrepancy between Sommerfeld's data and those of the other studies. If the failure of the cross-section is considered a two-dimensional scaling (i.e. the cross section fails as soon as a representative element within the cross section fails) then we have $n_d = 2$. This would lead to a strength decrease of about 16% for $m = 15$ and 40% for $m = 5$ in Equation 4.10 above. In no case does it appear that a Weibull-type statistical size effect is capable of explaining the large discrepancy between the data of *Sommerfeld* (1974) and the rest of the centrifugal data.

If a boundary layer of cracking near the notched cross section in the centrifugal tests is the origin of the tensile crack that precipitates failure, then a quasi-brittle scaling relation for failure at crack initiation might be appropriate for considering the size effect between Sommerfeld's data and the rest of the centrifugal data. A simple form for the quasibrittle size effect on the modulus of rupture (*Bažant*, 2005) is given by

$$f_r = f_{r\infty}\left(1+\frac{D_b}{D}\right) \tag{4.11}$$

where f_r is the modulus of rupture, $f_{r\infty}$ is the asymptotic large-size limit of strength, D_b is the length scale related to the boundary layer of microcracking and D is the characteristic specimen dimension. Though this relation is for a bending test rather than a uniaxial test, it can be derived from dimensional analysis in a more general sense by considering a strain gradient in a boundary layer near the surface of a material where a tensile crack initiates. There should be a strong strain gradient in the central cross section of the centrifugal samples, therefore correspondence may be achieved which would allow the use of Equation 4.11 here.

Therefore, as a complement to the size effect predictions made above using Weibull theory, Equation 4.11 was applied to compare the difference in strength values predicted using D = 45.3 mm for the width of the central notched zone in the standard centrifugal specimen and D = 106.7 mm reported by *Sommerfeld and Wolfe* (1972). Using a boundary layer length scale D_b of about 20 mm determined from experimental data (*Borstad and McClung*, 2009) and assuming that $f_{r\infty}$ is a material property (*Bažant*, 2005), Equation 4.11 predicts about a 25% reduction in the strength of the larger samples, all else the same.

In either formulation, the size effect alone does not explain the low strength values of *Sommerfeld* (1974). A different rate of acceleration of the spin tester is a likely partial explanation. Sommerfeld did not report the rate of acceleration of the modified (and otherwise much improved) testing machine, other than to state that the tester "accelerates rapidly." However, insufficient information was reported to analyze the remaining discrepancy.

4.1.2 In situ tests

The advent of in situ tensile tests offered a number of advantages to earlier centrifugal tests. First, the snow could be sampled in its natural state rather than extracted and transported to a lab with different environmental conditions. Second, larger specimen sizes could be tested. No laboratory facilities were necessary, which saved experimental costs, though the usual tradeoff was in the lower precision of in situ results.

Two primary means of measuring tensile strength in situ have been used. The first was by applying uniaxial tension by somehow gripping the snow sample and pulling on it while one end of the sample was fixed. The second was in bending, where typically a cantilevered beam was ruptured and the equations of beam mechanics were used to calculate the tensile stress at failure on the outer tensile fiber of the beam.

Uniaxial tension

The largest specimen sizes used to measure tensile strength were those of *McClung* (1979a) who used a rolling cart to slowly apply uniaxial tensile stress to naturally deposited snow. The stress was applied by gradually tilting the cart to increase the gravitational tensile body force while the upslope end of the sample was fixed relative to the downslope end. The geometry of the test specimens was similar to that in Figure 4.10 in the sense that rounded notches were cut into the samples to localize the failure. From the reported geometry of the samples, I estimated the stress concentration factor associated with these notches as about 1.5.

McClung's strength values are low, even after adjusting the reported nominal strengths using the stress concentration factor (Figure 4.9). Only a few samples exceed a (corrected) strength of 10 kPa. This is probably partly explained by the long loading times (on the order of minutes) for these tests, which likely placed the failures in the ductile (creep rupture) range of strain rates. No measurements or estimates of the strain at failure were reported. A size effect for these very large sample sizes (cross sectional area ~ 0.12 m^2) also likely led to lower strength values (*Sommerfeld*, 1980).

Conway and Abrahamson (1984), and later *Jamieson* (1988) and *Jamieson and Johnston* (1990), developed an in situ tensile test that involved inserting a slip sheet under a slab column to isolate the slab in tension. The slab was gripped on either side with frames that were pressed into the side of the snow (Figure 4.10). The frames were connected using a spreader bar, and the force to rupture the sample was applied by hand with a force gauge. Rounded notches were cut into the sample in order to localize the failure, though only the nominal strength values were reported.

Conway and Abrahamson (1984) did not report the exact geometry of the notched cross section in their tests, though from their schematic drawings the stress concentration factor was estimated to be between 1.5 and 3. The error bars for their data in Figure 4.9 represent this uncertainty. Each data point represents a mean tensile strength from several tests (up to 4 tests were conducted within each layer). A total of 32 tests

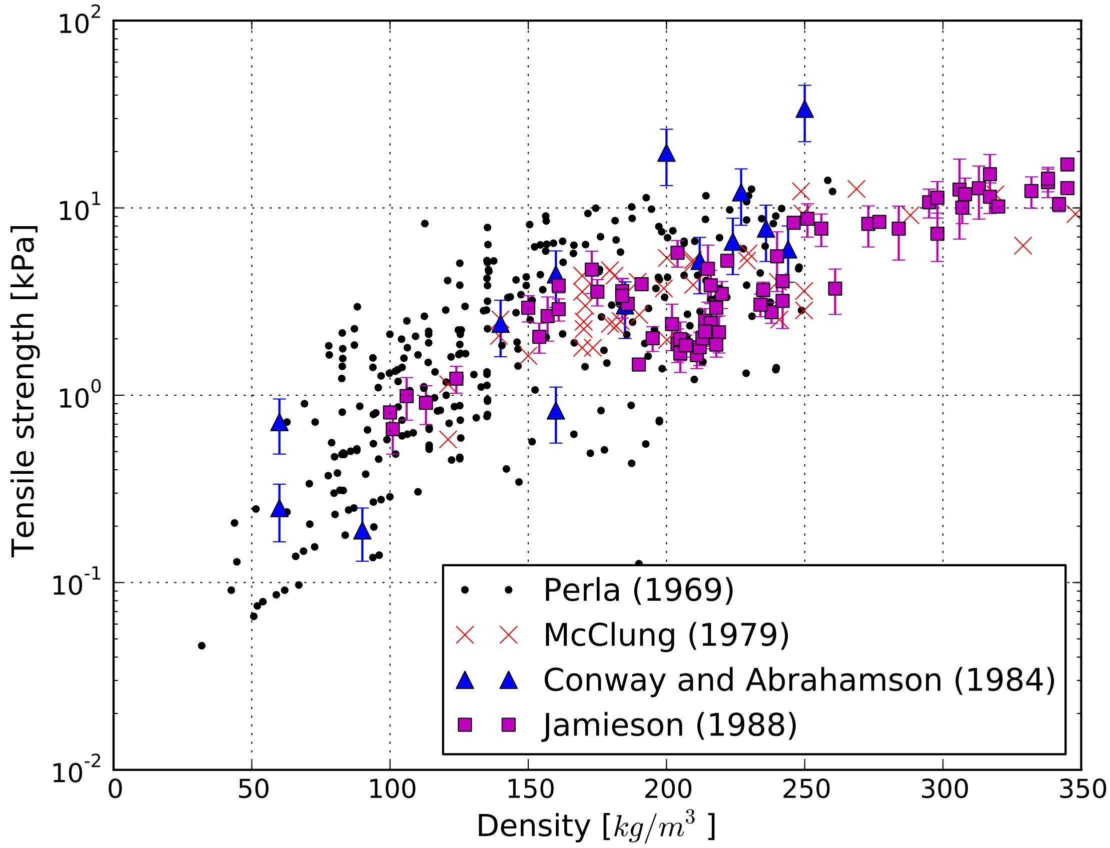

Figure 4.9: *Previously reported in situ tensile and flexural strength data. All values except Perla's were adjusted to account for the stress concentration factor associated with the notched tests.*

are represented by the data points plotted for *Conway and Abrahamson* (1984).

The values measured by *Jamieson* (1988) were lower than those of *Conway and Abrahamson* (1984). This holds for both the nominal and corrected values, and is surprising given that Jamieson had more data for densities above 250 kg/m^3, which was the highest density tested by *Conway and Abrahamson* (1984). Jamieson has more data overall, however, and the data appear more consistent than those of *Conway and Abrahamson* (1984). The data in Figure 4.9 from *Jamieson* (1988) represent a total of 457 tests in 66 different snow layers. The mean strength for each group is plotted, and the error bars represent the standard deviation in the measured strength values.

Further discrimination of the strength values of *Jamieson* (1988) is possible using the reported snow grain types. For a given density, snow containing faceted crystals or mixed rounded and faceted crystals was

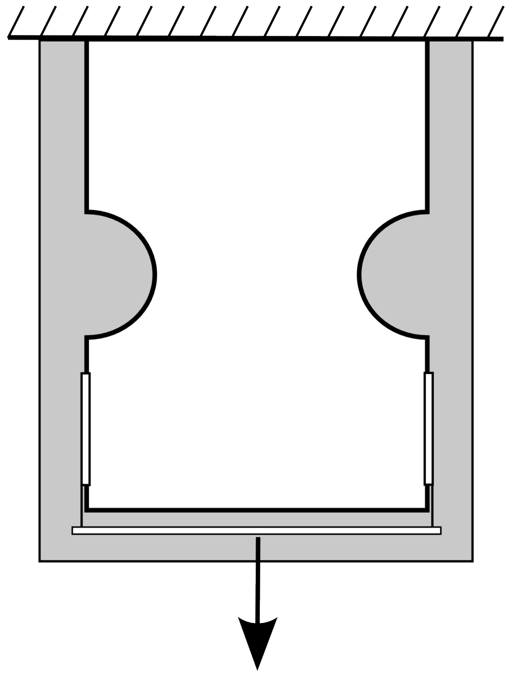

Figure 4.10: *Schematic of in-situ uniaxial tensile test geometry, top view. The samples were isolated in tension by inserting a low-friction plate (shown here in gray) below the slab, which remained connected to the rest of the snowpack on the upslope end. The downslope end of the sample, below the notches, was gripped on either side with frames that were pressed into the slab. A spreader bar was then used to distribute the force across both sides of the sample.*

weaker than other snow types (Figure 4.11). Some grain forms are also indirectly correlated with density through the age of the snow layer (specifically the time since deposition and history of metamorphism). Low density snow was typically still composed of new snow forms and decomposing and fragmented forms, while older and higher density snow was mostly composed of rounded grains.

Bending tests

Perla (1969) developed an in-situ cantilever beam test for measuring the strength of fragile newly fallen snow. A wide cantilever was loaded by rapidly removing the supporting snow underneath. This was achieved by inserting a plate underneath the layer of interest and rapidly withdrawing it by downward pressure, leaving a freely-cantilevered beam loaded by self weight. The length of this beam was increased by inserting the plate deeper and deeper until the beam at some point failed when the plate was dropped out from under the beam. This determined the failure length of the cantilever (S). The stress at failure, defined as the "beam

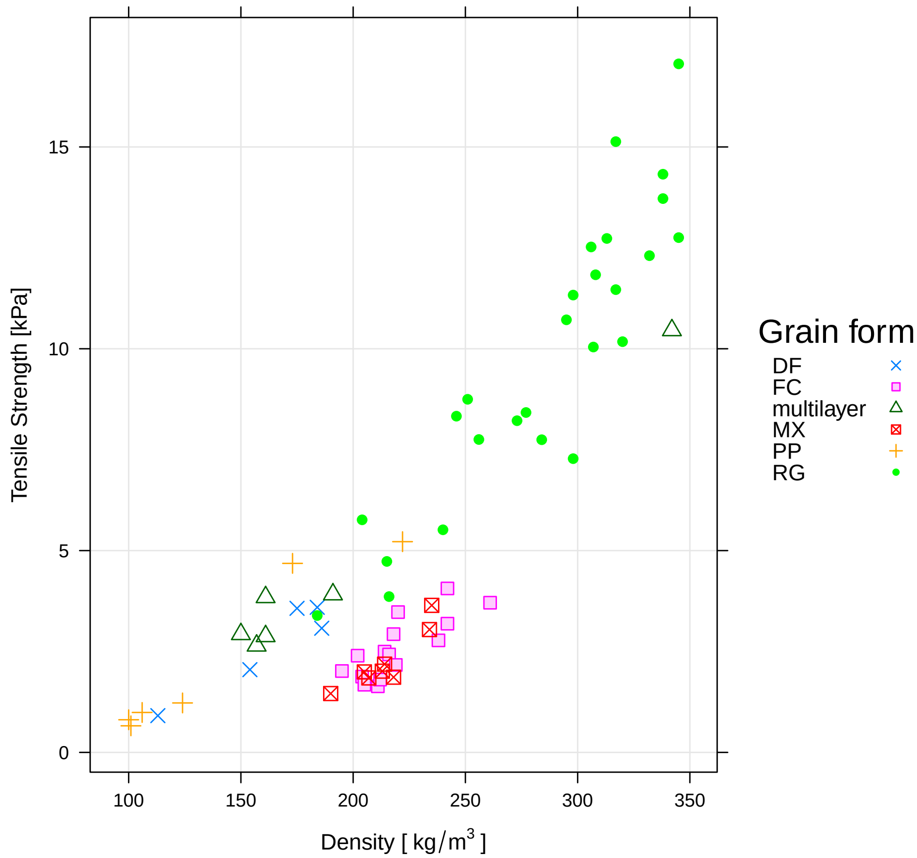

Figure 4.11: *Tensile strength versus density reported by Jamieson (1988), with plot symbols corresponding to different grain types: decomposing and fragmented (DF), faceted (FC), mixed rounded and faceted (MX), new snow or precipitation particles (PP) and rounded grains (RG).*

number" by Perla, is given by

$$\sigma = \frac{3S^2\rho g}{D} \tag{4.12}$$

where S is the span, ρ is the layer density, g is the magnitude of gravitational acceleration and D is the layer thickness. Perla's beam number data, which comprise around 280 tests, agree well with the uniaxial in situ results, though the scatter is large (Figure 4.9).

Perla (1969) observed some evidence for shearing deformation from the shape of the failed cross sections, which would lead to a slight overestimation of the true tensile strength of the tested layers using Equation 4.12. It should also be noted that viscous deformation was likely in many of these tests. The amount of deformation would depend on the strength of the snow, which would determine the time that the beam, of progressively increasing length, was cantilevered freely.

4.1.3 Laboratory tests

Similar to the in situ tests, previous laboratory tensile tests (excluding the centrifugal tests discussed above) used both uniaxial tension and bending to induce failure. The laboratory tests allowed for precise control over loading rate and environmental conditions compared to the in situ tests, though often at the expense of smaller data sets.

Uniaxial tension

The earliest reported tensile strength measurements were by Haefeli (1939), translated in *Bader et al.* (1954). Uniaxial tensile tests were conducted on homogeneous cylindrical samples of cross sectional area 26.4 cm^2 and length 19 cm. The ends of the samples were frozen to metal plates with roughened surfaces. Each strength test was preceded by an elongation test of duration 1–8 days at tensile stresses ranging from 2–40 kPa. Higher stresses and longer duration of pre-stressing generally led to higher tensile strength values, though the data are not consistent nor extensive enough to draw any firm conclusions on these points.

The tests were performed under load control at a rate of approximately 570 Pa/s. The time to failure for each sample was reported, with values falling in the range 26–211 seconds. These times to failure are well above the limit later specified by *Bader and Kuriowa* (1962) of 10 seconds or less to avoid inelastic deformation. No strain measurements were reported to allow the calculation of the strain rate. The large variability in Haefeli's results is likely due to both the scatter in material properties, differences in pre-stressing and also likely due to the load application method, which involved the pouring of shot into a bucket (small impulse loads were reported to cause failure in some tests).

Narita (1980) and *Narita* (1983) reported the uniaxial tensile strength of natural snow over the largest range of strain rates in the literature, spanning rates from about 5×10^{-7} s^{-1} to about 2×10^{-3} s^{-1}. The tests were carried out in a similar manner to those of Haefeli, by freezing cylindrical samples (cross sectional area about 20 cm^2) to end plates that were then pulled apart by a universal testing machine. Narita identified a creep-to-fracture transition strain rate (termed ductile-to-brittle transition at the time) from several characteristics of the data. First, the load displacement curves were distinctly different for brittle (fracture-dominated) compared to ductile (creep-dominated) failures. Second, visual observation of the failure surfaces allowed characterization of the type of failure into ductile (multiple and uneven cracking) or brittle (clean and fast fracture) modes. The tensile strength, for a given density of snow, peaked at the transition strain rate ($\sim 10^{-4}$ s^{-1}).

Narita reported the strength values as a function of the strain rate for different bins of density, therefore individual strength-density points cannot be reproduced. However, there is general agreement between Narita's uniaxial values and those of Haefeli (1939) in Figure 4.12. These strength values agree well with the uniaxial centrifugal data (Figure 4.4) discussed above, much more so than the in situ data (Figure 4.9).

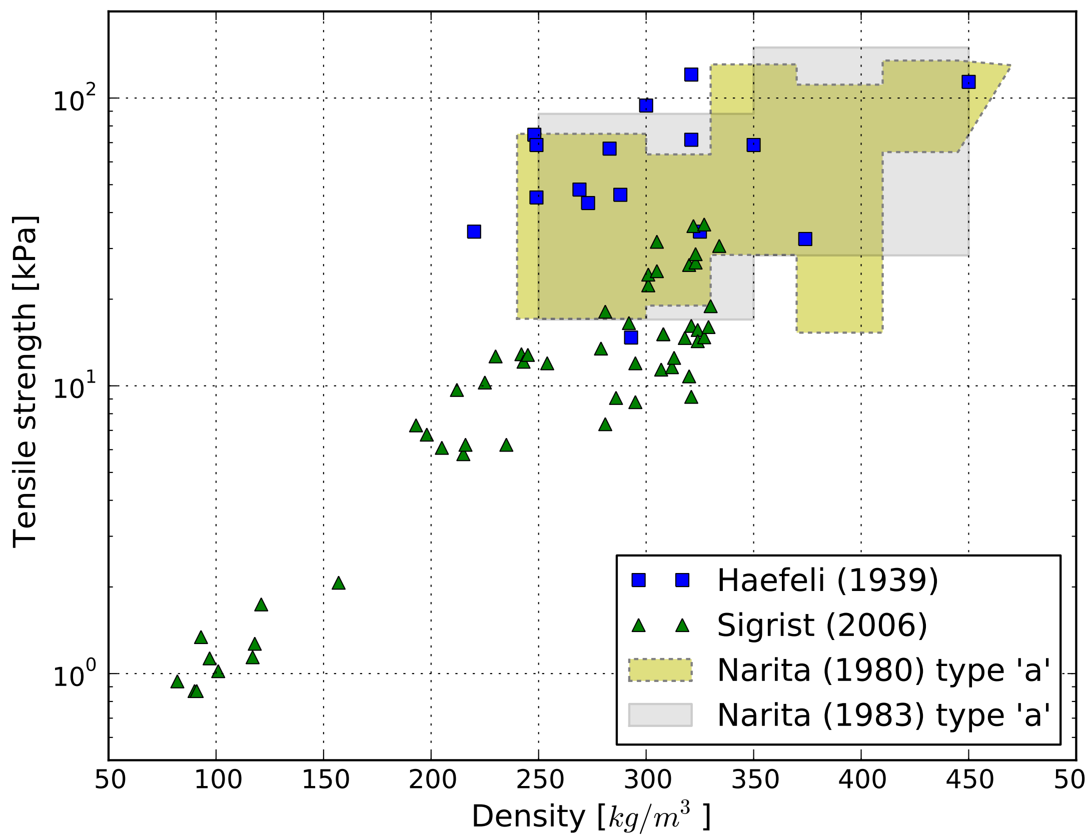

Figure 4.12: *Previously reported tensile/flexural strength data from laboratory tests. The data shown from Narita is limited to brittle-rate fractures (type "a"), or those above the creep-to-fracture transition, with strain rates of about 10^{-4}–10^{-3} s^{-1}.*

Bending tests

Sigrist (2006) calculated the modulus of rupture from unnotched three point bending tests (see Figure 4.13a for a schematic of the test geometry). The crosshead speed was 0.33 cm/s which resulted in strain rates in the outer fiber of 10^{-2} to 10^{-1} s^{-1}. The beam span to depth ratio S/D was 2 and the temperature was -9.5 $\pm$ 0.2 $^{\circ}C$ for all tests. The sample length was 50 cm (load span 40 cm), the beam depth D was 20 cm and the width was 10 cm.

Sigrist reported the modulus of rupture as the tensile strength, but this only holds for very slender beams in pure bending. For short beams with concentrated central loads, such as in the common laboratory three point bending test, the elastic stress distribution in the central cross section is altered from that predicted in pure bending. *Timoshenko and Goodier* (1951) related the elastic tensile stress to the nominal stress in three point bending as a function of the span to depth ratio, leading to the following expression for the tensile strength f_t in terms of the measured modulus of rupture f_r:

$$f_t = f_r \left(1 - 0.1773\frac{D}{S}\right). \tag{4.13}$$

This expression was used to correct Sigrist's data as presented in Figure 4.12. The bending data overlap somewhat with the uniaxial lab data for higher densities. In general, however, the beam tests resulted in lower strength values. There may be a small size effect for comparing the results of *Sigrist* (2006) to the uniaxial lab data. Furthermore, uniaxial tensile strength usually differs from flexural strength for the same material, with flexural strength being around 50% greater than tensile strength for concrete (e.g. *Banthia and Sheng*, 1996).

Summary

The results of around 2000 previous tensile strength tests have been reviewed in the first part of this chapter, summarized by test type, loading geometry and sample properties. The published values, many of them corrected to account for neglected stress concentrations, span four orders of magnitude from 0.1 kPa to 1000 kPa over a density range of 30–500 kg/m^3. The next section (Section 4.2) contains new strength data collected from laboratory bending tests in the present study. In a similar manner to the foregoing section, the influence of sample properties and testing conditions on the results are shown.

4.2 New Tensile Strength Data

A total of 245 unnotched beam bending tests were conducted for the calculation of tensile strength (technically, the flexural strength) in the present study. The tests were performed over the course of 20 days in the cold laboratory in the winters of 2007–2008 and 2008–2009. The tests were split among three point bending (n = 149) with the testing machine oriented vertically and four point bending (n = 96) with the machine oriented horizontally. All tests were weight compensated. Descriptions of the characteristics of the snow and the testing conditions for each individual test series are indicated in Table 4.3.

The majority of the results in the present section were obtained with a crosshead speed (V) of 1.25 cm/s and beam depth (D) of 10 cm. However, some of the unnotched test results here were drawn from series of tests on a particular day that were conducted to explore secondary variables such as loading rate, specimen size, or notched versus unnotched tests. For the analysis here only the unnotched data from such test series were used, and this explains the small number unnotched tests on some dates (Table 4.3).

This section begins with the derivation and definition of tensile strength for the data using beam theory. The strength results as a function of hardness and density are then discussed and placed in context with the published laboratory strength data discussed earlier in the chapter. In some test series, the influence of secondary variables such as grain size, loading rate and specimen size are explored.

Code	Date	n	$\bar{\rho}$ $[kg/m^3]$	R	$\bar{B}$ [N]	$\bar{T}$ [°C]	F, E [mm][1]	V [cm/s]	D [cm]	S/D	Type
A	080115	7	185 ± 2	3.3	N/A	-11.1 ± 0.3	RG, 0.5 / DF, 1	1.25	10	3	4PB
B	080117	24	318 ± 2	4	7.1 ± 0.8[2]	-7.1 ± 0.5	FCxr, 0.5-1	1.25	5,10	3	4PB
C	080118	20	327 ± 2	4.3	8.5 ± 0.9[2]	-8.5 ± 1.9	FCxr, 0.5-1	1.25	5,10,20	3	4PB
D	080119	20	294 ± 4	4.3	5.1 ± 0.6[2]	-7.8 ± 0.5	RG, 0.5	1.25	5,10,20	3	4PB
E	080128	7	269 ± 15[3]	3.7	4.0 ± 1.1[3]	-11.2 ± 0.7	FC, 1	1.25	10	3	4PB
F	080130	25	343 ± 17[3]	4.3	11.9 ± 2.9[3]	-9.0 ± 0.4	FCxr, 1	0.01-1.25	10	3	4PB
G	080302	7	243 ± 13[3]	4	3.8 ± 1.2[3]	-9.7 ± 1.2	RG, 0.5	0.05-1.25	5,10,20	3	3PB
H	090118	29	185 ± 1	3.3	3.2 ± 0.5	-9.0 ± 0.8	RG, 0.5-1 / DF, 1-2	1.25	10	2	3PB
I	090119	8	303 ± 3	4.3	11.7 ± 1.8	-6.7 ± 0.4	FCxr, 0.5-1	1.25	10	2.5	3PB
J	090121	9	317 ± 3	4.3	17 ± 5[2]	-7.5 ± 0.5	RG, 0.3-0.5	1.25	5,10,15	2	3PB
K*	090125	20	331 ± 3	4.3	14.7 ± 1.2[3]	-8.5 ± 0.5	RGxf, 0.5-1	1.25	10	2	3PB
L	090129	5	326 ± 5	4.3	12.2 ± 0.9	-6.7 ± 0.3	FCxr, 0.5	1.25	10	2.5	3PB
M	090202	4	227 ± 4	3	2.0 ± 0.2	-6.0 ± 0.8	FCxr, 0.5-1	1.25	10	2.5	3PB
N	090205	1	238 ± 20	3.3	2.3	-5.7	FCxr, 0.5-1	1.25	10	2.5	3PB
O	090215	12	296 ± 3	4	5.4 ± 0.7[4]	-6.4 ± 0.4	FCxr, 0.5-1	1.25	5,10,15,20	2	3PB
P	090301	9	152 ± 2	2	0[5]	-6.5 ± 0.6	DF, 0.5-1	1.25	10	2.5	3PB
Q	090321	10	334 ± 3	4	9.2 ± 1.2	-4.8 ± 0.7	RG, 1	0.125-1.25	10	2.5	3PB
R	090323	16	337 ± 3	4	9.9 ± 0.8	-4.7 ± 0.9	RG, 1	0.0125-1.25	10	2.5	3PB
S	090326	8	154 ± 2	3	2.1 ± 0.3	-5.1 ± 0.4	RG, 0.5 / DF, 1	1.25	10	2.5	3PB
T	090405	4	241 ± 4	3.7	5.7 ± 0.9	-3.9 ± 1.1	RG, 0.5	1.25	10	2.5	3PB

Table 4.3: *Series of unnotched beam bending experiments used for the calculation of tensile strength. Date is in* yymmdd *format. Other column variables include the number of tests (n), mean snow density ($\bar{\rho}$), mean blade hardness index ($\bar{B}$), mean snow temperature ($\bar{T}$), grain forms and grain size (F and E, respectively), testing machine crosshead speed (V), beam depth (D), and beam span to depth ratio (S/D). *the sample width varied in this test series, taking values of 5,10,15 and 20 cm (the standard sample thickness for all other tests was 10 cm).*

[1] *Following the International Classification for Seasonal Snow on the Ground (Fierz et al., 2009). Key: RG = rounded grains, DF = decomposing and fragmented crystals, FCxr = mixed rounded and faceted crystals; RGxf = rounded grains becoming faceted.*

[2] *Mean blade hardness index for entire test series (individual values of B not paired with individual strength tests).*

[3] *Mean of repeated in situ measurements in layer from which samples were extracted (not measured in lab).*

[4] *Blade hardness index not measured for smallest samples (D = 5 cm).*

[5] *Blade hardness gauge recorded 0 N, actual resistance in the range $0 < B < 1.7$ N.*

4.2.1 Strength calculation from beam theory

For unnotched three or four point bending, the "modulus of rupture" (flexural strength) can be defined as

$$f_r = \frac{6M}{bD^2} \tag{4.14}$$

where M is the bending moment in the central cross section of the beam, b is the beam width and D is the beam depth (*Bažant and Planas*, 1998). The bending moment in the central cross section for a three point bending test (Figure 4.13a) is

$$M = \frac{PS}{4} \tag{4.15}$$

where P is the applied central load and S is the load span. In four point bending, the bending moment in the central portion of the beam is constant between the two loading points, and is expressed by

$$M = \frac{Pa}{2} \tag{4.16}$$

where a is the distance between a load point and the adjacent support point (Figure 4.13b).

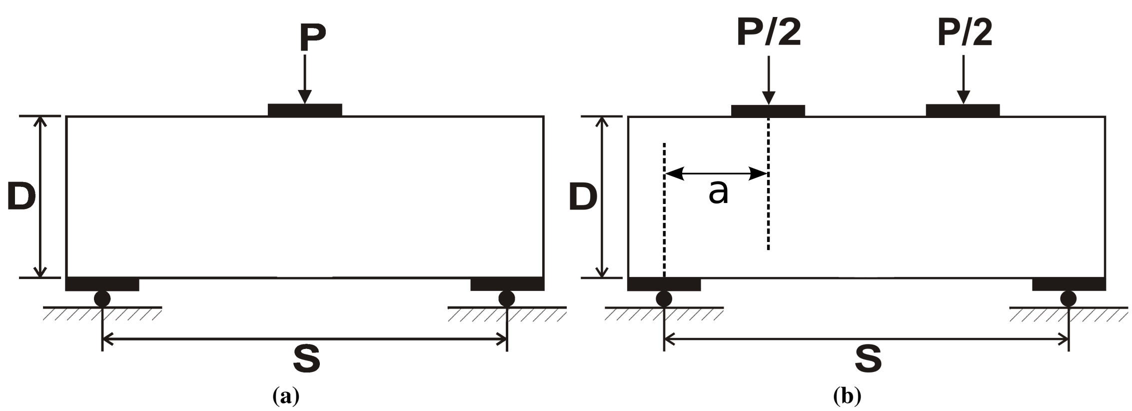

Figure 4.13: *Schematic of unnotched three point bending (a) and four point bending (b) test for determining the tensile strength.*

Using Equation 4.15 in Equation 4.14, the modulus of rupture for a three point bending test is

$$f_r = \frac{3PS}{2bD^2} \tag{4.17}$$

where P is here understood as the peak load measured in the test. Due to the effect of the concentrated central load in a three point bending test, the elastic tensile stress distribution in the central cross section is slightly different from that predicted by Equation 4.17. This difference diminishes as the slenderness (S/D) of the beam increases, i.e. as the beam asymptotically approaches a pure bending solution. The correction to simple beam theory that accounts for the concentrated central load (*Timoshenko and Goodier*, 1951) takes the form

$$\sigma_x = \frac{3PS}{2bD^2} - 0.266\frac{P}{bD} \tag{4.18}$$

where σ_x is the tensile stress in the outer fiber of the beam. If the maximum elastic tensile stress at failure is equated with the tensile strength ($\sigma_x = f_r$ at peak load), then combination of Equations 4.17 and 4.18 leads to

$$f_t = f_r\left(1 - 0.1773\frac{D}{S}\right) \quad [3PB]. \tag{4.19}$$

This equation coincides with Equation 4.13 used previously to correct the modulus of rupture data of *Sigrist* (2006). Note that the flat plates used in the bending tests (Figure 4.13, not necessarily to scale), necessary to prevent excessive crushing of snow at the contact points, are different from the rounded geometry of the concentrated load considered by *Timoshenko and Goodier* (1951) for arriving at Equation 4.19. This may lead to an actual stress distribution in the snow samples that lies somewhere between the predictions of simple beam theory (Equation 4.17) or the correction represented by Equation 4.19.

The solutions above allow for consistent definitions of tensile strength for the comparison of data from different sources that used different span to depth ratios. Given the difficulty in extracting and handling snow specimens, it is not possible to test very slender beams of snow. This makes a consistent definition of tensile or flexural strength important, as most beam data for snow, including those in the present study, were collected for deep beams (small span to depth ratios). *Sigrist* (2006) used beams of $S/D = 2$ primarily, and the new data presented here came from beams that varied in the range S/D = 2–3. These ratios lead to tensile strength values that are 6% ($S/D = 3$) to 9% ($S/D = 2$) lower than predicted using the simple modulus of rupture (Equation 4.17).

The maximum tensile stress in the outer fiber of a beam loaded in three point bending is only about 2% greater than the tensile stress a distance of 1/4D in from the outer fiber (*Timoshenko and Goodier*, 1951).

Therefore the bottom quarter of the central cross section, where the tensile crack coalesces, experiences roughly constant tensile stress in three point bending. The central axis of the beam experiences compressive stress, therefore the neutral axis is shifted toward the outer tensile face of the beam. Due to the short and deep beams tested and reviewed here, some shearing effects are also present in the beams. Though the shear is zero in the outer tensile fiber of the beam, the tensile crack is assumed to initiate in a boundary layer of finite thickness at the bottom of the beam where some shear stresses are present. However, these are expected to be minimal in the center of the beam where the crack coalesces.

In four point bending (Figure 4.13b), the tensile strength can be calculated from simple beam theory since the portion of the beam between the central loading points is under pure bending (no shear). The tensile strength is equal to the modulus of rupture in this case. Equating the tensile strength with the maximum elastic tensile stress in the outer fiber of the central cross section of the beam, we have from Equations 4.14 and 4.16

$$f_t = f_r = \frac{3Pa}{bD^2}. \tag{4.20}$$

For all four point bending tests, the loading was done at the third points of the beam. Therefore $a = S/3$ and Equation 4.20 can be written as

$$f_t = \frac{PS}{bD^2} \quad [4PB]. \tag{4.21}$$

The beam theory presented here also contains the assumption that the elastic modulus of the material is the same in compression and tension. This may not be an appropriate assumption for a highly porous material such as snow, for which experiments have shown that strain and Poisson's ratio under constant load are much different for compression and tension (e.g. Haefeli, 1939). This speaks to potential theoretical difficulties in interpreting the results of bending tests, despite their experimental advantages over uniaxial tests. However, for simplicity and consistency with other studies, the framework of simple beam theory is retained here.

4.2.2 Pertinent variables and range of values

The range of values recorded for the pertinent variables related to the tensile strength tests is shown in Figure 4.14. Recall from the Chapter 3 that the variable that correlated the best with tensile strength was the blade hardness index, followed by the density. Weaker correlations (that were still statistically significant)

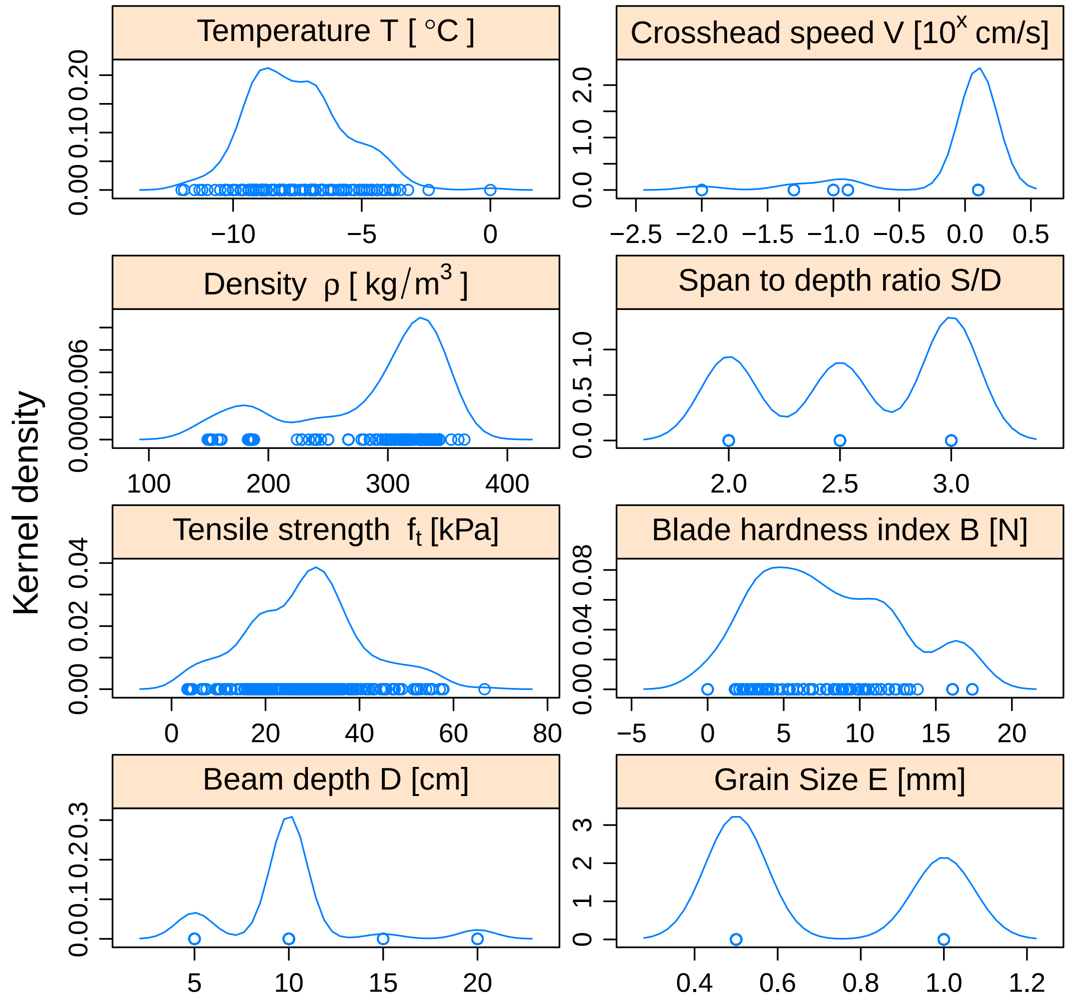

Figure 4.14: *Kernel density plots of the variables associated with flexural strength tests.*

were observed between strength and secondary variables including the grain size, beam depth and crosshead speed. The blade hardness index B was highly correlated with the density, and the strength of the correlation was nearly as high as that between the tensile strength and B. The temperature in the cold lab was adjusted to approximately match the temperature of the snow layer from which the samples were extracted, therefore the temperature data in Figure 4.14 approximately represents the natural temperatures of the snow layers at the time of sampling.

The heavy weighting of the data at densities higher than 300 kg/m^3 is evidence of the limited selection of homogeneous snow layers that were available to choose from for sampling, rather than a voluntary bias toward stronger and denser layers. Few layers at densities around 200 kg/m^3 were available that were greater than 10 cm in thickness, approximately homogeneous in density and hardness as a function of depth, and strong enough to permit sample extraction and handling. This is partly related to the elevation of the primary Rogers Pass study plot from which most samples were obtained (1320 m.a.s.l.).

4.2.3 Tensile strength versus blade hardness index

The relation between tensile strength and the blade hardness index is nearly linear (Figure 4.15). The data have a similar pattern as that between the centrifugal tensile strength and ram hardness (Figure 4.8a). Only data for which the blade hardness index was directly paired with a strength test is shown. For small samples with D = 5 cm, no blade hardness measurements were taken because of the risk of penetrating all the way through the sample and damaging the force gauge. In other instances, following the bending test, the snow sample fell off of the support plates and was damaged. This prevented a representative hardness measurement from being taken. In a few cases the force gauge battery died or the measurement was simply forgotten. For identifying individual data sets with particular variables or testing conditions, Figure 4.16 identifies groups of data against the date codes in Table 4.3.

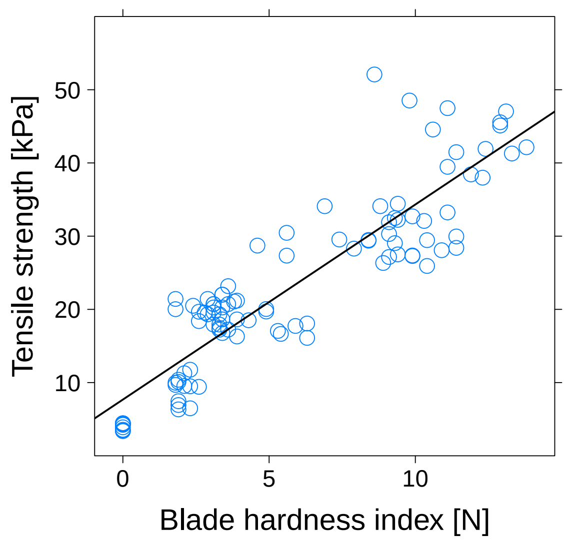

Figure 4.15: *Tensile strength versus blade hardness index, including only strength tests that were paired directly with a blade hardness measurement (n = 101, Table 4.3).*

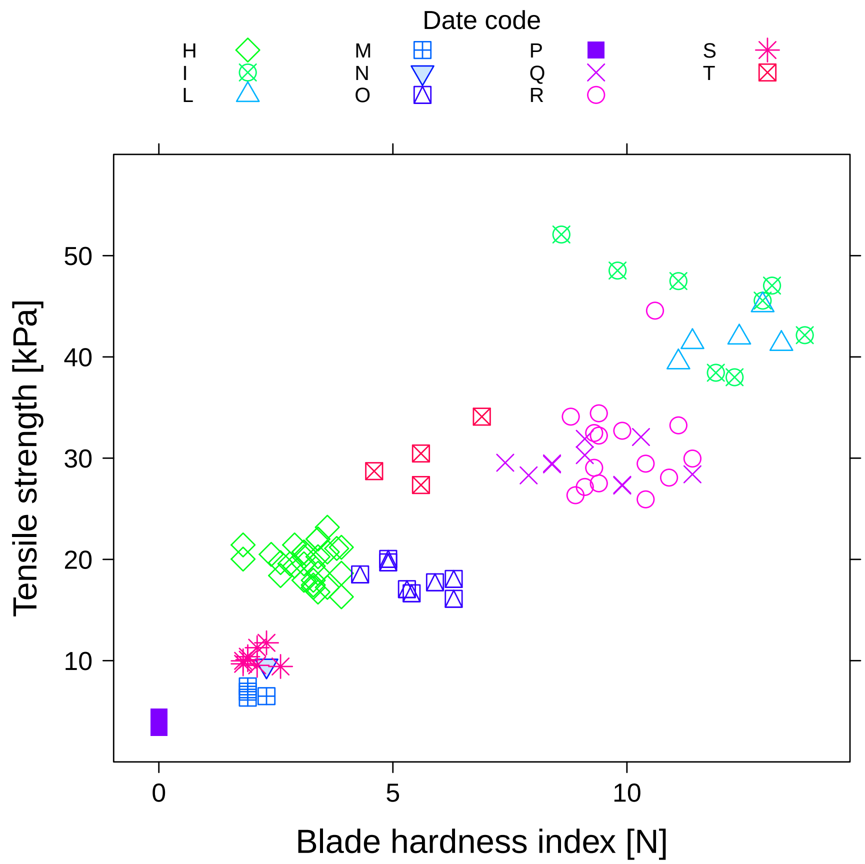

Figure 4.16: *Tensile strength versus blade hardness index, with different plot symbols indicating individual test series. Only tests which directly paired strength and blade hardness index are plotted (n = 101).*

4.2.4 Tensile strength versus density

The strength scales with the density in a similar manner as previous results from laboratory tests (Figure 4.17). Though the scatter is large when expressing strength as a function of density, the flexural tests of the present study agree well with the uniaxial tests of *Narita* (1980, 1983) at similar densities. Most of Haefeli's uniaxial data are higher than those of the present study, though Haefeli may have stored the samples for longer periods and the pre-stressing of samples prior to fracture testing likely influence the ultimate strength.

The data from the present study are higher than those from similar tests conducted by *Sigrist* (2006). This difference may be attributable to a systematic tendency for the snow sampled in the present study to be of higher hardness than that sampled by Sigrist. This may have resulted from the higher elevations from

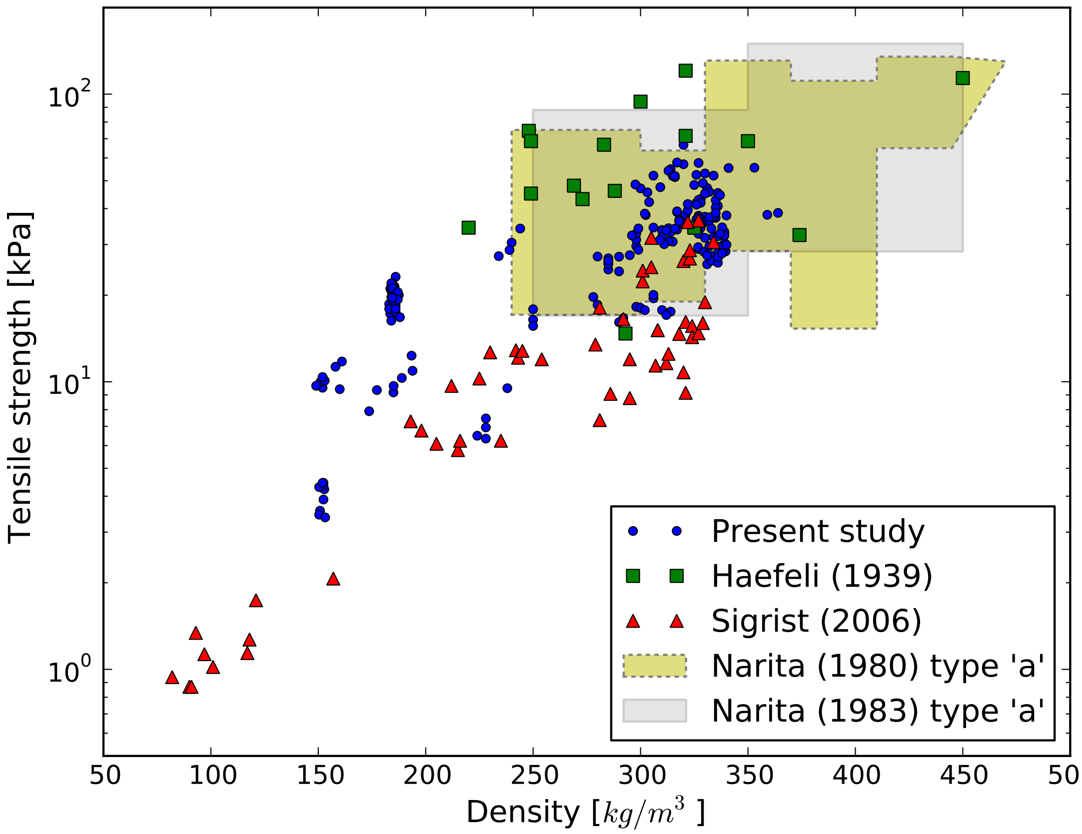

Figure 4.17: *Data from the present study in the context of previously measured tensile strength from laboratory tests.*

which snow was sampled in Sigrist's study (1562 and 2668 m.a.s.l) compared to the primary study plot in the present study at 1320 m.a.s.l. Most of the tests from the present study were conducted at a crosshead speed around four times greater than the standard speed used by Sigrist, though this systematic rate effect should lead to lower strength values for the present study, all else the same (lower strength for higher strain rate, as will be seen below).

The grouping of the test data by date of testing is shown in Figure 4.18, analogous to Figure 4.16. In many test series, there appears to be less scatter in density values (Figure 4.18) than blade hardness index values (Figure 4.16). This may be an indication that the blade hardness has greater sensitivity to the spatial variability of snow structure than density. However, several series are characterized by high scatter in density values as well. The tensile strength varies by a factor of about three for a density of around 300 kg/m^3, a greater degree of scatter than in the strength at any given blade hardness index (Figure 4.16).

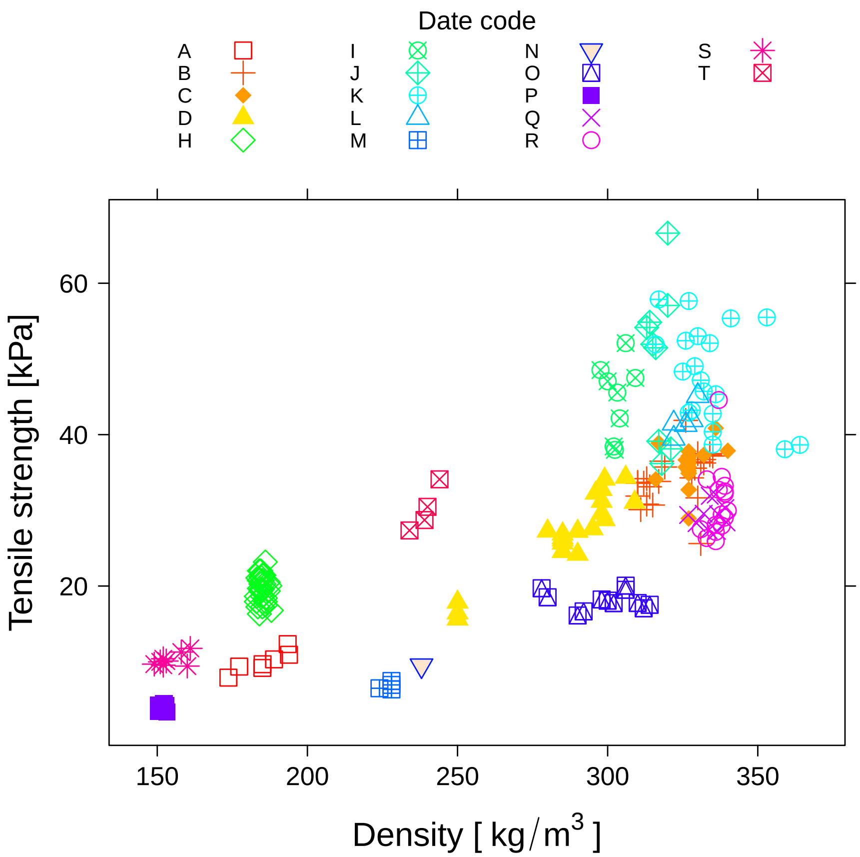

Figure 4.18: *Tensile strength versus density grouped by date of testing, excluding three series for which density was not measured in the lab (n = 206). The date codes reference Table 4.3.*

4.2.5 Influence of grain size

Cohesive snow with smaller grains is typically stronger than coarse-grained snow, all else the same. The grain size does not systematically explain the variability in the strength as a function of the blade hardness index (Figure 4.19a). This indicates that the blade hardness index may be implicitly accounting for the dependence of grain size on a structural property such as strength.

The grain size is not a particularly helpful variable for explaining the strength-density data either (Figure 4.19b). The larger grain sizes at low densities (less than 200 kg/m^3, series H and S) were due to the presence of decomposed and fragmented crystals in the young snow layers. However, the large grain sizes at higher densities (Series Q and R represent the coarse grains (1 mm) at densities around 340 kg/m^3 in Figure 4.19b) were all correlated with faceted or mixed rounded and faceted crystal forms. Faceted crystal forms typically grow in size at the expense of strength (*McClung and Schaerer*, 2006), and the in-situ uniaxial strength data of *Jamieson* (1988) confirm this.

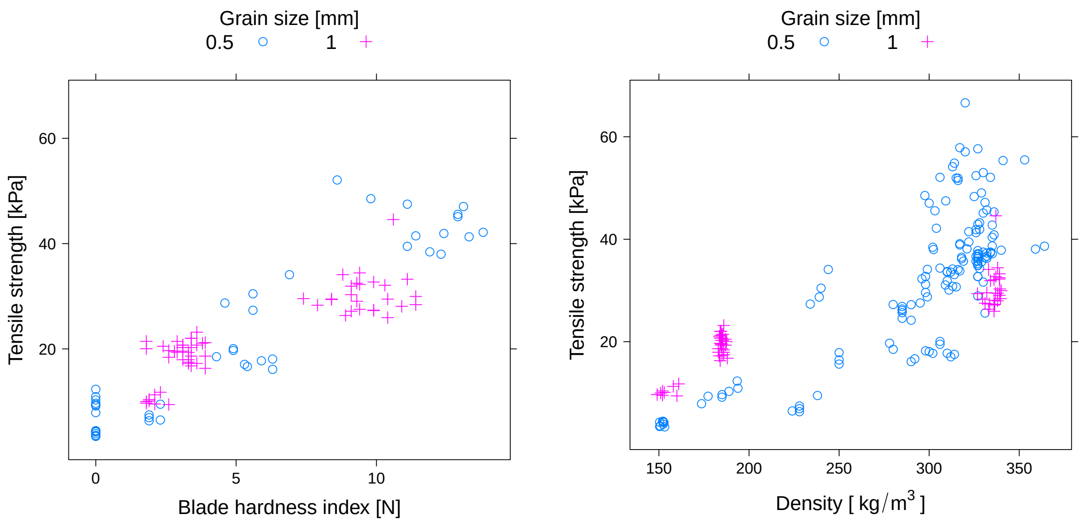

Figure 4.19: *Tensile strength versus blade hardness index (n = 101) and density (n = 206), showing the influence of the snow grain size.*

4.2.6 Loading rate effects

Most strength tests were conducted at the fastest possible crosshead speed (1.25 cm/s) to minimize viscous effects as much as possible. However, two of the test series (F and R) were designed to explore the rate dependence of tensile strength. Figure 4.20 shows the influence of the loading rate, expressed as the nominal strain rate in the outer fiber of the beam calculated using the following expressions from beam theory (e.g. *Timoshenko*, 1940)

$$\dot{\varepsilon}_N = \frac{6DV}{S^2} \qquad \text{[3PB]} \qquad (4.22)$$

and

$$\dot{\varepsilon}_N = \frac{4DV}{S^2} \qquad \text{[4PB]} \qquad (4.23)$$

where D is the beam depth, V is the crosshead speed, and S is the loading span. Note that these expressions are only approximate given the low span-to-depth ratios of the present study. Shearing deformation in the deep beams would lead to deformations and strains in the outer fiber of the beam that deviate from simple beam theory. However, since the beam geometry did not change in each of the two test series considered here, the simple expressions listed above give a self-consistent (though approximate) estimate of the rate dependence of the flexural strength measurements.

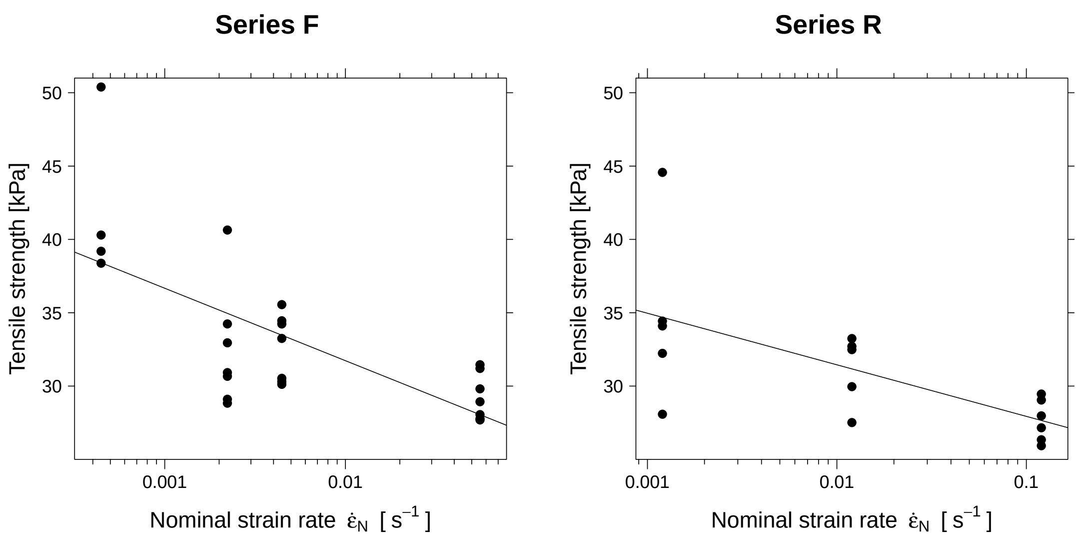

(a) **(b)**

Figure 4.20: *Tensile strength versus nominal strain rate for samples all taken from the same layer and all other experimental conditions the same. The slopes of the linear regressions had p-values of 0.012 (a) and 0.015 (b).*

The strength decreases with increasing strain rate, with the rate varying over about two orders of magnitude for both series in Figure 4.20. The linear regressions through the data have statistically significant slopes at the $\alpha = 0.05$ level for both series. The trends in Figure 4.20 are consistent with the data of *Mellor and Smith* (1966); *Narita* (1980, 1983) which show that strength decreases with increasing strain rate above the creep-to-fracture transition (around 10^{-4} s^{-1} for snow in tension). The data in Figure 4.20 are all above this transition strain rate.

There are little published data from quasi-static tests at strain rates higher than about 10^{-2} s^{-1} to compare with the highest strain rates in the present study (on the order of 10^{-1} s^{-1}). Some of the data presented by *Narita* (1983) suggest that the initial decrease in strength values above the creep-to-fracture transition may level off at higher strain rates, in agreement with observations made by *Mellor and Smith* (1966). This leveling-off is not apparent in the data from the present study, though such behaviour cannot be ruled out. For higher strain rates it may be necessary to consider data from cyclical loading tests (e.g. *Camponovo and Schweizer*, 2001). In very high frequency dynamic or cyclical tests, Young's modulus increases with frequency (*Mellor*, 1975) and therefore the strength may be expected to eventually increase again with increasing strain rate or loading rate. The data from the present study suggest that this transition to dynamics effects must be higher than the highest strain rates achieved in the experiments, greater than 10^{-1} s^{-1}.

4.2.7 Specimen size effects

Four different test series were carried out on unnotched beam samples with only the specimen size (beam depth) varied. The strength significantly decreased with increasing beam depth D for all but Series O (Figure 4.21). The greatest decrease in strength, expressed as a percentage decrease from the smallest to largest size, was for series J. In this series, the decrease in strength was slightly less than a factor of two as the size increased by a factor of three.

As noted in Chapter 2, only about one in four of the largest samples ($D = 20$ cm) which was extracted was successfully transported to the lab and tested. Most failed during extraction and removal from the cutter box or transportation to the lab. This fact raises the question of whether the samples that were successfully tested may have been damaged to an extent not sufficient to cause failure nor to be noticed. If this were the case, then the largest samples may have failed at lower nominal strength values for reasons unrelated to a purely deterministic or statistical size effect. However, for the three size effect test series in Figure 4.21 which included samples of beam depth $D = 20$ cm, only Series C (Figure 4.21a) would have the statistical significance of its size effect slope changed by excluding the largest samples. The values of the slopes do change, however, which has implications for physical theories which explain the observed size effects.

The loading rate was held constant for each of these test series, but the different beam depths led to different nominal strain rates in the outer fiber of the beam. Equations 4.22 and 4.23 indicate that the nominal strain rate from simple beam theory is proportional to the beam depth. Figure 4.22 indicates the change in nominal strain rate with changing beam depth. The strength data show a statistically significant correlation

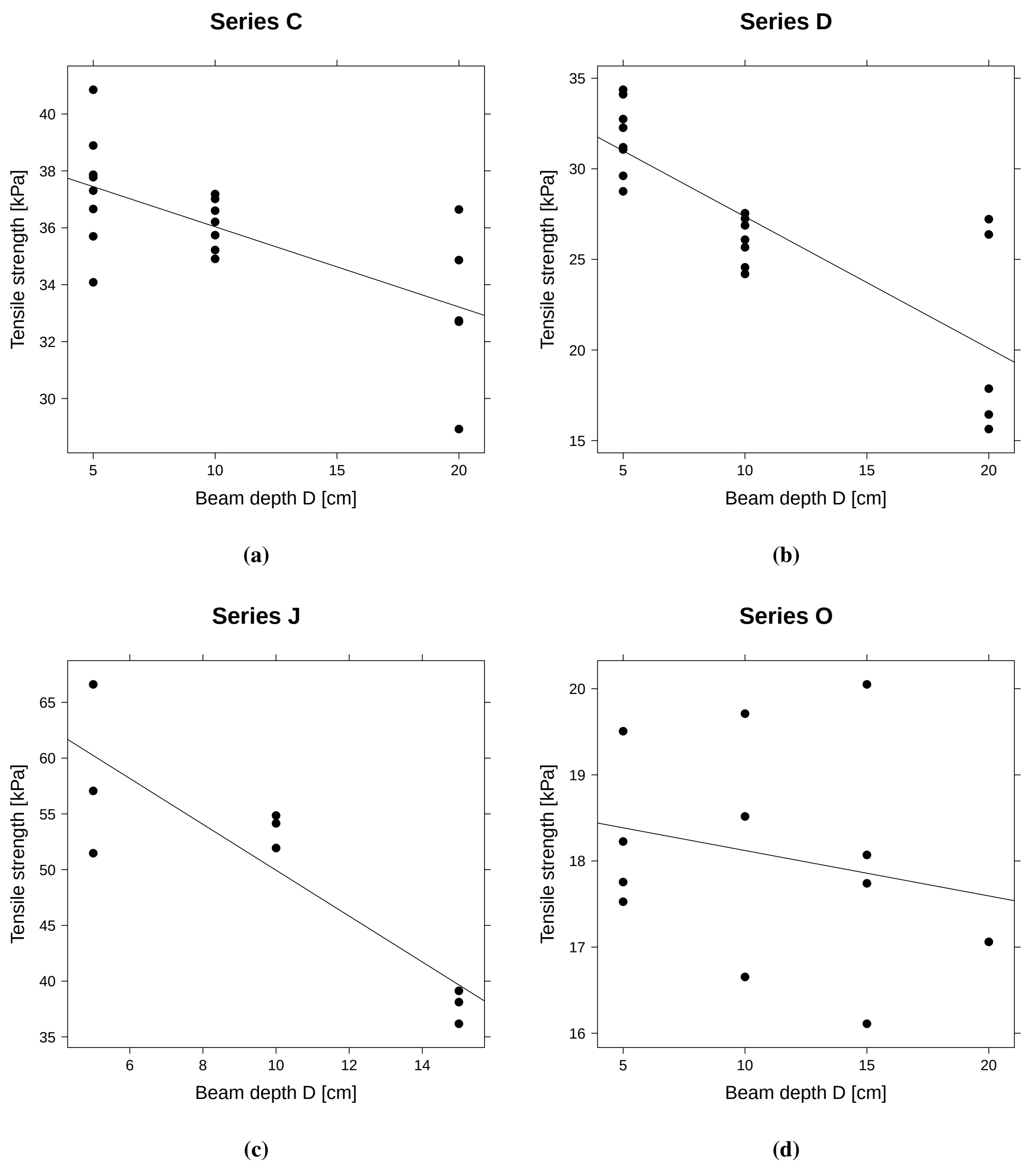

Figure 4.21: *Tensile strength versus beam depth for four different size-effect test series. The slopes of the linear regressions had p-values of 0.001 (a), <0.001 (b), 0.002 (c) and 0.49 (d).*

with the nominal strain rate for all but Series O, which was also the series that did not have a significant size effect. These results suggest that a rate effect on strength may be complicating the interpretation of the size effect (or vice-versa). Given the slower nominal strain rate of the largest samples, these samples may actually have failed at higher nominal strength values according to the rate-dependence of tensile strength observed by others (*Narita*, 1980). Thus the rate effects between the samples of different sizes may have actually weakened the size effect as observed in Figure 4.21, and is a reason that *Bažant and Gettu* (1992) suggest that a condition of constant time-to-failure t_p be used in size effect testing instead of constant loading rate. This trend (weakening of the size effect due to rate effects) would be the opposite as that which may have been caused by the damage and weakening of the largest samples during transportation and handling, which may have strengthened the apparent size effect.

Statistical and deterministic explanations for the size effects considered here, and their connection with material and fracture parameters, will be explored further in the next chapter. Due to the concerns given above about the size effect being complicated by the possible damage of large samples and the rate differences for different samples at constant crosshead speed, preference is given to methods of calculating fracture parameters that use medium-sized samples only.

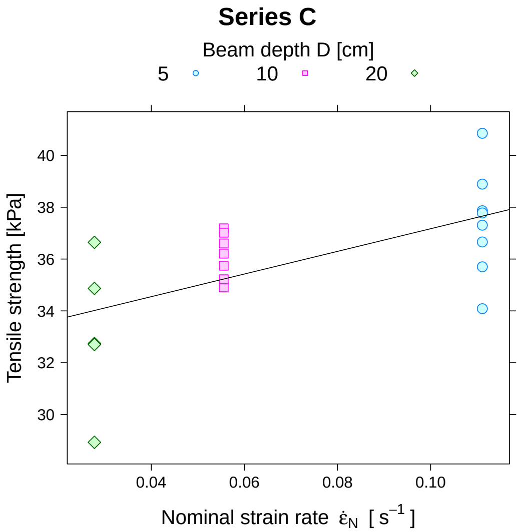

(a)

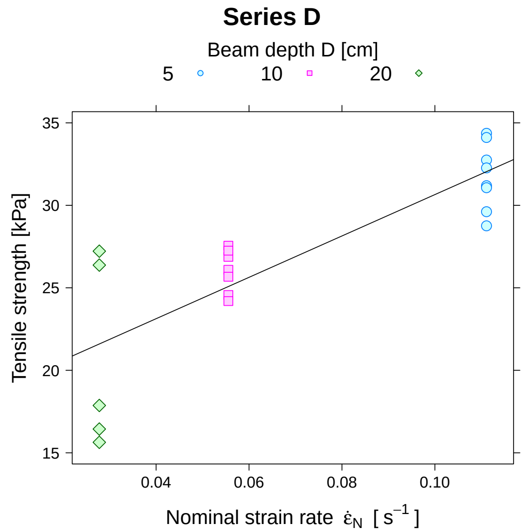

(b)

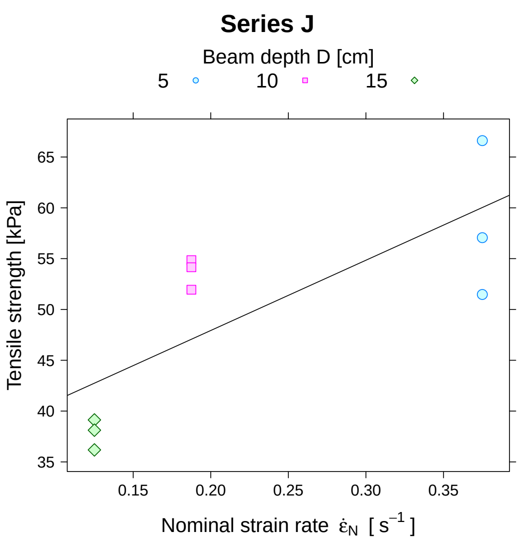

(c)

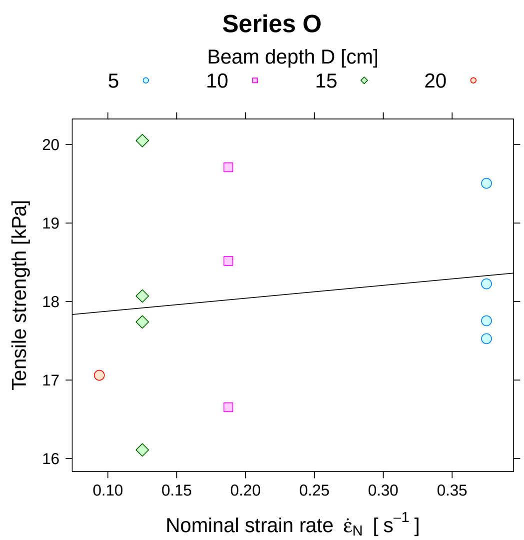

(d)

Figure 4.22: *Tensile strength versus nominal strain rate, grouped by beam depth, for the same size effect data as in Figure 4.21. All four test series had a constant crosshead speed of 1.25 cm/s. The slopes of the linear regressions had p-values of 0.004 (a), <0.001 (b), 0.016 (c), and 0.62 (d). These data indicate that part of the size effect on tensile strength (Figure 4.21) could be attributable to a nominal rate effect between samples of different sizes.*

Summary

The tensile strength data from the present study agree well with previous quasi-static laboratory data. Of all the variables related to the measurement of strength, the hardness and the density are the two most important. The blade hardness index is the best single variable for graphical representation and statistical correlation with tensile strength in the data from the present study. The snow type (structure) must be the same, together with other experimental controls, to ascertain the influence of secondary variables such as strain rate, temperature, and specimen size. Rate effects cannot be separated from size effects when constant-speed displacement controlled tests at different specimen sizes are conducted.

The next section contains several models developed to explain the mean tensile strength data considered thus far. The snow density and hardness are used, separately, as the predictor variables in these models, and comparison is made between the results using each variable.

4.3 Models of Tensile Strength

Regression models of strength allow for the systematic and reproducible use of strength data in analytical or numerical models. Least squares regression models using a single predictor variable, typically the snow density, are the most common for snow strength models. Least squares regression contains assumptions about the form of a model and the distribution of model errors, assumptions which should be checked and commented on when reporting regression results. Many techniques exist, such as transformation of variables, weighted regression, and variance modeling, for addressing violations of these assumptions. Violations of model assumptions can also indicate when the choice of a predictor variable, such as density, is inappropriate for explaining the mean structure of a dependent variable. Appendix B contains more detail about the implicit assumptions in least squares regression, common goodness of fit graphical and statistical techniques, and remedies for model violations applied in this section.

Only univariate models are considered here, primarily for comparison with previous models of the tensile strength of snow, nearly all of which are univariate functions of density. The most common model formulation for strength as a function of density is a power law. Models of this form are explored for explaining the data from the present study and those of several other studies. The ram hardness data of (*Martinelli*, 1971) is shown to be at least as good as density as a predictor variable for tensile strength. The blade hardness index, according to several goodness of fit measures, is also a better predictor than density for the strength data from the present study.

4.3.1 Density power law models

Snow properties such as strength are commonly expressed as functions of the bulk snow density, or the fraction of the density of pure ice. Power law models are perhaps the most common, though exponential models using the porosity or void ratio, which can be expressed as functions of density, have also been used (e.g. *Ballard and Feldt*, 1966; *Ballard and McGaw*, 1966; *Mellor and Smith*, 1966; *Keeler and Weeks*, 1968; *Keeler*, 1969). The most common power law function for the tensile strength has the form

$$f_t = a\left(\frac{\rho}{\rho_i}\right)^b \tag{4.24}$$

where ρ_i is the density of freshwater ice and a and b are the model parameters to be determined by fitting the relation through the strength-density data. Theoretically the value of a could be fixed at the tensile strength of pure ice, which is around 1.5–2 MPa (*Schulson and Duval*, 2009), leading to a single-parameter relation. However, a single monotonic expression such as Equation 4.24 is not expected to hold over the entire range of snow densities. Over the range of densities relevant for most avalanche applications ($\sim$100–350 kg/m^3) the strength is determined by the *structure* of the ice matrix, which as discussed previously is only loosely characterized by the bulk density. At higher densities than typical alpine snow, such as in multi-year polar or glacier firn snow, the snow will behave more as a porous solid which is likely to be governed more by the density. Therefore the parameters a and b should not be considered universal or material constants, but rather are limited to the specific range of snow densities that they arise from. However, the value of a should probably still fall within an order of magnitude of the tensile strength of ice, providing a rough check on the results.

Figure 4.23 shows regression fits of the form of Equation 4.24 through 17 of the data sources from this chapter. The strength values cover nearly three orders of magnitude, from less than 0.1 kPa for very low density snow to over 100 kPa for the highest densities typically found in seasonal alpine snow. For the lowest density snow, there is considerable agreement between the different data sources. The strength of very low density snow does not exceed 1 kPa until the density exceeds 100 kg/m^3. At higher densities, the lowest strength values come from *Sommerfeld* (1974), who had the largest sized specimens (though the loading rate is unknown). The in situ values of *Perla* (1969), *McClung* (1979a) and *Jamieson* (1988) agree very well and are the lowest excluding Sommerfeld's. The data of *Keeler and Weeks* (1968) are questionably far from the rest of the data, and raise questions about the presence of an unknown systematic error. The data of *Martinelli* (1971) cover the widest range of densities and are perhaps the best representative single data set of tensile strength, though these data are higher than all of the in-situ data for densities of 100 kg/m^3 and above. The slope of the data of *Butkovich* (1956) looks far too steep compared to the rest of the data, and could be due to the smaller number of data points and the small density range tested. Conversely, the slope of Haefeli's data (in *Bader et al.*, 1954) appears very flat, similar to the creep-fracture data of *Upadhyay et al.* (2007), which calls into question whether Haefeli's tests were also heavily influenced by creep. The model values from the present study fall right in the middle of the locus of values from other studies.

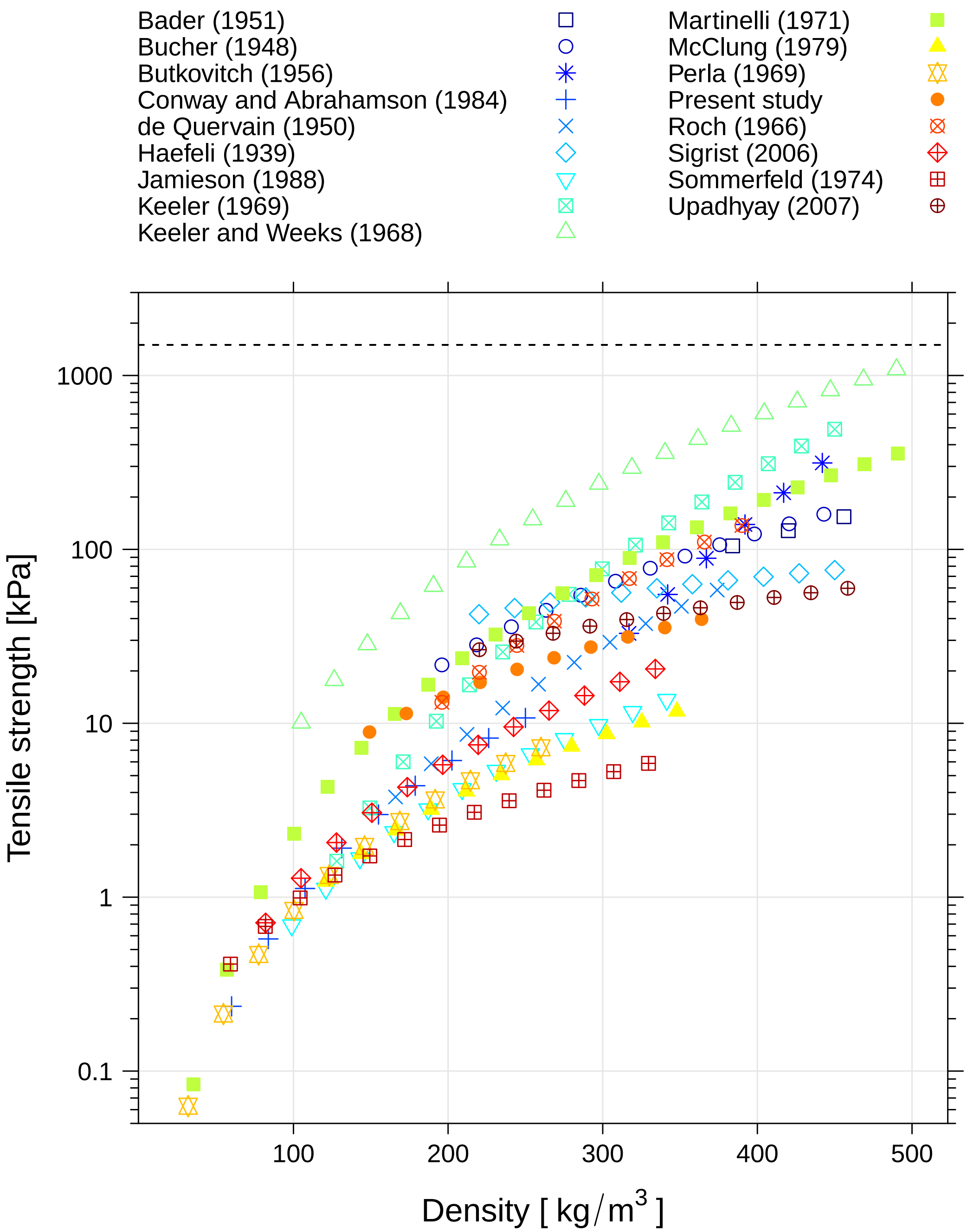

Figure 4.23: *Nonlinear regression of the form of Equation 4.24 through individual data sets. Data from other sources have been corrected to represent the ultimate tensile strength (rather than the nominal strength) where appropriate. The black dashed line is drawn to represent a lower-bound estimate of the uniaxial tensile strength of pure ice (1.5 MPa).*

New data from the present study

A subset of the tensile strength tests from Table 4.3, with the same specimen size and width (D = b = 10 cm) and loading rate (V = 1.25 cm/s), were considered for regression modeling as a function of density. The censored data set contained 123 tests. Fitting Equation 4.24 through this data led to a fit of the form

$$f_t = (200 \pm 30)\left(\frac{\rho}{\rho_i}\right)^{1.6\pm0.1} \qquad [\text{kPa}]. \tag{4.25}$$

Both regression parameters a and b were statistically significant at the α = 0.05 level (p-values $<$ 0.001 for both). The model residuals were not constant, displaying an increase with increasing density (Figure 4.24a). The residuals were neither normally distributed (Figure 4.24b) nor independent (Figure 4.24c). The fit had an R^2 = 0.65. See Appendix B for the definition of R^2 for nonlinear regressions, as the standard coefficient of determination in linear least-squares regression (referred to here using lower case r^2) differs. A Box-Cox profile likelihood was calculated (e.g. *Ritz and Streibig*, 2008) as a hypothesis test for whether a transformation of the data (such as a log-transform) would improve the fit of the model with respect to the residual structure. The 95% confidence interval for the parameter λ, which indexes the appropriate family of transformations, indicated that a transformation of the data would not significantly improve the fit.

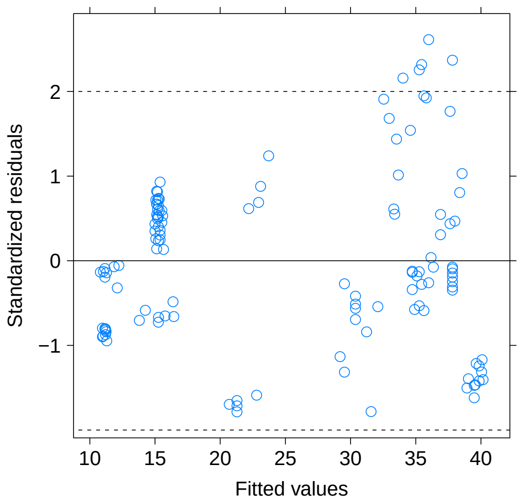

(a)

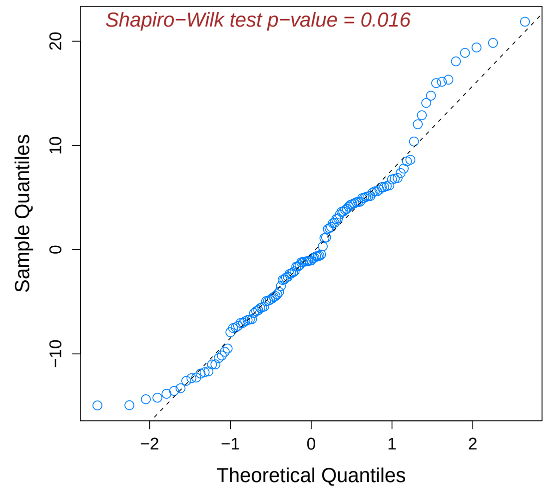

(b)

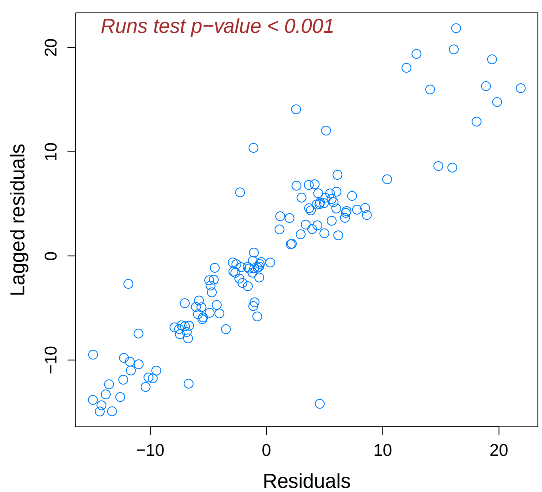

(c)

Figure 4.24: *Residual plots for assessing the goodness of fit of Equation 4.25. Standardized residuals versus fitted values (a), normal quantile plot of the residuals (b) and autocorrelation plot of the residuals (c). The null hypothesis of the Shapiro-Wilk test is that the residuals are normally distributed. The null hypothesis of the runs test is that the residuals are independent.*

In the absence of variable transformation, an alternative approach was taken in an attempt to improve the model fit before discarding density as an inappropriate predictor for the strength data. The positively correlated errors in Equation 4.25 (Figure 4.24c) were interpreted as a result of the indirect grouping of the data as a result of the experimental design. The test data in this study were grouped by date, and on a particular date all snow samples were taken from the same snow layer. This explains the clustering of the data by date of testing (Figure 4.18), with the date serving as a proxy for the snow layer of interest on that particular date. This sort of grouping typically produces positively correlated errors in regression modeling (*Rawlings et al.*, 1998). It is not appropriate to assume independent and constant variance in a regression model if the data are grouped, have different numbers of observations in each group, and the dependent variables are correlated within each group (*Rawlings et al.*, 1998), all of which are the case for the data considered here.

The strong autocorrelation among model residuals was addressed by computing the means of density and strength for each date of testing. These means were used in a subsequent weighted regression of the same form as Equation 4.24. The number of tests on a particular date divided by the variance of the strength values on that date was used a weighting factor for each of the subsequent 20 group means. The resulting model fit took the form

$$f_t = (360 \pm 160)\left(\frac{\rho}{\rho_{ice}}\right)^{2.3\pm 0.4} \qquad \text{[kPa]}. \tag{4.26}$$

In this case the parameter a is not statistically significant at the $\alpha = 0.05$ level (p-value = 0.06), though b is (p-value < 0.001). This fit had an $R^2 = 0.50$, lower than the previous model fit. The residuals of Equation 4.26 showed no obvious pattern as a function of density (Figure 4.25a) but the assumptions of normally distributed residuals (Figure 4.25b) and independent residuals (Figure 4.25c) were not satisfied at the α = 0.05 level. These plots indicate that the model represented by Equation 4.26 is a slightly improved fit in most regards over Equation 4.25.

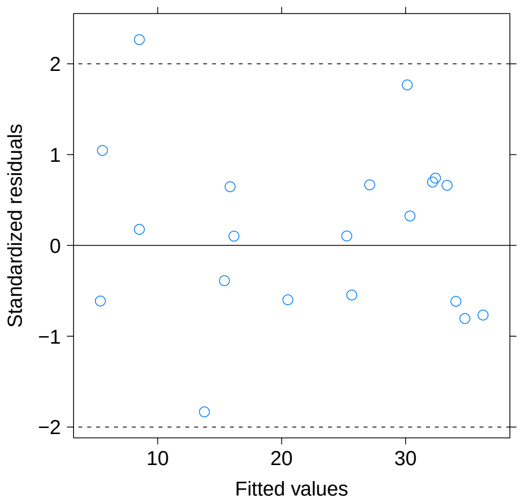

(a)

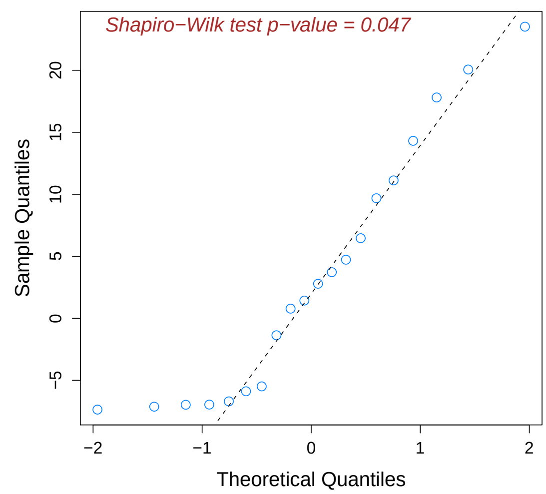

(b)

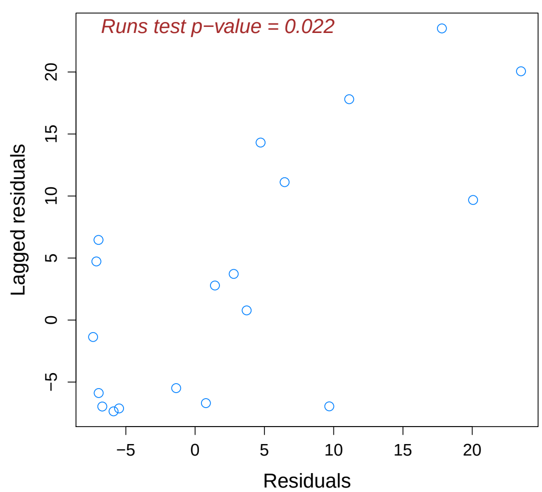

(c)

Figure 4.25: *Residual plots for assessing the goodness of fit of the weighted regression through the strength-density group means (Equation 4.26). Standardized residuals versus fitted values (a), normal quantile plot of the residuals (b) and autocorrelation plot of the residuals (c). The null hypothesis of the Shapiro-Wilk test is that the residuals are normally distributed. The null hypothesis of the runs test is that the residuals are independent.*

A Box-Cox profile likelihood indicated that a square-root transition might improve the residual structure of the group-means model of Equation 4.26. This transformation was performed and the data was re-fit to the power law model, leading to the following expression:

$$f_t = (350 \pm 140) \left(\frac{\rho}{\rho_i} \right)^{2.4 \pm 0.4} \qquad [\text{kPa}]. \tag{4.27}$$

Both model parameters were statistically significant at the $\alpha = 0.05$ level, and the fit had an improved R^2 = 0.62. The parameters did not change much compared to the original model of Equation 4.26. The transformation resulted in normally-distributed residuals (Figure 4.26b) but did not improve the autocorrelation of the residuals (Figure 4.26c). The distribution of residuals indicated a slightly worse fit, as the residuals decreased with increasing density (Figure 4.26a) moreso than in the un-transformed model (Figure 4.25a).

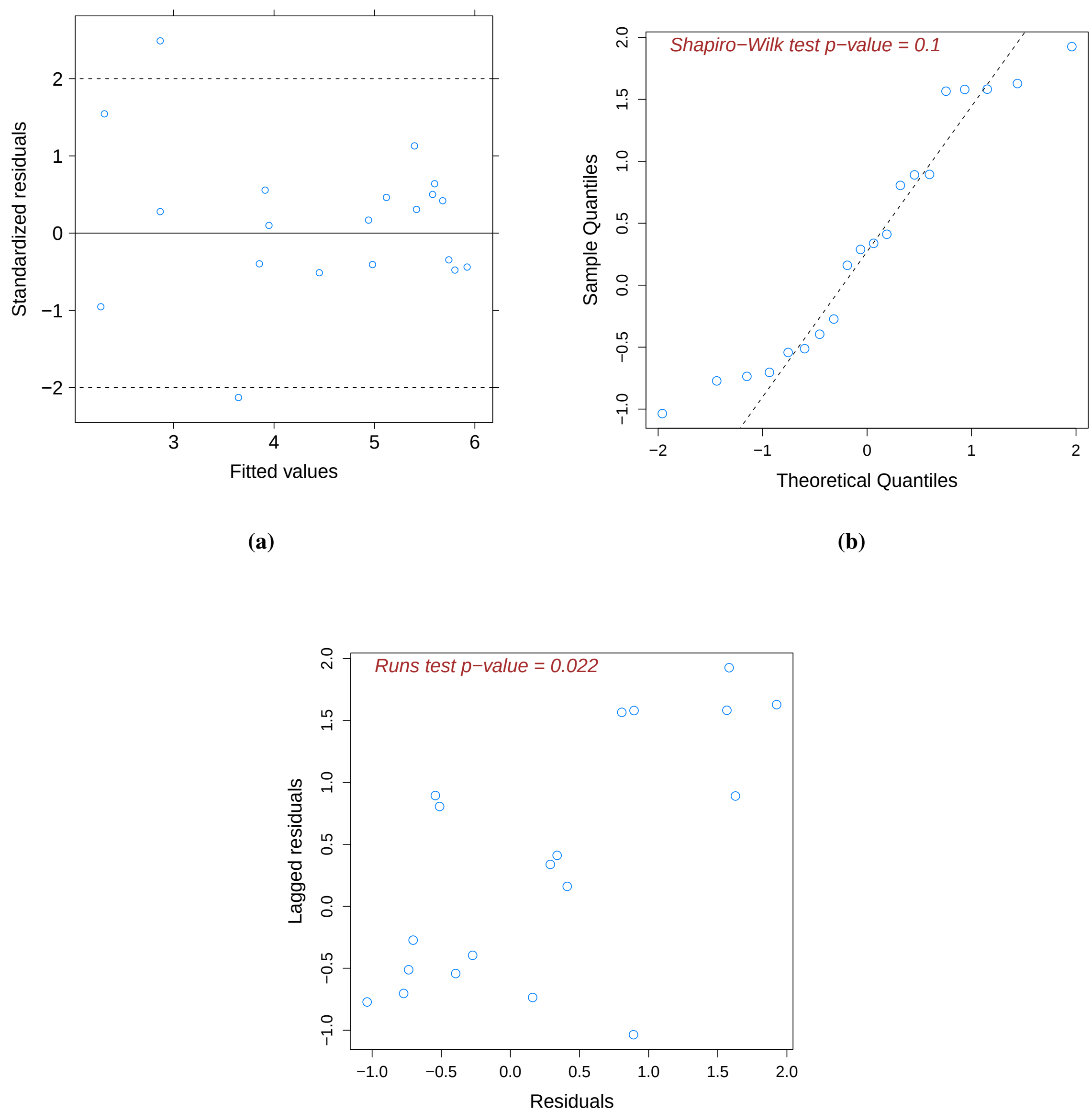

(a) **(b)**

(c)

Figure 4.26: *Residual plots for assessing the goodness of fit of the weighted regression through square-root transformed strength-density group means (Equation 4.27). Standardized residuals versus fitted values (a), normal quantile plot of the residuals (b) and autocorrelation plot of the residuals (c). The null hypothesis of the Shapiro-Wilk test is that the residuals are normally distributed. The null hypothesis of the runs test is that the residuals are independent.*

The model fits of Equations 4.25, 4.26, and 4.27 are shown together in Figure 4.27. The weighted regressions through group means of Equations 4.26 and 4.27 led to greater curvature in the mean function, expressed by the higher power law exponent. Owing to the smaller variance of strength values in Series A and P compared to Series H, the weighted regression models (Equation 4.26 and 4.27) shifted the mean function downward relative to Equation 4.25. This is in spite of the fact that Series H contained the largest number of tests of any series. The single model residual for Equation 4.26 that lies outside of 2 standard deviations from the mean (Figure 4.25a) corresponds to Series H in Figure 4.27. This is a drawback of the otherwise improved fit represented by Equation 4.26.

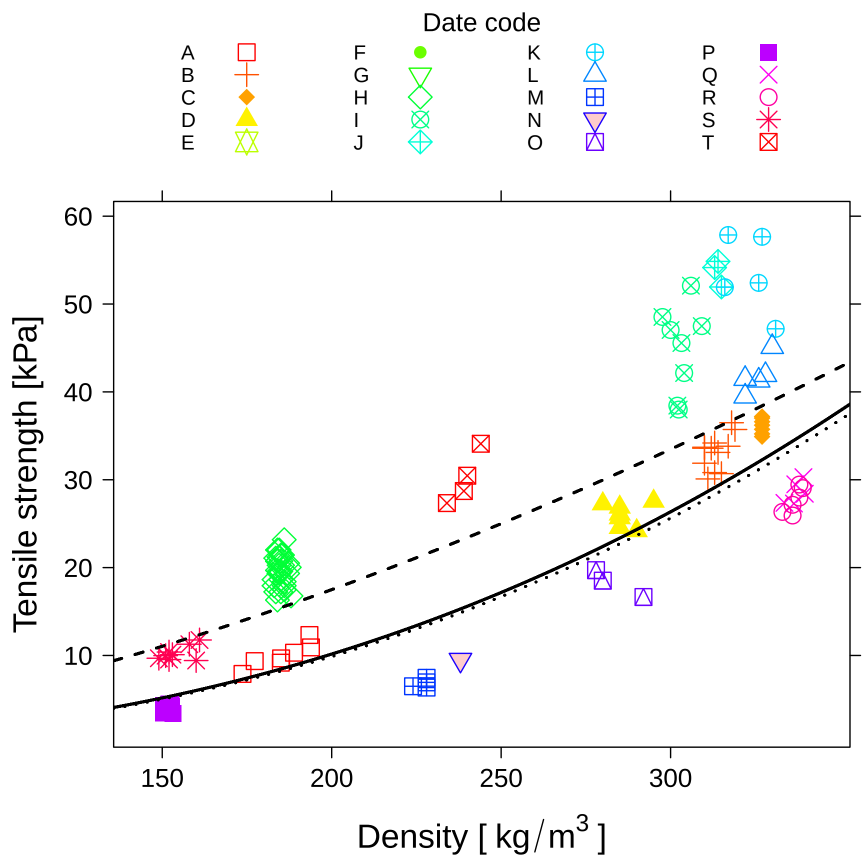

Figure 4.27: *Tensile strength versus density, grouped by date of testing, with regression model fits. The top dashed curve is the original model of Equation 4.25 through individual data points, the solid curve is the regression fit of Equation 4.26 through group means and the bottom dotted curve that of Equation 4.27 through the square-root transformed group means. The date codes are further explained in Table 4.3.*

None of the regression models capture the data in a wholly satisfactory manner from a visual perspective. The square-root transformation made a marginal difference to the visual appearance of the model of

Variable	Regression through full data set Equation 4.25 r_s	p	Weighted regression through group means Equation 4.26 r_s	p
grain size E	0.09	0.3	-0.32	0.17
beam slenderness S/D	-0.47	<0.001	-0.27	0.25
*blade hardness index B	0.33	0.002	0.34	0.16
temperature T	-0.32	0.001	-0.17	0.48

Table 4.4: *Spearman's correlation coefficients r_s and p-values for the residuals of the tensile strength versus density models tested against other variables. *Correlations excluded Series A for which the blade hardness index was not measured.*

Equation 4.27. The dotted line of Equation 4.27 is hardly discernible from the original model, the solid line of Equation 4.26. From the numerous goodness of fit statistics and the relative simplicity of the model, Equation 4.26 is considered the best model among the three.

Correlations between model residuals and other variables not represented in the regression models (in other words, variables other than density) offer a final check on the goodness of fit of the regression models. The original regression model through individual data points (Equation 4.25) and the first weighted regression model through group means (Equation 4.26) are compared in Table 4.4. For the model through individual data points, the residuals were significantly correlated with the span to depth ratio of the beams, the blade hardness index, and the temperature. The direction of these correlations are as expected: more slender beams and colder snow were correlated with lower strength, and higher hardness snow was correlated with higher strength (for Equation 4.25). The model through group means (Equation 4.26) did not have any statistically significant residual correlations. This is an indication that this model is a better representation of the mean structure of the tensile strength data, at least when expressed as a function of density. Therefore the best regression model here is that of Equation 4.26, re-written here for convenience: $f_t = 360(\rho/\rho_i)^{2.3}$, with f_t in kPa.

Jamieson's data

Jamieson (1988) reported a nonlinear regression of the form of Equation 4.24 through his in situ uniaxial tensile strength data. His data were not corrected for the difference between the nominal and maximum stress at failure, and took the form $80\,(\rho/\rho_i)^{2.4}$. I refit this data, composed of the mean uniaxial tensile strength of 43 layers, excluding layers composed of faceted or mixed rounded and faceted crystals. The number of tests in each snow layer divided by the variance of strength values were used to weight the individual means in the regression, as performed above in Equation 4.26. Residual plots of the initial fit showed a variance structure that was largely homogeneous and normally distributed. A Box-Cox profile likelihood of the model indicated that a square root transformation of both sides would improve the fit (Jamieson's fit was through log-transformed data). The resulting model took the form

$$f_t = (150 \pm 25) \left(\frac{\rho}{\rho_i} \right)^{2.4 \pm 0.1} \qquad \text{[kPa]}. \tag{4.28}$$

Both regression parameters were statistically significant at the $\alpha = 0.05$ level, and the fit had an R^2 = 0.94. The residual plots for Equation 4.28 indicate that the variance structure is mostly homogeneous. The residuals slightly decrease with increasing density (Figure 4.28a) but are normally distributed (Figure 4.28b) and independent (Figure 4.28c). These findings indicate that the density alone can adequately represent the strength data of *Jamieson* (1988).

The model of Equation 4.28 is slightly less than a factor of 2 greater than that reported by *Jamieson* (1988). This can be attributed to the stress concentration factor that was calculated and accounted for here. For the sample dimensions reported by *Jamieson* (1988) (test geometry in Figure 4.10), the stress concentration factor took values in the range 1.7–2.1. Individual values were calculated for each layer in the data set, since the geometric dimensions for each layer were published.

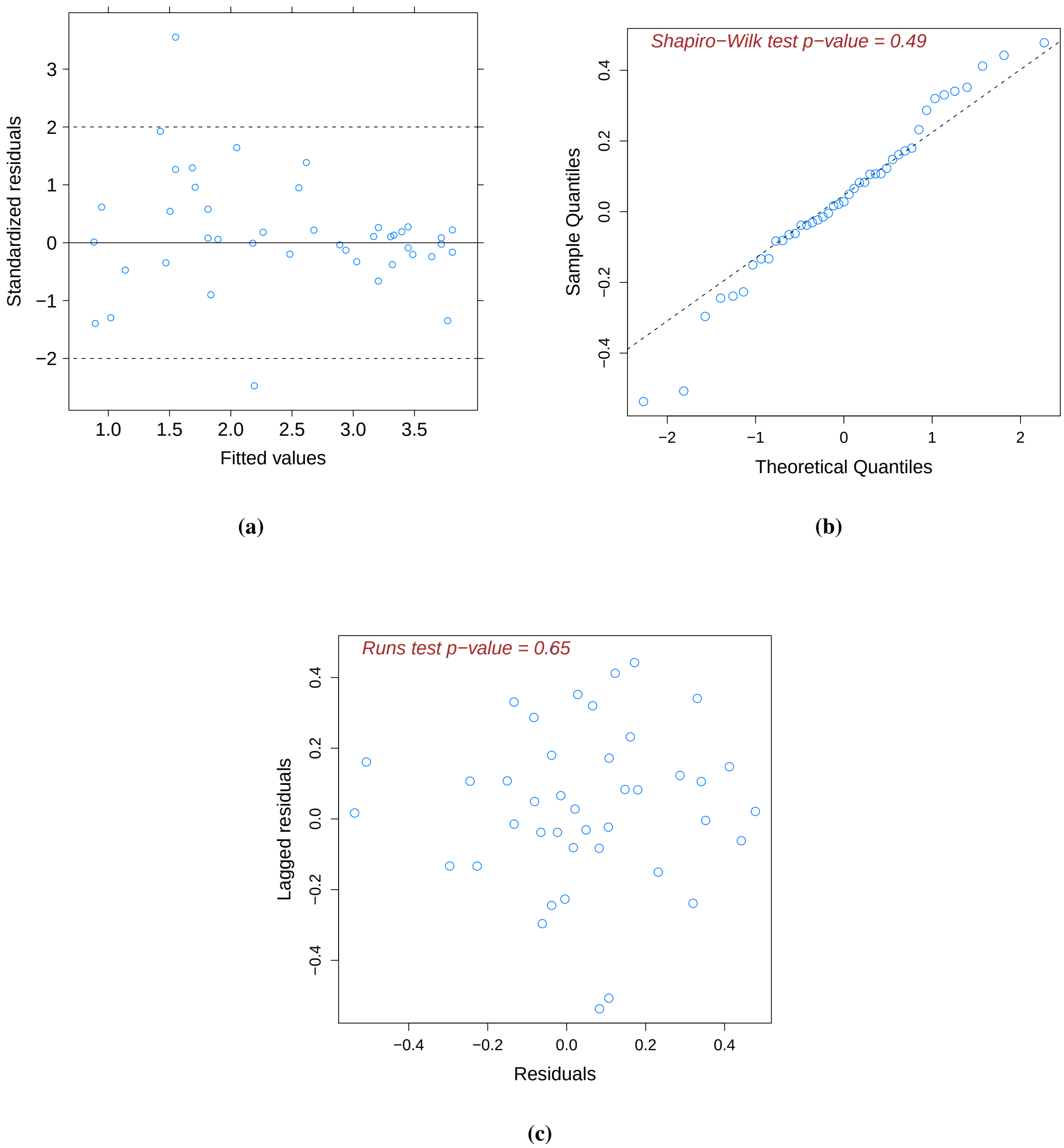

Figure 4.28: *Residual plots for assessing the goodness of fit of the log-transformed strength-density data of Jamieson (1988) (Equation 4.28). Standardized residuals versus fitted values (a), normal quantile plot of the residuals (b) and autocorrelation plot of the residuals (c). The null hypothesis of the Shapiro-Wilk test is that the residuals are normally distributed. The null hypothesis of the runs test is that the residuals are independent.*

Sigrist's data

Sigrist (2006) kept all variables other than the sample density the same for his tensile strength test series. I fit his data, corrected using the relationship between the tensile strength and modulus of rupture in Equation 4.19, to the general power law expression of Equation 4.24. The initial fit showed strongly heterogeneous residuals, with the variance increasing sharply with the mean. The residuals were non-normally distributed, but did pass the runs test for independence. This is likely the result of the smaller data set that was designed just to measure the tensile strength, so all other experimental variables were held exactly the same across the data set.

I next transformed Sigrist's data using a log transformation of both sides, and the resulting model fit was improved compared to the initial fit. The fit through the transformed data took the form

$$(230 \pm 30)\left(\frac{\rho}{\rho_i}\right)^{2.4\pm0.1} \qquad [\text{kPa}]. \tag{4.29}$$

The fit had an $R^2 = 0.91$, and both regression parameters were statistically significant at the $\alpha = 0.05$ level. The residual structure was still heterogeneous, with increasing variance with increasing density (Figure 4.29a). The residuals remained normally distributed (Figure 4.29b) and independent (Figure 4.29c). *Sigrist* (2006) reported similar parameter estimates ($f_t = 240\,(\rho/\rho_i)^{2.44}$). The primary discrepancy is the correction applied here for the difference between the modulus of rupture and the tensile strength in three point bending, a correction which reduces the elastic tensile stress in the outer fiber of the beam.

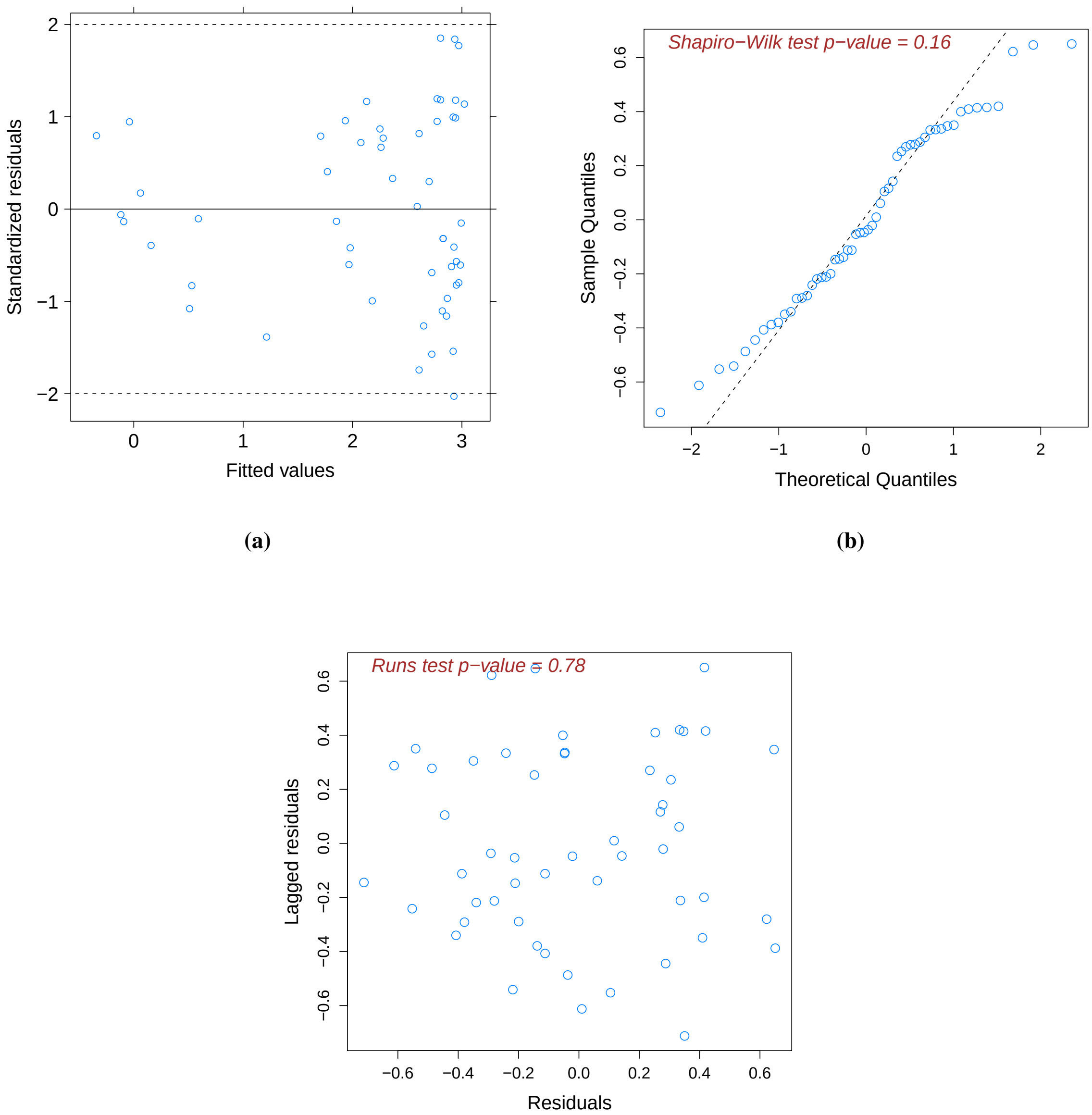

(a) **(b)**

(c)

Figure 4.29: *Residual plots for assessing the goodness of fit of Equation 4.29 for the data of Sigrist (2006). Standardized residuals versus fitted values (a), normal quantile plot of the residuals (b) and autocorrelation plot of the residuals (c). The null hypothesis of the Shapiro-Wilk test is that the residuals are normally distributed. The null hypothesis of the runs test is that the residuals are independent.*

Martinelli's data

I fit the centrifugal data of *Martinelli* (1971), corrected for the stress concentration, as a function of density using a model of the form of Equation 4.24. The initial fit showed strong heteroscedasticity and autocorrelation of the residuals. A power law transformation, determined using the Box-Cox profile likelihood approach, led to a best fit of the form

$$f_t = (3400 \pm 600)\left(\frac{\rho}{\rho_i}\right)^{3.4\pm0.2} \tag{4.30}$$

with approximate 95% confidence intervals on the parameters and f_t in kPa. The fit had an $R^2 = 0.88$. The parameter a is about an order of magnitude higher than those of the previous models, but the power law exponent is also greater by about one, which accounts for this order-of-magnitude discrepancy. Figure 4.30 shows the goodness of fit plots for this model. It shows normality in the model residuals and no apparent pattern in the variances, but the residuals were autocorrelated. The model fit through the data is shown in Figure 4.31 for eventual comparison with the same strength data modeled using the ram hardness.

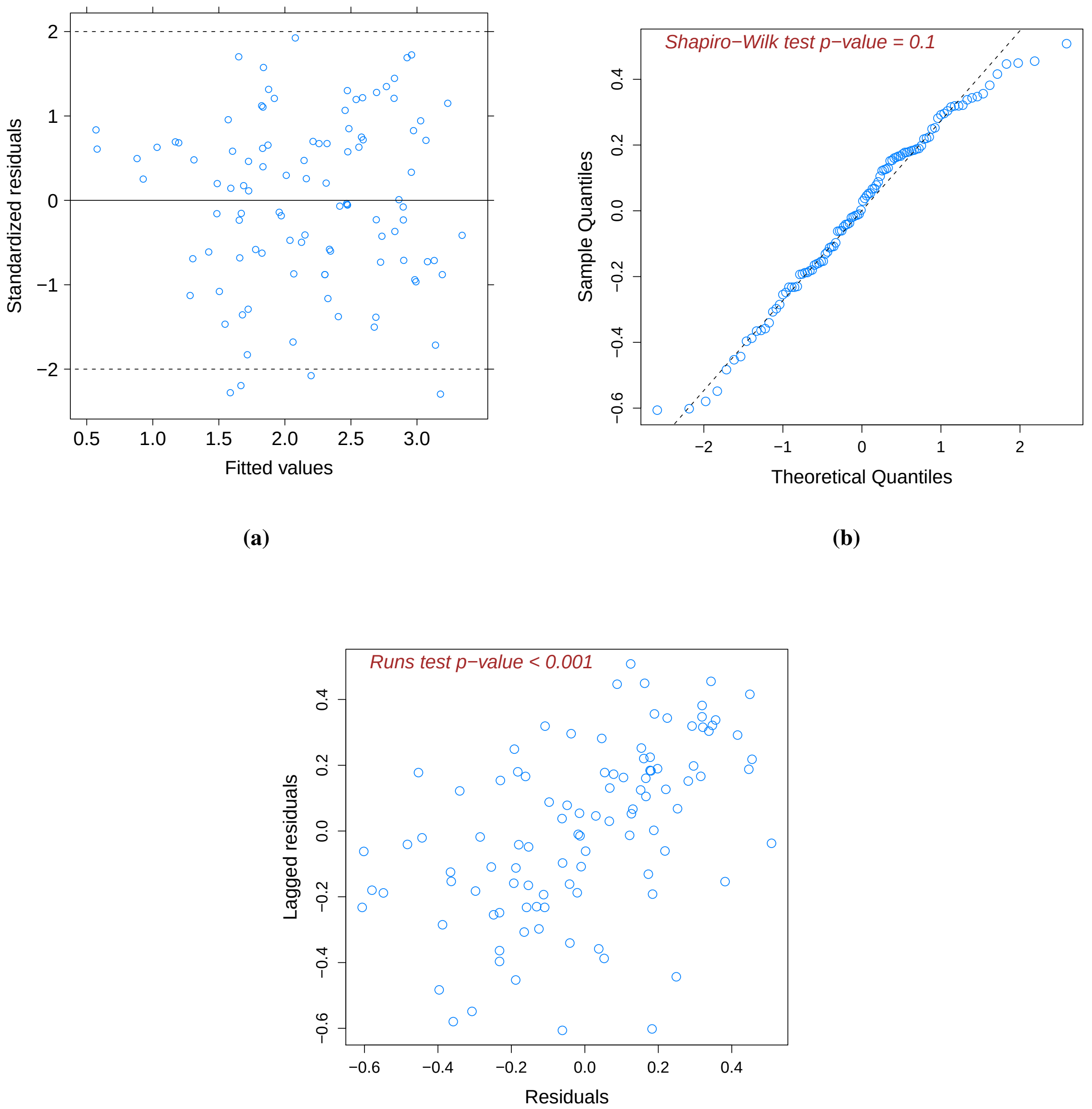

(c)

Figure 4.30: *Residual plots for assessing the goodness of fit of Equation 4.30 for the data of Martinelli (1971). Standardized residuals versus fitted values (a), normal quantile plot of the residuals (b) and autocorrelation plot of the residuals (c). The null hypothesis of the Shapiro-Wilk test is that the residuals are normally distributed. The null hypothesis of the runs test is that the residuals are independent.*

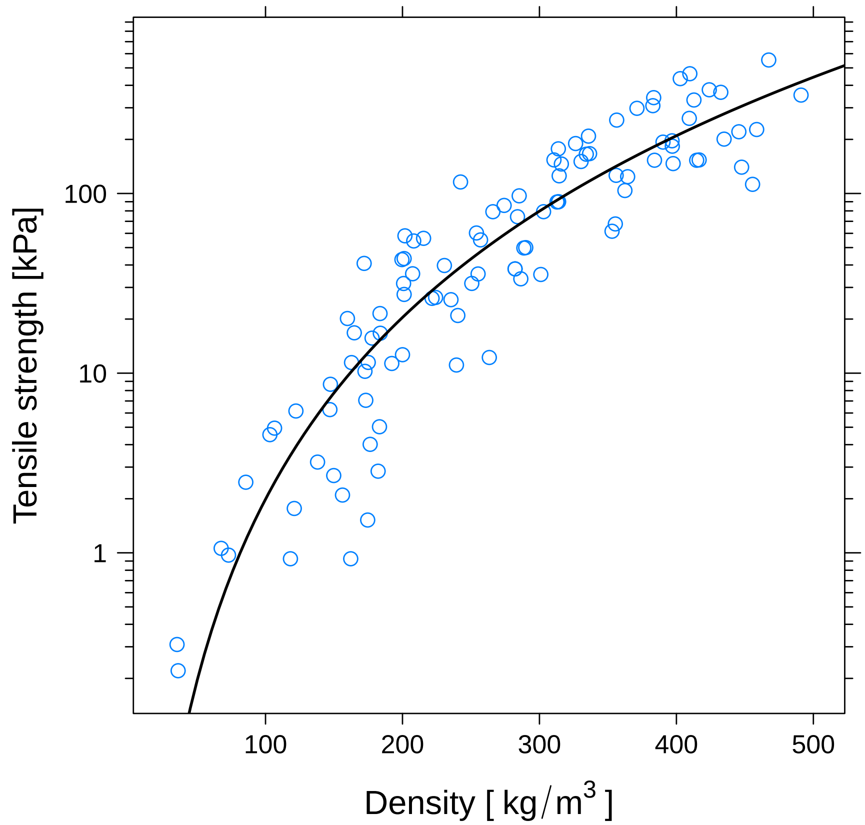

Figure 4.31: *Tensile strength versus density data from Martinelli (1971) with the regression fit of Equation 4.30.*

4.3.2 Hardness models

Strength versus blade hardness index

Recall that the tensile strength correlated better with the blade hardness index than the density. The tensile strength versus blade hardness data from Figure 4.15 appeared roughly linear. As with the tensile strength data, the full data set was first censored to include only the same values of beam depth, width and crosshead speed during testing. The resulting data set contained 81 test results. A linear fit through this data took the form

$$f_t = (7.7 \pm 1.0) + (2.8 \pm 0.15)\,B \tag{4.31}$$

with f_t in kPa and adjusted $r^2 = 0.82$ (note that lower-case 'r' here refers to the standard coefficient of determination in least squares linear regression). The model residuals have no clear pattern, but several key outliers are present (Figure 4.32a). The residuals are not normally distributed according to the Shapiro-Wilk test (Figure 4.32b) nor are they independent, showing the familiar positive autocorrelation (Figure 4.32c).

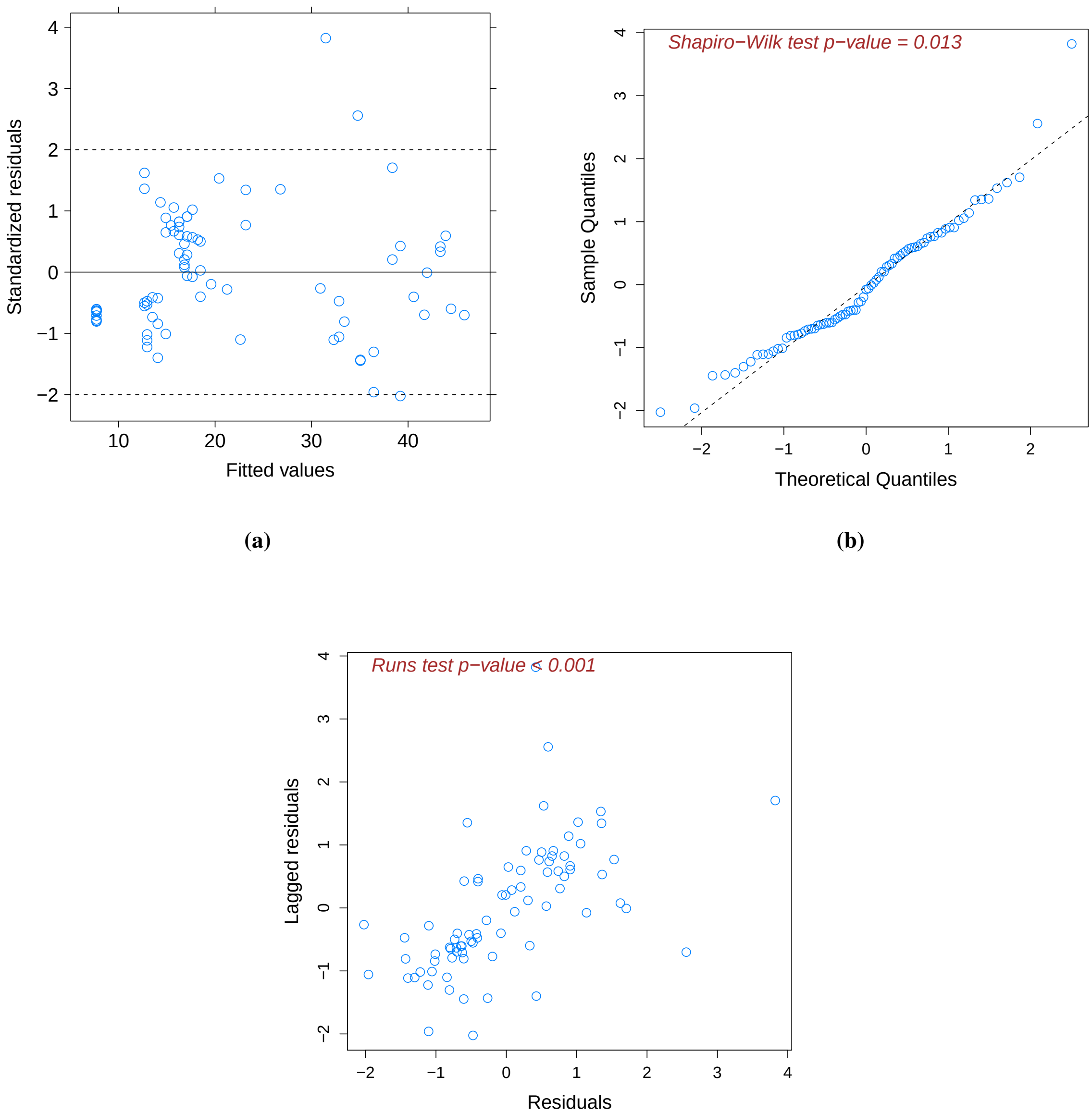

(c)

Figure 4.32: *Residual plots for assessing the goodness of fit of the linear regression model of tensile strength versus blade hardness index (Equation 4.31). Standardized residuals versus fitted values (a), normal quantile plot of the residuals (b) and autocorrelation plot of the residuals (c). The null hypothesis of the Shapiro-Wilk test is that the residuals are normally distributed. The null hypothesis of the runs test is that the residuals are independent.*

A power-law model was then tested of the form $f_t = a\,(B)^b$. Fitting this relation through the strength-hardness data led to the equation

$$f_t = (8.8 \pm 0.6)\, B^{0.61 \pm 0.03} \qquad \text{[kPa]}. \tag{4.32}$$

This fit had a (nonlinear regression) coefficient of determination of $R^2 = 0.82$. As with the linear model, the residuals of the power law model had no clear pattern, but several outliers were again present (Figure 4.33a). The lack of normality and independence of the residuals (Figures 4.33b and 4.33c) was about the same as for the linear model. A Box-Cox profile likelihood indicated that a transformation of the data would not significantly change the parameter estimates.

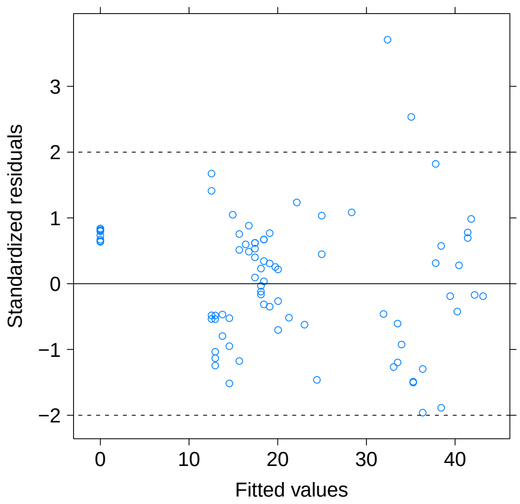

(a)

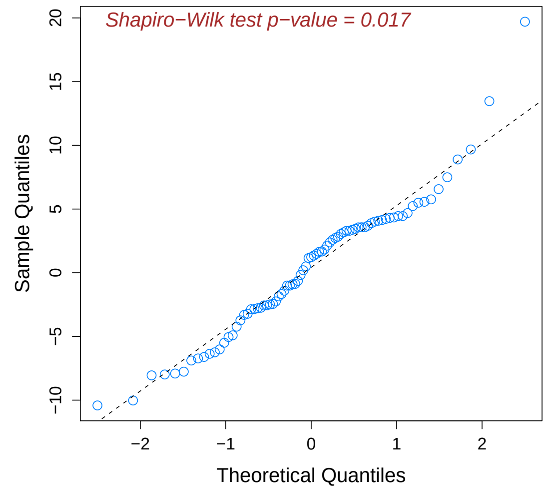

(b)

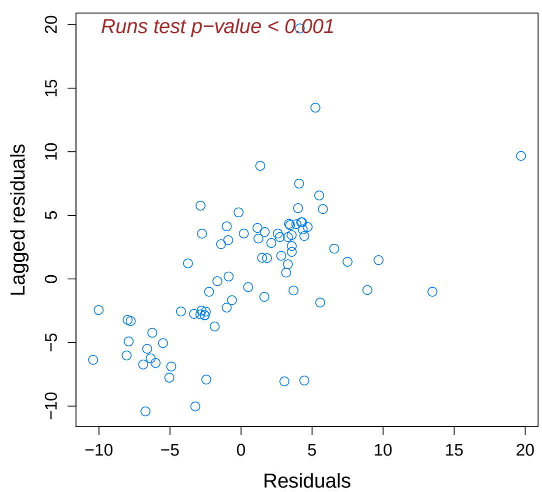

(c)

Figure 4.33: *Residual plots for assessing the goodness of fit of the power law model of tensile strength versus blade hardness index (Equation 4.32). Standardized residuals versus fitted values (a), normal quantile plot of the residuals (b) and autocorrelation plot of the residuals (c). The null hypothesis of the Shapiro-Wilk test is that the residuals are normally distributed. The null hypothesis of the runs test is that the residuals are independent.*

As with the density models above, weighted regression through group means was performed to address the positive autocorrelation of the residuals in both the linear and power law models above. Other than

Series A, for which no blade hardness measurements were taken, the same groups of data were used as with the density regressions above. A total of 133 tests in 19 different groups (days) were used for the following regressions. The means of each relevant variable from each date of testing were computed, and the variance in strength values was again used in combination with the number of tests to weight each data point.

The weighted linear regression took the form

$$f_t = (4.3 \pm 1.2) + (3.1 \pm 0.2)\,B \qquad \text{[kPa]}. \tag{4.33}$$

The slope and intercept of this model were statistically significant at the $\alpha = 0.05$ level, and the model had an adjusted $r^2 = 0.9$, higher than the linear regression through all the data points. The residuals displayed no spatial pattern, with only two residuals falling outside of two standard deviations from the mean. The residuals were normally distributed (Shapiro-Wilk test p-value = 0.63) and independent (runs test p-value = 0.1). These results indicate a good model selection and fit to the data.

The weighted power law regression through the group means took the form

$$f_t = (6.6 \pm 1.4)B^{0.73 \pm 0.09} \quad [kPa]. \tag{4.34}$$

This model had a coefficient of determination of $R^2 = 0.88$, higher than the power law regression through all the data points. The model residuals had no spatial pattern, with most residuals falling within one standard deviation from the mean and only one residual falling outside two standard deviations from the mean. The residuals were normally distributed (Shapiro-Wilk test p-value = 0.33) and independent (runs test p-value = 0.49).

The linear model through the individual data points (Equation 4.31) had one fewer residual which was significantly correlated with remaining variables than the power law model through the individual points expressed by Equation 4.32. Residual correlations for all four hardness models considered here are listed in Table 4.5. Both regression models through the group means appear better than models through individual points from the perspective of the residual correlations. The group-mean models have significant negative correlations between residuals and grains size, indicating weaker snow for larger grain size. The simplicity of the linear group-mean model (Equation 4.33) points to this model as being the most appropriate for representing the strength-hardness data here.

	Model using all data points				Model using group means			
	Linear model Equation 4.31		Power law model Equation 4.32		Linear model Equation 4.33		Power law model Equation 4.34	
Variable	r_s	p	r_s	p	r_s	p	r_s	p
grain size E	0.13	0.25	**-0.27**	**0.01**	**-0.52**	**0.02**	**-0.60**	**0.01**
beam slenderness S/D	**-0.52**	$<$**0.001**	-0.16	0.16	0.24	0.32	0.09	0.71
density ρ	-0.06	0.58	**-0.25**	**0.03**	-0.29	0.23	-0.21	0.39
temperature T	**-0.53**	$<$**0.001**	**-0.39**	$<$**0.001**	-0.23	0.33	-0.22	0.37

Table 4.5: *Spearman's correlation coefficients r_s and p-values for the residuals of the tensile strength versus blade hardness models tested against other raw variables. Bold face indicates statistically significant correlations at the $\alpha = 0.05$ level.*

Both linear regression models considered here are represented in Figure 4.34 together with the respective data that they were fit to. Both models fit the data quite well visually. The slopes of the models are similar, the main difference is in the larger intercept for the model of Equation 4.31 (Figure 4.34a) than Equation 4.33 (Figure 4.34b). However, the smaller intercept of the latter model is probably more appropriate physically. The blade hardness index data of Series P was recorded for each test as 0 N, though the actual penetration resistance was somewhere in the range 0 N $< B <$ 1.7 N. If the data for this series shifted to the right to represent the true resistance of the snow, then the intercept of the linear model would be pulled closer to the origin. For this reason, the regression model of Equation 4.33 is considered the most appropriate single model for the dependence of the tensile strength on the blade hardness index. For convenience, the model is re-written here: $f_t = 4.3 + 3.1B$ [kPa].

Compared to the strength models as a function of density, the blade hardness regression models produced better fits using a number of measures. The residual structure (homoscedasticity, normality and independence of residuals) was in general better for the blade hardness models than the density models. Fewer model residuals were significantly correlated with other variables for the hardness models than the density models, suggesting that the blade hardness index better captures the mean structure of the strength data using a single variable. A simple linear regression provided a good fit to the strength-hardness data, while all previous strength-density data sets are nonlinear with large power-law exponents.

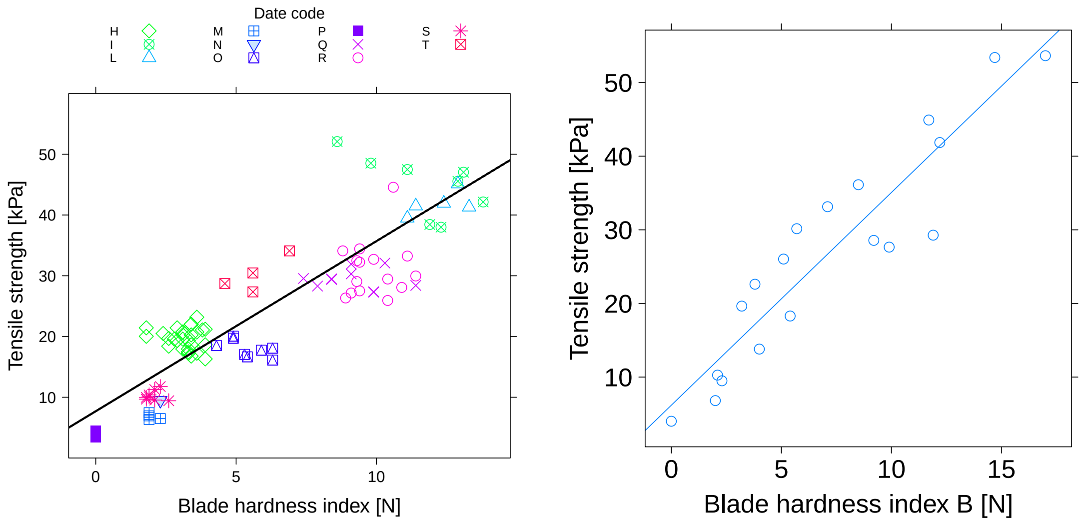

(a) **(b)**

Figure 4.34: *Tensile strength versus blade hardness index, grouped by date of testing (a) and plotted using mean strength and hardness for each date (b). The regression model through individual points in (a) is represented by Equation 4.31, and the model through group means in (b) by Equation 4.33. The model through the group means is a better fit from the perspective of the residual correlations in Table 4.5.*

Strength versus ram hardness

I next fit the centrifugal data of *Martinelli* (1971) as a function of the ram hardness R_{ram}. I first used a power law formulation similar to that used above for the blade hardness index. The initial fit showed strongly heteroscedastic, non-normal and autocorrelated residuals. A Box-Cox profile likelihood suggested a cubic-root transformation, which led to a best fit of the form

$$f_t = (0.8 \pm 0.2)\, R_{ram}^{0.84 \pm 0.04} \tag{4.35}$$

with approximate 95% confidence intervals on the parameters, f_t in kPa and R_{ram} in N. This fit also had a relatively high $R^2 = 0.88$. The residuals had no serial structure and were normally distributed (Shapiro-Wilk test p-value = 0.92). The residuals were positively autocorrelated, however, with a runs test p-value = 0.001. In general, the residual structure of this fit is better than the corresponding residual structure from the same strength data modeled using the density (Equation 4.30 above).

The power law exponent of Equation 4.35 is close to 1, suggesting that a linear model may be appropriate. A linear regression led to a model of the form

$$f_t = (17 \pm 7) + (0.25 \pm 0.01) \times R_{ram} \tag{4.36}$$

with f_t again in kPa and R_{ram} in N. This fit had an adjusted $r^2 = 0.79$. This fit was not as good from the perspective of the variance structure of the residuals. The residuals were not normally distributed (Shapiro-Wilk test p-value < 0.001) nor independent (runs test p-value = 0.008). Figure 4.35 shows both ram hardness model fits through the data. The fits are of a similar visual quality compared to the strength-density relation for the same data set (Figure 4.31).

In the data of *Martinelli* (1971), no clear distinction can be made about which variable, density or hardness, is better for modeling the strength data. The density data appear to show less scatter about the model fit (Figure 4.31), and the amount of scatter appears nearly constant with density. The scatter in the hardness data increases with increasing hardness (Figure 4.35). The residual structure of the the density and ram hardness relations were of similar quality in terms of normality and homoscedasticity of residuals. In all of Martinelli's data, positive autocorrelation among the residuals was present. The ability of a linear model of hardness to provide a fairly good representation of the mean structure of the strength data is a strong argument in favor of hardness as the better predictor. However, both variables have about the same predictive capability for the centrifugal tensile strength data of *Martinelli* (1971).

In many individual data sets, where as many of the experimental variables as possible have been controlled, the density can be used to adequately characterize the tensile strength of snow in a univariate power law formulation. Measures of snow hardness, however, can also account for the mean structure of strength data equally as well, if not better, than the density. The ram hardness gauge has been largely discarded by practitioners due to the heavy and bulky nature of the probe and the difficulty with interpretation of the test results. The blade hardness index measurement developed in the present study appears to be a promising alternative as an in situ or lab measure of snow hardness for relating to tensile strength.

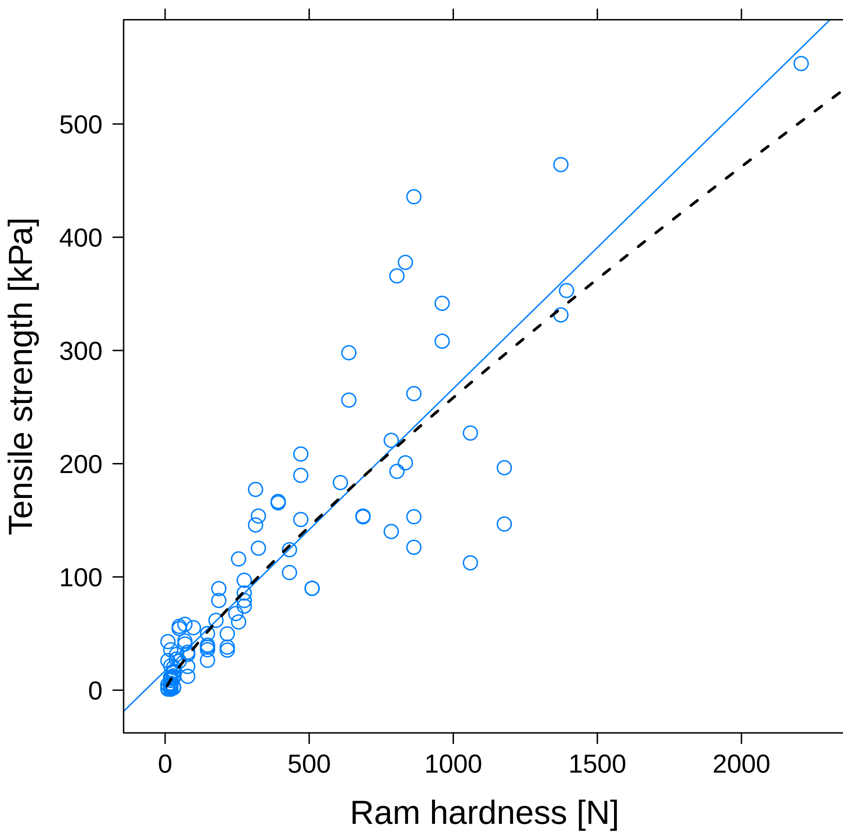

Figure 4.35: *Tensile strength versus ram hardness data from Martinelli (1971). The dashed line is the power law regression of Equation 4.35, the solid line is the linear regression of Equation 4.36.*

Conclusions

Figure 4.36 shows the tensile strength data from the present study in context with all the strength data from this chapter. The data from the present study agree well with the previous laboratory and centrifugal data and the upper range of the in situ data. The large scatter in the data is due to variations in snow microstructure, temperature, loading rate and size effects both within and across data sets. The greatest variability in test results is for the centrifugal test data, which is also the largest data set. The highest measured tensile strength values have come from centrifugal testing. Few laboratory results, and no in situ data, have exceeded 100 kPa.

The greatest agreement in strength values among different test methods is for the lowest sample densi-

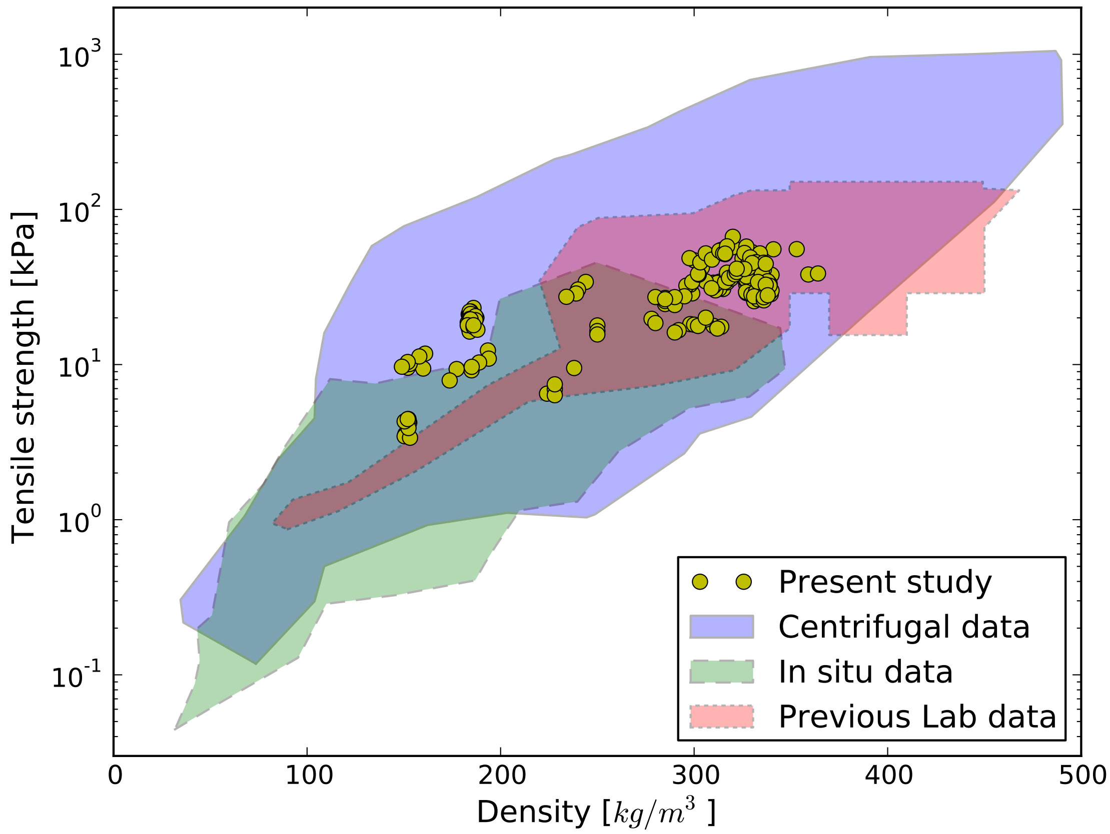

Figure 4.36: *Shaded regions of tensile strength versus density for the data groupings discussed above. The centrifugal data sources are represented in Figure 4.4, the in situ data in Figure 4.9 and the previous lab data in Figure 4.12. Altogether over 2000 strength tests from 20 different sources are represented in this plot.*

ties. At higher densities the lower strength values in the centrifugal data agree well with the lab and in situ data. The upper bound values for the centrifugal data are, for some densities, nearly an order of magnitude greater than data obtained using other testing methods. The higher centrifugal strength values are heavily weighted by the *Keeler and Weeks* (1968) data, which are typically a factor of 2-3 greater than the data from *Martinelli* (1971) and *Keeler* (1969) at similar densities.

A great deal of the variability in the data in Figure 4.36 is also due to indexing strength as a function of density. Density does not characterize the microstructural dependence of snow properties such as strength. It has been and continues to be used, however, due to a lack of a better (and widely agreed upon) alternative.

The ram hardness appeared to be a good index for strength, but this measurement, owing to the heavy and bulky nature of the ram probe, has fallen out of favor in the avalanche industry. The simple and easy blade hardness measurement developed in the current study is a promising alternative. The blade hardness index was shown here to be a better measure than density for correlating with strength and may be a promising measure for indexing other mechanical properties of snow.

The tensile strength of snow, however it is expressed, is a fundamental property for the analysis of snow slab avalanche release. This chapter contains the most extensive analysis of published tensile strength data for seasonal dry snow in the literature. Altogether over 2000 strength test results were assessed, and, within the expected scatter across and within data sets, the results largely agree, with just a few notable exceptions. More in-depth multivariate analysis of the data may help to elucidate many of the secondary influences of different variables on strength. However, reporting standards have varied widely across tensile strength studies, and few variables other than density are available to provide a more complete picture of second-order properties and conditions that influence strength. A move toward more complete, thorough and consistent reporting standards in snow mechanics would be beneficial to the field.

Chapter 5

Determination of Fracture Parameters using Nonlinear Fracture Mechanical Scaling Laws

The destructive potential of a slab avalanche is in part determined by the volume of snow cut loose by shear and tensile fractures. The spatial extent of the initial shear fracture propagation is limited by the tensile fracture properties of the overlying slab. Determining appropriate values of fracture parameters relevant to these processes requires extrapolating the results of small-scale lab or in-situ measurements possibly an order of magnitude in size to the avalanche scale. Therefore, well-calibrated size scaling laws are needed to arrive at fracture-mechanical predictions of the slab release dimensions (*McClung and Schweizer*, 2006).

Tensile fractures associated with slab avalanche release may be affected by two different types of size effects which relate the decrease of nominal strength of a snow slab with increasing slab depth, all else the same. The first is a fracture mechanical (deterministic) size effect, which arises from the release of strain energy associated with the creation of surface area during crack propagation (e.g. *Bažant and Planas*, 1998). The second is a statistical size effect related to the distribution of defects or the randomness of material properties, as in Weibull theory (e.g. *Hertzberg*, 1996). Many previous studies on the fracture

Section 5.3 in this chapter contains material published as *Borstad and McClung* (2009). Additional information on this publication is described in the Preface.

of snow have reported a size effect on strength, both in shear (*Perla*, 1977; *Sommerfeld and King*, 1979; *Perla and Beck*, 1983) and tension (*Sommerfeld*, 1974; *Jamieson*, 1988; *Sigrist et al.*, 2005b; *Sigrist*, 2006). These effects have been explained using both deterministic fracture mechanical scaling laws (*Bažant et al.*, 2003; *McClung*, 2009b) and Weibull statistical theory (e.g. *Sommerfeld*, 1980). However, these competing scaling laws have important differences in their large size asymptotic strength predictions.

The common experimental procedure for determining fracture properties for either type of size scaling law is to directly measure the dependence of nominal strength on specimen size and infer the relevant fracture or statistical parameters—such as the fracture toughness, fracture process zone size, or Weibull modulus—by fitting the data to the scaling law. The best fitting model, both numerically and physically, can then be used to extrapolate the lab-scale results to the structural scale of interest. This type of inverse method was applied in this chapter to determine the appropriate type of scaling law and the resulting fracture parameters for describing the tensile fracture of snow.

A number of working hypotheses informed the following analysis. First, physical arguments and previous preliminary results have suggested that the nonlinear fracture process zone ahead of a crack tip in snow is likely large relative to typical specimen dimensions (*McClung*, 1987, 1996; *Sigrist et al.*, 2005a,b; *McClung and Schweizer*, 2006; *Sigrist*, 2006). This should lead to nonlinear fracture behaviour, implying that a linear theory such as linear elastic fracture mechanics (LEFM) would not be applicable for analysis of experimental data. However, it was also hypothesized that a simple correction for this nonlinear response using an equivalent elastic crack, allowing the framework of LEFM to be used, may be sufficient for accounting for any observed nonlinearity. Finally, given sufficiently high experimental loading rates, it was hypothesized that viscous effects in snow experiments would be sufficiently small (e.g. *Camponovo and Schweizer*, 2001) that an elastic framework for analysis would be acceptable. This follows from similar analyses of concrete fracture data which contain rate-dependent creep effects (*Bažant and Gettu*, 1992), for which the creep strains at failure were small enough relative to the instantaneous elastic strain that an equivalent elastic analysis was deemed appropriate. Note that similar implicit assumptions were made in the existing literature and analysis in the previous chapter.

In the following, the theoretical background of LEFM is first outlined, followed by the equivalent elastic crack concept for homogenizing snow as a continuum and accounting for nonlinearity in fracture caused by a large and diffuse fracture process zone. Then, following primarily the work of Bažant, three different size effect laws are derived, one each for notched and unnotched size effects and a third that bridges notched and unnotched tests. Experimental size effect data sets are fit to each of the three size effect laws, resulting in three independent sets of fracture parameters for comparison. For the unnotched size effect data, the alternative statistical scaling law is also compared to the fracture mechanical scaling law for goodness of fit and self-consistency, and the fracture mechanical size effect is found to be the best explanation of the available data. Finally, the fracture parameters, hypotheses, and assumptions of the analysis are considered in aggregate to confirm the validity of the equivalent elastic crack approach.

5.1 Background

The framework of linear elastic fracture mechanics (LEFM) provides the foundation for much of the present analysis. The quasi-brittle fracture mechanical size effect laws of Bažant, which are derived and utilized in this chapter, are based in principle on determining the length of a brittle crack in a homogeneous elastic specimen which obeys LEFM and achieves some sort of far-field equivalence with the actual heterogeneous and nonlinear specimen (*Bažant*, 1984; *Bažant and Kazemi*, 1990a,b; *Bažant and Li*, 1996; *Bažant and Planas*, 1998; *Bažant*, 2005). First, I begin with a brief outline of the application of LEFM to the problem of a notched beam in bending. Then I discuss some physical reasons for which a specimen may deviate from the behaviour predicted by LEFM, followed by some data for snow that show such nonlinearity. Finally, I outline the basic approach to accounting for this nonlinearity using the concept of the equivalent elastic crack.

5.1.1 Linear elastic fracture mechanics (LEFM)

The general expression for the mode I stress intensity factor K_I for a crack loaded by a remote opening stress is

$$K_I = \sigma\sqrt{\pi a}\, f(a/D) \tag{5.1}$$

where σ is the applied stress, a is the crack length (or half length, depending on the geometry), and $f(a/D)$ is a dimensionless function of the specimen geometry that takes as an argument the ratio of the crack length to a representative length D (e.g. *Bažant and Planas*, 1998; *Cotterell and Mai*, 1996; *Hertzberg*, 1996). By defining the ratio $\alpha = a/D$ and, for convenience in analyzing the experimental data, a nominal stress measure σ_N as a function of an applied moment or load, Equation 5.1 can be rewritten as

$$K_I = \sigma_N \sqrt{\pi \alpha D}\, f(\alpha) = \sigma_N \sqrt{D} \sqrt{\pi \alpha}\, f(\alpha) \tag{5.2}$$

which shows the explicit size dependence of the fracture on the specimen size D (*Bažant and Planas*, 1998). For further convenience, the last two terms on the right hand side of Equation 5.2 can be lumped into a single dimensionless function $k(\alpha) = \sqrt{\pi\alpha} f(\alpha)$. Identifying the critical stress intensity factor (the fracture toughness) K_{Ic} as the value of K_I at the ultimate value of nominal stress σ_{Nu} (defined at peak load or ultimate bending moment), we have

$$K_{Ic} = \sigma_{Nu} \sqrt{D}\, k(\alpha). \tag{5.3}$$

Expressions of the function $k(\alpha)$, or, more commonly, $f(\alpha)$, are tabulated in handbooks for various standard test geometries (e.g. *Tada et al.*, 2000). For the notched beam bending tests considered in this study, the following form is adopted:

$$k_{S/D}(\alpha) = \frac{\sqrt{\alpha}}{(1+2\alpha)(1-\alpha)^{3/2}} p_{S/D}(\alpha) \tag{5.4}$$

where the subscript S/D indicates a value for a given beam span-to-depth ratio and $p_{S/D}(\alpha)$ is a polynomial for a given S/D (*Bažant and Planas*, 1998). Superposition of polynomials for standard or commonly tabulated values of S/D allows the value of $k_{S/D}(\alpha)$ to be computed for any arbitrary value of S/D. Established values of $p(\alpha)$ for $S/D = 4$ and $S/D = \infty$ (pure bending case) are used here (*Bažant and Planas*, 1998):

$$p_4(\alpha) = 1.900 - \alpha\left[-0.089 + 0.603(1-\alpha) - 0.441(1-\alpha)^2 + 1.223(1-\alpha)^3\right] \tag{5.5}$$

and

$$p_\infty(\alpha) = 1.989 - \alpha(1-\alpha)\left[0.448 - 0.458(1-\alpha) + 1.226(1-\alpha)^2\right]. \tag{5.6}$$

With these two expressions, the value of $p_{S/D}(\alpha)$ in Equation 5.4, valid for arbitrary span-to-depth ratios (*Bažant and Planas*, 1998), is

$$p_{S/D}(\alpha) = p_\infty(\alpha) + \frac{4}{S/D}\left[p_4(\alpha) - p_\infty(\alpha)\right]. \tag{5.7}$$

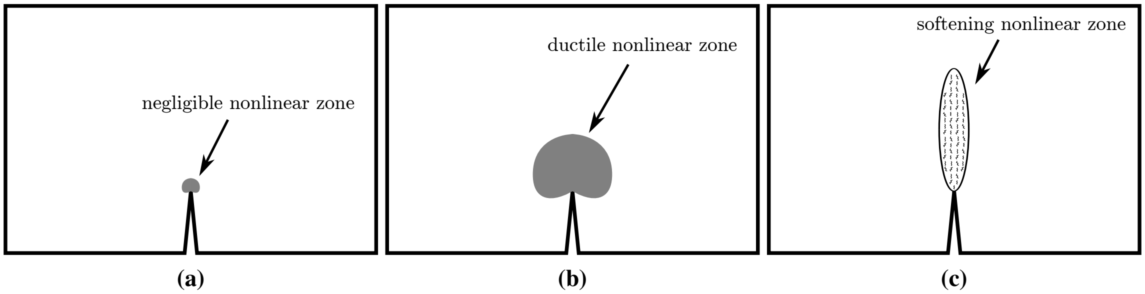

Figure 5.1: *Schematic of nonlinear crack tip zones for a fully brittle material (a), ductile material with a hardening nonlinear crack-tip zone (b) and quasi-brittle material with a softening fracture process zone (c). Adapted with modifications from Bažant and Planas (1998).*

Combining Equations 5.4 through 5.7 and substituting $k_{S/D}(\alpha)$ for $k(\alpha)$ in Equation 5.3 allows the calculation of the tensile fracture toughness for any beam size or geometry, provided the restrictions on the applicability of LEFM are justified.

5.1.2 Sources of deviation from LEFM

The applicability of LEFM requires two key criteria to be met. First, the size of any nonlinear elastic or inelastic zone surrounding the crack tip must be negligible relative to the specimen dimensions (Figure 5.1a). Second, the bulk behaviour of the material must be linear elastic. Violation of either of these criteria will lead to specimen response which deviates from predictions of LEFM.

There is typically some region of nonlinear behaviour in the vicinity of a crack tip (Figure 5.1). The relative size of this zone is partially a function of the structure or specimen size. A material that is fully brittle and obeys LEFM at one scale will be quasi-brittle and nonlinear if the specimen size is sufficiently reduced (*Bažant*, 2005).

The shape and size of the nonlinear zone surrounding the crack tip depends on the material properties and the specific micromechanisms of failure. Ductile or yielding materials such as metals have a crack tip surrounded by a zone of plastic yielding (Figure 5.1b). This plastic zone, characterized by work hardening as the material plastically yields and flows, serves to blunt the crack tip. The size of the plastic zone was estimated by Irwin as

$$R_c^{\text{ductile}} = \frac{1}{\pi}\left(\frac{K_{Ic}}{\sigma_y}\right)^2 \tag{5.8}$$

where σ_y is the yield stress of the material (Irwin (1958), in *Bažant and Planas*, 1998). The field of elasto-plastic fracture mechanics deals with materials that have large ductile or plastic zones associated with fractures.

Heterogeneous and strain-softening materials do not plastically yield or harden in the vicinity of a crack tip. For these materials, the nonlinear zone is a region of damage and softening (Figure 5.1c). Softening is the result of microcracking, frictional slip between grains, or void formation (*Bažant and Planas*, 1998). The zone of softening damage is labeled the Fracture Process Zone (FPZ). Materials with a relatively large nonlinear zone of softening damage are considered quasi-brittle.

The distinction between the two types of nonlinear zones in Figures 5.1b and 5.1c is important. The size of the FPZ in a quasi-brittle material is as much as an order of magnitude larger than predicted by Equation 5.8 for a ductile material for the same global strength and fracture toughness (*Bažant and Planas*, 1998). Therefore elasto-plastic expressions for the minimum specimen size allowable for validity of LEFM are inapplicable for a quasi-brittle material. *Bažant and Planas* (1998) suggest a generalized form of Irwin's relation (Equation 5.8) for the estimate of the process zone size for a quasi-brittle material:

$$R_c^{\text{quasibrittle}} = \gamma \left(\frac{K_{Ic}}{f_t} \right)^2 \tag{5.9}$$

where the tensile strength f_t has been substituted in place of the yield strength σ_y and γ is a constant which has a lower bound of $1/\pi$ (Irwin's estimate). *Bažant and Planas* (1998) suggest a value of γ in the range of 2–5 for concrete, and *Sigrist* (2006) used $\gamma = 9\pi/32$ for snow. These bounds indicate that the FPZ in concrete is up to 15 times larger than the estimate from elasto-plastic fracture mechanics, and for snow the FPZ may be about 3 times larger than the Irwin estimate.

Commonly cited standards suggest that, for LEFM to be applicable, no length scale in the specimen or structure, measured from the tip of the crack, should be smaller than about $8R_c$ (e.g. *ASTM E399 - 05*, 2005). Violation of this restriction will lead to a nonlinear specimen response, which may take the form of a deviation from linearity prior to reaching the peak load in an experiment or a broad-shaped load-displacement peak rather than a sharp peak as in a fully brittle experiment.

The presence of significant viscous effects during an experiment violates the second criterion for validity of LEFM. Viscous energy dissipation reduces the amount of elastically-recoverable strain energy available for crack formation. For snow, energy dissipation associated with viscous effects elevates the strength of the snow and the amount of energy input necessary to cause fracture (*Brown and Lang*, 1975). If experiments have significant viscous effects, an additional time-dependent material length scale associated with relaxation will be present in addition to any length scale associated with a nonlinear zone ahead of the crack tip (*Bažant and Planas*, 1998). If either of the two LEFM criteria here are violated, the nominal strength will not scale with specimen size following the LEFM power law scaling exponent of $-1/2$.

5.1.3 Experimental evidence of deviation from LEFM in snow

From Equation 5.3 it can be seen that the nominal strength in LEFM scales with specimen size D as

$$\sigma_{Nu} \propto D^{-1/2}, \tag{5.10}$$

where "size" is taken here as the characteristic length of the fracture specimen. In beam bending fracture tests, the characteristic length is the beam depth. If geometrically similar notched or pre-cracked samples of the same material, and thus same fracture toughness and geometric function $k(\alpha)$, are fractured, the scaling exponent of nominal strength versus specimen size should be equal to $-1/2$ if the material and testing conditions conform to LEFM. If the experimental data have a power law scaling exponent different from $-1/2$, this is evidence of a deviation from LEFM which may be caused by a large fracture process zone.

The first experimental evidence that tensile fractures in snow did not scale according to LEFM was shown by *Sigrist et al.* (2005a,b); *Sigrist* (2006). Size effect test series were conducted using deep beams of cohesive snow extracted from the natural snow cover, stored in a cold lab for up to 2 days, and fractured in edge notched three point bending. In all test series, the nominal strength had a weaker scaling with size than predicted by Equation 5.10, which was explained by the presence of a large FPZ (*Sigrist*, 2006).

This deviation from LEFM was confirmed in the present study. Figure 5.2 shows the results of five size effect test series represented on a log-log plot of nominal strength versus beam depth. In each series, geometrically-scaled beams of depth $D = 5$ cm, 10 cm and 20 cm were extracted from the same homogeneous snow layer, notched, and tested in either three-point or four-point bending. The nominal strength for each test was calculated from the peak load using beam theory (see Section 4.2.1). As the figure shows, in only one case does the test data appear to conform to the LEFM power-law exponent of $-1/2$. However, as will be seen later, this apparent agreement is actually due to viscous effects, for this test series used a much lower

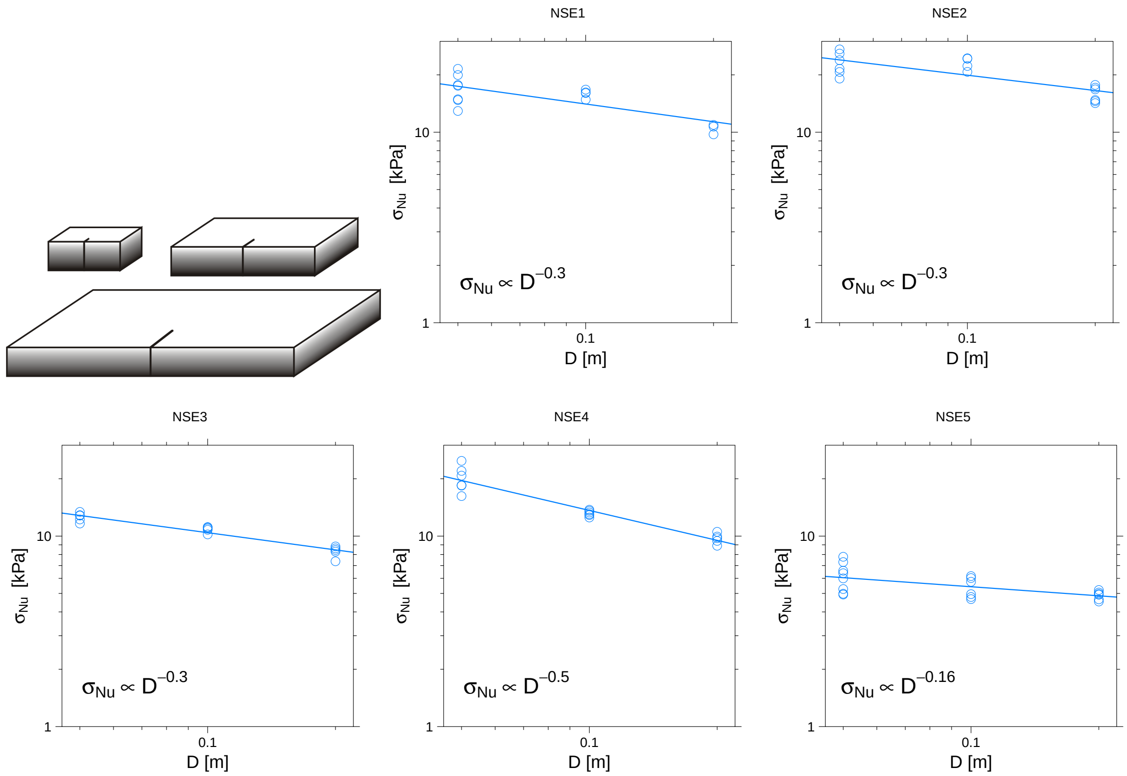

Figure 5.2: *Scaling of nominal strength with specimen size from results of five series of notched, geometrically similar beams tested in weight-compensated bending. The test series NSE1-NSE5 will be discussed further in Section 5.2.*

crosshead speed than all other test series. For the typical quasi-elastic loading rates, the size effect is weaker than predicted by LEFM. The data in Figure 5.2 will be discussed in further detail in Section 5.2.

Further evidence of deviation from LEFM behavior, in the absence of tests conducted at different sample sizes, is in the load-displacement response of a fracture experiment. Any significant deviation from linearity in the loading curve prior to peak load is evidence of a significant deviation from LEFM. The more broadly-shaped the load-displacement curve near peak load, the greater the deviation from LEFM behaviour (*Cotterell and Mai*, 1996; *Bažant and Planas*, 1998). These nonlinear load-displacement features are interpreted as arising from a non-negligible zone of softening damage ahead of the notch or crack tip.

Characteristic load-displacement curves for snow tested at different rates are shown in Figure 5.3. All show apparent strain softening, though the nature of the softening curve depends on the loading rate. The curve in Figure 5.3a came from a test using the slowest rate of loading in the present study, which led to a nominal tensile strain rate on the order of 10^{-3} s^{-1}, just above the creep-to-fracture transition. The stair-step nature of the softening curve for this test was observed for all tests at the same rate in this test series, and was also observed for other snow types at the same loading rate. This pattern indicates that the tensile fracture proceeded in jumps which may have been influenced by viscous relaxation surrounding the crack front. Even if viscous effects are accounted for using an elastic-viscoelastic correspondence, this type of softening curve is incompatible with a brittle (LEFM) interpretation of the fracture propagation from the notch tip.

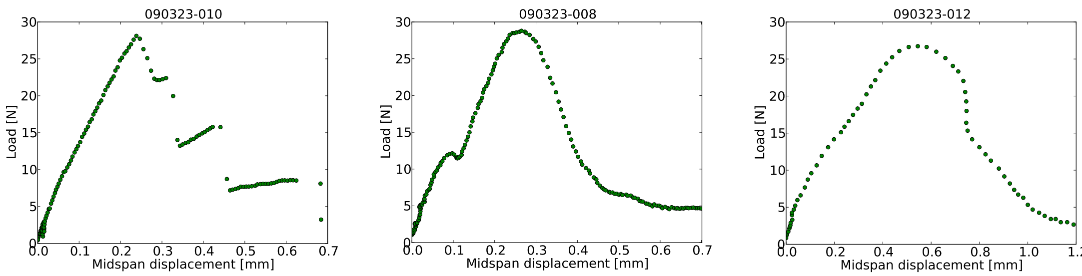

(a) *slow* **(b)** *medium* **(c)** *fast*

Figure 5.3: *Load-midspan displacement curves from notched bending tests at three different rates. Crosshead speeds were 0.0125 cm/s for (a), 0.125 cm/s for (b) and 1.25 cm/s for (c), corresponding to nominal tensile strain rates in the outer fiber of the beam on the order of* 10^{-3} s^{-1}, 10^{-2} s^{-1}, *and* 10^{-1} s^{-1}, *respectively. All tests were conducted in weight-compensated three point bending with a span to depth ratio of 2.5, beam depth D = 10 cm, and notch depth 3 cm. Snow density was in the range 336–338 kg/m*^{3} *for the three tests, blade hardness index was in the range 8–10 N, hand hardness index 4, mean snow temperature at time of testing was* $-5°C$, *grains were rounded forms of size 1 mm.*

The intermediate loading rate for the curve in Figure 5.3b is closest to the crosshead speed used by *Sigrist* (2006). At this rate of loading, it was common to observe a saw-tooth shape to the loading curve. In Figure 5.3b only one decrease in load was measured prior to peak load, but often as many as five or more such features were observed prior to reaching the peak. The loading curve near peak load was more broadly shaped in tests conducted at this rate of loading than for the slowest tests (Figure 5.3a), and the strain softening following peak load occurred more gradually. The broad shape of the peak and the strain softening following peak load are also inconsistent with LEFM.

The most common and fastest rate of loading in the present study is represented by the curve in Figure 5.3c. The loading curve appears nonlinear, the shape of the curve near peak load is very broad, and strain softening following peak load is also apparent. Though the nature of these curve features varied with different types of snow, the qualitative features were largely consistent in the present study for similar tests conducted at the same loading rate. Softer and less dense snow was often much more nonlinear than the hard, strong snow represented in Figure 5.3c. Compared to the slow tests represented in Figure 5.3a, the common fast test speed led to strain rates that are assumed to be mostly elastic, though the failure does not appear brittle.

The effect of notch depth on the load-displacement response in bending tests is shown in Figure 5.4. The snow in this test series was lower density and softer than that in Figure 5.3. The loading curve of the unnotched test was highly nonlinear (Figure 5.4a) and was characterized by one drop in load prior to reaching the peak. The region of dense data points just prior to peak load is indicative of crushing of the snow sample in the vicinity of the support plates. After a period of crushing and gradual increase in load, the sample finally fractures in tension with apparent strain softening following peak load (*apparent* because the stability loss at peak load was coincident with a rebound of the load cell and rocker supports, which obscures the true form of the post-peak displacement of the sample). A similar influence of snow crushing on the load-displacement curves for unnotched tests was observed for other types of snow with low density and low hardness. Only for very strong and stiff snow was crushing minimal—often undetectable—for unnotched tests.

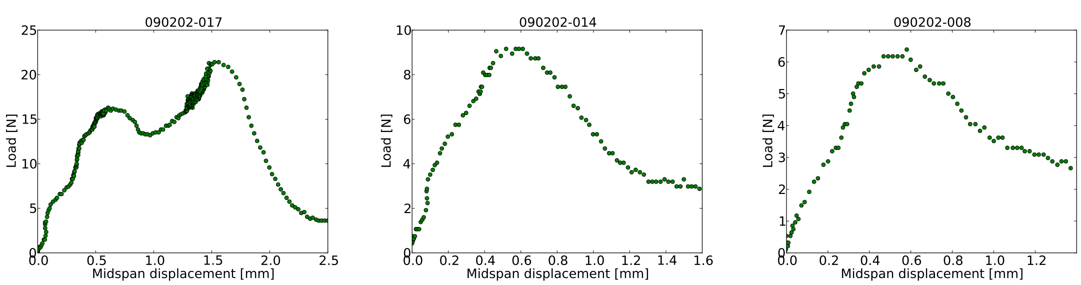

(a) *unnotched* **(b)** *3 cm notch* **(c)** *5 cm notch*

Figure 5.4: *Load-midspan displacement curves from bending tests with different initial notch depths. All tests were conducted in weight compensated three point bending with a span to depth ratio of 2.5, beam depth D = 10 cm, loading rate 1.25 cm/s. Snow density was 227 $\pm$ 2 kg/m^3, mean blade hardness index was 2 N, hand hardness index 3, mean snow temperature at time of testing was $-6^\circ C$, snow was composed of faceted crystals of size 0.5–1 mm.*

For notched tests from the same series (Figures 5.4b and 5.4c), the loading curves are closer to linear. However, the peak load for both tests is broadly shaped and followed by strain softening. For this series of tests, the break detect signal for stopping the testing machine crosshead was set at 3 N following to peak load, so the full softening curve was not measured. However, the features of all three curves in Figure 5.4 show details which cannot be explained using LEFM.

The examples shown in Figures 5.3 and 5.4 are just a few of hundreds of examples of results that deviate from linear and brittle fracture behaviour. Clearly a general and consistent homogenization scheme is necessary to analyze the data using the same linear continuum framework, and a single scheme cannot be expected to have general applicability for all types of snow. However, the equivalent elastic crack homogenization scheme, outlined below, is able to approximate the nonlinear behaviour seen here with generally good agreement.

5.1.4 Nonlinear correction using equivalent elastic crack

The concept of the equivalent elastic crack as a homogenization scheme involves replacing the actual crack in the heterogeneous or discontinuous material with an equivalent elastic crack that achieves some sort of far-field equivalence between the actual and equivalent specimen. This type of approach tacitly limits the domain of interest to the far-field (or global) response of the specimen rather than to the micromechanical details within the fracture process zone. In other words, this approach is not designed to determine the actual physical size or details of the fracture process zone itself, instead treating the process zone as a sort of "black box" (*Mindess*, 1991). If the desire was to investigate the physical mechanisms governing the physics of the process zone, a number of direct or indirect methods of probing the nature of the FPZ would be available (*Cotterell and Mai*, 1996). However, the advantage of the equivalent elastic crack approach is the ability to calculate fracture parameters using only the peak loads from experiments (*Bažant and Planas*, 1998). It then remains to relate the equivalent elastic crack length to the actual physical length of the fully-developed fracture process zone.

For snow, a material that is highly porous and heterogeneous (Figure 5.5a), the equivalent crack approach can be conceptualized as a homogenization scheme that allows the use of continuum mechanics. The location of the tip of the equivalent crack relative to the actual notch in the highly porous matrix of snow grains is defined by

$$a_e = a_\circ + \Delta a_e \tag{5.11}$$

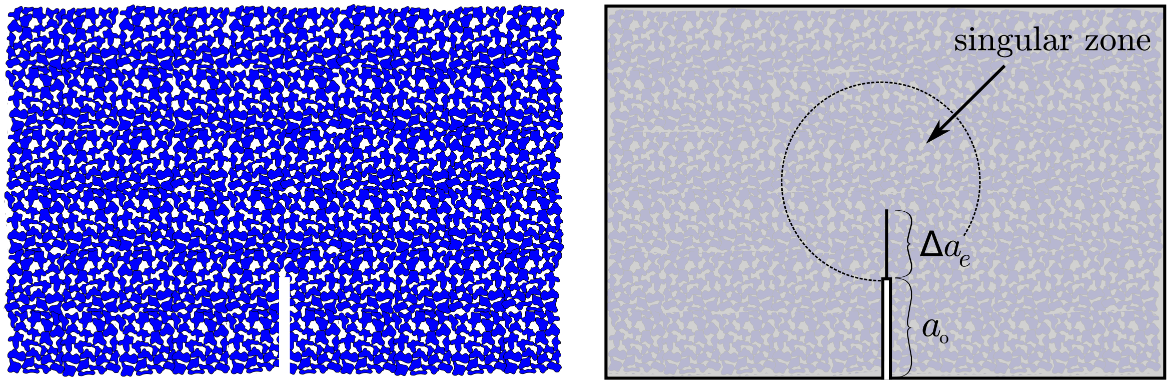

(a) **(b)**

Figure 5.5: *Conceptualization of heterogeneous structure of a notched snow sample (a) and homogenization using equivalent elastic crack concept (b). The actual notched snow sample is approximated as a linear elastic continuum with a sharp crack tip placed a distance Δa_e ahead of the notch. This distance is determined such that the actual and equivalent specimen have equivalence of fields such as stress and displacement outside the singular zone.*

where a_e is the equivalent crack length for a given load level, $a_\circ$ is the original crack or notch length, and Δa_e is the equivalent crack extension (Figure 5.5b). The key to this approach is the determination of the appropriate value of Δa_e in order to achieve the desired or appropriate equivalence between the actual and equivalent specimen. This equivalence is sought outside the singular zone, or the zone in which the first term in the series expansion of stress around the crack tip dominates, i.e. the field defined by the dominance of $\sigma_{ij} \propto K_I r^{-1/2}$, where σ_{ij} is the stress tensor, K_I is the stress intensity factor and r is the distance from the crack tip in curvilinear coordinates.

The length scale Δa_e may have a dependence on specimen size for small scales, but should approach a constant value for sufficiently large specimens. The value of Δa_e also, in general, depends on the load level in the material. The analysis in this chapter will focus on methods that utilize the critical (peak load) condition only. Since Δa_e can in general have a load level dependence and specimen size dependence, the equivalent crack extension c_f is defined as

$$c_f = \lim_{D \to \infty} \Delta a_{ec} \tag{5.12}$$

where Δa_{ec} is the critical crack extension at peak load (*Bažant and Planas*, 1998). The length scale c_f is assumed to be a material property because any dependence on geometry disappears in the limit to infinite specimen size.

The relationship between "apparent" fracture toughness measured in an individual experiment, which may have specimen size or geometry dependence, and true fracture toughness as a material property can be expressed using Equations 5.3, 5.11, and 5.12. First, we can define the apparent fracture toughness as

$$K_{INu} = \sigma_{Nu}\sqrt{D}k\left(\alpha_{\circ}\right) \tag{5.13}$$

and the true fracture toughness, using the equivalent elastic crack in place of the actual crack or notch, as

$$K_{Ic} = \sigma_{Nu}\sqrt{D}k\left(\alpha_{ec}\right), \tag{5.14}$$

following *Bažant and Planas* (1998). Combining these two equations leads to

$$K_{INu} = K_{Ic}\frac{k\left(\alpha_{\circ}\right)}{k\left(\alpha_{ec}\right)}. \tag{5.15}$$

Now, the equivalent crack concept as outlined here only applies in the limit $c_f << D$, for otherwise far-field equivalence could not be achieved—the singular zone would take up most or all of the specimen—and higher-order nonlinear fracture mechanics methods would be needed. If c_f is small relative to the specimen dimensions, then we can approximate $\Delta a_{ec} \approx c_f$ and write, for the equivalent crack length,

$$\alpha_{ec} = \alpha_{\circ} + \frac{\Delta a_{ec}}{D} \approx \alpha_{\circ} + \frac{c_f}{D}. \tag{5.16}$$

Using this expression in Equation 5.15, expanding $k(\alpha_{ec})$ in a Taylor series about c_f/D and taking a further series expansion of the result about $c_f/D = 0$, we come to

$$K_{INu} = K_{Ic}\left[1 - \frac{k'\left(\alpha_{\circ}\right)}{k\left(\alpha_{\circ}\right)}\frac{c_f}{D}\right] \tag{5.17}$$

as $c_f/D \to 0$, with error on the order of $(c_f/D)^2$ (*Bažant and Planas*, 1998). The measured apparent fracture toughness approaches the true fracture toughness for $D >> c_f$.

Determining the material parameters K_{Ic} and c_f now follows from experimental data on the size effect on nominal strength. Bažant's famous size effect law can be derived by first solving Equation 5.14 for the nominal strength,

$$\sigma_{Nu} = \frac{K_{Ic}}{\sqrt{D}k(\alpha_{ec})} = \frac{K_{Ic}}{\sqrt{Dk^2(\alpha_{ec})}} = \frac{K_{Ic}}{\sqrt{Dk^2(\alpha_\circ + c_f/D)}}. \tag{5.18}$$

Expanding the term $k^2(\alpha_\circ + c_f/D)$ in a Taylor series about $\alpha_\circ$ and truncating it after the second term,

$$k^2(\alpha_\circ + c_f/D) \approx k^2(\alpha_\circ) + 2k(\alpha_\circ)k'(\alpha_\circ)\frac{c_f}{D} \tag{5.19}$$

and adopting the notation $k_\circ = k(\alpha_\circ)$ and $k'_\circ = k'(\alpha_\circ)$, Equation 5.18 can be rewritten as

$$\sigma_{Nu} = \frac{K_{Ic}}{\sqrt{D(k_\circ^2 + 2k_\circ k'_\circ c_f/D)}} = \frac{K_{Ic}}{\sqrt{k_\circ^2 D + 2k_\circ k'_\circ c_f}}. \tag{5.20}$$

Equation 5.20 is now a two-parameter relation that can be used to determine the fracture parameters K_{Ic} and c_f given experimental data for the nominal strength σ_{Nu} at different sizes D. The effects of specimen geometry are accounted for in the dimensionless functions $k_\circ$ and $k'_\circ$.

Equation 5.20 can also be expressed in the form

$$\sigma_{Nu} = \frac{\mathtt{B} f_t}{\sqrt{1 + D/D_\circ}} \tag{5.21}$$

if we define

$$\mathtt{B} f_t = \frac{K_{Ic}}{\sqrt{2k_\circ k'_\circ c_f}} \tag{5.22}$$

and

$$D_\circ = \frac{2k'_\circ}{k_\circ} c_f, \tag{5.23}$$

following again (*Bažant and Planas*, 1998). The parameter $\mathtt{B}$ is a geometric parameter, f_t is the tensile strength, and $D_\circ$ is known at the "transitional size" which determines the intersection of the horizontal asymptote for $D \to 0$ with the LEFM asymptote for $D \to \infty$ in the size effect law. Using the transitional size, Bažant's brittleness number β is defined as

$$\beta = \frac{D}{D_\circ}. \tag{5.24}$$

For β less than about 0.1, plastic limit analysis applies for the determination of the nominal strength.

For $\beta > 10$, the relative error between the size effect law (Equation 5.21) and LEFM is less than 5%. For intermediate sizes in the range $0.1 < \beta < 10$, nonlinear fracture mechanics is required (*Bažant and Planas*, 1998). The nonlinearity is accounted for here using an equivalent elastic crack expressed using the parameter c_f.

The only application of this type of size effect analysis using experimental data for snow was by *Sigrist* (2006). A mean value of $D_\circ$ was determined by linear regression of Equation 5.21 through the data from four notched size effect test series. A mean value of $D_\circ \approx 30$ cm was reported, which, for the beam depths in the experiments (D = 8, 13, 20 and 32 cm) leads to brittleness numbers of $\beta \approx 0.25 - 1$.

Sigrist (2006) used the derived mean value of $D_\circ$ to rewrite Equation 5.17 in the form

$$K_{Ic} = \sqrt{1 + \frac{D_\circ}{D}} K_{INu}. \tag{5.25}$$

This relation, using the mean value of $D_\circ$ as a constant for all types of snow, was used to correct apparent fracture toughness data from individual notched three point bending tests over an entire data set, consisting of tests mostly at a single specimen size. This led to the relation for the density-dependence of the fracture toughness,

$$K_{Ic} = (7 \pm 7) \times 10^{-6} \rho^{2.3 \pm 0.2} \qquad [\text{kPa m}^{1/2}], \tag{5.26}$$

though the goodness of fit of the regression was poor owing to the high degree of scatter in the data.

Background summary

Recently it has become clear that the tensile fracture of snow does not conform to the predictions of Linear Elastic Fracture Mechanics. This is mostly due to the highly porous and heterogeneous nature of snow and in part due to viscous effects since snow exists so close to its absolute melting temperature. However, LEFM is a convenient and well-developed theoretical framework for analysis. The approximate correction for nonlinear behavior using the concept of the equivalent elastic crack is therefore a popular and appropriate approach for a first-order approximation for nonlinear quasi-brittle fracture behaviour. Indeed, equivalent elastic fracture mechanics is the bedrock on which much of Bažant's quasi-brittle fracture mechanics rests.

Using this framework, the bulk of the remainder of this chapter is devoted to experimental determination of fracture parameters such as c_f and K_{Ic} from experimental data.

5.2 Notched Size Effect Method

Bažant's notched size effect law, expressed in the form of either Equation 5.20 or 5.21, is relatively straightforward to fit to experimental data. All that is required are the peak loads from tests on geometrically similar notched bending specimens over a size range of about 1:4 or greater (*Bažant and Planas*, 1998). Fitting the size effect law through the data leads to two of the following parameters: K_{Ic} or G_c and c_f or $D_\circ$. Except for $D_\circ$, these parameters are defined as material properties, independent of size and shape, for an infinitely sized specimen ($D_\circ$ has a geometry dependence). The term "infinite" is probably a bit misleading, as Bažant defines this to mean only an order of magnitude larger than the lab-scale specimen dimensions over which the size effect law was fit (*Bažant and Kazemi*, 1990b). This definition implies that fracture parameters calculated from size effect tests on snow specimens over a size range of around 5–20 cm would be applicable as material properties, independent of geometry and size, for snow slabs of around one meter in depth or more, assuming similar homogeneous slab properties. The majority of slab avalanches have a slab depth of less than 1 m (*Perla*, 1977; *McClung and Schaerer*, 2006), so some size and geometry dependence may need to be considered in applying fracture parameters derived from lab-scale size effect tests to thinner snow slabs.

Sigrist (2006) was the first to carry out notched size effect tests on natural samples of dry snow slabs. Four test series were conducted, and for each the transitional size $D_\circ$ was calculated. However, Sigrist stopped short of calculating the fracture toughness from the size effect tests, instead using a mean value of $D_\circ$ to correct apparent fracture toughness values across an entire data set of notched tests, most of which were conducted at one specimen size, using Equation 5.25.

This section contains the results of five new series of notched size effect tests. Additionally, a re-analysis of data from three of the series reported by *Sigrist* (2006) was conducted (inconsistencies in the reporting of data prevented the unambiguous determination of the details of a fourth series). The result is a collection of values of K_{Ic}, c_f and $D_\circ$ expressed as functions of density and loading rate.

5.2.1 Methods

The fracture parameters K_{Ic} and c_f were determined by nonlinear least-squares regression of the following form of the size effect law:

$$y = \ln\left(\frac{M}{\sqrt{N + e^{x}}}\right) \tag{5.27}$$

where x = ln D and y = ln σ_{Nu} (*Bažant and Planas*, 1998). Nonlinear regression is considered better for determining the size effect law parameters than linear regression through a log-log transform of the size effect law (*Bažant and Planas*, 1998). This is in part due to the requirement of assuming multiplicative rather than additive model errors when taking a log-transform a-priori. Given values of M and N from the regression, the fracture toughness was calculated as $K_{Ic} = k_{\circ}M$ and the effective fracture process zone length as $c_f = Nk_{\circ}/(2k'_{\circ})$. The geometric functions $k_{\circ}$ and $k'_{\circ}$ were calculated for each test geometry, given the span-to-depth ratio and initial notch depth, using the superposition method outlined above in Equations 5.4 through 5.7.

The regressions were performed using the `nls` function in the statistical software *R*. Starting estimates for the parameters M and N were supplied by a linear regression through a log-log linearized form of Equation 5.20. The standard errors of the regression constants M and N were calculated using sandwich estimators (*Ritz and Streibig*, 2008) since the variance structure of model residuals did not all follow the assumptions of normality and independence (see the discussion of standard assumptions in least-squares regression in Appendix B). The uncertainties in K_{Ic} and c_f were then calculated using the estimated standard errors of M and N by summation in quadrature.

For one test series (NSE4), the nonlinear regression did not converge. For this series, a linearized form of Equation 5.20 was solved using linear least squares (linear regression type I, p. 141, *Bažant and Planas*, 1998).

5.2.2 Results

Five series of notched size effect tests were conducted during the first two winters of field research. The description of each series is in Table 5.1. Schematics of each test series are shown in Figure 5.6. The notched size effect data reported by *Sigrist* (2006) are also listed for comparison. Sigrist's tests had shorter relative notch depths (α = 0.1) than used in the present study (α = 0.3). No description of the method of sample notching was given by *Sigrist* (2006), and no estimate of the uncertainty in the notch depth was given. It is known that three point bending tests are very sensitive to the notch depth for $\alpha = 0.1$ (*Bažant and Kazemi*, 1990b), a fact that may explain some of the large scatter in Sigrist's data.

Code	Date	n	$\bar{\rho}$ [kg/m^3]	R	$\bar{B}$ [N]	$\bar{T}$ [°C]	F, E [mm][1]	V [cm/s]	D [cm]	S/D	α	Type
NSE1	070306	14	305 ± 3	3*	N/A[2]	-9.9 ± 1.5	RG, 0.5 / FCxr, 0.5-1	0.5	5, 10, 20	2	0.3	3PB
NSE2	070308	16	385 ± 3	N/A[3]	N/A[2]	-6.5 ± 1.0	RG, 0.5 / FCxr, 0.5	0.5	5, 10, 20	2	0.3	3PB
NSE3	080131	15	346 ± 2	4.3*	8.8 ± 0.7	-8.9 ± 0.3	FCxr, 0.5-1	1.25	5, 10, 20	3	0.3	4PB
NSE4	080316	17	261 ± 2	4*	7.5 ± 1.2	-4.8 ± 0.7	RG, 0.5	0.05	5, 10, 20	1.5	0.3	3PB
NSE5	080330	20	229 ± 3	3.3*	3.4 ± 0.9	-5.4 ± 0.4	RG, 1	1.25	5, 10, 20	1.5	0.3	3PB
E[4]		17	186 ± 12	1.5**	N/A	-14.5***	DF / RG, 0.5-1	0.33	8, 13, 20, 32	2	0.1	3PB
H[4]		22	239 ± 9	2**	N/A	-9.5***	RG / DF, 0.5-1	0.33	8, 13, 20, 32	2	0.1	3PB
I[4]		22	256 ± 19	2.5**	N/A	-9.1***	RG / DF, 0.5-1	0.33	8, 13, 20, 32	2	0.1	3PB

Table 5.1: *Notched size effect data. Date is in* yymmdd *format, other column variables include the number of tests (n), mean snow density ($\bar{\rho}$), hand hardness index (R), mean blade hardness index ($\bar{B}$), mean snow temperature ($\bar{T}$), grain forms and grain size (F and E, respectively), crosshead speed (V), beam depth (D), beam span-to-depth ratio (S/D), and relative notch depth (α). All uncertainties are standard deviations from the mean.*

[1] *Following the International Classification for Seasonal Snow on the Ground (Fierz et al., 2009). Key: FCxr = mixed rounded and faceted crystals; RG = rounded grains; DF = decomposing and fragmented crystals.*

[2] *Blade hardness gauge not in use yet.*

[3] *Field notes containing hand hardness lost for this data series.*

[4] *Data reported by Sigrist (2006) from similar notched size effect tests.*

* *Hand hardness index values following 15 N force standard in Fierz et al. (2009), with "+" and "-" qualifiers expressed using deviations of 0.3 from the integer index values.*

** *Index values following 50 N force standard of Colbeck et al. (1990). These index values may need to be increased one or more levels for comparison with the index values from the present study.*

*** *No information given on temperature measurements, may have been the lab air temperature.*

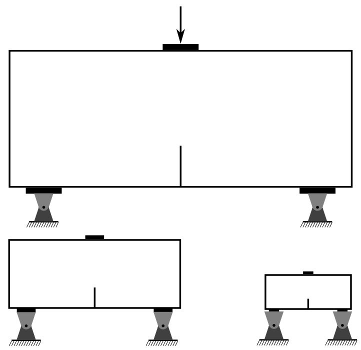

(a) *NSE1, NSE2*

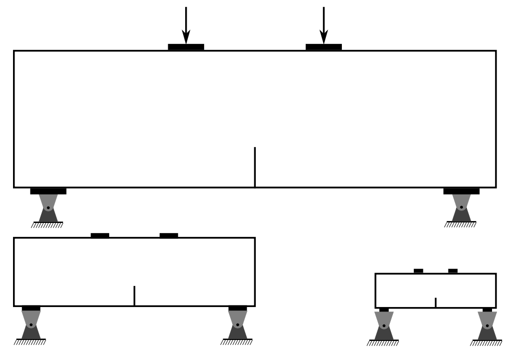

(b) *NSE3*

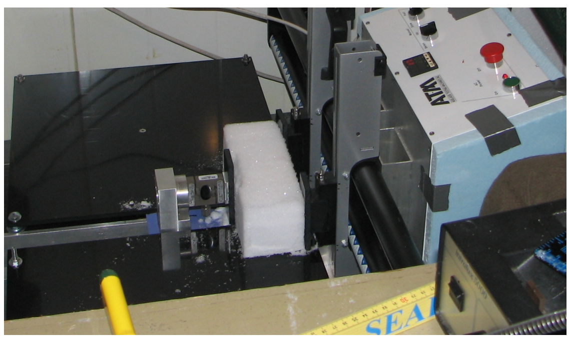

(c) *Horizontal weight compensation*

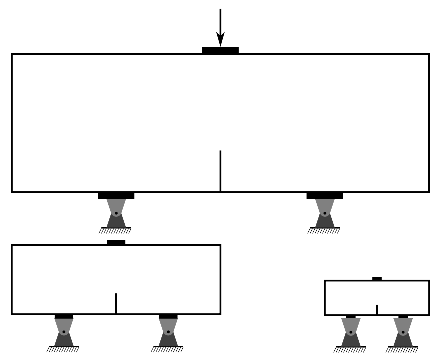

(d) *NSE4, NSE5*

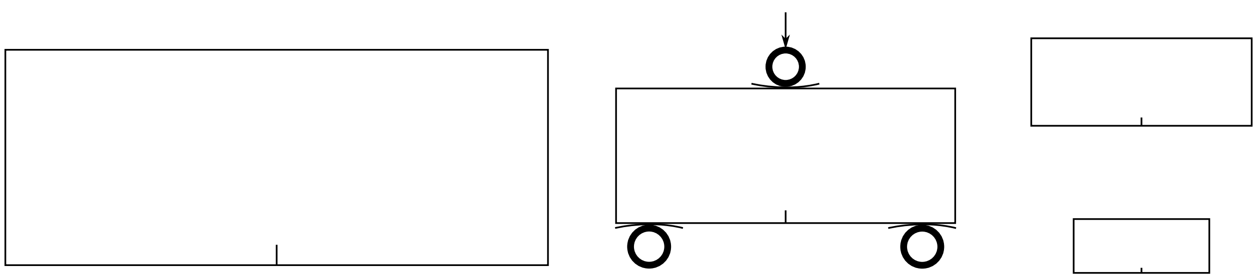

(e) *Sigrist (2006) Series E, H, I*

Figure 5.6: *Schematics of notched size effect test series, all relatively scaled. Codes NSE1-NSE5 reference the data in Table 5.1. All tests in the present study were weight compensated, which was achieved for series NSE1, NSE2, and NSE3 by orienting the testing machine horizontally and supporting the samples on a smooth table (c). Series NSE4 and NSE5 (d) were conducted with the testing machine oriented vertically. Weight compensation was achieved by moving the supports in to the quarter points of the beam to cancel the bending moment due to gravity in the central cross section. The tests of Sigrist (2006) (e) were not weight compensated. Sigrist did not report whether the cylindrical supports were allowed to roll or were fixed. Thin aluminum plates were placed between the cylinders and the snow sample, and there is evidence of flexing of the top plate (as drawn)in a time sequence of images during one test (p. 72, Sigrist, 2006).*

Regression fits to the size effect law

Table 5.2 contains the fracture parameters calculated by fitting the size effect law through each data series. The fracture toughness values have less scatter than either c_f or $D_\circ$, indicating that these length scales are more sensitive to the data scatter. This feature has been observed in fitting the size effect law to other materials (e.g. *Bažant and Kazemi*, 1990b). In general, the goodness of fits, represented by the nonlinear R^2, was better for the data from the present study than Sigrist's data (see Appendix B for the definition of R^2 and comparison with the standard coefficient of determination r^2 in linear least squares regression). Each regression model had normally distributed residuals as measured by the Shapiro-Wilk test of normality (p-value > 0.05 for each regression). In all but two test series (E and I), the runs test indicated independence of model residuals at the $\alpha = 0.05$ level. All but series NSE4 had brittleness numbers that fell within the transitional range (between approximately 0.1 and 10) for which quasi-brittle fracture mechanics is applicable (and LEFM is not).

Test series	K_{Ic} [kPa m$^{1/2}$]	c_f [cm]	$D_\circ$ [cm]	β	R^2
NSE1	5.5 ± 0.6	1.2 ± 0.7	6 ± 3	0.8-3	0.61
NSE2	8.5 ± 0.8	1.7 ± 0.7	9 ± 3	0.6-2	0.66
NSE3	4.6 ± 0.2	1.3 ± 0.3	6.6 ± 1.5	0.8-3	0.92
NSE4	4.0 ± 0.1	0.05 ± 0.05	0.3 ± 0.8	20-70	0.31[1]
NSE5	2.9 ± 0.4	4.3 ± 1.8	22 ± 9	0.2-0.9	0.34
E	1.7 ± 0.2	2.1 ± 1.2	19 ± 11	0.4-2	0.40 (0.34)[2]
H	2.3 ± 0.3	2.3 ± 0.9	21 ± 8	0.4-1.5	0.37 (0.39)[2]
I	3.1 ± 0.5	4.0 ± 1.9	37 ± 18	0.2-0.9	0.20 (0.18)[2]

Table 5.2: *Fracture parameters determined by fitting the size effect law of Equation 5.20 to the data series described in Table 5.1. The range reported for the brittleness number β corresponds to the range in specimen sizes D used in the experiments. R^2 values for the nonlinear regression are calculated relative to the mean function in the limit of $D \to 0$, see Appendix B.*
[1]*Adjusted r^2 from a linear regression through a log-log linearized form of Equation 5.20.*
[2]*Values in parenthesis are coefficient of determination (r^2) values for the linear regressions reported by Sigrist (2006).*

The data from the present study fit to the notched size effect law of Equation 5.21 is represented in Figure 5.7. The data series NSE4 stands out as particularly brittle, with the data clearly falling on the LEFM asymptote for large brittleness number ($\beta > 10$). The remainder of the data sets fall within the range of brittleness numbers for which the nonlinear size effect law is necessary, i.e. $0.1 < \beta < 10$. Aside from the scatter inherent in tests using natural snow, each series appears visually to fit the size effect law well.

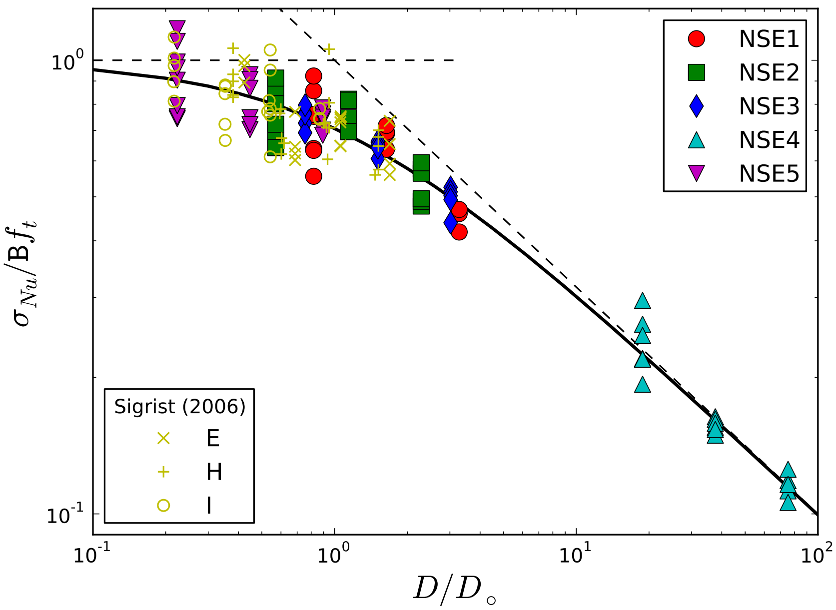

Figure 5.7: *Notched size effect test series fit to Bažant's size effect law (Equation 5.21), including data published by Sigrist (2006) and re-analyzed here.*

The data from *Sigrist* (2006) are included in Figure 5.7, and these data also fall within the transitional range of brittleness numbers. However, scatter in the data is greater and the visual quality of the fit to the size effect curve is poorer, which follows from the lower values of R^2 for the regression models for Sigrist's data (Table 5.2).

Rate effects associated with different crosshead speeds largely explain the variability in the brittleness numbers. The crosshead speeds for all but one test series (NSE4) were within a factor of four of each other (0.33–1.25 cm s^{-1}). Series NSE4, however, was conducted at a speed an order of magnitude slower than the rest of the data (0.05 cm s^{-1}). The rate effect is stark, as Figure 5.8 shows. The slower crosshead speed made the tests appear much more brittle. This is likely due to the enhanced viscous effects at the slower test speed. Viscous relaxation in the bulk of the sample during the slow loading likely led to a reduced zone of stress concentration surrounding the notch tip. This would explain the very low value of c_f for series NSE4 (Table 5.2). This result is consistent with rate dependence of concrete, which also appears more brittle (higher β and lower c_f) in size effect tests conducted at slower-than-usual loading rates (*Bažant and Gettu*, 1992). The time to failure of the experiments in series NSE4 was on the order of several seconds, which is still about two orders of magnitude below the relaxation time for snow in tension (*Shinojima*, 1966). If the creep strains are small at failure relative to the instantaneous elastic strain–which should be the case for series NSE4, even though viscous effects are certainly present–an analysis of the data using an effective elastic framework should be acceptable, provided that an appropriate secant modulus or creep compliance is used in place of the elastic modulus (*Bažant and Gettu*, 1992).

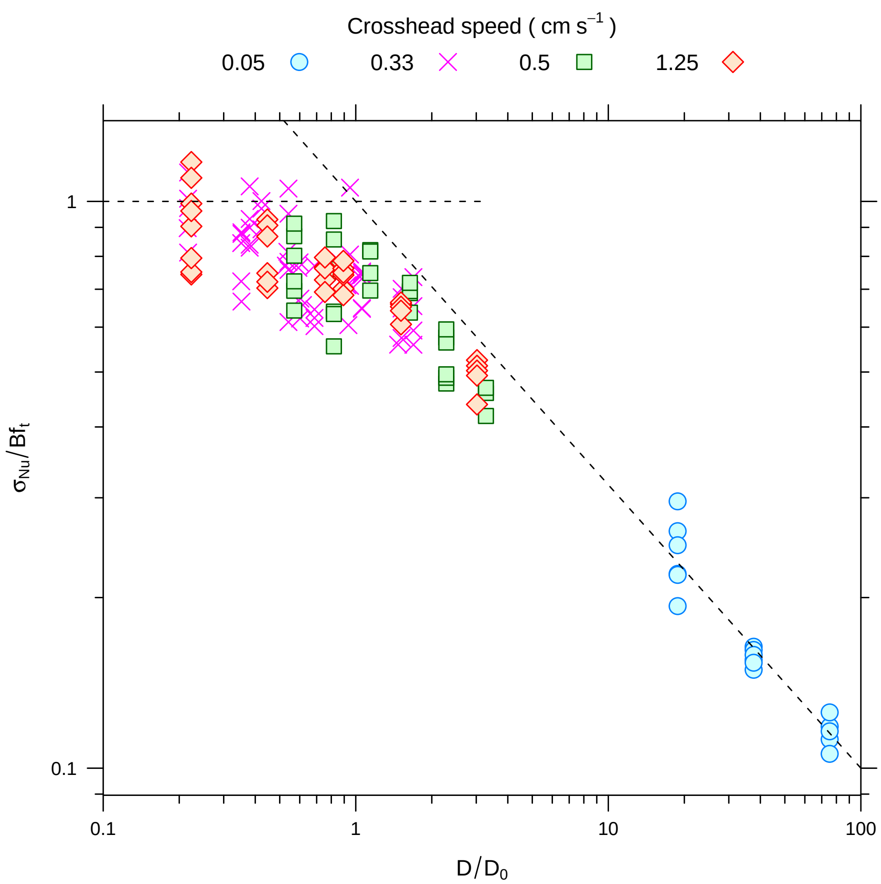

Figure 5.8: *Notched size effect test series fit to Bažant's size effect law (Equation 5.21), sorted by crosshead speed.*

The remainder of the data in Figure 5.8 do not appear to have a clear relation with crosshead speed, at least as far as the brittleness number $D/D_\circ$. Considering only data from the present study, the fastest crosshead speed (1.25 cm s^{-1}) appears to result in slightly lower values of the brittleness number compared to a slightly slower speed of 0.5 cm s^{-1}. This relation is not consistent when considering Sigrist's data as well (0.33 cm s^{-1}), though enhanced notch sensitivity and associated data scatter in these results likely obscures any comparison with the rate effects in the data from the present study.

Fracture toughness

The fracture toughness values from Table 5.2 are plotted in Figure 5.9 as a function of the mean density of the snow samples. The data from the present study cover a higher range of densities than the data from *Sigrist* (2006), though the two data sets appear to line up well together. There is much more scatter in Sigrist's density values, but the scatter in the computed fracture toughness values is comparable for both data sets. There is no indication from Figure 5.9 that the fracture toughness for series NSE4 was carried out at a much lower loading rate; the apparent elastic fracture toughness value falls in line with the higher-rate values.

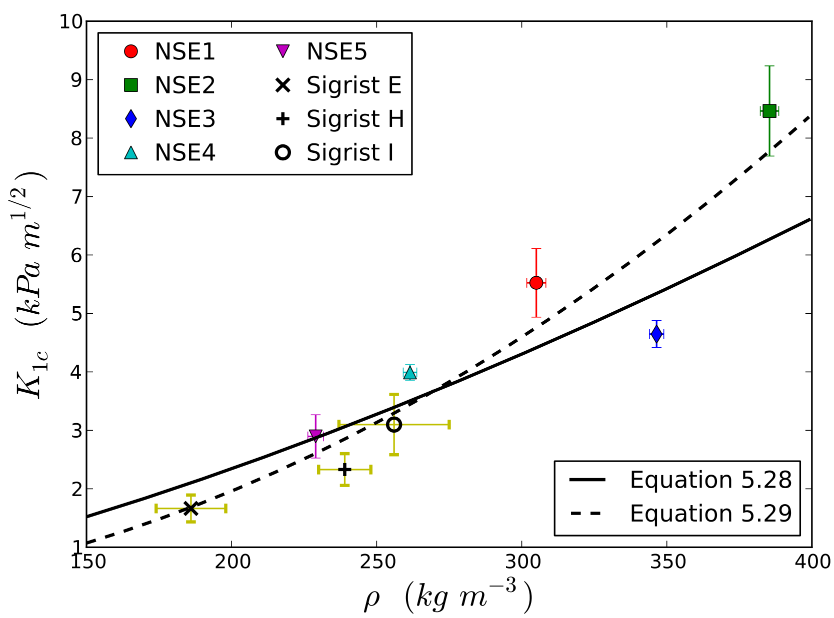

Figure 5.9: *Fracture toughness, calculated from fitting the notched size effect law of Equation 5.20 through the experimental data, as a function of the mean snow density. Error bars on the fracture toughness are estimated standard errors from the regression fit, density error bars from sampling variability are listed in Table 5.1.*

A power-law relationship between fracture toughness and density of the form $K_{Ic} = a(\rho/\rho_{ice})^b$ was fit through the data using weighted nonlinear least squares. The varying quality of the fracture toughness data points was taken into account by calculating regression weights using the reciprocal square of the estimated standard error of each point (the y-errors in Figure 5.9). Note that this weighting technique involves an assumption that the experimental variance is a good estimate of the true variance for each data point (*Ritz and Streibig*, 2008; *Rawlings et al.*, 1998). This assumption may not be entirely correct here, as the varying experimental conditions among the data also likely contributed to the different errors for individual data points. However, the experimental errors are still the best available estimate of the true errors for the following analysis. The resulting power law model took the form

$$K_{1c} = (23 \pm 10)\left(\frac{\rho}{\rho_{ice}}\right)^{1.5\pm0.4} \tag{5.28}$$

with K_{1c} in $\mathrm{kPa\,m^{1/2}}$ and R^2 = 0.78. The p-values for the regression parameters (a = 23 and b = 1.5), calculated using sandwich estimators as above, were 0.07 and 0.007, respectively. The residual structure of this model had constant variance, evidence that the regression weights were appropriate. Furthermore, the model residuals passed statistical tests for normality and independence at the $\alpha = 0.05$ level, as measured by the Shapiro-Wilk test and the runs test for independence, respectively. This expression is represented by the solid line in Figure 5.9.

For comparison, an unweighted model was also fit through the data. The resulting model, represented by the dashed line in Figure 5.9, took the form

$$K_{1c} = (48 \pm 14)\left(\frac{\rho}{\rho_{ice}}\right)^{2.1\pm0.2} \tag{5.29}$$

with K_{1c} again in $\mathrm{kPa\,m^{1/2}}$. This fit had a goodness of fit of R^2 = 0.87, and the p-values for the regression parameters (a = 48 and b = 2.1) were 0.01 and 0.0001, respectively. The model residuals were normally distributed and independent. However, the structure of the model residuals was poor. The variance increased with increasing density, which violates a standard least-squares assumption. This was the result of treating each data point as having the same quality.

The unweighted model has a visually appealing fit through the data in Figure 5.9. However, the unweighted model predicts a fracture toughness about 35% greater than that measured in Series NSE3 for the same density. Series NSE3 had one of the lowest relative errors of all the data in Figure 5.9, but the unweighted model passes much closer to Series NSE1 and NSE2, which had much greater uncertainty. Below a density of about 275 kg m^{-3}, the discrepancy between the two models is not as great. As will be seen in subsequent analysis, however, the weighted model is more consistent with data from other sources and test methods.

Equivalent elastic crack extension c_f

The parameter c_f, for all the data series but NSE4 (including Sigrist's data), was on the order of 1–4 cm. This is in the range of about 25–90 times the mean grain size in the snow specimens (Figure 5.10). The range of c_f for the data series from the present study only (again excluding NSE4), was about 20–40 times the grain size. For series NSE4, c_f was 0.5 mm, the size of a single grain.

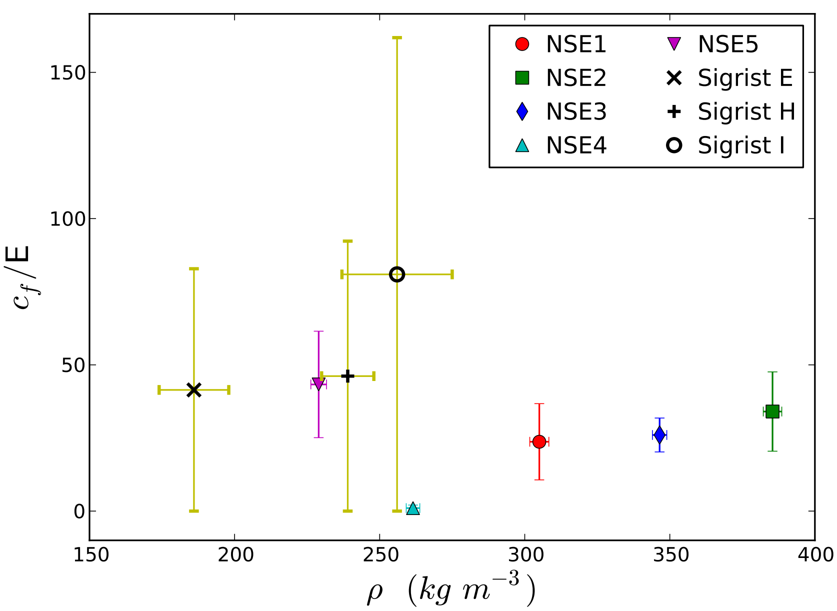

Figure 5.10: *Critical equivalent crack extension c_f, normalized by the grain size* E*, versus density.*

The sensitivity of c_f to the scatter in the data is apparent in Figure 5.10. The largest estimates for c_f come from the data with the most scatter (Sigrist's data). The weighted mean value of c_f, excluding NSE4, was 1.5 $\pm$ 0.2 cm. This corresponds to about 30 times the mean grain size (0.5 mm) of the different types of snow considered here. It should be noted, however, that the visual determination of grain size is highly subjective. An additional uncertainty associated with variability in grain size determination for different observers should be considered when representing any length scale as a multiple of the grain size.

There is no clear relation between c_f and density (Figure 5.10). It appears that c_f may be larger for lower-density snow. This would be an opposite trend than suggested by *Sigrist et al.* (2005b) for the fracture process zone size as a function of density. However, given the scatter in the data, no statistically significant relationship between c_f and density can be discerned from the data here.

Rate effects are much more important in determining the apparent size of the fracture process zone than density. The slower crosshead speed and resulting strain rate for series NSE4 led to a very small value of c_f (Figure 5.11). The nominal tensile strain rate in the outer fiber of the beam was calculated from beam theory (e.g. *Timoshenko and Goodier*, 1951) as

$$\dot{\varepsilon}_N = \frac{6DV}{S^2} \quad [s^{-1}]. \tag{5.30}$$

The nominal strain rate for series NSE4 was on the order of $10^{-2}\ s^{-1}$, which is still high compared to the strain rate of about $10^{-3}\ s^{-1}$ at which many investigators consider snow to be fully elastic. If this were indeed the case, such a strong rate effect would not be expected here. Above a strain rate of about $10^{-1}\ s^{-1}$, the value of c_f appeared to be rate-independent.

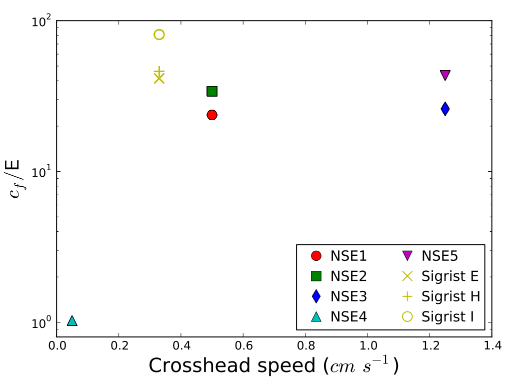

(a)

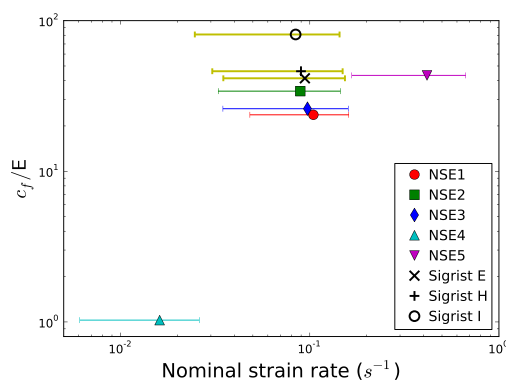

(b)

Figure 5.11: *Rate dependence of the critical equivalent crack extension c_f, normalized by the grain size* E.

Transitional size $D_\circ$

The transitional size $D_\circ$ is not a material constant in the framework of the notched size effect law, as it contains a geometry dependence in the functions $k_\circ$ and $k'_\circ$ (Equation 5.23). Therefore comparison of individual values of $D_\circ$ arising from fitting the notched size effect data here requires caution. All of the tests of *Sigrist* (2006) had the same span to depth ratio and the same relative notch depth, so the geometric functions $k_\circ$ and $k'_\circ$ are the same across this data set. The same cannot be said for the data from the present study, as S/D varied between data series, though this difference alone leads to a very small change in $k'_\circ/k_\circ$. However, the relative notch depth of $\alpha = 0.3$ used in the present study and that used by Sigrist ($\alpha = 0.1$) contribute to a more significant difference in $D_\circ$. There is nearly a factor of 2 difference between the ratio $k'_\circ/k_\circ$ in the definition of $D_\circ$ between these two data sets.

For these reasons, the size effect law expressed as a function of c_f (Equation 5.20) instead of $D_\circ$ (Equation 5.21) should be used when comparing or using data with different geometries, since c_f is defined as a constant independent of both specimen size and geometry. This point is illustrated in Figure 5.12. The weighted mean value of $D_\circ$ from Sigrist's data is 23 cm, while that from the present data, excluding series NSE4, is just 7 cm (including NSE4 leads to a weighted mean of just 2 cm). The primary difference is the initial notch depth. The only length scale which can be properly averaged across both data sets is c_f.

5.2.3 Discussion

In many respects the data from the present study agree reasonably well with the data reported by *Sigrist* (2006). Both data sets confirm that, under high enough rates of loading to consider snow to be mostly elastic, the brittleness number β is transitional between 0.1 and 10. The size of the critical elastic crack extension c_f is on the order of centimeters, and the transitional size $D_\circ$, depending on geometry, is about an order of magnitude larger.

The notched size effect data in the present study showed much less scatter than data reported by *Sigrist* (2006). This is probably due in part to the relative notch depth of $\alpha = 0.1$ used by Sigrist, a value at which the LEFM geometric functions $k(\alpha)$ are much more sensitive to the notch depth (e.g. *Bažant and Kazemi*, 1990b; *Tang et al.*, 1996). Since notch cutting in the present study was a manual process using a metered taping knife, there was inherent uncertainty in the actual depth and straightness of the notch. Even with

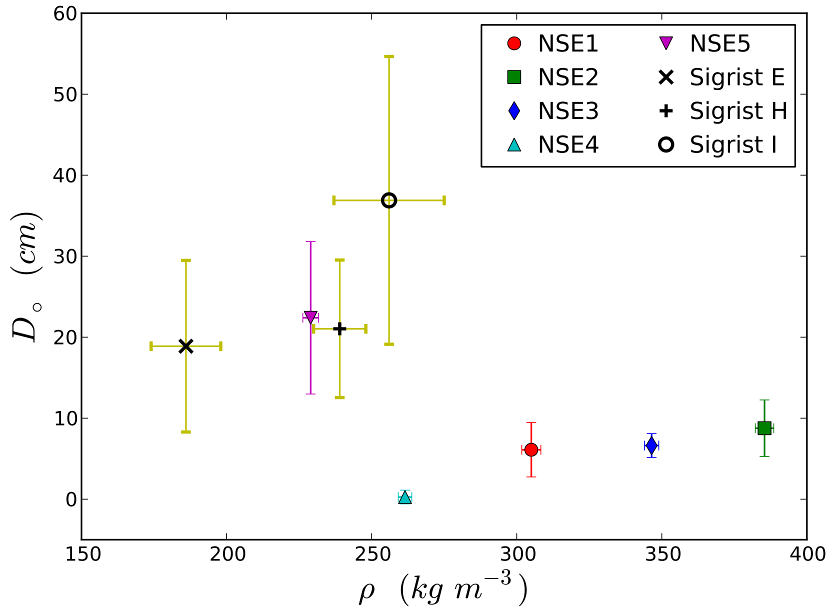

Figure 5.12: *Notched size effect transitional size $D_\circ$ versus density. The different relative notch depths between the experiments in the present study and those of Sigrist (2006) contribute to the geometry-dependent difference in values of $D_\circ$ between the two studies.*

carefully guided knife penetration, the estimated uncertainty in the notch depth was on the order of a least a few millimetres. This amount of uncertainty around a relative notch depth of $\alpha = 0.3$ leads to little change in the value of $k(\alpha)$ for typical beam bending tests. Though *Sigrist* (2006) did not report his notching technique, the notch depth uncertainty in his data is likely also on the order of several millimetres, which propagates much more uncertainty in $k(\alpha)$.

The wider scatter in Sigrist's data could also be a function of the apparently wider range of densities in his data, as expressed in the uncertainties around the mean values in Table 5.1. This could be a function of either the in-situ sampling technique or simply a difference in reporting the uncertainty in the group mean. The density values and uncertainties reported for the present study were calculated as weighted means using the individual values of ρ and $\delta\rho$ for each test, with total series uncertainty expressed using standard error propagation techniques. However, it is unclear how Sigrist calculated density for each test and arrived at a group mean and uncertainty, so these comments are speculative.

A final possible source of increased scatter in the data of *Sigrist* (2006) is in the lack of weight compensation in the tests. It was reported that the bending moment in the central cross section of the beam due to gravitational acceleration contributed greater than one-third of the ultimate bending moment. This large moment could have contributed to pre-test viscous effects after a snow sample had been mounted but prior to testing. These effects would be compounded by the enhanced notch sensitivity given the short relative notch depths. For these reasons, and given the weak nature of snow, weight compensation is probably much more important in bending tests than other engineering materials.

For accurate determination of fracture parameters using the linearized form of the size effect law of Equation 5.21, the RILEM recommendation outlined in *Bažant and Planas* (1998) suggests that the coefficients of variation (COV) of the linear regression parameters should be no more than 10% for the slope and 20% for the intercept. Linear regressions were performed for each data set to assess this recommendation, and none of the data sets met this standard. The COV of the slope was in the range 7-32% for data from the present study and 28-54% for Sigrist's data, and the COV of the intercept was in the range 14-300% for the present study (300% was for NSE4, the range was 14-46% excluding this series) and 21-25% for Sigrist's data. It should be noted, however, that these recommended COV levels do not directly translate to the nonlinear regressions that were used in the present analysis. Furthermore, the RILEM recommendation is not without controversy with regard to adoption, especially because the fracture energy calculated using this method may underestimate the true value (e.g. *Cotterell and Mai*, 1996).

The single data series with the lowest scatter was NSE3, which had a 10% COV for the slope and a 22% COV for the intercept. This data series also had the largest span-to-depth ratio of any series, and was also the only series that used four point bending (third point loading) rather than three point bending (center point loading). These results suggest that better data (lower scatter) in future studies might be obtained by using larger span-to-depth ratios and third point loading.

Another method to reduce scatter would be to test over a wider range of specimen sizes. However, it would be difficult to extract, handle, transport and successfully test natural snow samples over a wider size range than about 1:4, the range used both in the present study and by *Sigrist* (2006).

Rate effects are clearly important in governing the tensile fractures related to avalanches. The one notched size effect series conducted at a much lower crosshead speed provided a great deal of information about the nature of cracking when viscous effects are more prevalent. The low value of c_f from this series was likely due to viscous relaxation during the tests, reducing the size of the region of stress concentration around the notch tip. No other physical explanation appears in the data which would otherwise explain the anomalously low value of c_f from this data set. At the same time, however, the value of fracture toughness from this data set falls in line with the other values calculated here. This result suggests that the viscous relaxation in this test series provides approximately the same crack-tip blunting effect as a distributed fracture process zone from the perspective of global fracture toughness. More data would certainly be valuable to further address and quantify this type of important rate effect in the fracture of snow.

Notched size effect summary

The fracture toughness and critical elastic crack extension were determined from notched size effect tests fit to Bažant's notched size effect law. The equivalent elastic crack extension c_f, which is related to the fracture process zone size, is about 25–50 times the grain size in length. This length scale does not appear to vary with density, hardness, or other snow properties, but is sensitive to the loading rate. The best estimate of c_f is about 30 times the grain size, provided the strain rate is high enough to minimize viscous effects. The fracture toughness determined using this method is in the range of 1–10 kPa m$^{1/2}$, and is less sensitive to rate effects.

5.3 Unnotched Size Effect Method

The tensile fracture that initiates at the base of a snow slab after shear fracture propagation is assumed to initiate from a highly stressed but smooth boundary layer at the base of the slab (*McClung and Schweizer*, 2006). In other words, the slab fails at crack initiation. Therefore unnotched tensile or flexural test data may be more applicable to the study of tensile fractures in avalanches. However, structures which fail at crack initiation may also be influenced by a statistical size effect in addition to, or instead of, a deterministic fracture mechanical size effect.

Four series of size effect tests on the flexural strength (the modulus of rupture, see Section 4.2.1) were conducted and analyzed using both statistical (Weibull) and deterministic theories of the size effect. Additionally, data from several other studies were analyzed and synthesized to compare with results from the present study. The aim was to determine the most appropriate theory for explaining the unnotched size effect, both from the perspective of fitting the data and providing the most plausible explanation from a physical standpoint. Though scatter in the data still hampers conclusiveness, the deterministic explanation of the size effect is more consistent with the data and the present physical understanding of tensile fracture initiation in snow. Furthermore, the resulting fracture parameters are consistent with those calculated from notched size effect tests.

5.3.1 Background

Statistical size effect

Weibull (1939) postulated that the distribution of defects in a brittle material would lead to a size effect on strength, with increasing probability of finding a flaw large enough to cause failure with increasing specimen size. This type of statistical analysis related to the population of defects in a material has been applied widely since. It was the first type of size effect analysis applied to snow (*Sommerfeld*, 1974).

The two key assumptions necessary to apply a Weibull-type theory to explain observed size effects are (*Bažant and Planas*, 1998):

1. Failure occurs right at initiation of a macroscopic fracture

2. There is no characteristic length scale in the material

The first assumption precludes any stable crack growth before failure, a condition which should be met for tensile failure in slab avalanches. The second assumption only holds if the fracture process zone (or any other material length scale) is negligible in size compared to the specimen dimensions.

The Weibull statistical size effect can be expressed in many ways, but the following simple form for the dependence of the mean nominal strength $\bar{\sigma}_{Nu}$ on size D suffices for analysis of the experimental data here:

$$\bar{\sigma}_N = h_\circ D^{-n_d/m} \tag{5.31}$$

where $h_\circ$ is a constant depending on the sample geometry, n_d is the similitude dimension (n_d = 2 for the scaled beam tests here) and m is the Weibull modulus (*Bažant*, 2005). Experimental size effect data expressed on a log-log plot of nominal strength versus size will have a linear relationship with slope equal to $-n_d/m$ if this type of statistical size effect law is applicable. This is one of several methods of calculating the

Weibull modulus m for a material. However, similitude requirements must be followed to avoid introducing shape effects into the data, otherwise $h_\circ$ would not be constant in Equation 5.31, leading to two unknowns and an indeterminate solution.

When size effect data are not available, the Weibull modulus can be calculated by fitting experimental data at a single size to the Weibull distribution using, for example, the maximum likelihood method or least squares. The modulus m can also be related to the scatter in the data, as lower values of m correspond to more random scatter in the data, and vice-versa. The coefficient of variation (COV) of strength data at one size and geometry can be used to calculate the Weibull modulus using the approximate relation

$$\mathrm{CoV} = (0.462 + 0.783m)^{-1} \tag{5.32}$$

which is applicable in the range $5 \leq m \leq 50$ with accuracy within 0.25 percent (*Bažant and Planas*, 1998). For a given set of strength data it may be possible to calculate m in more than one way, and the values of m should coincide if Weibull theory is applicable.

Deterministic size effect

The coalescence of a macroscopic tensile crack in a boundary layer of distributed cracking can also be analyzed using the concept of equivalent elastic fracture mechanics. Far-field equivalence between the actual specimen and the equivalent elastic specimen may be achieved by replacing the boundary layer of distributed cracking with an equivalent elastic crack of length c_f emanating from a smooth elastic boundary. Equation 5.20, which related the nominal strength to the fracture toughness using the equivalent elastic crack length $\alpha = \alpha_\circ + c_f/D$ (following the two-term Taylor series expansion of $k^2(\alpha)$ around c_f/D), is repeated here for convenience:

$$\sigma_{Nu} = \frac{K_{Ic}}{\sqrt{k_\circ^2 D + 2k_\circ k'_\circ c_f}}, \tag{5.33}$$

where the notation $k(\alpha_\circ) = k_\circ$ has again been used for brevity. For further simplicity in notation, we write $g_\circ = k_\circ^2$ (*Bažant and Planas*, 1998) and rewrite Equation 5.33 as

$$\sigma_{Nu} = \frac{K_{Ic}}{\sqrt{g_\circ D + g'_\circ c_f}}. \tag{5.34}$$

For the problem of crack initiation from a smooth surface (in the actual specimen), the initial crack length $\alpha_\circ = 0$, for which the geometric function $g_\circ = 0$. However, the derivatives of $g_\circ$ ($g'_\circ$ and $g''_\circ$) are nonzero. For this reason, the third term in the Taylor series expansion of $k^2(\alpha) = g(\alpha)$ about c_f/D should be retained, since the first term vanishes (*Bažant*, 1997). Following this additional expansion, Equation 5.34 becomes

$$\sigma_{Nu} = \frac{K_{Ic}}{\sqrt{g'_\circ c_f + \frac{1}{2} g''_\circ c_f^2 D^{-1}}}. \tag{5.35}$$

The large size asymptotic limit of the modulus of rupture $f_{r\infty}$ (which is sometimes interpreted as the tensile strength, e.g. *Bažant and Li* (1995)), adopting the notation of *Bažant and Planas* (1998), can be written as

$$f_{r\infty} = \frac{K_{Ic}}{\sqrt{g'_\circ c_f}} \tag{5.36}$$

and the thickness of the boundary layer over which the average elastic tensile stress is $f_{r\infty}$ can be written as

$$D_b = \frac{c_f}{4g'_\circ} \left\langle -g''_\circ \right\rangle. \tag{5.37}$$

The Macaulay brackets $\langle X \rangle = max(X,0)$ in Equation 5.37 are used to as an ad-hoc technique to exclude from the size effect analysis specimen geometries for which the maximum stress is not at the surface but rather increases with distance from the surface (*Bažant and Li*, 1996). For unnotched bending beams, the maximum tensile stress from beam theory is always at the surface, so the geometric function $g''_\circ < 0$ and $\langle g''_\circ \rangle$ is nonzero.

Using Equations 5.36 and 5.37 in Equation 5.35, we come to

$$\sigma_{Nu} = f_r = f_{r\infty} \left(1 - \frac{2D_b}{D}\right)^{-1/2} \approx f_{r\infty} \left(1 + \frac{D_b}{D}\right) \tag{5.38}$$

where the two-term Taylor series expansion of the expression $(1-2x)^{-1/2} \approx 1 + x$ has been used (*Bažant*, 1997, 2005). Equation 5.38 represents the deterministic size effect law for the modulus of rupture f_r, based on replacing the boundary layer of distributed cracking with an equivalent elastic crack of length c_f.

5.3.2 Methods

The modulus of rupture was calculated from the results of four test series that had specimen sizes which spanned a range of at least 1:4. Two series were conducted in four point bending and two in three point bending. See Section 4.2.1 for a description of the calculation of the modulus of rupture from the peak load in the bending tests. All tests were weight compensated. For the four-point bending tests, weight compensation was achieved by orienting the testing machine horizontally and supporting the samples on low-friction lexan tables. The friction between the sample and the tables was accounted for in the calculation of the modulus of rupture. For the three-point bending tests, weight compensation was achieved by placing the sample supports at the quarter points of the beam in order to cancel the gravitation bending moment in the central cross section of the beam. The test geometries and weight compensation techniques are the same as represented in Figure 5.6, without the notches.

5.3.3 Results

The unnotched data series are characterized in Table 5.3. The variation in snow density across the four series is only around 10%, and the hand hardness index values are nearly equal. These similarities offer the opportunity for investigating the effects of variables other than density, such as the blade hardness index, type and size of snow grains, temperature, and loading geometry on the results.

Series	Date	n	$\bar{\rho}$ [kg/m^3]	R	$\bar{B}$ [N]	$\bar{T}$ [$^\circ C$]	Grain Forms/Size[1]	V [cm/s]	D [cm]	S/D	Type
USE1	080118	20	327 ± 2	4.3	8.1 ± 0.9	-8 ± 2	FCxr, 0.5-1 mm	1.25	5, 10, 20	3	4PB
USE2	080119	20	294 ± 4	4.3	5.7 ± 0.6	-7.8 ± 0.5	RG, 0.5 mm	1.25	5, 10, 20	3	4PB
USE3	090121	11	317 ± 3	4.3	17 ± 5	-2 ± 2	RG, 0.3-0.5 mm	1.25	2.5, 5, 10, 20	2^*	3PB
USE4	090215	15	297 ± 3	4	5.3 ± 0.7	-5 ± 3	FCxr, 0.5-1 mm	1.25	2.5, 5, 10, 15, 20	2	3PB

Table 5.3: *Unnotched size effect data. Date is in* yymmdd *format, other column variables include the number of tests (n), mean snow density ($\bar{\rho}$), hand hardness index (R), mean blade hardness index ($\bar{B}$), mean snow temperature ($\bar{T}$), crosshead speed (V), beam depth (D), and beam span-to-depth ratio (S/D). All uncertainties are standard deviations from the mean.*

[1] *Following the International Classification for Seasonal Snow on the Ground (Fierz et al., 2009). Key: RG = rounded grains; FCxr = mixed rounded and faceted crystals.*

* *Smallest samples (D = 2.5 cm) were not weight compensated due to apparatus limitations, so for these samples S/D = 3.6. The effect of self weight was factored into the calculation of the modulus of rupture for these samples, and the geometric functions $k(\alpha)$ were scaled accordingly.*

Scaling of flexural strength with size

The power-law scaling of the modulus of rupture as a function of beam depth is shown in Figure 5.13. For series USE1 and USE4, the size effect is weak. In fact, for series USE4 the size effect slope is not statistically significant. Series USE2 and USE3 have strong size effects with equal scaling exponents.

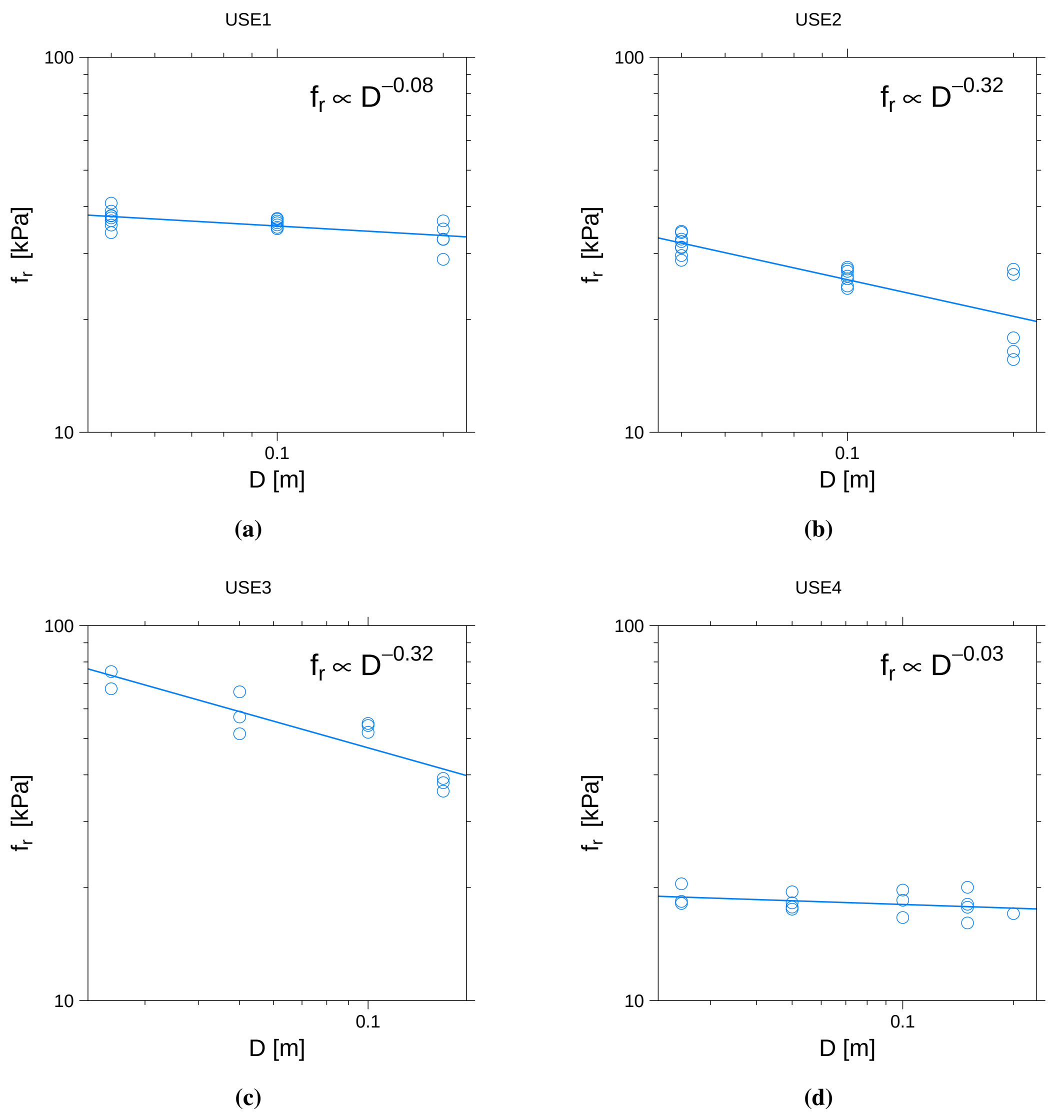

Figure 5.13: *Modulus of rupture as a function of beam size, showing the scaling exponents. Plot titles correspond to data series listed in Table 5.3. The slopes of the linear regressions are statistically significant at the* $\alpha = 0.05$ *level for all but series USE4 (d).*

The difference in scaling exponents in Figure 5.13 cannot be attributed simply to differences in snow hardness, temperature, or loading geometry. One plausible explanation lies in the type and size of grain forms. Series USE1 and USE4, which had weak size effects, were composed of mixed rounded and faceted grains that were coarser (larger in size) than series USE2 and USE3, which both had strong size effects and were composed of finer, rounded grains. Snow composed of rounded grains is stronger than snow with faceted grains at the same density (*Jamieson*, 1988). In concrete, increasing strength leads to a greater degree of brittleness for the same geometry and loading (*Gettu et al.*, 1990). However, the modulus of rupture values do not correlate with the grain type and size well enough to explain the difference in strength values. All of the subplots in Figure 5.13 are shown on the same y-axis limits, and there is no clear relationship between the mean values of the modulus of rupture and the grain type–or any other variable for that matter.

Even though the grain type and size does not explain the variation in strength values in this case, it may still be a factor in explaining the scaling exponents. The faceted crystal forms in series USE1 and USE4 may have led to a much more distributed zone of cracking in the specimens, such that the beams failed in a manner closer to plastic collapse. If this were the case, there would be no deterministic cause for a size effect, and the weak size effect observed would likely have a statistical source. These comments, though physically plausible, have no basis in observation, however.

Weibull modulus

The Weibull modulus for each series was calculated from the power law scaling exponents (Figure 5.13) according to Equation 5.31. The results varied in the range 6–60 (Table 5.4), though the highest confidence is in the lowest values, which came from data with the strongest size effects and the best linear fits in Figure 5.13. The mean coefficient of variation (COV) for all of the test data, grouped by beam size, was about 8%. Using Equation 5.32, this leads to another prediction of the Weibull modulus, $m = 16$.

The second section of Table 5.4 shows calculations of the Weibull modulus from in-situ uniaxial tensile strength data reported in the studies of *Jamieson* (1988); *Jamieson and Johnston* (1990). The data from the largest series in these studies (n = 42) were first fit directly to the Weibull distribution using least squares estimation, leading to $m = 5.8$. These studies reported COV on the order of 20%, which leads to predictions of m on the order of 5-6 from Equation 5.32. These COV values, from tests with manually-applied loading, are about 2.5 times as large as from the lab tests in the present study and lead to a corresponding difference in m. Furthermore, the in situ tests did not have constant sample dimensions–the slab depth and tensile cross

m	Source	Calculation Method
24 ± 7	USE1	Equation 5.31
6 ± 1	USE2	Equation 5.31
6 ± 1	USE3	Equation 5.31
60 ± 40	USE4	Equation 5.31
16	USE1-USE4	Equation 5.32
5.8 ± 0.5	*Jamieson* (1988)	least-squares[1]
5.8	*Jamieson and Johnston* (1990)	Equation 5.32[2]
5.2	*Jamieson and Johnston* (1990)	Equation 5.32[3]
0.9–1.6	*Sommerfeld* (1974)	least-squares[4]
1.5 ± 0.5	*Kirchner et al.* (2004)	maximum likelihood[5]

Table 5.4: *Calculated and reported values of the Weibull modulus* m.
[1] *Fit of largest uniaxial tensile strength data set to Weibull distribution (n = 42).*
[2] *Using reported* COV *(20%) of two largest data sets (n = 42 and n = 30).*
[3] *Using mean* COV *(22%) of all data, covering hundreds of tests.*
[4] *Fit of centrifugal tensile strength data to Weibull distribution.*
[5] *Fit of cantilever beam data to Weibull distribution.*

section area varied within each data set (*Jamieson*, 1988).

The last part of Table 5.4 shows values of the Weibull modulus reported in other studies. *Sommerfeld* (1974) performed centrifugal tensile strength measurements on samples of natural snow (reviewed in Chapter 4) and fit the data to the Weibull distribution using least squares estimation. The specimen dimensions were constant over this data set. *Kirchner et al.* (2004) carried out notched cantilever beam tests on samples of natural snow, and fit the data to the Weibull distribution using the maximum likelihood method. These tests had differing sample dimensions and cantilever length and therefore did not follow similitude requirements. Both studies reported extremely small values of m, which imply huge size effects according to Weibull theory (e.g. Equation 5.31). Ironically, *Kirchner et al.* (2004) concluded that the strength of snow was independent of size, a conclusion that is contradictory to the reported value of m and which has been invalidated in subsequent studies (*Sigrist et al.*, 2005b; *Sigrist*, 2006).

Fits to unnotched size effect laws

Each of the four unnotched size effect data sets was fit to Equation 5.38 using nonlinear least squares. The resulting fits are shown in Figure 5.14. Series USE2 and USE3, which had strong size effects, fit the steeper part of the size effect curve for which the boundary layer of cracking takes up an appreciable fraction of the

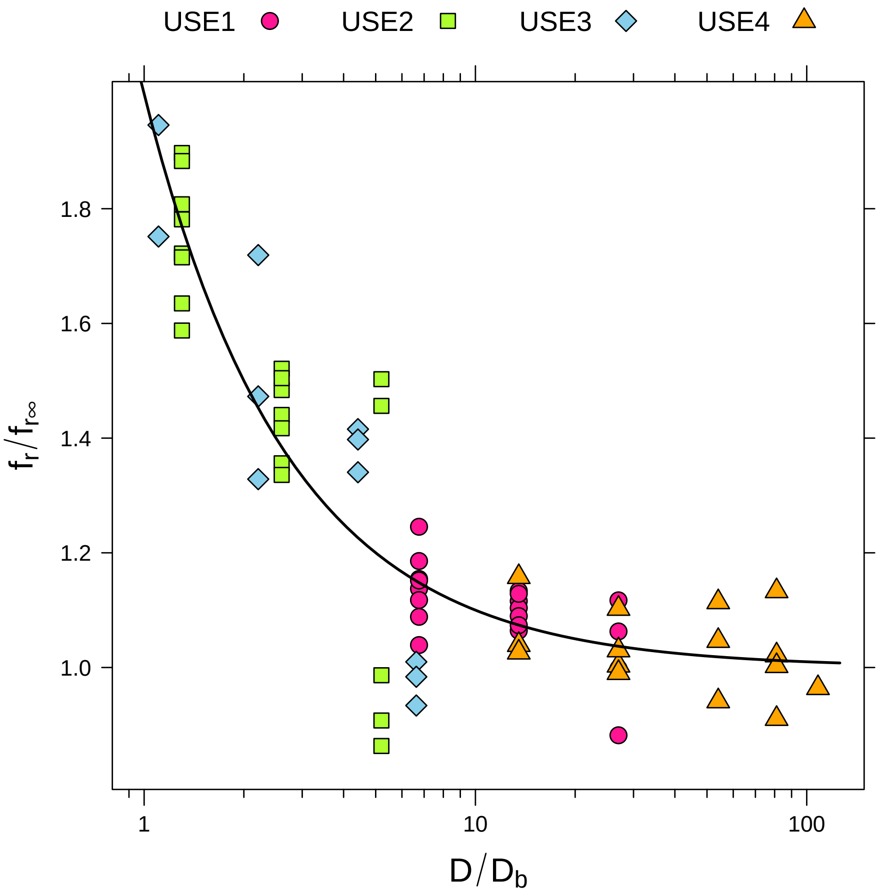

Figure 5.14: *Unnotched size effect test series fit to the size effect law for the modulus of rupture, Equation 5.38.*

beam depth ($0.1 < D_b/D < 1$). Series USE1 and USE4, with weak size effects, fall on the flatter portion of the size effect curve for larger D/D_b. Note that this result is incompatible with the physical explanation offered above for the weak size effect in series USE1 and USE4, namely that the faceted crystals in these series may have led to a greater spatial distribution of cracking and a failure closer to plastic collapse of the beams. The size effect on the modulus of rupture can be extended to include a horizontal asymptote for small beam sizes approaching plastic failure (e.g. *Bažant et al.*, 2007), though attempts to fit such a model–with additional and uncertain model parameters–did not prove fruitful. This was likely in part due to the large scatter in the unnotched data here.

The parameters $f_{r\infty}$ and D_b from the size effect law (Equation 5.38) and their related equivalent elastic fracture parameters K_{Ic} and c_f (from Equations 5.36 and 5.37, respectively) are all given in Table 5.5.

Test series	K_{Ic} [kPa m$^{1/2}$]	c_f [cm]	$f_{r\infty}$ [kPa]	D_b [cm]	R^2
USE1	5.3 ± 1.0	0.7 ± 0.2	33 ± 1	0.7 ± 0.3	0.37
USE2	6.7 ± 1.3	3.5 ± 1.0	18 ± 2	3.8 ± 1.1	0.68
USE3	9.5 ± 1.4	1.8 ± 0.4	39 ± 3	2.3 ± 0.5	0.74
USE4	1.2 ± 0.5	0.15 ± 0.1	17.7 ± 0.5	0.2 ± 0.1	0.12

Table 5.5: *Fracture parameters determined by fitting the size effect law of Equation 5.38 to the unnotched data series described in Table 5.3. The goodness of fit of the nonlinear regression with respect to the embedded constant model is R^2. The model residuals in each case passed statistical tests for normality and independence at the $\alpha = 0.05$ level.*

Considering the similar range of densities across all data sets, the scatter in values is large–more than can be explained by the factor of three range in blade hardness index across all the data. As was the case with fracture parameters obtained from the notched size effect law, the relative scatter is greater for the length scales (c_f and D_b here) than for the fracture toughness. Note the large values of D_b for series USE2 and USE3, which had strong size effects. If the boundary layer of microcracking has a thickness of about $D_b/2$ (*Bažant*, 2005), then for these series this layer occupies around 1–2 cm. The implication for USE2 and USE3 is that the boundary layer over which the crack coalesces occupies the majority of the tensile half of the beam for the smallest smallest samples of both series.

The fracture toughness had no clear relationship with density (Figure 5.15a), though this was to be expected given the small range in densities across the four data sets. The highest fracture toughness did correlate with the data set that had the highest value of the blade hardness index (Figure 5.15b). However, there is no clear overall trend of toughness as a function of hardness. If the data were classed according to grain forms, the series with strong size effects (USE2 and USE3) and weak size effects (USE1 and USE4) would both have increasing trends of fracture toughness with blade hardness. More data would be necessary to confirm such relationships, but they are consistent with trends between tensile strength and blade hardness index (Chapter 4).

There was no clear relationship between c_f (or D_b) and either density or the blade hardness index. Classing the data according to grain forms would lead to an increasing trend in c_f with increasing blade hardness index for faceted grains but an opposite trend for rounded grains, a contradictory relationship that would be difficult to justify or explain physically.

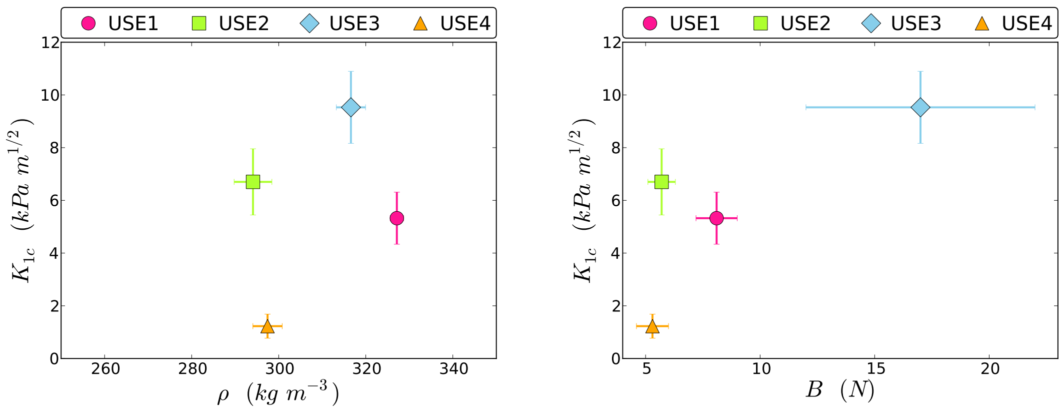

(a) **(b)**

Figure 5.15: *Elastic equivalent fracture toughness calculated from unnotched size effect data, versus density* ρ *(a) and blade hardness index* B *(b).*

5.3.4 Discussion

In order for Weibull statistical theory to be applicable to explain the size effect in brittle fractures, the Weibull modulus m should be a material property invariant with respect to different methods of calculating it (*Bažant*, 2005). The wide range in calculated and reported values of m in Table 5.4 indicates that this statistical theory does not likely hold for snow. These differences can be explained partly by differences in experimental methods. All of the in situ tests inherently have more scatter–thus higher COV and lower m via Equation 5.32. The COV of hand-operated testing techniques, such as the in situ tests of *Jamieson* (1988), should probably not be used to calculate material properties from a statistical theory, since the variability of test results will be due to much more than material randomness. However, the lab tests of *Sommerfeld* (1974)–calculated from the mean COV of centrifugal tests over a wide range of densities–resulted in values of m as low as the field tests of *Kirchner et al.* (2004). Therefore the low values of m from field tests cannot be ruled out on the basis of the testing technique alone.

Experimental techniques or other factors related to calculation methods or snow properties do not seem to be able to explain the variability in apparent values of the Weibull modulus as a material property. It may be that considering all snow as the same "material" may not be appropriate, and that something like a Weibull modulus may only have strict applicability within data sets from the same kind of tests or the same snow properties–weak faceted snow has different material and structural response than dense and sintered snow. However, the huge inconsistency between values of m calculated from the data in present study does cast doubt on the applicability of Weibull theory.

The second requirement for the applicability of Weibull statistics to explain the fracture of snow, namely the absence of a material characteristic length scale, does not seem physically reasonable for snow at the laboratory scale or at most sizes related to slab avalanches. The values of the length scale c_f (or D_b) that arise from fitting the experimental data to the size effect law for the modulus of rupture are not negligible compared to the experimental specimen dimensions, nor are the process zone lengths calculated from the notched size effect data. These results therefore support the assumption of a characteristic length scale related to the snow microstructure. It would be necessary to extend the size scale of laboratory tests by an order of magnitude or more before the length scale c_f would be negligible and Weibull theory might apply as an asymptotic limit, but experimental verification would be next to impossible.

A statistical generalization of the unnotched size effect law may allow satisfaction of both statistical and deterministic sources of the size effect (e.g. *Bažant et al.*, 2007). For the data considered in the present study, the use of such a generalization would require either (1) a very high Weibull modulus to account for the flat slope of the USE4 data with an apparently high ratio of D_b/D or (2) modification to allow for a horizontal asymptote as $D \to 0$ and a more reasonable value of the Weibull modulus, which would allow (or force) USE4 onto the part of the size effect curve for $D/D_b \to 0$. However, series USE4 clearly does not fit the size effect law well in its present form and would not likely fit a statistical-deterministic generalization any better.

For the series with the weakest size effect (USE4), the equivalent elastic crack has a length scale on the order of the grain size according to the deterministic size effect law. This does not seem physically realistic, but the slope of the size effect for this series was not statistically significant and there were only a few samples at each size. Excluding this series, the equivalent elastic crack lengths for the remaining series were on the order of about 10-70 times the grain size. These lengths agree well with the analogous values derived from the notched size effect law above and seem to be the right order of magnitude physically.

The experimental size effect data considered here (as well as the notched data above) is complicated by two factors which were discussed in the previous chapter. First, the largest specimens ($D = 20$ cm) were difficult to extract, transport and handle prior to testing, and some of the specimens that were successfully tested at this size may have been somewhat damaged, leading to lower strength values. Second, the experiments were conducted at constant crosshead speed, which leads to different nominal strain rates in specimens of different beam depth. The rate effects may have weakened the observed size effect, countering the first factor above, since the largest beams would have had the lowest nominal strain rates. These factors complicate the interpretation of the size effect data in this chapter and give more support to the zero-brittleness (notched-unnotched) data at a single, and more manageable, specimen size, to be introduced below.

Unnotched size effect summary

Overall, the unnotched size effect data have greater scatter than the notched size effect data discussed above and the notched/unnotched data to be discussed in the following section. The high variability of unnotched test results at a fast loading rate, which is largely unavoidable, makes conclusiveness difficult on any of the questions raised here regarding the applicability of statistical versus deterministic size effect theories. The most physically plausible explanation is the deterministic explanation of tensile crack initiation in a finite boundary layer near the bottom of the beam, characterized using the equivalent elastic crack concept. The values of fracture toughness and equivalent elastic crack length agree with values calculated using notched size effect tests, within the typical experimental scatter. The range of values of the ratio D/D_b fall roughly in line with concrete data fit to similar relations (*Bažant*, 2005). The assumptions necessary for the applicability of Weibull theory, analyzed systematically against experimental data here for the first time, do not appear to be justifiable. Given the inherent scatter and uncertainties in experimental data on snow, however, a conclusive assessment of the applicability of Weibull theory cannot lie solely in the data. Physical reasoning related to the microstructure of snow and the homogenization of snow as a continuum suggest that a deterministic size effect is the best theoretical foundation on which to analyze the tensile failure of snow.

5.4 Zero-Brittleness (Notched-Unnotched) Method

For some common test geometries, varying the notch size only while holding the specimen size constant leads to a sufficient variation in the brittleness number to allow the calculation of fracture properties using a quasi-brittle size effect law (*Tang et al.*, 1996). This is effectively equivalent to testing geometrically-scaled specimens of different size, as in the notched size effect method previously discussed. For notched bending beams, a popular test geometry for determining fracture properties of many materials, variation of the notch length alone does not lead to a large enough variation in the brittleness number to allow accurate calculation of fracture parameters using the notched size effect law (*Tang et al.*, 1999). This limitation was overcome using a method that allowed the combined analysis of notched and unnotched test results using specimens of the same size (*Bažant and Li*, 1996). According to the definition of the Bažant's brittleness number (Equation 5.24), unnotched specimens are always characterized by $\beta = 0$, hence the term "zero-brittleness" for the combined notched/unnotched test method. The zero-brittleness method utilizes a formulation of what Bažant calls a "universal" size effect law (*Bažant and Li*, 1996; *Bažant*, 2005), so-called because this equivalent elastic relation satisfies all of the appropriate asymptotic properties for $D \to 0$ and $D \to \infty$ for both notched and unnotched specimens.

The zero-brittleness method was used in the present study as the third method to determine tensile fracture properties of snow slabs. Notched and unnotched specimens of one size only were tested in the usual bending geometry. The use of a single size was convenient from the perspective of snow sample extraction and handling, uniformity of size and shape, and maximizing the number of samples that could be tested in one day using snow from a single layer. The fracture parameters calculated using this method agree well with those determined using either the notched or unnotched size effect. The zero-brittleness method has several advantages, though. First, the experimental convenience of this method increased the size of the resulting data set for analysis. Second, the universal size effect law is a higher-order equivalent elastic approximation than either the notched or unnotched size effect laws–both of which are first-order approximations–which increases confidence and accuracy in the results.

5.4.1 Methods

In a similar fashion as the derivation of the unnotched size effect law in the previous section, we first start with a general expression for the nominal strength of a material with an equivalent elastic crack of length $\alpha_\circ + c_f/D$,

$$\sigma_{Nu} = \frac{K_{Ic}}{\sqrt{Dk^2\left(\alpha_\circ + c_f/D\right)}} = \frac{K_{Ic}}{\sqrt{Dg\left(\alpha_\circ + c_f/D\right)}} \tag{5.39}$$

which has the same form as Equation 5.18. Expanding $g(\alpha)$ in a Taylor series about $\alpha_\circ$ and recalling the notation $g(\alpha_\circ) = g_\circ$, we can write a general form of the nominal strength of the equivalent elastic specimen as

$$\sigma_{Nu} = \frac{K_{Ic}}{\sqrt{D}} \left[g_\circ + g'_\circ \frac{c_f}{D} + g''_\circ \left(\frac{c_f}{D}\right)^2 + \cdots \right] \tag{5.40}$$

after *Bažant and Li* (1996). In Section 5.3, the second and third terms of this expansion were retained because, for unnotched tests, $g_\circ = 0$. However, when considering notched and unnotched tests together, all three terms (at minimum) are needed. Keeping only the terms shown, Equation 5.40 can be rearranged as

$$\sigma_{Nu} = \frac{K_{Ic}}{\sqrt{g'_\circ c_f}} \left(\frac{D}{D_\circ} + 1 - \frac{2D_b}{D} \right)^{-1/2} \tag{5.41}$$

where $D_\circ$ has the same definition as in Equation 5.23 and D_b the same as in Equation 5.37 (*Bažant and Li*, 1996).

Following a series expansion, the introduction of a horizontal asymptotic value of the nominal strength for $D \to 0$, controlled by the empirical term ηD_b, and some rearrangement, Equation 5.41 can be written in the final form

$$\sigma_{Nu} = \frac{K_{Ic}}{\sqrt{g'_\circ c_f}} \left(1 + \frac{D}{D_\circ}\right)^{-1/2} \left\{ 1 + \left[\left(\eta + \frac{D}{D_b}\right) \left(1 + \frac{D}{D_\circ}\right) \right]^{-1} \right\} \tag{5.42}$$

which has been termed the "universal size effect law" (*Bažant and Li*, 1996; *Bažant*, 2005). A value of $\eta = 0.5$ appears to be common, a value that can be interpreted as defining the size limit ($D = 0.5D_b$) below which a rectangular beam fails by plastic collapse (*Bažant et al.*, 2007). In the present analysis, the value of η was varied in the limit $0 < \eta < 1$ and found to have little effect on the regression results. The value of $\eta = 0.5$ was therefore adopted for consistency with other studies.

Equations 5.41 and 5.42 are nearly identical to the expression derived by *Bažant and Li* (1996), except that here I take the value of c_f to be the same in notched and unnotched tests. *Bažant and Li* (1996) assumed that c_f takes a 40% larger value for unnotched tests due to a larger zone of damage associated with crack initiation. This assumption was based on a sound physical argument, but it is not clear if or how it is supported by data from concrete tests. In a relation similar to Equation 5.41, *Bažant and Li* (1996) multiplied c_f in the universal size effect law by a scaling factor `k` which toggled between 1.4 (or some other constant value) for unnotched tests and 1 for notched tests. From the present study, the calculated values of c_f for notched and unnotched tests (Table 5.2 and 5.5, respectively) are not significantly different, so there was no experimental basis on which to follow the same assumption. Furthermore, the apparent goodness of fit of the resulting regressions increases with increasing `k` (as will be evident below), so there was additional impetus to avoid introducing this arbitrary parameter.

In a similar manner as outlined by *Bažant and Li* (1996), I rearranged Equation 5.42 into a form $y = Ax + C$ that could be solved using an iterative linear least squares algorithm with

$$y = \frac{\chi}{\sigma_{Nu}^2 \, g'_\circ}, \tag{5.43}$$

$$\chi = \left\{ 1 + \left[\left(\eta + \frac{D}{D_b} \right) \left(1 + \frac{D}{D_\circ} \right) \right]^{-1} \right\}^2 \tag{5.44}$$

and

$$x = \frac{g_\circ}{g'_\circ} D. \tag{5.45}$$

The regression constants are then functions of the unknown and desired fracture parameters K_{Ic} and c_f,

$$A = \frac{1}{K_{Ic}^2} \tag{5.46}$$

and

$$C = \frac{c_f}{K_{Ic}^2}. \tag{5.47}$$

These relations differ from the regressions outlined in *Bažant and Li* (1996) in that I wrote them as a function of the fracture toughness instead of the fracture energy. Solving for the fracture energy requires knowledge of the appropriate value for Young's modulus, or an effective elastic modulus using an elastic-viscoelastic correspondence principle. The modulus is a highly uncertain term in snow mechanics, and I desired to avoid introducing it whenever possible. Thus the quasi-brittle calculations in this chapter all focused on the fracture toughness rather than the fracture energy.

The unknown parameter c_f, to be solved for by fitting the universal size effect law to the experimental data, is contained in the definitions of D_b and $D_\circ$ in the expression for y in Equation 5.43, which actually makes the equation system nonlinear. This system was solved by writing an iterative solution procedure, in which the value for χ was initially set to 1. Following the solution of the linear equation $y = Ax + C$, an updated estimate of c_f was obtained and used to update the value of χ and thus y for a subsequent iteration. This procedure was repeated until the L_2-norm of χ was less than a specified tolerance (10^{-4}). The algorithm typically converged in less than 10 iterations.

Now it can be seen that, since D_b is proportional to c_f, using a value of $\mathtt{k} > 1$ to modify c_f for unnotched tests will result in a smaller value of χ and therefore smaller y for unnotched tests. This has the effect of decreasing the relative scatter of the y-values for unnotched tests relative to notched tests, which, according to the preceding regression procedure, makes the fit look better from the perspective of least squares. Therefore, lacking a clear empirical or theoretical foundation on which to specify `k`, treating c_f as the same for notched and unnotched tests seemed the most appropriate.

5.4.2 Results

Eight notched/unnotched test series were conducted, with all experimental conditions but the presence or absence of a notch held constant (Table 5.6). In two test series (Z2 and Z3), the notch length was varied, but in the regressions the combined weight of all the notched tests was set to be the same as the unnotched tests since the range in brittleness numbers from varying only the notch length was small (*Bažant and Li*, 1996). For two other series (Z5 and Z6), subsets of notched-unnotched tests were conducted at different rates to investigate rate effects on the resulting fracture parameters.

Beams of depth $D = 10$ cm were used, as this was the specimen size which was the most consistent from the perspective of extraction, handling, mounting, testing, and uniformity of size. This size also struck a balance between being large enough size for reasonable results and not so large as to limit the number of samples that could be extracted in a reasonable amount of time during a short winter day and in a small enough spatial area to avoid significant changes in snow properties due to natural spatial variability. All tests were weight compensated, and all but one test series was carried out in three point bending with the testing machine oriented vertically. Table 5.6 contains a description of each data series.

Code	Date	n	$\bar{\rho}$ [kg/m^3]	R	$\bar{B}$ [N]	$\bar{T}$ [$^\circ C$]	Grain Forms/Size[1]	V [cm/s]	S/D	Type
Z1	080115	14	186 ± 2	3.3	N/A	-11.1 ± 0.2	RG 0.5 mm / DF 1 mm	1.25	3	4PB
Z2	090129	20	325 ± 3	4.3	12.2 ± 0.8	-6.7 ± 0.3	FCxr 0.5 mm	1.25	2.5	3PB
Z3	090202	18	227 ± 2	3	2.0 ± 0.3	-5.8 ± 0.7	FC 0.5-1 mm	1.25	2.5	3PB
Z4	090301	18	152 ± 1	2	$0 < \bar{B} < 1.7$	-6.7 ± 0.6	DF 0.5-1 mm	1.25	2.5	3PB
Z5	090321	20	334 ± 2	4	9 ± 1	-4.7 ± 0.8	RG 1 mm	0.125 (n = 10)	2.5	3PB
								1.25 (n = 10)		
Z6	090323	32	337 ± 2	4	10 ± 1	-4.7 ± 0.9	RG 1 mm	0.0125 (n = 10)	2.5	3PB
								0.125 (n = 10)		
								1.25 (n = 12)		
Z7	090326	18	155 ± 2	3	2.0 ± 0.5	-5.2 ± 0.5	RG 0.5 mm / DF 1 mm	1.25	2.5	3PB
Z8	090405	8	239 ± 3	3.7	5.8 ± 0.8	-4.2 ± 0.9	RG 0.5 mm	1.25	2.5	3PB

Table 5.6: *Notched/unnotched (zero brittleness) test data. Date is in* yymmdd *format, other column variables include the number of tests (n), mean snow density ($\bar{\rho}$), hand hardness index (R), mean blade hardness index ($\bar{B}$), mean snow temperature ($\bar{T}$), crosshead speed (V), beam depth (D), and beam span-to-depth ratio (S/D). All samples had a beam depth $D = 10$ cm. All uncertainties are standard deviations from the mean.*

[1]*Following the International Classification for Seasonal Snow on the Ground (Fierz et al., 2009). Key: RG = rounded grains; DF = decomposing and fragmented grains; FCxr = mixed rounded and faceted crystals; FC = faceted crystals.*

Regression fits to universal size effect law

Treating the rate effect subsets of series Z5 and Z6 separately, a total of 11 independent series were fit to the universal size effect law of Equation 5.42 using the iterative regression procedure outlined above. The nominal strength for each test was calculated the same as for the size effect experiments above, using the peak load in the appropriate beam equation depending on the loading points and span-to-depth ratio (Section 4.2.1).

Figure 5.16 shows the results of the regressions and goodness of fit, represented by the adjusted r^2 of the linear regression, for each series. In nearly every case, the fit was quite good. In every series except those that included variable notch length (Z2 and Z3), the adjusted r^2 was greater than 0.9. The "intrinsic size" × (*Bažant and Planas*, 1998) for these specimen sizes and geometries varies from 0 cm for unnotched tests to around 2 cm for the notched tests.

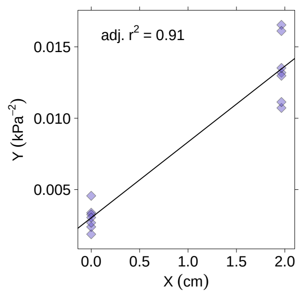

(a) *Z1*

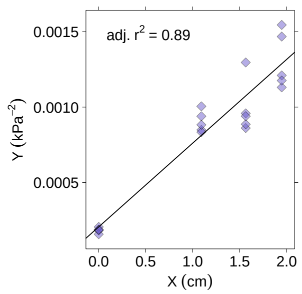

(b) *Z2*

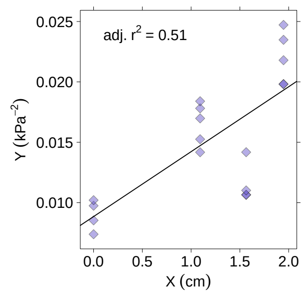

(c) *Z3*

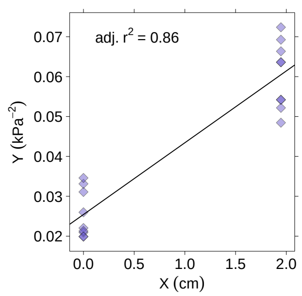

(d) *Z4*

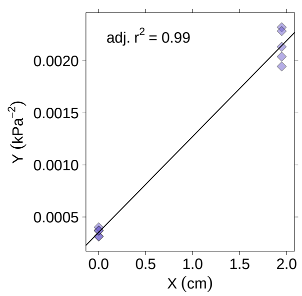

(e) *Z5m*

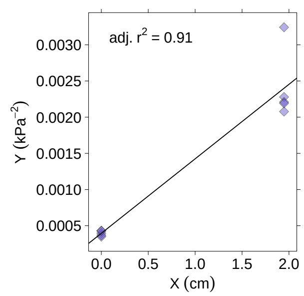

(f) *Z5f*

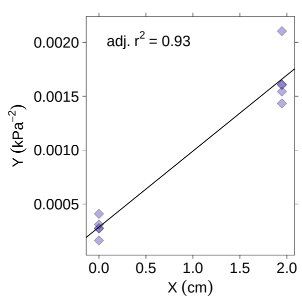

(g) *Z6s*

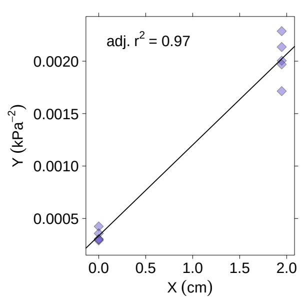

(h) *Z6m*

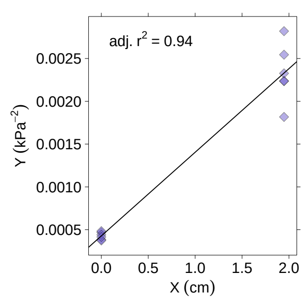

(i) *Z6f*

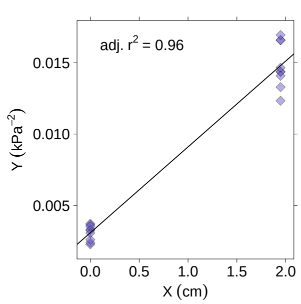

(j) *Z7*

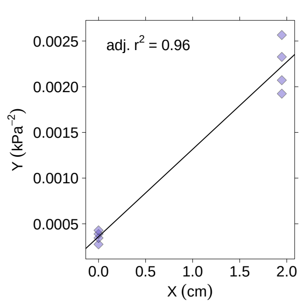

(k) *Z8*

Figure 5.16: *Linear regressions of notched/unnotched test data fit to the universal size effect law of Equation 5.42. Labels correspond to data series described in Table 5.6. Unnotched tests all have an "intrinsic size" $x = 0$, notched tests all have an intrinsic size around 2 cm.*

Fracture parameters

The fracture toughness and equivalent elastic crack extension c_f were calculated from the regression constants determined in fitting the notched/unnotched test data to the universal size effect law (Table 5.7). The toughness values are close to those determined using the notched and unnotched size effect laws, if a little lower. The same can be said for the value of c_f. The fracture toughness values were mostly in the range of 1–4 kPa m$^{1/2}$ and in most cases c_f was around 0.5 cm or less. The values of $D_\circ$ were lower than those calculated for the notched size effect data, mostly due to differences in test geometry (primarily the span to depth ratio). The boundary layer length scale D_b was slightly larger than c_f for all series but the variable-notch series (Z2 and Z3).

Series	K_{Ic} [kPa m$^{1/2}$]	c_f [cm]	$D_\circ$ [cm]	β	D_b [cm]	adj. r^2
Z1	1.4 ± 0.1	0.30 ± 0.07	1.5 ± 0.4	7	0.34 ± 0.08	0.91
Z2	4.2 ± 0.3	0.021 ± 0.006	0.14 ± 0.04*	70**	0.013 ± 0.004*	0.89
Z3	1.4 ± 0.3	1.7 ± 0.5	11 ± 3*	0.9**	0.9 ± 0.3*	0.51
Z4	0.75 ± 0.07	1.4 ± 0.2	7 ± 1	1.4	1.7 ± 0.2	0.86
Z5-f	3.1 ± 0.3	0.4 ± 0.2	2.0 ± 0.8	5	0.5 ± 0.2	0.91
Z5-m	3.3 ± 0.1	0.44 ± 0.06	2.0 ± 0.3	5	0.47 ± 0.07	0.99
Z6-f	3.2 ± 0.2	0.4 ± 0.1	2.3 ± 0.5	4	0.5 ± 0.1	0.94
Z6-m	3.4 ± 0.2	0.39 ± 0.08	2.0 ± 0.4	5	0.5 ± 0.1	0.97
Z6-s	3.8 ± 0.3	0.4 ± 0.1	2.1 ± 0.7	5	0.5 ± 0.2	0.93
Z7	1.29 ± 0.06	0.51 ± 0.07	2.6 ± 0.4	4	0.63 ± 0.09	0.96
Z8	3.2 ± 0.3	0.4 ± 0.1	1.9 ± 0.6	5	0.5 ± 0.1	0.96

Table 5.7: *Fracture parameters determined by fitting notched/unnotched data to the universal size effect law of Equation 5.42. The fracture toughness K_{Ic} and equivalent elastic crack extension c_f are applicable for the full data sets. The transitional size $D_\circ$ listed is only applicable for the notched tests, as $D_\circ = \infty$ for $\alpha = 0$. The brittleness number $\beta = D/D_\circ$ is for the notched tests only. The boundary layer length scale D_b listed is only applicable for the unnotched tests, as $D_b = 0$ for $\alpha > 0$.*
**Mean value for test series which had different notch depths, as each notch depth led to a different value of $D_\circ$ and D_b.*
***Calculated using the mean value of $D_\circ$.*

The length scales c_f, $D_\circ$, and D_b were more sensitive to scatter in the data than K_{Ic}, also in agreement with previous results. The two series with the poorest linear regression fits (Z3 and Z4) had the largest calculated values of all three length scales. This is the same trend observed in the notched size effect data, where the data from *Sigrist* (2006) had the poorest fits to the size effect law and the largest mean value of

c_f. This greater sensitivity of the size effect length scales to scatter in the data is a general feature of the size effect law and is not specific to the snow data here (*Bažant and Planas*, 1998). However, the data from the present study, much of it with less scatter than any previous data used to calculate fracture parameters, suggest slightly smaller values than previously reported for quasi-brittle length scales such as the effective process zone length.

The rate dependence on c_f was not apparent in either of the series for which rate effects were tested (Figure 5.17). The value of c_f was not significantly different for either series Z5 or Z6 when the nominal strain rate was varied by 1–2 orders of magnitude. This was surprising given the rate dependence observed for the notched size effect test series NSE4 conducted at a slow loading rate (Figure 5.8), even though the lowest crosshead speed for series Z6-s was a factor of four lower than for series NSE4 which had a very low value of c_f. The snow temperature was the same for series NSE4 (Table 5.1) and Z5 and Z6 (Table 5.6). All three series had snow with rounded grains. The grain size was coarser for Z5 and Z6, however, and the snow was also denser and had slightly higher mean blade hardness index. These characteristics might explain the lack of an otherwise expected rate effect for the length scale c_f here. However, the lowest strain rates in these tests were still well above the creep-to-fracture transition of about 10^{-4} s^{-1} for snow in tension.

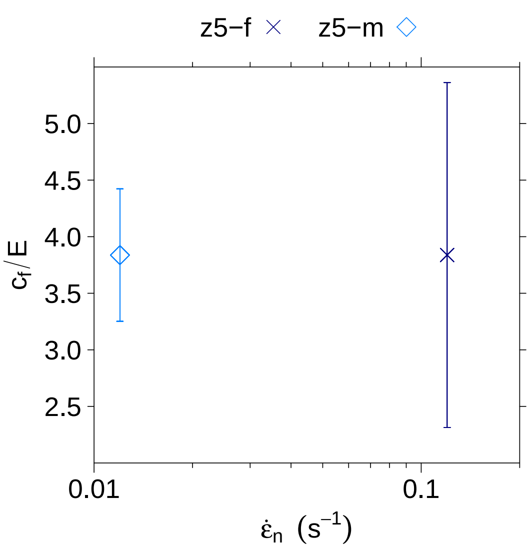

(a)

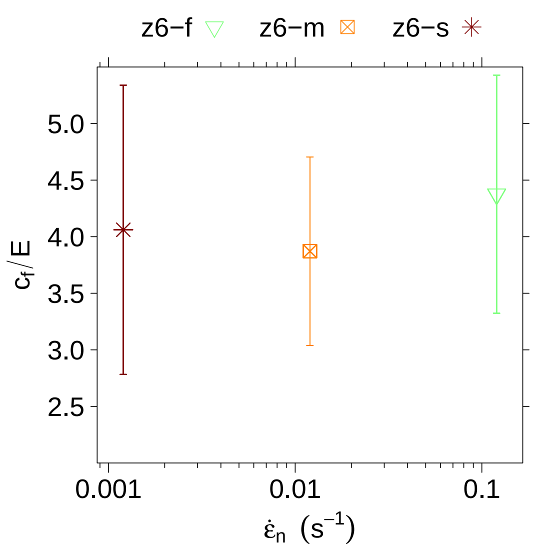

(b)

Figure 5.17: *Critical equivalent elastic crack length c_f, normalized by grain size E, as a function of the nominal tensile strain rate for two different test series.*

There is a rate effect on the fracture toughness for the same two data series (Figure 5.18). With increasing strain rate the fracture toughness decreased, though the effect was weak. However, the trend was consistent with the reported increase in fracture toughness of concrete with increasing time to failure (decreasing strain rate) due to the influence of creep (*Bažant and Gettu*, 1992).

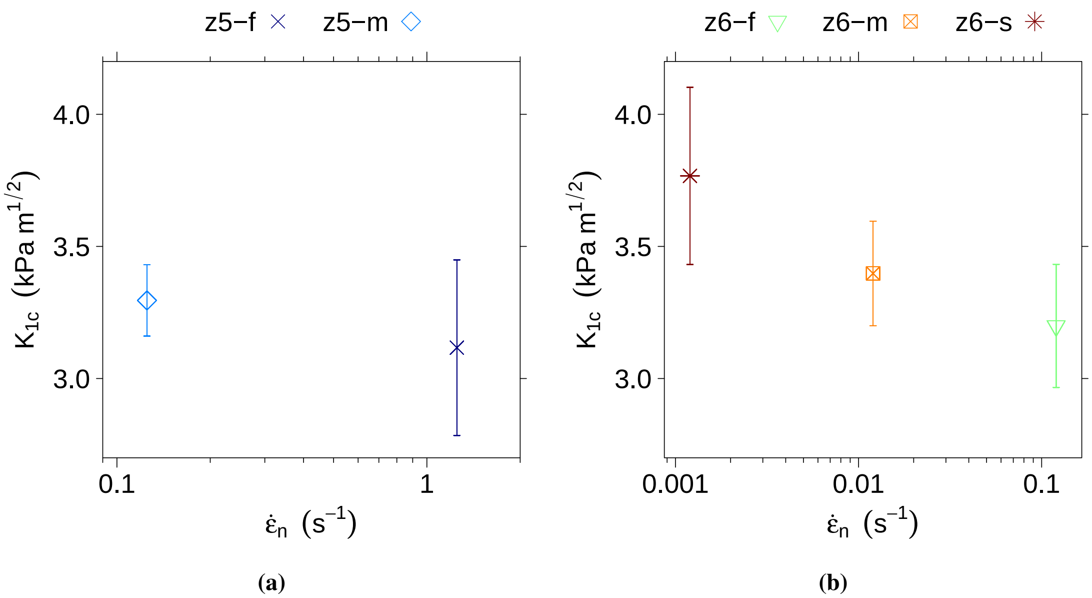

Figure 5.18: *Fracture toughness as a function of the nominal tensile strain rate for the two rate-effect test series.*

The fracture toughness correlated better with the blade hardness index than with the density (Figure 5.19). The relation between toughness and penetration resistance was linear, and there was much less scatter around the regression model as a function of blade hardness (Figure 5.19b) than density (Figure 5.19a). The only notable outlier in the toughness-hardness plot (Figure 5.19b) corresponded to the data from series Z8. However, series Z8 is one of several that are far from the density regression line in Figure 5.19a.

The best regression fit through the fracture toughness data as a function of density was

$$K_{Ic} = (15 \pm 3)\left(\frac{\rho}{\rho_{ice}}\right)^{1.5 \pm 0.2} \tag{5.48}$$

with K_{Ic} in kPa m$^{1/2}$. This model was obtained by weighted nonlinear regression using the inverse of the variance of the toughness values as the weights. Both regression coefficients were statistically significant

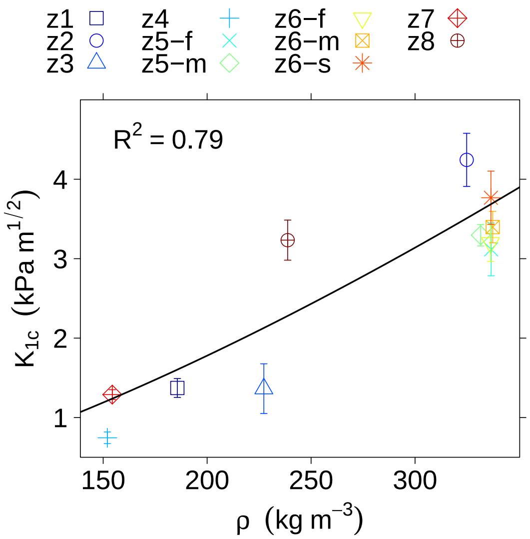

(a)

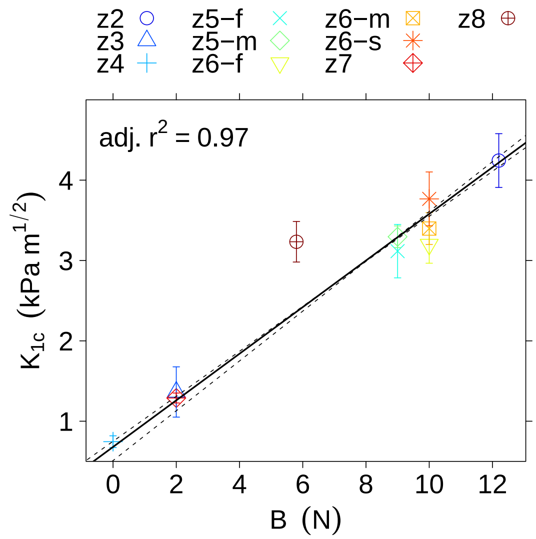

(b)

Figure 5.19: *Fracture toughness expressed as a function of (a) density, with a regression curve corresponding to Equation 5.48; (b) blade hardness index B, with the solid regression line corresponding to Equation 5.49. The dashed lines correspond to regressions using the limit values of $B = 0$ N and $B = 1.7$ N for series Z4.*

and model residuals were normal and independently distributed at the $\alpha = 0.05$ level. The fit had a nonlinear $R^2 = 0.89$.

The regression fit though the toughness data as a function of the blade hardness index B is a much better fit to the data. The equation for the solid line in Figure 5.19b took the form

$$K_{Ic} = (0.68 \pm 0.08) + (0.29 \pm 0.02)\,B \tag{5.49}$$

with K_{Ic} again in kPa m$^{1/2}$. This model was obtained by weighted linear least squares regression, with regression weights the same as for Equation 5.48. Both the slope and intercept terms were statistically significant at the $\alpha = 0.05$ level. The overall goodness of fit, characterized by the coefficient of determination, was very high at (adjusted) $r^2 = 0.97$. The residual structure of the model was good except for the presence of the data point for series Z8, a strong outlier which influenced the statistical tests for normality and independence. There is no clear indication as to the reason why this particular data series stood out as an outlier; none of the remaining characteristic variables from this data set seem to explain the high value of fracture toughness given either the density or the hardness of the snow.

Equation 5.49 was arrived at using the value of $B = 0.5$ N for the data from series Z4. All of the samples from this series registered below the threshold of 1.7 N for which the digital force gauge was insensitive. Preliminary data obtained using a new and more sensitive force gauge in January 2011 suggest that snow with a hand hardness index of 2 has a mean blade hardness index of about 0.5 N. The precise value of B for series Z4 is of little numerical consequence, however. The dashed lines in Figure 5.19b show the limit cases associated with using $B = 0$ N and $B = 1.7$ N, the valid limits for B in this test series (Table 5.6). The difference between these outer limits is about 10% for the slope and about 35% for the intercept, but all three lines fit the data equally well, as they all have an adjusted $r^2 = 0.97$.

Zero-brittleness summary

The fracture toughness and critical equivalent crack extension were determined from the zero-brittleness (notched/unnotched) method. The resulting values agree well with those calculated using the notched and unnotched size effect methods. However, the confidence in the results from the zero-brittleness method are much higher than either of the size effect methods. This is in part due to the experimental advantages of the one-size method and partly due to the higher order accuracy of the series approximations used to derive the universal size effect law which underlies the zero-brittleness method. The fracture toughness was better expressed using the blade hardness index than the density. Some rate dependence in the fracture toughness was apparent in two data series but no rate dependence in c_f was observed, though all tests were conducted well above the creep-to-fracture transition.

5.5 Aggregate Results

The three methods of determining fracture parameters in this chapter lead to mean values which, within the scatter in the data, largely overlap. This suggests that the equivalent elastic approach gives self-consistent results for different types of snow fracture data. However, the uncertainties associated with each of the methods used in this chapter are quite different. The highest confidence in fracture toughness values comes from the combined notched/unnotched tests, followed by the notched size effect method (Figure 5.20). The fracture toughness values determined from the unnotched size effect method have the largest scatter and highest relative uncertainties, which is primarily due to the large scatter for unnotched beam tests.

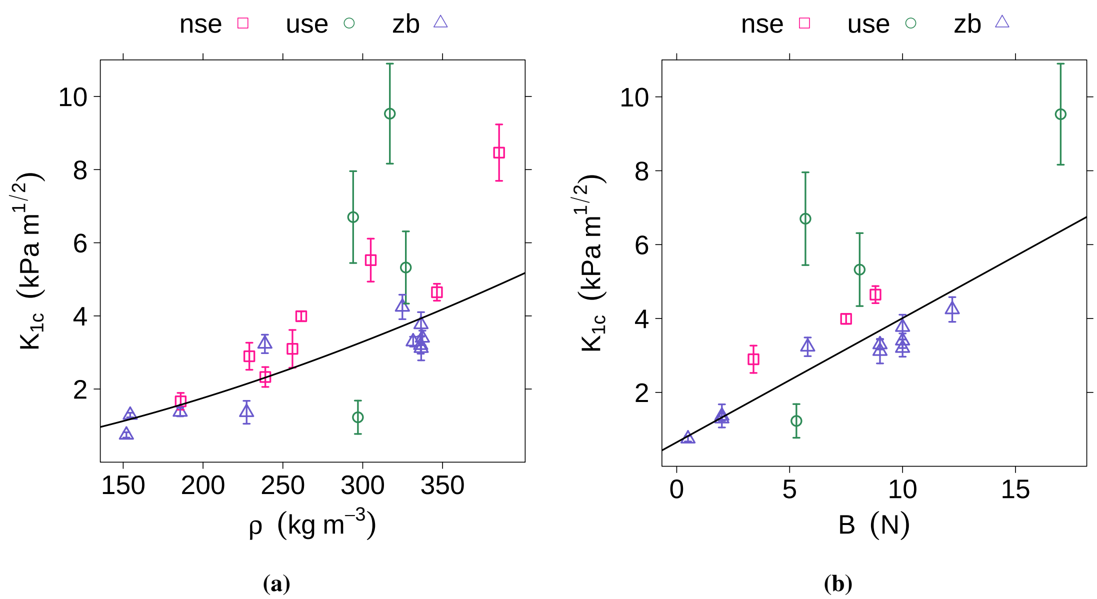

Figure 5.20: *(a) Fracture toughness versus density (n = 23) for all data sets from this chapter, with the best fit of Equation 5.50; (b) Fracture toughness versus blade hardness index B for only those series for which the blade hardness was measured (n = 17). Data points are grouped by type of experimental method and analysis, with "nse" = notched size effect method, "use" = unnotched size effect method and "zb" = zero-brittleness (notched/unnotched) method.*

5.5.1 Fracture toughness versus density

Using density as the predictor variable for fracture toughness, a weighted nonlinear regression through all the data in this chapter led to the model

$$K_{Ic} = (19 \pm 4)\left(\frac{\rho}{\rho_{ice}}\right)^{1.5\pm0.2} \tag{5.50}$$

with K_{Ic} in kPa $m^{1/2}$. This relation is represented by the solid line in Figure 5.20a. Both regression coefficients were statistically significant at the $\alpha = 0.05$ level. Not surprisingly, the goodness of fit of this relation was relatively poor (R^2 = 0.58), due to aggregating data with varying relative uncertainties from different data sets. The residual structure of this model was constant except for one outlier, and the residuals were normally distributed. The runs test indicated lack of independence of the residuals, but this is often the case when grouping data from different sources (see, for example, Section 4.3).

Since the largest relative weight in the regression was given to the high-confidence data points from the notched/unnotched tests, Equation 5.50 is very close to the regression model that resulted from the notched/unnotched method alone. The leading coefficient is about 25% higher here due to the influence of the slightly higher values of fracture toughness from the notched size effect tests. The weighted regression gave very little relative weight to the data points from the unnotched test series.

It is noteworthy that the fracture toughness scaling exponent of 1.5 in Equations 5.50, 5.48, and 5.28 is equal to the theoretical value for the scaling of fracture toughness with relative density (bulk density divided by the solid density of the matrix material) for an open-celled solid (*Gibson and Ashby*, 1988). This study is the first to find such agreement. Previous relations for the scaling of fracture toughness with relative density (Figure 5.21) have always found larger scaling exponents. High scaling exponents are a drawback of expressing snow properties using power laws as a function of density (*Mellor and Smith*, 1966).

The theoretical foundation for cellular solids only applies for relative densities less than about 0.3 (*Gibson and Ashby*, 1988), which for snow is about 275 kg m^{-3}, only partially inclusive of the density range of interest in avalanche studies. Additionally, the most fundamental structural property of a cellular solid is the relative density (bulk density divided by solid density) (*Gibson and Ashby*, 1988), which, though widely used for snow studies and used throughout this thesis, is not the most fundamental property of snow. The inadequacy of density to completely describe the mechanical properties of snow has been stated widely in snow mechanics, and has been soundly demonstrated by the penetration resistance data in this study. This calls into question the general applicability of cellular solid theory for snow mechanics (e.g. *Kirchner et al.*, 2001), though there may be some parallels in the theory that could shed light on the response of low density snow, including relations that describe the anisotropy and connectivity of the matrix structure.

5.5.2 Fracture toughness versus blade hardness index

For the test series in which the blade hardness index B of the samples was measured (Figure 5.20b), the relation between fracture toughness and B, found using weighted least squares linear regression, took the form

$$K_{Ic} = (0.65 \pm 0.17) + (0.34 \pm 0.03)\,B, \tag{5.51}$$

with K_{Ic} in kPa m$^{1/2}$ and B in N. This relation had an adjusted $r^2 = 0.87$, and visually explains the data better than the toughness-density relation (Equation 5.50). The blade hardness index was better at explaining the variability in the fracture toughness data from the unnotched size effect tests, though the scatter in these results is still quite large. Note also that fewer data points are present in Figure 5.20b than Figure 5.20a because some test series did not include measurements of the blade hardness index. For the points that are in common for both graphs and regressions, the blade hardness index relation (Equation 5.51) is a better representation of the fracture toughness data.

Both regression curves in Figure 5.20 essentially neglect the unnotched size effect data points. Standard unweighted regression was not considered appropriate here given the grouped nature of the data and the large difference in relative uncertainties both within and among data sets.

5.5.3 Comparison with previous fracture toughness regression models

A comparison between previously reported relations between fracture toughness and density is superimposed on data from the present study in Figure 5.21. The scaling exponents from previous studies vary in the range 1.9–2.4. The relations reported by *McClung and Schweizer* (2006) and *Sigrist* (2006) are the only other results that considered the effects of a large fracture process zone; the remaining studies applied fully brittle (LEFM) relations *a priori* to experimental data.

The relation expressed by Equation 5.50 in Figure 5.21 predicts the highest mean fracture toughness of any published relation for snow densities below about 225 kg m^{-3}. At higher densities, only the relations reported by *Sigrist* (2006) and *McClung and Schweizer* (2006)–the only other quasi-brittle relations–predict higher mean toughness, owing to the higher scaling exponents in these relations. However, these two relations overshoot the second-order accurate data from the zero-brittleness method, clustered around a density of 330 kg m^{-3}, falling nearer to the less accurate first-order data from the notched and unnotched size effect methods.

5.5.4 Error terms in size effect law derivations

The series expansions of the geometric functions $g(\alpha)$ and $k(\alpha)$ used in the derivation of each size effect relation in this chapter contained the ratio c_f/D. For both the notched and unnotched size effect relations, expansions were truncated beyond terms linear in c_f/D (hence the first-order accuracy). This truncation–as

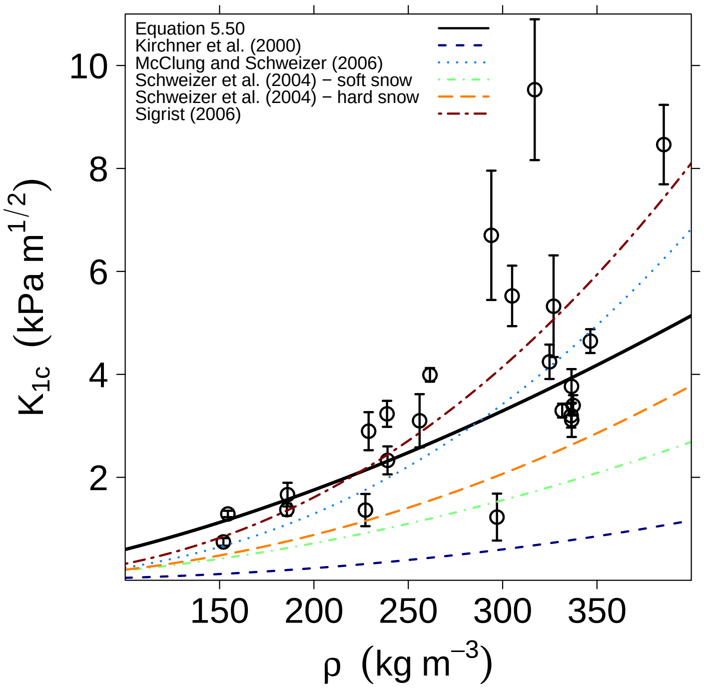

Figure 5.21: *Comparison of the fracture toughness-density data and regression model from the present study to relations reported in other studies.*

well as the use of c_f in place of Δa_{ec} in each derivation–requires an assumption that c_f/D is small, or, rather, that sufficiently large test specimens are used. This important assumption is revisited here. Figure 5.22 shows kernel density plots of the ratio c_f/D for each of the three groups of data in this chapter. For the notched and unnotched size effect data (Figures 5.22a and 5.22b, respectively), c_f/D typically falls between about 0.05 and 1 with a central tendency for each series around 0.2.

The error in the linear series expansion for the notched and unnotched relations is on the order of $(c_f/D)^2$. For the notched size effect data, this second-order error term has a mean, across all series and specimen sizes, of just under 10%. However, the maximum error terms in each series, arising from the smallest specimen sizes, is as high as 25% for series I from Sigrist's data and 75% for series NSE5. For the unnotched size effect data, the aggregate mean error term is also around 10%, but the maximum values are around 50%. These results suggest that the smallest sample sizes used in the size effect tests–both in the present study and by *Sigrist* (2006)–are probably too small for valid analysis using Bažant's first-order size effect laws.

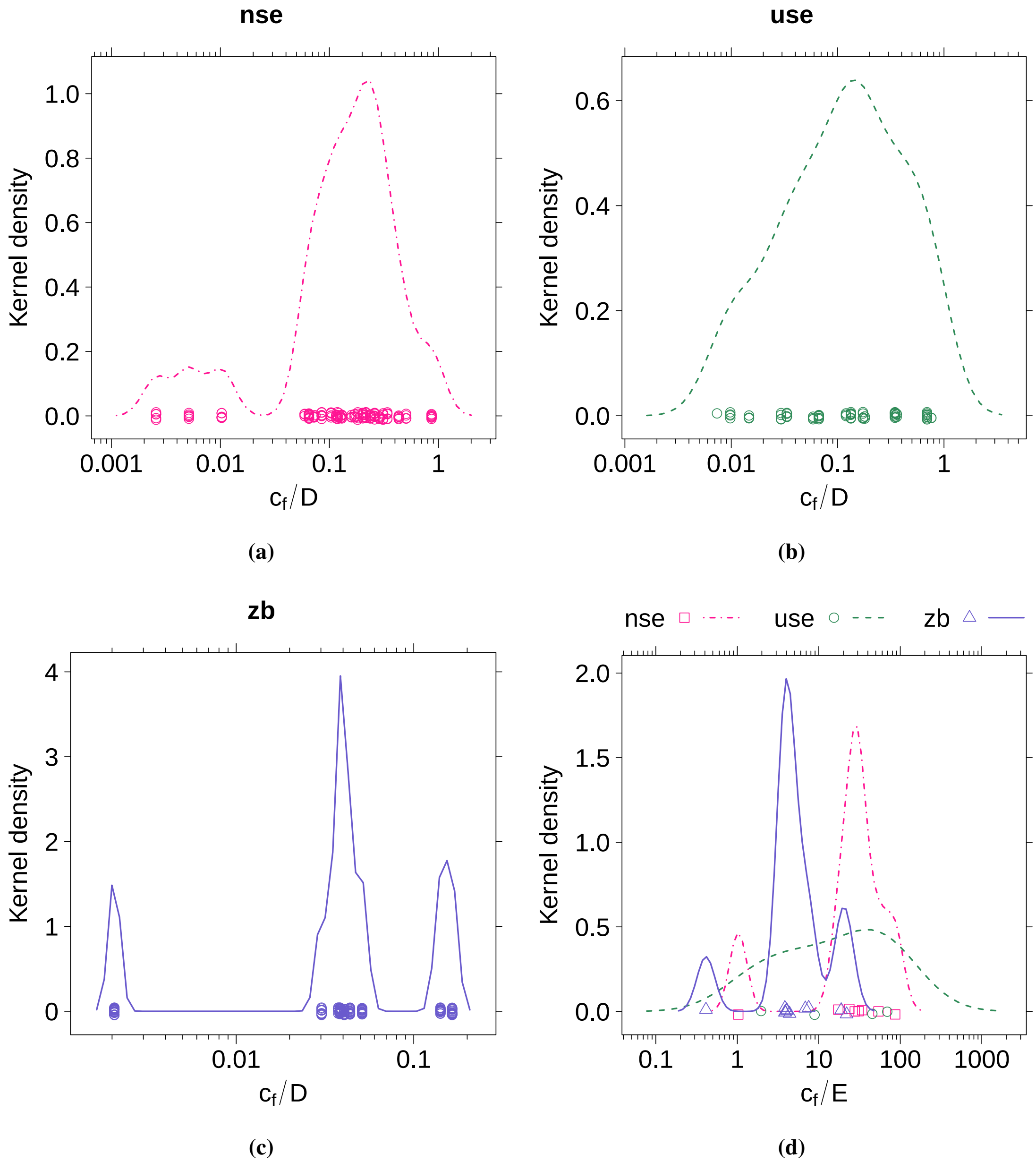

Figure 5.22: *Ratios of c_f/D used in the series approximations and expansions in the derivation of the size effect laws (a-c) and ratio c_f/E expressing the scaling of the effective process zone length with the grain size (d). Data points are grouped by type of experimental method and analysis, with "nse" = notched size effect method, "use" = unnotched size effect method and "zb" = zero-brittleness (notched/unnotched) method.*

For the zero-brittleness data, the ratio c_f/D is much smaller (Figure 5.22c). The series expansion for the universal size effect law retained the term quadratic in c_f/D, so the error in the series expansion is on the order of $(c_f/D)^3$. The mean value of this error term is around 0.1%, and the maximum error is less than 0.5% for the notched/unnotched test data analyzed here. This is in stark contrast with the errors associated with the two first-order size effect relations. The higher-order accuracy likely explains the lower uncertainty in the fracture parameters determined using the zero-brittleness method. The use of c_f in place of Δa_{ec} in the equivalent elastic crack approximation (e.g. the limit in Equation 5.12) appears to be more appropriate for the notched-unnotched testing technique and subsequent data collected here.

The value of c_f, non-dimensionalized using the grain size E, is compared for each of the three size effect data sets in Figure 5.22d. For the notched and unnotched size effects, this ratio peaks between 10 and 100 times the grain size. For the zero-brittleness data, the peak lies around 4-5 times the grain size but the mean value is 10 times the grain size.

In the absence of micromechanical relations or experimental data on strain localization, expressing a relationship between c_f and the actual process zone size involves assuming a specific form of the softening-displacement relationship (e.g. *Bažant and Kazemi*, 1990b). Since the form of the tensile strain softening relationship for snow is still highly uncertain, the actual relationship between c_f and the length of the fracture process zone for snow remains unknown. If the true length of the fracture process zone for snow is around $2c_f$, as it is for concrete (*Bažant and Planas*, 1998; *Bažant*, 2005), then the data here suggest a best estimate, using the zero-brittleness data, of about 10–20 times the grain size for the process zone length.

Conclusions

Three different types of test methods aimed at determining fracture mechanical parameters from experimental data were conducted. A total of 23 new test series covering nearly 300 tests were compiled in the present analysis. The fracture toughness and equivalent fracture process zone length were determined using size effect laws derived from equivalent elastic fracture mechanics. These fracture parameters, calculated from lab-scale tests, are by definition applicable as material properties at the slab avalanche scale, or up to about an order of magnitude larger than the lab scale.

The zero-brittleness method, which allows the combination of notched and unnotched data from a single specimen size, was found to be the most reliable experimental method for determining fracture properties and led to the highest confidence in the resulting parameters. The first-order notched and unnotched size effect laws should probably not be applied to experimental data for snow in the future unless very large specimens are used, though experimental difficulties with the largest specimen sizes successfully tested in this study suggest that larger and sufficiently slender specimens may not be practical to attempt. That said, all three methods considered here give self-consistent results, lending support to the hypothesis that nonlinearity in the fracture of snow can be accounted for using the concept of an equivalent elastic crack. The calculated brittleness numbers suggest that, for all but the very largest avalanches, nonlinear fracture mechanics is necessary to explain the tensile fracture of snow slabs.

Chapter 6

Numerical Simulation of Bending Experiments using Nonlocal Damage Mechanics

6.1 Introduction

The bulk of the analysis in this study has utilized primarily the peak loads measured in bending experiments, which were then used in theoretical relations from beam theory and quasi-brittle fracture mechanics to calculate material parameters related to the tensile fracture of snow. The ability of a continuum damage model to simulate the full load-displacement curves–in addition to capturing the peak load–for both notched and unnotched tests was investigated using the calculated fracture parameters from the experimental data. This provided an indirect check on the applicability of the quasi-brittle relations used to calculate parameters such as the fracture toughness and effective process zone length. An additional aim of the numerical modeling was to explore the applicability of a continuum damage model to simulate the fracture of snow and to provide an initial calibration of model parameters for future predictive modeling applications.

The nonlocal isotropic damage model was selected for numerical simulations of the zero-brittleness (notched-unnotched) data. The model selection was based on physical reasoning related to the heteroge-

This chapter contains material under revision for publication.

neous microstructure of snow and the ability of the nonlocal model to smear out these effects in a tractable, homogeneous continuum framework. The zero-brittleness data were selected for simulating because these data cover a wide range of snow properties and the fracture parameters derived from these data are known with a relatively high level of confidence. Furthermore, deflection measurements were made at three different points of the beam samples in all but one of the zero-brittleness test series, which allowed for the partial separation of the effects of snow crushing at the load point and supports from the true bending of the snow sample as an effective beam, as well as the calculation of an effective elastic modulus and fracture energy from the data. The resulting numerical model parameters were constrained by enforcing a given amount of fracture energy in the local constitutive model during crack advance.

A sensitivity analysis was performed on the model parameters with the most uncertainty, including the nonlocal interaction radius (an important internal length scale), Poisson's ratio, and the stiffness of the bending fixture used in the experiments. A consistent technique was then developed for determining model parameters from the experimental results of each data series. Once this procedure was optimized, all simulations were performed without any additional tuning of model parameters beyond their initial values. Simulations of each of the zero-brittleness series were performed, including the rate-effect test series.

In general, good agreement was found between the numerical and experimental curves for the notched tests. For the unnotched tests the agreement was less satisfactory due to several effects in the experimental data, such as loss of elastic stability at peak load, crushing of snow at the supports and the compliance of the testing machine, all of which complicated the determination of appropriate model parameters. However, considering the highly variable nature of experimental data for snow–which is inherently a random and heterogeneous material–and the lack of additional parameter tuning to improve the fits, the numerical procedure was largely successful as a first step toward more sophisticated modeling scenarios related to avalanche triggering and release.

6.1.1 Continuum approximations of heterogeneous materials

Snow and other heterogeneous materials such as ice, concrete, rocks, and ceramics are all assumed to develop a relatively large and diffuse zone of microcracking prior to the coalescence and propagation of a traction-free macrocrack and ultimate tensile failure. This has been shown conclusively using spatially located acoustic emission data for materials such as concrete (*Otsuka and Date*, 2000), for kilometer-scale ice shelf rifts using seismic signals (*Bassis et al.*, 2007), and is supported qualitatively by the rate of acoustic emissions observed in snow fracture experiments (*St. Lawrence et al.*, 1973; *St. Lawrence and Bradley*, 1975). The presence of a large fracture process zone leads to a number of important features in the global response of these structures to loads, including inelastic stress-strain response prior to peak load, strain softening, and a nonlinear size effect on nominal strength and fracture energy. Furthermore, the existence of a relatively large fracture process zone introduces an intrinsic material length scale related to the material microstructure (*Cotterell and Mai*, 1996).

The physical source of an intrinsic material length scale in quasi-brittle materials is related to the heterogeneity of the microstructure. This heterogeneity has a number of implications, notably a minimum length scale for which the material can be reasonably approximated using homogeneous continuum concepts (*Bažant and Jirásek*, 2002). For many quasi-brittle materials, this length scale can be related to the presence and interaction of microcracks ahead of the fully localized macrocrack or to a minimum length scale over which strain can localize, features which are often scaled with the grain size (e.g. *Bažant*, 1991, 1994; *Bažant and Planas*, 1998). For a highly porous material such as snow, this length scale might be related to the grain size, the pore size, or the grain spacing (or some combination thereof). For cohesive snow at the grain scale, continuum concepts clearly do not apply in the strict sense. One must go to a length scale or a Representative Volume Element (RVE) that includes many grains before continuum relations, such as common stress-strain laws, can be applied with generality to independent (though no longer infinitesimal) volume elements (e.g. *Salm*, 1971).

Compared to LEFM, for which closed-form analytical solutions exist for many types of crack problems, it is often more advantageous to investigate quasi-brittle material numerically. However, numerical models of quasi-brittle tensile failure can suffer from a number of problems, notably spurious localization of damage and energy dissipation into a zone of decreasing size with mesh refinement (e.g. *Pijaudier-Cabot and Bažant*, 1987). Furthermore, strain softening and localization leads to a loss of ellipticity of the boundary value problem describing the material physics, and mathematically the problem becomes ill-posed (*Jirásek and Patzák*, 2002).

These numerical difficulties associated with continuum approximation of a heterogeneous material have been successfully addressed, in a smeared sense, using variety of nonlocal extensions of the constitutive relation whereby a reasonably chosen variable (often the strain) is formulated as an integral or gradient function of neighboring points in addition to the point of interest (*Bažant and Jirásek*, 2002). This average strain measure then accounts for, in a smeared sense, the material heterogeneity and effectively sets a lower bound on the length scale over which strain can localize in the model. A damage function, which acts to degrade the stiffness or load-bearing capacity of the material once an elastic threshold is reached, is expressed as a function of the nonlocally calculated strain measure. Nonlocal damage formulations have proven successful in replicating observed experimental features in quasi-brittle fracture tests (such as strain softening and size effects), without mesh sensitivity problems, for many materials (*Bažant and Jirásek*, 2002). However, this approach has never been applied–until now–to the fracture of snow.

6.2 Background

6.2.1 Continuum damage mechanics

Continuum damage mechanics is a theoretical framework that accounts for the *effects* of cracking on material response without explicitly seeking to resolve individual cracks as in fracture mechanics. Compared to fracture mechanics, which needs fine mesh resolution in the vicinity of crack tips to capture the stress singularity, damage mechanics is relatively efficient computationally. The primary elements of continuum damage mechanics are (e.g. *Lemaitre*, 1996):

1. Quantification of damage with a state variable ω, which can take values between 0 (fully intact material) and 1 (fully damaged or cracked)

2. Modification of the constitutive relation using the damage variable

3. Evolution of damage according to first principles or empirical relations appropriate for the material

An advantage of this theory over fracture mechanics is the ability to use the existing constitutive formulation of the undamaged material. In this chapter, linear elasticity is assumed as an appropriate framework. The strain rate in the experiments was high enough that any creep strains at failure should be small, which allows a quasi-elastic analysis using a secant modulus or an inverse compliance function in place of Young's modulus (*Bažant and Gettu*, 1992). However, the same general approach can be applied in a viscous (creep damage) framework (*Pralong and Funk*, 2005) or a viscoelastic framework (*Pralong et al.*, 2006) with the same physical interpretation of the damage variable.

In a standard "local" continuum, the stress at a mathematical point depends uniquely on the strain (or strain rate) at the same point. In heterogeneous materials, however, the Representative Volume Element (RVE) over which a continuum mechanical approximation of the material behaviour is appropriate is limited by a lower bound length scale. For example, the lower-bound length scale for homogeneous continuum approximation of polycrystalline ice is on the order of 10–100 times the grain size (e.g. *Dempsey et al.*, 1999b; *Mulmule and Dempsey*, 2000; *Schulson and Duval*, 2009). In other words, the concept of a mathematical point does not strictly apply when writing continuum physical relations for heterogeneous materials. The RVE must be large enough to smear out the actual material heterogeneity in a continuum approach. This can be done by defining the stress at a point using a spatially averaged field of strain in the vicinity of the point. The "nonlocal" length scale over which this averaging is taken should be physically related to the scale of the material heterogeneity, which governs the length scale over which energy is dissipated by microcracking and other damage processes in macroscopic crack formation and propagation (*Bažant and Jirásek*, 2002).

For a highly porous material such as snow, the RVE should be expected to have a size many times larger than the grain size (Figure 6.1). The length scale characterizing the RVE might also be expected to be related to a continuum fracture mechanical length scale, such as the critical equivalent elastic crack extension c_f. In the previous chapter, the effective process zone length scale c_f arose from a homogenization technique for analyzing the nonlinear fracture properties of snow using an equivalent elastic crack which obeys LEFM. Conceptually, the "nonlocal" continuum damage mechanics approach outlined here is a similar homogenization technique. The difference is that damage mechanics is particularly well-suited to numerical modeling.

Fundamental to nonlocal formulations of continuum damage mechanics is the definition of the characteristic length scale that represents the extent of the damage zone associated with cracking. Numerically, including this length scale in the continuum formulation (and any resulting scaling laws) ensures that the numerically-resolved regions of damage and the trajectory of major cracks are insensitive to the orientation and resolution of the finite element mesh. Traditional or "local" continuum fracture and damage mechanical models often suffer from mesh sensitivity problems (e.g. *Bažant and Planas*, 1998). Nonlocal models are

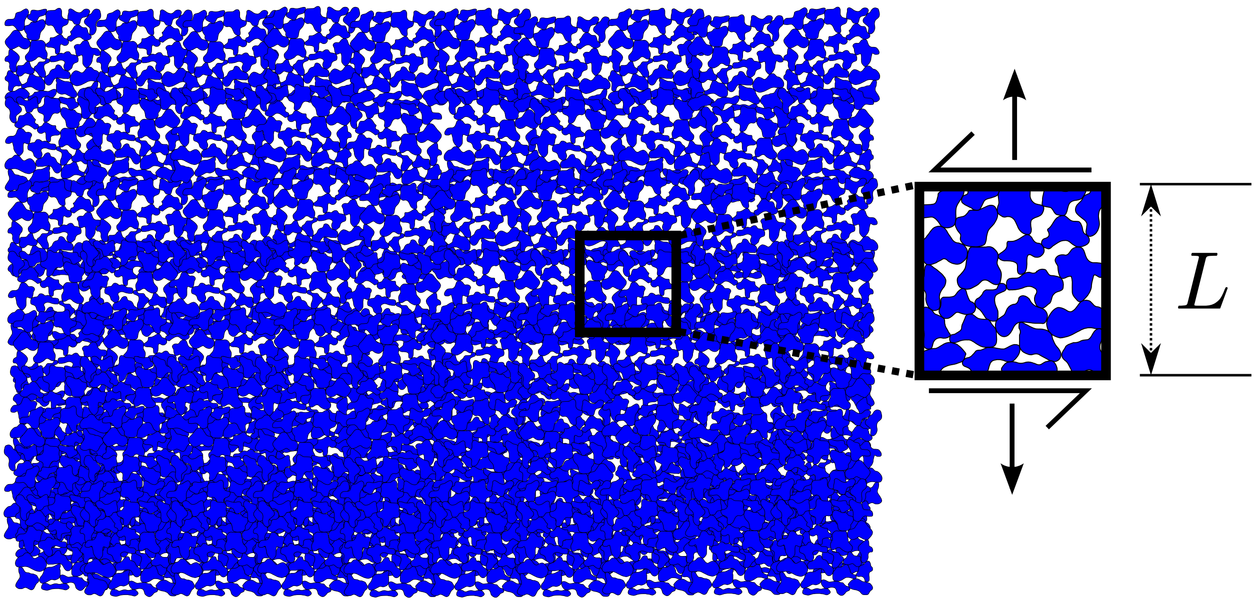

Figure 6.1: *Representative Volume Element (*RVE*) in the homogenization of snow as a continuum for numerical modeling. A length scale L, some multiple of the grain size, defines the minimum size for which continuum relations are valid for an arbitrarily selected* RVE.

insensitive to the mesh resolution as long as the element size is smaller than about 1/3 the width of the damage zone around the crack (*Bažant and Jirásek*, 2002). This allows nonlocal damage models to have much coarser mesh resolution than would be required if using fracture mechanics.

6.2.2 Nonlocal isotropic damage model

In elastic damage mechanics, the damage state variable ω typically degrades the material stiffness. If the degradation of stiffness is assumed to take place isotropically, ω is a scalar variable at all points in the material. However, the nature by which cracks are oriented with respect to applied stresses typically leads to some degree of anisotropy of material properties during damage. The isotropic assumption can be relaxed in numerous ways, all of which lead to a tensorial form of ω (*Bažant and Jirásek*, 2002). However, the simplifying assumption of isotropic stiffness degradation is appropriate for materials which fail due to void formation and growth (*Jirásek and Grassl*, 2008), and should therefore be a reasonable starting point for a highly porous material such as snow.

The nonlocal isotropic damage model (e.g. *Jirásek and Patzák*, 2002) was chosen for the numerical simulations. Assuming a linear elastic framework, the constitutive relation for the damage model takes the form

$$\boldsymbol{\sigma} = (1-\omega)\boldsymbol{D}^e\boldsymbol{\varepsilon} \tag{6.1}$$

where $\boldsymbol{\sigma}$ is the stress, $\boldsymbol{\varepsilon}$ is the strain, $\boldsymbol{D}^e$ is the elastic stiffness matrix and ω is the scalar damage parameter, which can take values between 0 (virgin linear elastic material) and 1 (fully damaged). Bold symbols indicate tensor quantities.

A loading function, analogous to the plastic potential function in plasticity, defines the elastic space of the material. The loading function has the form

$$g(\boldsymbol{\varepsilon}, \kappa) = \bar{\varepsilon}(\boldsymbol{\varepsilon}) - \kappa \tag{6.2}$$

where κ is an internal history variable corresponding to the maximum previous level of equivalent strain reached in the material and $\bar{\varepsilon}$ is the nonlocal scalar equivalent strain. Several definitions of equivalent strain are possible. Here we use the Rankine criterion of maximum principal stress, which is first calculated locally as

$$\tilde{\varepsilon} = \frac{1}{E}\sqrt{\langle \boldsymbol{s}^e \rangle^T \langle \boldsymbol{s}^e \rangle} \tag{6.3}$$

where $\tilde{\varepsilon}$ is the local strain, E is Young's modulus, $\boldsymbol{s}^e$ is a column matrix of principal effective stresses, and the positive-part operator is used to restrict the damage formulation to tensile stress states only, since most quasi-brittle materials fail mainly in tension (*Jirásek and Patzák*, 2002). This simplification may not be entirely applicable for snow in general, but should be appropriate for simulation of the flexural experiments in which the primary failure of the snow samples was in tension.

To make the damage formulation nonlocal, the nonlocal equivalent strain $\bar{\varepsilon}$ is calculated from the local equivalent strain $\tilde{\varepsilon}$ via an integral formulation:

$$\bar{\varepsilon}(x) = \int_V \alpha(x,\xi)\tilde{\varepsilon}(\xi)d\xi \tag{6.4}$$

where $\alpha(x,\xi)$ is the nonlocal weight function which depends only on the distance $r = \|x-\xi\|$ between the current integration point (x) and a neighboring point (ξ). A piecewise polynomial bell-shaped weight function is used here, which has the form

$$\alpha(r) = \begin{cases} \left(1 - \frac{r^2}{\mathsf{R}^2}\right)^2 & \text{if } |r| < \mathsf{R} \\ 0 & \text{if } |r| \geq \mathsf{R} \end{cases} \tag{6.5}$$

where R is defined as the nonlocal interaction radius. The proper value of R depends on the material microstructure and is commonly taken as half the fracture process zone width (e.g. *Hadjab-Souag et al.*, 2007). If the fracture process zone length is about $2c_f$, and if the length and width of the FPZ are about the same, then to a first approximation $\mathsf{R} \approx c_f$.

An exponential strain softening law was chosen for the evolution of the damage parameter ω,

$$\omega = \begin{cases} 0 & \text{if } \kappa \leq \varepsilon_0 \\ 1 - \frac{\varepsilon_0}{\kappa} \exp\left(-\frac{\kappa - \varepsilon_0}{\varepsilon_f - \varepsilon_0}\right) & \text{if } \kappa > \varepsilon_0 \end{cases} \tag{6.6}$$

where $\varepsilon_0 = f_t/E$ is the limit elastic strain under uniaxial tension and ε_f is a ductility parameter related to the initial post-peak slope of the softening curve. The parameters ε_0 and ε_f are related by

$$\varepsilon_f = \varepsilon_0 - \frac{f_t}{E_t} \tag{6.7}$$

where f_t is the uniaxial tensile strength and $E_t < 0$ is the initial post-peak tangent modulus of the exponential softening law.

Jirásek et al. (2004) showed that the energy dissipated by the nonlocal isotropic damage model in a uniaxial tensile test is

$$G_F = kRg_f \tag{6.8}$$

where k is a proportionality constant in the range 1.5–1.8 depending on the ratio of $\varepsilon_f/\varepsilon_\circ$, R is the nonlocal interaction radius, and g_f is the local dissipation density, equal to the area under the local stress-strain curve. For the exponential softening relation used here, the area under the stress-strain curve is $g_f = f_t(\varepsilon_f - \varepsilon_\circ/2)$ and is interpreted as the energy dissipated per unit volume of fully damaged material in uniaxial tension

(*Jirásek and Patzák*, 2002). Plugging this relation for g_f into Equation 6.8 leads to the following relation

$$\varepsilon_f = \frac{G_F}{k\mathsf{R}E\varepsilon_\circ} + \frac{\varepsilon_\circ}{2} = \frac{G_F}{k\mathsf{R}f_t} + \frac{\varepsilon_\circ}{2} \tag{6.9}$$

which can be used to enforce the correct amount of fracture energy dissipation in the model (*Jirásek et al.*, 2004). The parameter $\varepsilon_\circ$, though defined as a uniaxial strain value, was specified here from the results of bending tests. From Equation 6.9, different combinations of R and ε_f can achieve the same energy dissipation. The ductility of the local constitutive relation can be expressed by the ratio $\phi = 2\varepsilon_f/\varepsilon_\circ - 1$.

In this formulation of the isotropic damage model, the strain is fully reversible upon unloading but the damage is not–the material stiffness is degraded for any subsequent reloading. This type of approach could be extended to include the effects of viscosity or plasticity, which would allow for permanent strains and might be more realistic in some scenarios. However, the experiments being simulated here were designed to fail in a single rapid load step in a manner similar to the tensile failure in slab avalanches. Repeated loadings, cumulative damage or load hysteresis, which would certainly be present in cyclic loading for most types of snow, were beyond the scope of the present analysis and modeling.

The required input parameters for this version of the nonlocal isotropic damage model are Young's modulus E, Poisson's ratio ν, the strain parameters ε_0 and ε_f, and the nonlocal interaction radius R. The polycarbonate load and support plates in the experiments were also represented in the finite element simulations here, and were specified as linear elastic with two parameters E and ν. The elements corresponding to the load and support plates were excluded from the nonlocal averaging in the damage model.

6.2.3 Beam theory for experimental load-displacement curves

Selection of model parameters required a determination of the appropriate value of Young's modulus for the experiments. Given the short load span used in most of the bending experiments in the present study, the central beam deflection was affected by shearing within the beam. The effects of shearing were accounted for using Timoshenko beam theory. The total deflection at the midspan of a simply-supported beam with a central load, accounting for the effects of shearing, is

$$\delta = \frac{PS^3}{48EI_z}\left(1 + 2.85\left(\frac{D}{S}\right)^2 - 0.84\left(\frac{D}{S}\right)^3\right) \tag{6.10}$$

where P is the peak load, S is the beam span, E is Young's modulus, I_z is the second moment of area and D is the beam depth (*Timoshenko*, 1940). Thus an effective value of Young's modulus E can be calculated from the measured deflection δ at the bottom of the beam for a given load P. For a beam with a rectangular cross section, $I_z = bD^3/12$. All of the zero-brittleness data simulated in this chapter had a span to depth ratio S/D = 2.5 and beam depth D = 10 cm. Substitution of the values into Equation 6.10 led to the following relation for an effective Young's modulus given the peak load and total deflection at peak load via

$$E = \frac{5.48P}{b\delta}. \tag{6.11}$$

Since peak values of P and δ were substituted into Equation 6.11, the resulting values of E are formally secant moduli at peak load. However, pairs of P, δ at any appropriate point of the loading curve, such as the proportional limit, could be used to calculate E. For the experimental data in the present investigation, it was not possible to uniquely and consistently determine a point on the loading curve that could be considered a proportional limit.

Given values of E calculated using Equation 6.11 and fracture toughness K_{Ic} from the zero-brittleness data analysis (Chapter 5), the fracture energy for each series was calculated using the Griffith-Irwin relation

$$G_F = \frac{K_{Ic}^2}{E}. \tag{6.12}$$

The fracture energy values were used, in combination with E and f_t from the experimental data (as well as the critical equivalent crack extension c_f, which was used to select the nonlocal interaction radius R) to determine the numerical model parameters via Equation 6.9.

6.2.4 Experimental methods

The experimental data considered in this chapter were composed of notched and unnotched tests of a single specimen size. The experimental procedures for these experiments and the calculation of material and fracture parameters were discussed in Section 5.4. For all but series Z1, deflection measurements were made (in addition to the crosshead displacement) at the midspan of the beam and on top of the beam above one of the supports using LVDTs. The placement of these LVDTs is shown schematically in Figures 6.2 and 6.3 with the finite element meshes used in the numerical simulations. Refer to Table 5.6 for information on the remainder of the zero-brittleness test series (page 205).

6.2.5 Numerical methods

The finite element meshes used in the notched and unnotched simulations are shown in Figures 6.2 and 6.3. The meshes were created using the meshing software *Gmsh* (*Geuzaine and Remacle*, 2009). For the unnotched simulations, the element size was smallest (on the order of 1 mm) at the bottom of the sample where the tensile stresses and strains were highest. For the notched tests, a similar element size was used near the notch tip. Constant-strain triangular elements were used throughout, and the analysis was conducted assuming plane stress conditions.

A displacement-controlled boundary condition was applied to the top central node of the support plate (tip of the arrow in the figures). The polycarbonate load plate and supports were assumed to behave linear elastically. Young's modulus of the supports was varied to investigate the effect of the fixture compliance on the results.

The simulations were performed using the open source finite element software OOFEM, version 2.0 (*Patzák and Bittnar*, 2001; *Patzák et al.*, 2001) operating on an Ubuntu Linux desktop PC with 2 GB of RAM and a dual-core 3.2 GHz processor. Post-processing of numerical results was carried out using ParaView, and the python library matplotlib was used for plotting.

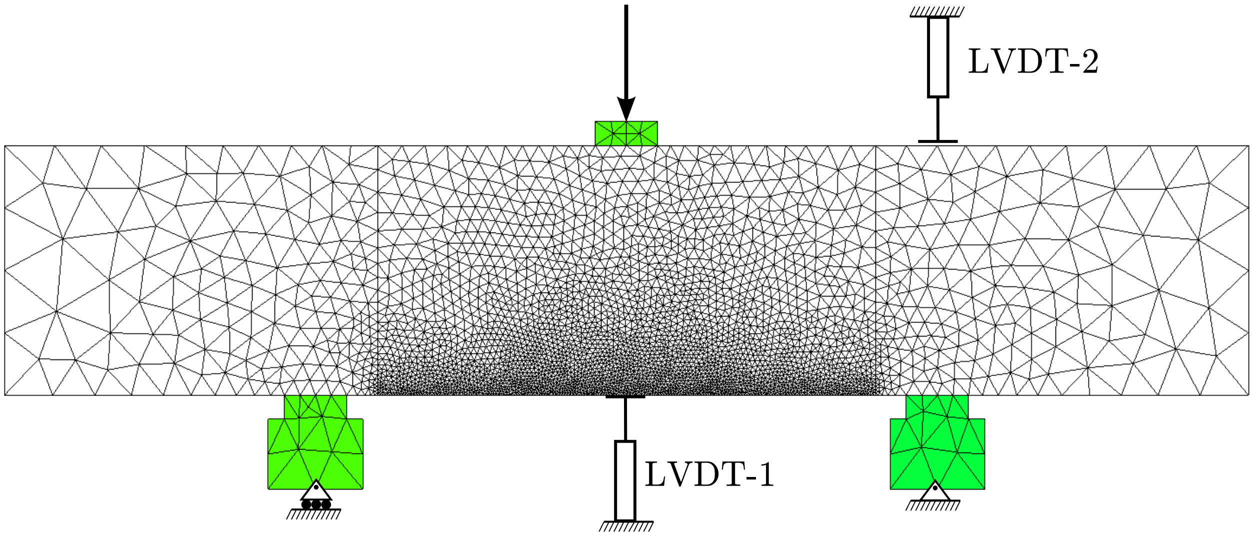

Figure 6.2: *Finite element mesh for simulating unnotched beam bending tests, showing boundary conditions and the location of displacement measurements in both the experiments and the simulations. The midspan deflection measured by* LVDT-*1 was referenced to* LVDT-*2 to account for any effects of settling or crushing at the supports.*

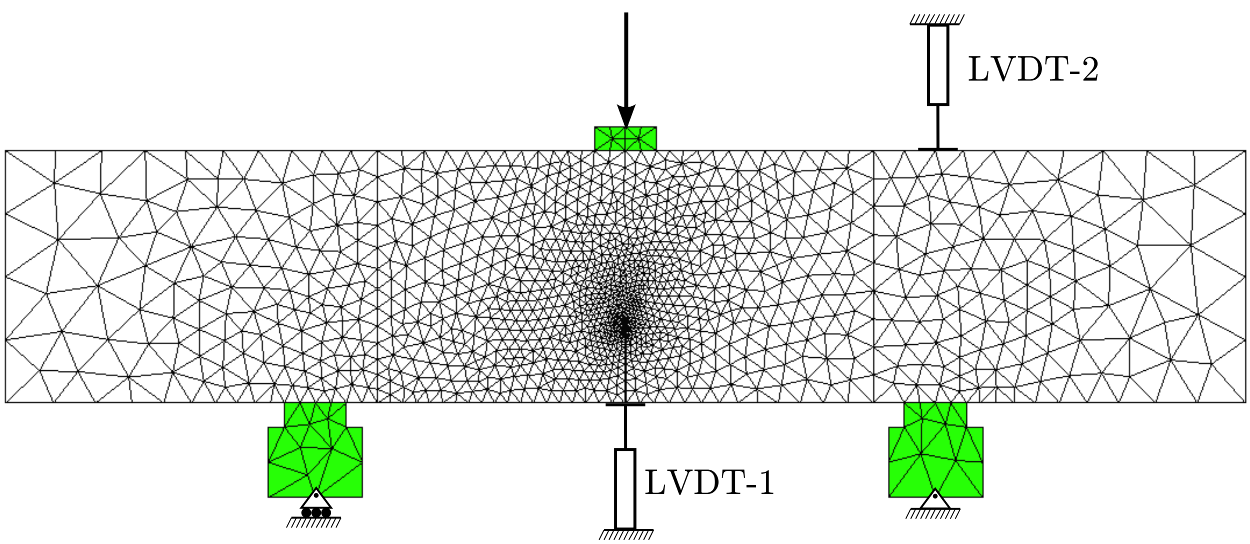

Figure 6.3: *Finite element mesh for simulating notched beam bending tests (relative notch depth* $\alpha = 0.3$*), showing boundary conditions and the location of displacement measurements in both the experiments and the simulations.*

6.3 Experimental Results and Analysis

For convenience, the descriptive data for series Z7, which was chosen for a model sensitivity analysis, are given again in Table 6.1. This series was chosen for the sensitivity analysis because the snow was among the lowest density and hardness that was successfully tested, and therefore most likely to be strongly influenced by nonlocal effects. For example, the brittleness of concrete increases with increasing strength (*Gettu et al.*, 1990) and the same might be expected for snow.

The nominal strain rate in the outer fiber of the beams was estimated from simple beam theory as $\dot{\varepsilon} = 6DV/S^2$. For most of the experiments the crosshead speed was $V = 1.25$ cm/s, which leads to a nominal strain rate of about 10^{-1} s^{-1}. Since this strain rate is about three orders of magnitude above the creep-to-fracture transition rate for snow in tension (e.g. *Narita*, 1980), and since the time to failure of the experiments conducted at this rate was on the order of 0.1–0.2 s, the sample response should be predominantly elastic.

For series Z5 and Z6, some tests were conduced at lower speeds and had resulting nominal strain rates of around 10^{-2} s^{-1} or 10^{-3} s^{-1} depending on the loading rate (see e.g. Figures 5.17 and 5.18), though the time to failure of these slow-loading experiments was still small compared to the relaxation time for snow in tension, which is around 300 seconds (*Shinojima*, 1966) . Thus an effective elastic analysis using a secant modulus should be a reasonable approximation to a full viscoelastic solution (e.g. *Bažant and Gettu*, 1992; *Dempsey and Palmer*, 1999).

The measured load-displacement data for series Z7 are shown in Figure 6.4. The loading curves for the notched tests had peak loads around one-third those of the unnotched tests. The notched curves are also

Date	n	$\bar{\rho}$ [kg/m^3]	R	$\bar{B}$ [N]	$\bar{T}$ [°C]	F, E [mm][1]	V [cm/s]
090326	18	155 ± 2	3	2.0 ± 0.5	-5.2 ± 0.5	RG 0.5 / DF 1	1.25

Table 6.1: *Zero-brittleness (notched-unnotched) data set Z7 (originally presented in Chapter 5, Table 5.6) used for numerical model sensitivity analysis, re-presented here for convenience. Samples were fractured in weight-compensated three-point bending with S/D = 2.5, D = 10 cm and loading speed V = 1.25 cm/s. Date is in* yymmdd *format, other column variables include the number of tests (n), mean snow density ($\bar{\rho}$), hand hardness index (R), mean blade hardness index ($\bar{B}$), mean snow temperature ($\bar{T}$), grain forms and grain size (F and* E*, respectively), and crosshead speed (V).*
[1] *Following the International Classification for Seasonal Snow on the Ground (Fierz et al., 2009). Key: RG = rounded grains, DF = decomposing and fragmented crystals.*

more consistently shaped. The loading curves in the load-crosshead displacement data (Figure 6.4a) for unnotched tests are quite irregular, which is interpreted as an effect of crushing of snow below the loading plate and at the supports. This was unavoidable given the low density and low hardness nature of this snow layer. This was a primary reason to measure the displacement at several points of the beam, to be able to approximately account for such effects separate from the deflection of the snow as a bending beam.

The loading curves for all notched tests have some period of linearity up to about 50–75% of the peak load. This is most evident in Figures 6.4b and 6.4c. Near peak load the curves are broadly shaped. Similar qualitative features were observed in the bending experiments of *Sigrist* (2006), though only the crosshead displacement was measured. The loss of pre-peak linearity and rounding of loading curves near peak load in fracture (notched) experiments of other heterogeneous materials is interpreted as the onset of cracking and damage in a relatively large and diffuse fracture process zone (e.g. *Cotterell and Mai*, 1996).

The load-midspan displacement curves (Figure 6.4b) are quite distinct from the load-crosshead curves. The loading curves of the unnotched tests were again more variable than those of the notched tests. The notched curves appear to show a smooth and gradual softening following peak load, while the unnotched curves have a large rounded peak and an apparent snap-back point following peak load.

The measurements of deflection on top of the beam above one of the supports, as shown schematically for LVDT-2 in Figures 6.2 and 6.3, gave an indication of the combined effects of crushing at the supports and the compliance of the bending fixture. The relative midspan displacement measurements in Figure 6.4c were calculated by subtracting the deflections measured by LVDT-2 above the beam from those at the midspan below the beam by LVDT-1. This displacement calculation gives an estimate of the true bending deflection of the beam alone. A similar deflection measurement can be made using a yoke which establishes a similar reference point on top of the beam above the supports. This type of relative deflection measurement using a yoke has been used and recommended for calculations of fracture parameters from bending tests of concrete (e.g. *Banthia and Trottier*, 1995; *Bažant and Planas*, 1998).

The loading curves for the relative midspan displacement measurements (Figure 6.4c) rise more steeply and indicate an apparently stiffer response for the snow than the displacement measurements using the midspan displacement alone (Figure 6.4b). This is moreso the case for the unnotched experiments, which failed at higher loads and suffered greater crushing at the supports than the notched experiments. The

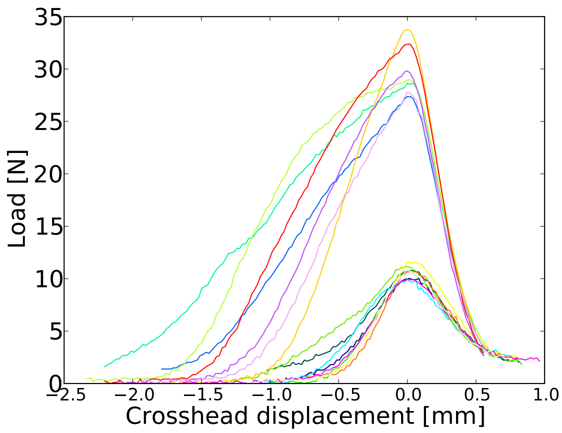

(a)

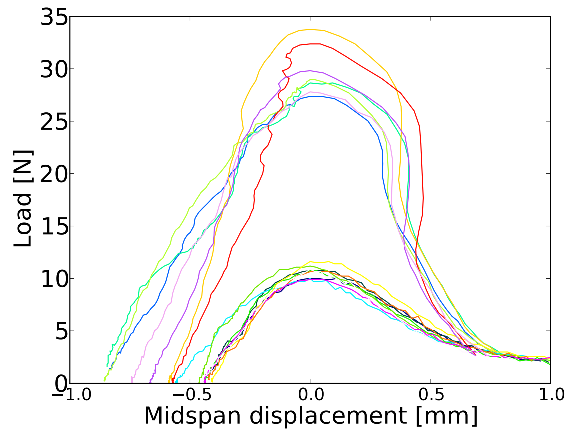

(b)

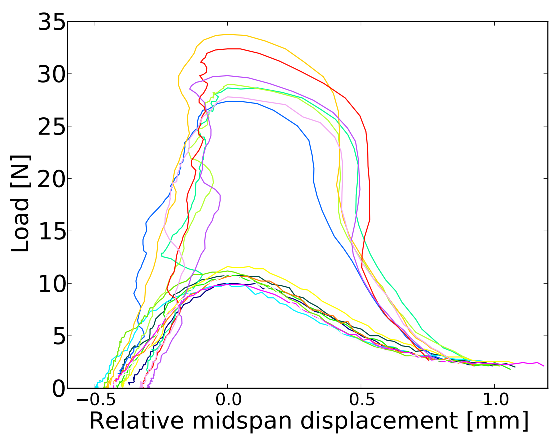

(c)

Figure 6.4: *Loading curves using deflection measured at three different points of the beam in the notched-unnotched (zero-brittleness) series Z7. For clarity in plotting, all deflection measurements are shown relative to peak load.*

negative jumps in displacement for some of the unnotched curves in Figure 6.4c is evidence of an abrupt settling or crushing of the sample at the support below LVDT-2.

The consistent shape of the post-peak curves for the unnotched experiments was interpreted as a result of the loss of elastic stability at peak load (though similar features were observed in notched tests of stronger snow). The bending experiment may be envisioned as a series combination of a spring through which the sample is loaded, with the stiffness of the spring representing the stiffness of the entire testing machine and bending fixture (*Bažant and Cedolin*, 1991). The elastic strain energy stored during the deflection of the load cell and bending fixture recovers elastically near peak load as the tensile crack coalesces and the sample stiffness degrades. This can cause a snap-back in the softening response of the experiment (*Bažant and Planas*, 1998), as observed in Figures 6.4b and 6.4c. The apparent softening response measured using the crosshead displacement (Figure 6.4a) is therefore not a true softening displacement but rather simply a measure of the elastic rebound of the load cell before the crosshead stops.

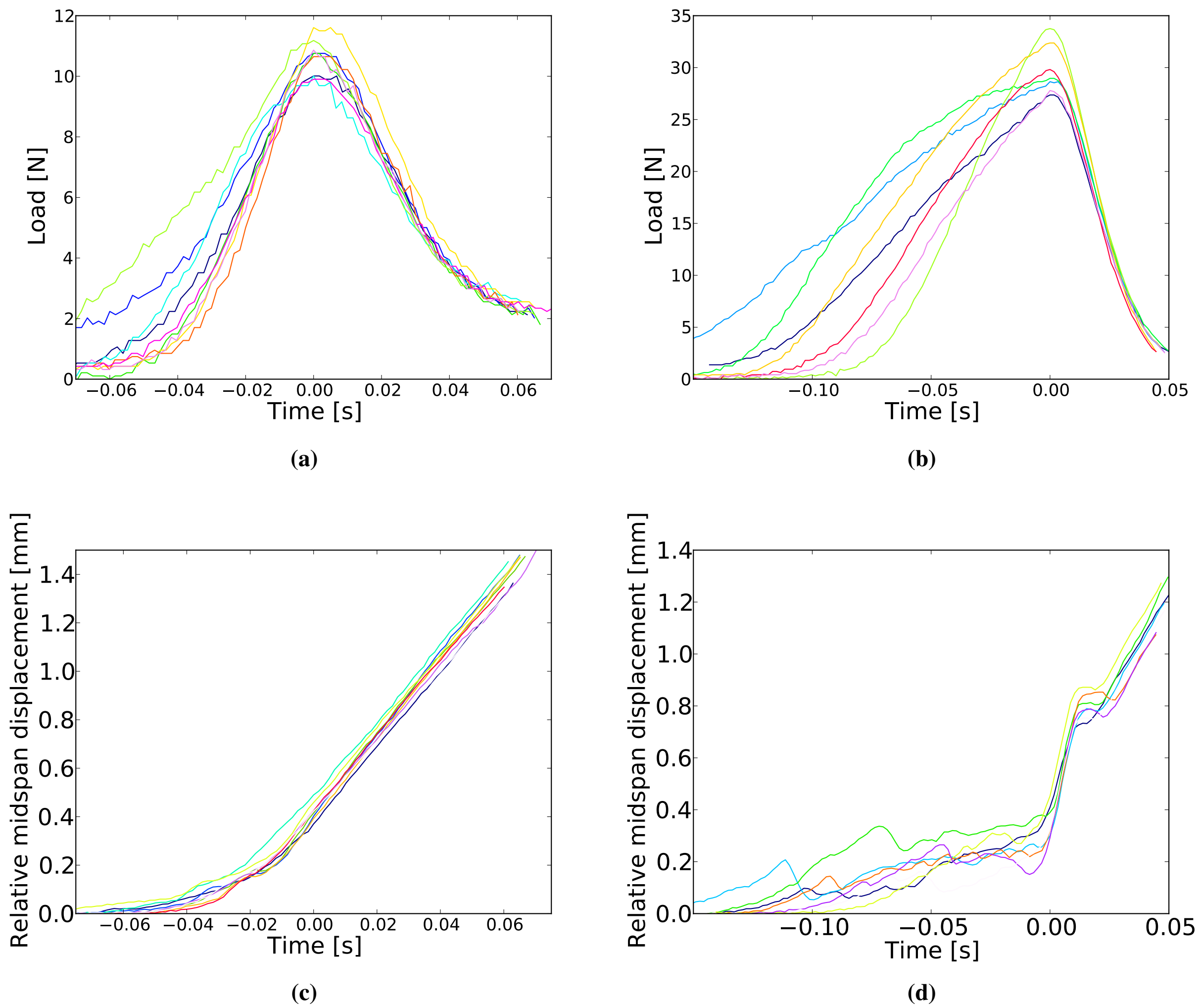

Figure 6.5: *Load and displacement data plotted versus time, showing the dynamic loss of elastic stability near peak load in the experiments. Notched tests are shown in (a) and (c), unnotched in (b) and (d).*

The loss of elastic stability of in the experiments is shown more clearly using the measurements of time that were also recorded during the experiments. The notched and unnotched experiments are separated in

Figure 6.5. The load versus time measurements for the notched and unnotched tests are shown in Figures 6.5a and 6.5b, respectively. These curves have the same shape as their respective load-crosshead displacement curves. The abrupt change in the slope of the relative midspan displacement measurements, plotted on the same time scale, indicate a velocity change near peak load. For the notched experiments (Figure 6.5c), the velocity increases gradually up to the peak load (referenced to $t = 0$ s) and thereafter the sample deflects at a constant velocity. The slope of the displacement-time curve after peak load indicates a deflection speed of about 1.5-1.7 cm/s, which is just slightly higher than the crosshead speed and indicates a small influence of the elastic rebound of the system.

The change in velocity near peak load is much more stark for the unnotched tests (Figure 6.5d). The slope of the displacement-time curve just after peak load in this case indicates a velocity of around 4 cm/s, much higher than the crosshead speed. After a brief period at this speed, the velocity changes again and drops below zero at a time which is coincident with the snap-back point. Thereafter, the velocity levels off to an approximately constant value, closer to the crosshead speed, for the remainder of the softening displacement. These features indicate that the unnotched tests are more influenced by a dynamic rebound of the bending fixture as the tensile crack first coalesces. This is primarily a function of the higher peak load experienced in the unnotched tests. The change in velocity (acceleration) at the bottom of the beam in both Figures 6.5c and 6.5d occurs slightly before the peak load, which is further evidence of the onset of cracking and damage prior to the coalescence of a traction-free crack and ultimate failure of the sample.

6.4 Numerical Results

6.4.1 Model sensitivity analysis

The most uncertain model parameters for the present analysis were Poisson's ratio, the nonlocal interaction radius R, the stiffness of the bending fixture, represented by Young's modulus of the polycarbonate load and support plates, and the fracture energy. In this section, sensitivity analyses of each of these parameters is presented.

As a first approximation, the initial estimate of the nonlocal interaction radius R was taken to be equal to the critical equivalent crack extension c_f computed in Chapter 5. Using this initial value, the ductility parameter ε_f was calculated using Equation 6.9 given an assumed value of $k = 1.5$ and experimentally-derived values of G_F, f_t and E. Figure 6.6 shows the sensitivity of the simulated load-relative midspan displacement curves to a range in values of R. Table 6.2 contains the associated model values, including the ductility parameter ε_f that varied with R to ensure that the same amount of fracture energy was dissipated locally in each of the curves in Figure 6.6.

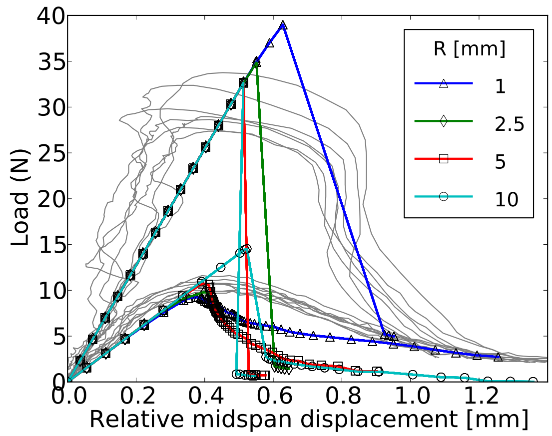

Figure 6.6: *Variation in model results for different values of the nonlocal interaction radius* R. *Corresponding values of ε_f for each simulation are shown in Table 6.2.*

Nonlocal radius	ε_f	ϕ
R = 1	0.040	22
R = 2.5 mm	0.017	9
R = 5 mm	0.0094	4
R = 10 mm	0.0055	2

Table 6.2: *Model parameters for the sensitivity analysis curves in Figure 6.6. The parameter ε_f controls the ductility of the local constitutive relation. The parameter $\phi = 2\varepsilon_f/\varepsilon_\circ - 1$ characterizes the ductility non-dimensionally, with smaller values indicating more brittle response. Parameters that were common to each simulation were a Young's modulus of E = 2.9 MPa, Poisson's ratio of $\nu = 0.3$, and elastic limit strain $\varepsilon_\circ = 0.0034$.*

The simulations for R $= 1$ mm are approximately equivalent to fully local (rather than nonlocal) formulations since the element size was about 1 mm in the regions where the damage initiated for both the notched and unnotched simulations. These simulations also appeared the most ductile for a given fracture energy, as evident in Figure 6.6 and as quantified using the ductility parameter ϕ in Table 6.2. Local models are known to suffer from mesh sensitivity problems (e.g. *Bažant and Jirásek*, 2002) especially if the element size is larger than about 1/3 the interaction radius (*Bažant*, 2005), which was the case for R $= 1$ mm and 2.5

mm here. For increasing interaction radius, the simulated response became more brittle for a given fracture energy. There was little difference for either the notched or unnotched simulations between R = 5 mm and 10 mm. From these simulations, the initial estimate of R $\approx c_f$ appears reasonable.

Published values of Poisson's ratio for snow vary widely depending on the loading rate and geometry and the snow density (e.g. *Shapiro et al.*, 1997), with values as high as 0.5 reported for tension (*Shinojima*, 1966). Differences in Poisson's ratio in tension versus compression have been observed for snow of the same type (e.g. *Bader et al.*, 1954; *Shinojima*, 1966) which further complicates the selection of a single representative value in a model which is conceptually simple relative to the complexity of snow as a model material. Increasing values of Poisson's ratio led to steeper post-peak response in unnotched simulations, with post peak snapback for $\nu = 0.4$ and above. For the notched simulations, the peak load slightly decreased with increasing ν. The results of the sensitivity analysis on Poisson's ratio did not suggest an appropriate selection of ν, so an intermediate value of $\nu = 0.3$ was chosen for subsequent model runs.

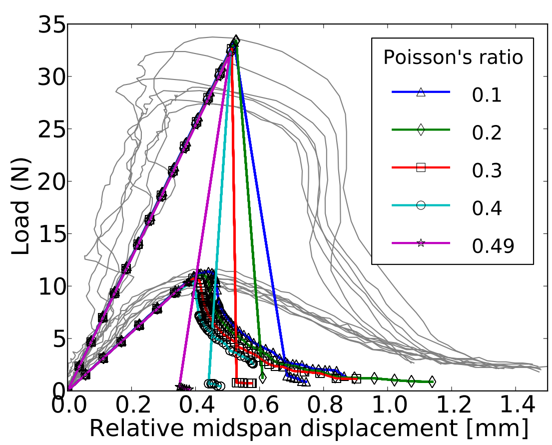

Figure 6.7: *Variation in model results for different values of Poisson's ratio. The remaining model parameters were the same as those listed in Table 6.2 for* R = *5 mm.*

The stiffness of the supports in the experiments was related to the initial unstable post-peak response. The influence of the support stiffness was investigated in the static simulations by varying the ratio between Young's modulus for the supports (E_m, 'm' for 'machine') and that of the snow (E_s). For the notched curves, which had low peak loads and therefore little stored elastic deformation in the supports, there was no discernible difference between any of the simulated curves. There was also little difference between either the notched or unnotched simulations as the stiffness ratio increased from 10 to 100. However, if the supports had the same stiffness as the snow, the peak load in unnotched simulations was reduced and the post-peak response had a shallower slope (Figure 6.8). This is a partial confirmation of the interpretation outlined above for the unstable response of the experimental curves in the vicinity of peak load. Several experiments were conducted with a stiff block of wood in place of the snow to estimate the stiffness of the load cell and bending fixture. The loading curves from these experiments suggested a Young's modulus for the supports of about 30 MPa, which implicitly includes the stiffness of the load cell. This value was used in subsequent model runs, and was in the range of about 1–10 times the modulus of the snow samples depending on the test series.

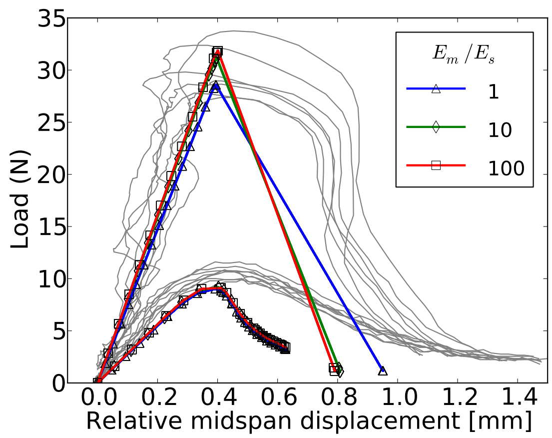

Figure 6.8: *Variation in model results for different values of the ratio between machine stiffness (E_m) and snow stiffness (E_s = 2.9 MPa). Other model parameters were* $\varepsilon_\circ = 0.0024$, $\varepsilon_f = 0.012$, R *= 5 mm and* $\nu = 0.3$.

The simulations in Figures 6.6–6.8 all showed a more brittle response than observed in the experiments. This may have been the result of a calculated value of fracture energy which was too low. *Cotterell and Mai* (1996) argued that the fracture energy calculated from Bažant's size effect methods may underestimate the true fracture energy. *Bažant* (2005) admits that the fracture energy obtained from the quasi-brittle size effect laws is about a factor of 2.5 less than the fracture energy obtained from the work-of-fracture method, which corresponds to the complete area under the stress-strain curve for a softening material. Bažant's fracture energy corresponds to the area defined by the post-peak tangent of the softening curve at which point stability is lost. Since the fracture energy calculated above arose from the quasi-brittle size effect laws, it may therefore be a factor of 2.5 too low for specification in a numerical model which requires a full softening-displacement energy dissipation.

Figure 6.9 shows simulation results for a fracture energy of 2.5 times that calculated above from the Griffith-Irwin relation using the fracture toughness (Chapter 5) and an effective elastic modulus for this test series. Especially for the notched tests, an increased level of energy dissipation led to greater agreement in the shape of the load-displacement curves. For the unnotched simulations, the post-peak response was still rather brittle, though the experimental data may have actually resembled these curves more closely if the load cell and bending fixture been less compliant.

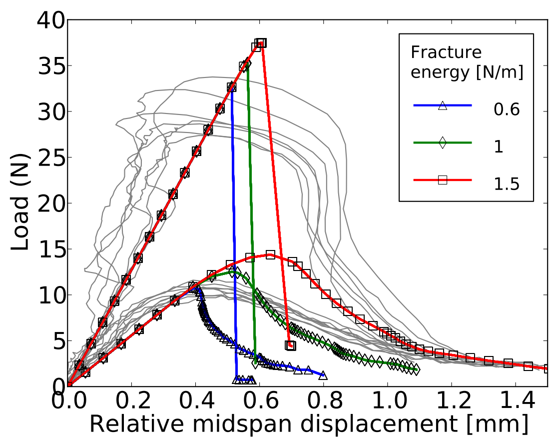

Figure 6.9: *Variation in model results for different values of fracture energy, which determines the model parameter ε_f via Equation 6.9. The remaining model parameters were the same as those listed in Table 6.2 for* R *= 5 mm.*

Though the shapes of the simulated curves, especially for the notched simulations, better resembled the test data, the peak loads increased with increasing fracture energy. Recall that the constitutive relation of the damage model specified the tensile strength and limit elastic strain (and fracture energy, for that matter) as *uniaxial* values, though they were specified here from the results of flexural tests. In general, the flexural strength of quasi-brittle materials is about 15% higher or more than the uniaxial tensile strength (e.g. *Banthia and Sheng*, 1996). As will be seen below, better agreement between simulated and experimental curves was obtained by reducing the flexural strength by 15% from that calculated using the unnotched beam data.

The influence of the boundary conditions at the supports was also investigated, since in the experiments the supports were both pinned. However, the low amount of friction between the snow and the smooth polycarbonate support plates allowed some frictional sliding during the deformation of the beam. For this reason, the use of pinned-pinned boundary conditions in the simulations led to load-displacement curves which were much greater than in the experiments, because in the model no relative sliding was allowed between the snow and the supports. Conversely, the use of roller-roller boundary conditions led to loading curves which fell below the experimental curves. The use of pinned-roller boundary conditions, as depicted in Figures 6.2 and 6.3, led to the best agreement between model and experiment, even though the model boundary conditions did not exactly correspond physically to those in the experiments. Implementing a frictional law between the snow and the support plates and applying pinned-pinned boundary conditions for the supports would be more realistic physically. However, it would also be more realistic to implement a model that allowed some crushing at the supports at the same time, an approach that would be difficult to calibrate.

6.4.2 Simulations of zero-brittleness data sets

Fracture parameters for each of the zero-brittleness data sets were calculated for both notched and unnotched simulations. For Series Z3, Z4 and Z7, Young's modulus was calculated as a secant modulus at peak load using Equation 6.11, with the relative midspan deflection used for δ. However, for the stiffer snow in Series Z2, Z5, Z6 and Z8, the relative midspan deflection at peak load was often very small due to the effects of crushing at the supports. Note the very small deflection at peak load for the unnotched experimental curves in Figure 6.10a, which led to unreasonably high calculations for the modulus. For these test series, the mean of the unadjusted and relative midspan displacements at peak load were used to calculate E. For all modulus calculations, only the unnotched experimental data were used. The values of E used for each series are listed in Table 6.3.

The tensile strength f_t was also calculated from the unnotched experiments and reduced by 15% for the simulations, based on the results of the sensitivity analysis. The modulus of rupture from the bending tests was first calculated using Equation 4.17 and then corrected for the elastic stress distribution caused by the central load using Equation 4.19 (page 114). The fracture energy G_F was calculated using the Griffith-Irwin relation given E and the fracture toughness K_{Ic} from Table 5.7 (page 208), and was then increased by a factor of 2.5 (in Bažant's notation, this achieves approximate equivalence between G_f from the size effect law(s) and G_F which represents the area under the full softening displacement curve). The fracture energy values

Series	E [MPa]	$0.85 f_t$ [kPa]	$2.5 G_f$ [N/m]	R [mm]	$\varepsilon_\circ$	ε_f
Z2	18	18	2.5	5/10	0.00097	0.019 / 0.0099
Z3	2.0	3.5	2.3	5/10	0.0017	0.087 / 0.044
Z4	1.3	2.5	1.1	5/10	0.0019	0.057 / 0.029
Z5-f	14	16	1.7	4/8	0.0011	0.018 / 0.0095
Z5-m	11	17	2.5	4/8	0.0016	0.025 / 0.013
Z6-f	10	16	2.5	4/8	0.0015	0.027 / 0.014
Z6-m	12	18	2.4	4/8	0.0014	0.023 / 0.012
Z6-s	10	19	3.6	4/8	0.0019	0.031 / 0.016
Z7	2.9	8.5	1.4	5/10	0.0029	0.024 / 0.013
Z8	9.3	17	2.8	4/8	0.0018	0.029 / 0.015

Table 6.3: *Model parameters used in simulations of notched-unnotched experimental data. Young's modulus E (secant modulus at peak load), tensile strength f_t, and fracture energy G_F were all calculated directly from the experimental data. Dual values for* R *and ε_f represent values for notched and unnotched tests, respectively. All simulations used a Poisson's ratio of 0.3 for the snow and a Young's modulus and Poisson's ratio for the polycarbonate supports and loading plate of 30 MPa and 0.37, respectively.*

listed in Table 6.3 are near the upper bound values calculated by *McClung* (2007b) for dry slab avalanche tensile fractures.

Based on the sensitivity analysis performed for the nonlocal interaction radius, in notched simulations R was taken as c_f for all series that had an adjusted $r^2 > 0.9$ for the zero-brittleness regression fits. For series Z2, Z3 and Z4, which had poorer fits and more uncertainty about c_f, R was taken as 10 times the mean grain size for notched simulations. For all unnotched simulations, the value of R was doubled to represent the greater area over which damage is expected during the initiation of a crack in an unnotched test (e.g. *Bažant and Li*, 1996). The limit elastic strain for the local constitutive relation was calculated as $\varepsilon_\circ = 0.85 f_t / E$, and the ductility parameter for the exponential softening law ε_f was calculated using Equation 6.9. Note that ε_f was also a function of R and thus had different values for notched and unnotched simulations.

In general, the notched simulations had better correspondence with the experiments than the unnotched simulations (Figure 6.10). For each of the notched simulations, the peak loads were predicted well. For the softer snow of Series Z3, Z4, and Z7, the notched simulations predicted a more ductile response. For the higher hardness (stiffer) snow in Series Z2 and Z8, the unnotched simulations under-predicted the peak loads in the experiments by a wide margin. However, the slopes of the unnotched curves prior to peak load agreed well with the experimental data in each case. The dynamic post-peak rebound in the experimental data is stark for the stiffer snow of Series Z2 and Z8, and the unnotched simulations for these series showed the greatest discrepancy with the experimental data.

All experimental curves in Figure 6.10 show evidence of crushing of snow either at the supports or at the point of load application. The blade hardness indices of the snow in Series Z3, Z4, and Z7 were all quite low (≤ 2 N), which made this crushing inevitable. This crushing caused the experimental curves for the unnotched tests in Series Z3 (Figure 6.10b) to have highly irregular shapes, which questions the applicability of a homogeneous elastic theory for these particular tests. However, the simulations still appeared reasonable for this series, though the dissipated fracture energy may be too large.

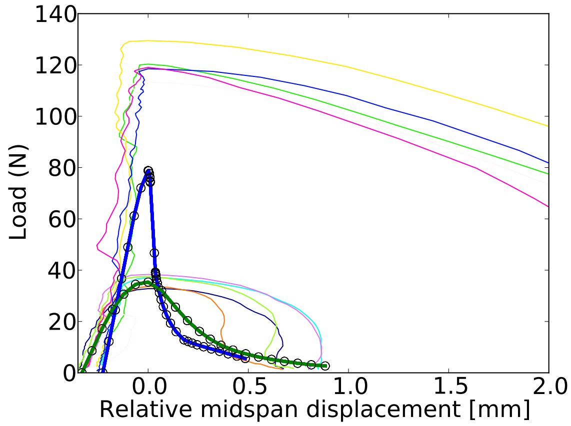

(a) *Z2*

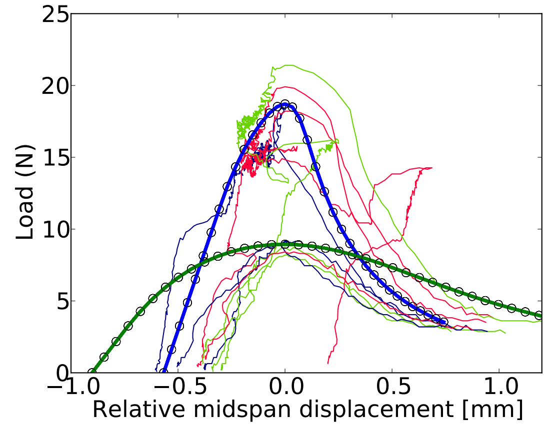

(b) *Z3*

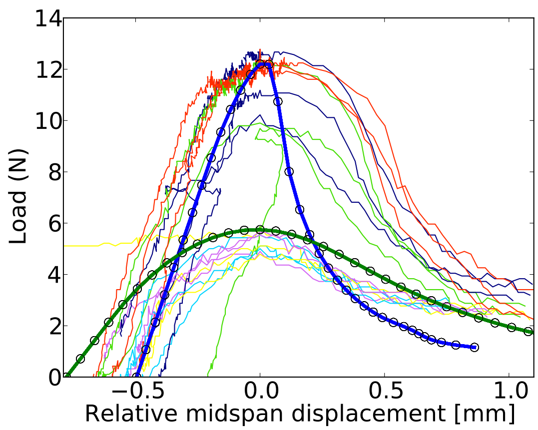

(c) *Z4*

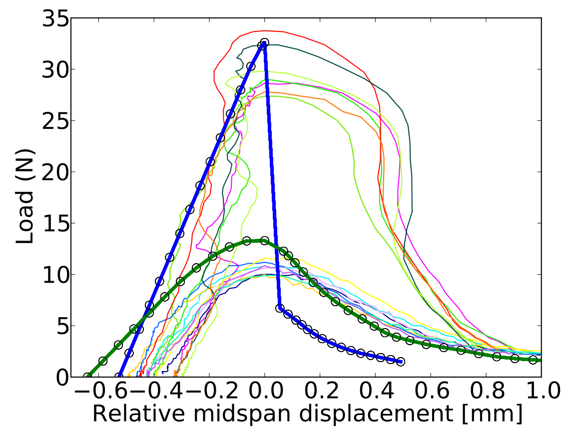

(d) *Z7*

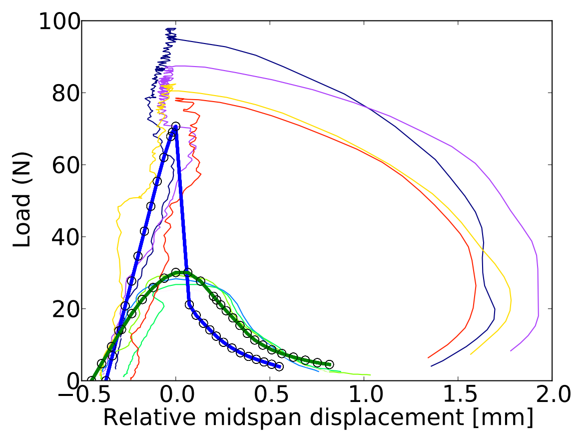

(e) *Z8*

Figure 6.10: *Load-relative midspan displacement curves for experiments (thin lines) and simulations (thick lines with circles). The thick blue and green lines are for unnotched and notched simulations, respectively. Parameters for each model are listed in Table 6.3.*

For the two series that tested for rate effects (Z5 and Z6), separate simulations were run for each of the given loading rates. Both series had very similar snow properties–high density, relatively high blade hardness index, same grain type and size, and similar testing temperatures (Table 5.7). These facts help to isolate the influence of rate effects in these two series as separate from other influences such as differences in snow structure.

The results for series Z5 are shown in Figure 6.11. The difference in experimental loading curves at different rates is stark. For the typical fast loading rate used in this study (1.25 cm/s, Figures 6.11a and 6.11b), the unnotched experimental curves showed evidence of crushing both at the supports (abrupt decreases in relative midspan displacement at constant load) and at the load point (brief periods of crosshead displacement at constant load in a few cases).

For the medium-speed tests (loading rate 0.125 cm/s), the experimental loading curves have a characteristic sawtooth pattern. This pattern was observed for most experiments in the present study at the same loading rate and was interpreted as a rate effect unique to a narrow range of nominal strain rates (around 10^{-2} s^{-1}). The load-crosshead displacement curves, for both notched and unnotched tests (Figure 6.11c), showed periodic decreases in load with increasing displacement. The corresponding load-relative midspan displacement curves (Figure 6.11d) indicate that these features are not due solely to crushing of the snow. In many cases, a decrease in displacement at constant load was followed by a decrease in load with increasing displacement, with this pattern repeating for each saw-tooth in the corresponding load-crosshead displacement curve. These features might be interpreted as a combined effect of settling or crushing at the supports with the failure of small, weakly-bonded regions within the snow sample. The failure of these small regions was not catastrophic enough to cause a propagating fracture in the sample–likely owing to the presence of a small amount of viscous stress relaxation–thus the sample recovered and loaded monotonically until the next micro-failure.

As with the previous simulations, agreement with the experimental curves was somewhat better for the notched simulations (Figures 6.11b and 6.11d). The peak loads in the notched simulations agreed better with the experimental data than the unnotched simulations, which again largely under-estimated the peak loads, though the discrepancy was reduced for the slower loading rate data. However, the notched simulations at the slower loading rate appeared too ductile, which may be an indication of reduced elastic fracture energy dissipation and enhanced viscous energy dissipation in the experiments.

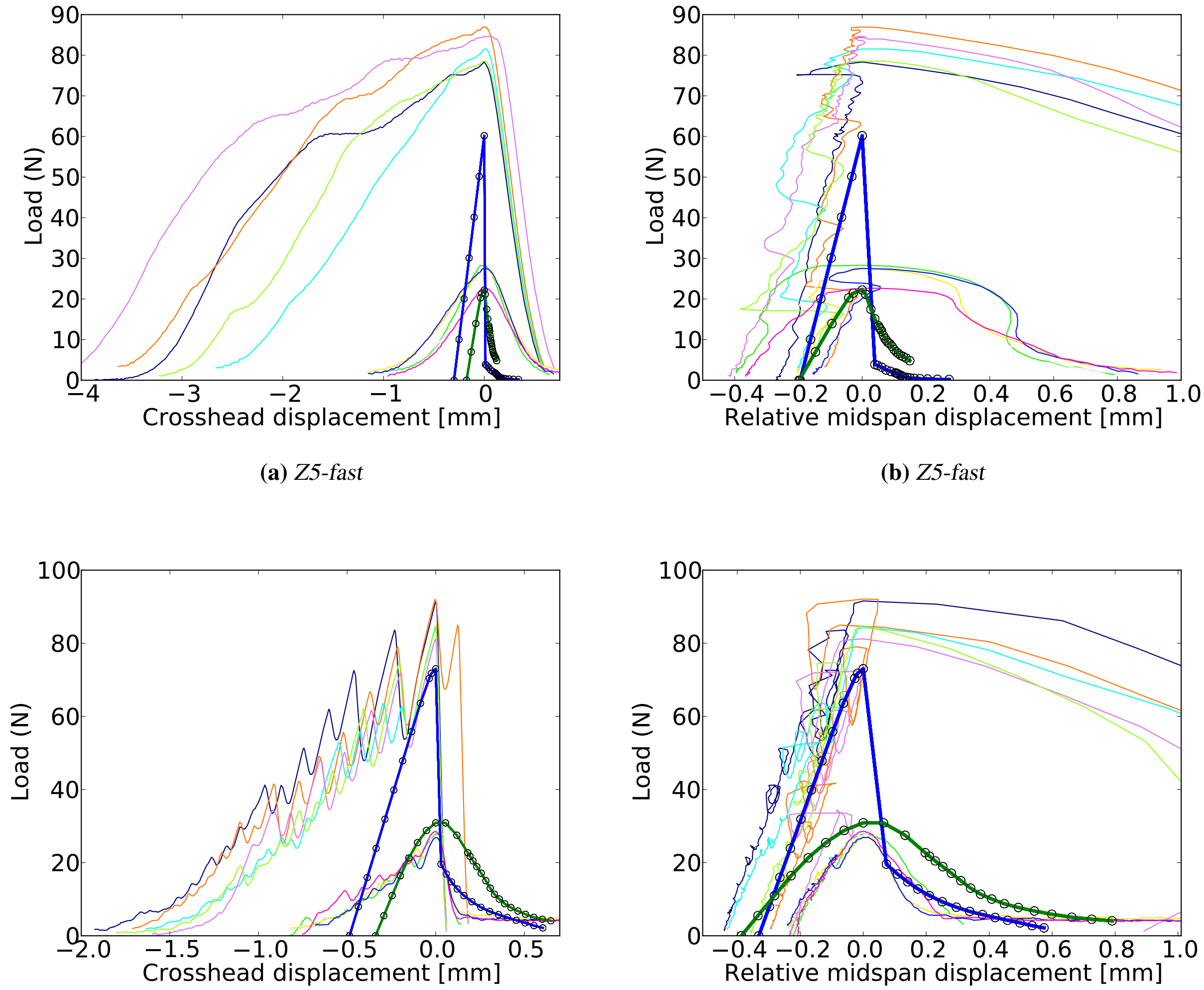

(a) *Z5-fast*

(b) *Z5-fast*

(c) *Z5-med*

(d) *Z5-med*

Figure 6.11: *Load versus crosshead displacement (a and c) and relative midspan displacement (b and d) for notched-unnotched series Z5, conducted at two different loading rates (V = 1.25 cm/s and 0.125 cm/s). Thick blue and green curves are unnotched and notched simulations, respectively. All thin lines are experimental measurements. All displacements are taken relative to the displacement at peak load. Model parameters for the simulations in (b) and (c) are listed in Table 6.3.*

The results for the series conducted at three different loading rates (Z6) are shown in Figure 6.12. For the fast loading rate (1.25 cm/s, Figures 6.12a and 6.12b) similar features were observed as in other experiments at the same speed, including loss of stability at peak load and moderate snow crushing at the supports and loading point. The unnotched simulation underestimated the measured peak loads but the agreement was good for the notched simulation. The full loading curves for the notched simulations agreed very well with the experimental data at this loading rate.

For the medium-speed tests in Series Z6 (0.125 cm/s, Figures 6.12c and 6.12d), similar features were observed as in the tests at the corresponding rate for Series Z5. The sawtooth loading pattern was observed and again interpreted as a combination of bond-scale failures combined with some snow crushing and perhaps viscous relaxation. The unnotched simulations again underestimated the measured peak loads, though the agreement was better than for the fast-speed tests. The notched simulations appeared more ductile than the experiments, though the peak loads were predicted well.

The slowest loading rate for Series Z6 was 0.0125 cm/s, which corresponds to a nominal tensile strain rate on the order of 10^{-3} s^{-1}. The sawtooth loading pattern was still observed at this loading rate, but at a lower frequency and not in every test. The sampling frequency of the load cell and LVDTs for this loading rate had to be reduced to about 20 Hz to keep the file storage below 1200 data points, which was the maximum that the testing machine software would allow. For this reason, the abrupt shifts in the relative midspan deflection measurement associated with the sawtooth features were not recorded (the frequency was still high enough that the peak load, which was approached slowly in every case, was probably accurately recorded. For reference, the fast tests in this study were nearly all recorded at a frequency of 500-600 Hz or more, and the medium tests here were recorded at around 250 Hz).

The best agreement between simulation and experiment for unnotched tests was for the slow experiments in Figures 6.12e and 6.12f. The loading slope for the simulated load-crosshead curve agreed very well with the experiments, though the peak load was still under-predicted. The experimental data was largely free of the spurious post-peak rebound inherent in the fast crosshead speed data, and the experimental post-peak crosshead displacement curve matched the experiments well. The notched simulations appeared slightly more ductile than the experiments, which may again be a sign of elevated viscous effects in the experiments. These results seem to suggest that, in the absence of the effects caused by dynamic stability loss–which were pronounced at the typical fast loading rate used in this study, especially for unnotched tests–the experimental data can be simulated reasonably well using a homogeneous continuum damage model. However, uncertainty remains around the appropriate value for the fracture energy for simulating experimental data with undeniable viscous effects.

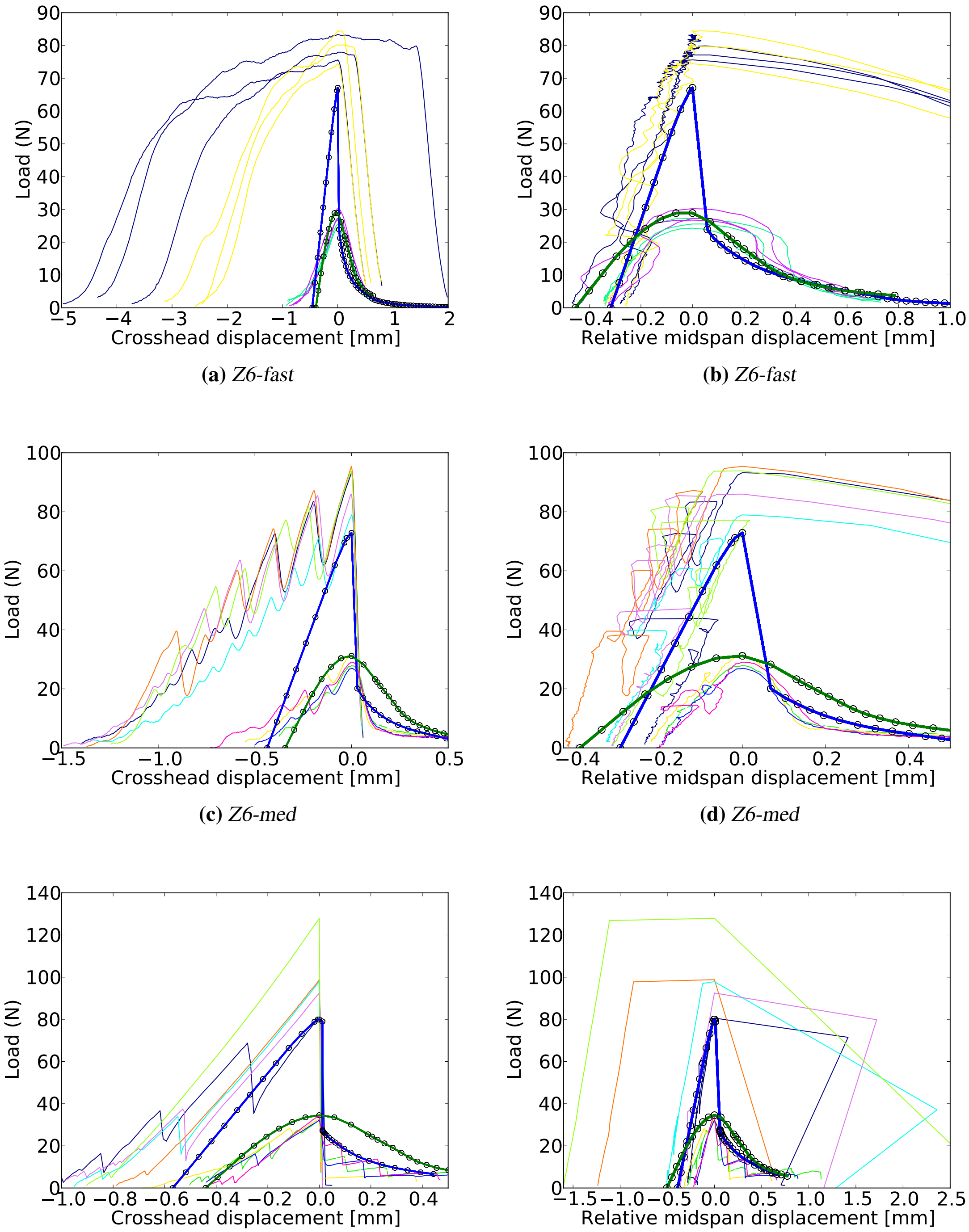

(a) *Z6-fast* **(b)** *Z6-fast*

(c) *Z6-med* **(d)** *Z6-med*

(e) *Z6-slow* **(f)** *Z6-slow*

Figure 6.12: *Load versus midspan and relative midspan displacement for notched-unnotched series Z6, conducted at three different loading rates. Model parameters are listed in Table 6.3.*

6.5 Discussion

The purpose of the numerical simulations presented here was to develop and test a modeling procedure for applicability beyond simply fitting experimental curves. Ultimately, a well-calibrated numerical model would be very useful for investigations of the deformation and fracture of snow slabs related to avalanches. For example, there is still uncertainty regarding the avalanche triggering process due to the layered and highly irregular nature of an alpine snowpack (*Schweizer et al.*, 2003), and the spatial scale over which the relevant triggering processes act is too large to permit full-scale laboratory testing. Numerical models may help to further our understanding of the mechanics of avalanche triggering, fracture propagation, and release.

The experimental data from paired notched and unnotched bending tests were useful for an *initial* model calibration. Some shortcomings of the model and the procedure for selecting model parameters were identified. First, the limit elastic strain determination for the local constitutive model (linear elastic up to the local uniaxial tensile strength followed by exponential strain softening) needs to be refined. The flexural strength was converted to an approximate uniaxial tensile strength value using an empirical relation arising from extensive concrete data, though the validity of this reduction factor (15%) for snow is an open question. It will likely be necessary to develop an empirical relationship for converting the results of experimental bending tests into uniaxial values using snow-specific data.

Explicit modeling of size effect data may help to constrain the selection of the nonlocal interaction radius and the fracture energy via the ductility parameter ε_f. Though the size effect on nominal strength can be reproduced with different combinations of R and ε_f that dissipate the same amount of local fracture energy, the size effect on the fracture energy may help to constrain the appropriate value of R (*Jirásek et al.*, 2004). The values of R used here were based on a motivation to link the values directly to microstructural parameters of the snow, in this case the effective process zone length, though this procedure should still be viewed as preliminary.

On a case-by-case level, better model results could no doubt have been obtained by further tuning of model parameters beyond their initial estimates according to the prescriptive algorithm developed here. However, the relatively good agreement between the model and the experiments is already quite promising for future predictive applications of this modeling procedure.

The fact that the simulations showed better agreement with the notched experimental data suggest that notched rather than unnotched test data would be more appropriate for further calibration of model parameters. The notched experimental data were less affected by localized crushing of the snow and interaction of the sample with a compliant bending fixture, which was related to the dynamic stability loss upon crack initiation in the unnotched tests. Furthermore, in many modeling scenarios related to avalanche triggering and release it will not be necessary to model crushing of the snow under localized compressive forces. During shear fracture propagation beneath the snow slab, the predominant stresses in the slab are tensile (e.g. *McClung*, 1981). The energy dissipation associated with localized crushing of the snow in the experiments is no doubt significant, and may be related to the tendency of the numerical simulations to underestimate the measured peak loads, but these concerns will have less importance in full scale models of avalanche release. Modeling the deformation of a snow slab during the initial triggering of the unstable shear fracture may require the consideration of higher compressive loads causing some compressive failure, but in these cases model calibration using dedicated compressive loading tests will be necessary.

Alpine snow is a highly rate dependent material and is prone to viscous deformation unless strained very rapidly. The experiments considered here likely contained some viscous effects, especially for the slower loading rates of Series Z5 and Z6. However, the use of a secant modulus in place of Young's modulus–provided that the creep strains at failure are not too large–should allow for an effective elastic solution as a reasonable approximation of a full viscoelastic solution (*Bažant and Gettu*, 1992), at least for predicting global structural response. That said, the relationship between the fracture toughness and fracture energy specified by the Griffith-Irwin relation may not be appropriate for localized calculations of energy dissipation in regions undergoing cracking and damage.

A desire for relative numerical simplicity combined with physical reasoning related to the microstructure of snow motivated the selection of the nonlocal isotropic damage model for the simulations. Comparison of this model with other quasi-brittle tensile failure models (local and nonlocal) should be conducted to determine the best model for general applicability to snow. For example, a model like the rotating crack model (*Jirásek and Zimmerman*, 1998) might better address the stress locking observed in the present study when the crack tip reached the compressive stress region caused by the flat load plate (though for practical applications related to avalanche fractures rather than experiments, this detail is unimportant). Extending the scalar isotropic damage model to an anisotropic formulation may be more appropriate for asymmetric stress fields and ensuring mesh objectivity (*Jirásek and Grassl*, 2008).

The nonlocal formulation of the isotropic damage model leads to results that converge with mesh refinement and do not depend on the orientation of the elements in the mesh. This result was not shown here but is well documented (e.g. *Bažant and Jirásek*, 2002). However, it may have been possible to run more efficient simulations by using coarser finite element meshes to achieve the same results. A more stringent procedure for determining the appropriate mesh resolution should be developed, and confirmation that the simulations have converged by using meshes of varying resolutions should be checked.

Conclusions

The nonlocal isotropic damage model was applied for the first time to simulate the tensile fracture of snow. The model was able to simulate fracture initiation from a smooth boundary as well as fracture propagation emanating from a pre-existing notch. A sensitivity analysis was performed to help determine the selection of several unknown model parameters and to explore the behavior of the model. Ten different experimental test series that paired notched and unnotched tests at the same specimen size were used for the numerical simulations. Model parameters were calculated from relations that ensured a fixed amount of energy dissipation in the local constitutive model, based on calculations of the fracture energy from the experiments. The simulated load-displacement curves showed better agreement with the notched experimental data than the unnotched data, which was due to the effects of localized compressive crushing of the snow at the supports and load point and the dynamic loss of elastic stability upon crack initiation in the unnotched experimental data.

The simulation of snow—a highly irregular, porous, time-dependent, nonlinear material—using a homogeneous elastic damage model hinges on a consistent homogenization scheme that preserves the influence of the heterogeneous material microstructure and the intrinsic length scale associated with the fracture process zone. The length scale over which damage localizes in the nonlocal isotropic damage model, which was explicitly tied to the effective process zone length c_f in the simulations, can be thought of as the minimum length scale applicable for the homogenization of snow as a continuum. The relatively good agreement between much of the experimental data and the simulations provides support for the interpretation of snow as a quasi-brittle material—having a relatively large and distributed zone of softening damage during crack initiation and propagation—over most length scales relevant to slab avalanches.

Chapter 7

Conclusions

There is no material of broad engineering significance that under normal conditions displays the bewildering complexities found in snow. If constitutive equations and failure criteria could be formulated with complete generality for snow, they would probably cover all contingencies for all real solids....Elegant simplification of complicated behaviour is very much needed.

–Malcolm Mellor

The present research project encompassed in situ measurements of fundamental and index snow properties, laboratory measurements of strength and fracture mechanics parameters, and numerical simulation of the tensile fracture of dry, cohesive alpine snow. Many simplifying assumptions were required to enable the analysis of the collected data, and attempts were made to ensure that each was appropriate for the given application. Many of the guiding principles, hypotheses, and assumptions laid out in Chapter 1 and applied throughout the present study are revisited here to check for their validity. Embedded within the discussion are lessons learned and recommendations for future research that both utilizes and builds upon the extensive experimental data synthesized here.

7.1 Rate Effects and Validity of Effective Elastic Analysis

The analysis of experimental data using the framework of linear elasticity is certainly a simplification for a material such as snow over most rates of static loading. The validity of this approach is addressed here using measured values of the time to peak load (t_p) in a mix of 370 notched and unnotched bending experiments covering the full range of loading rates in the present study. The fastest and most common crosshead speed (1.25 cm s^{-1}) led to median failure times around 0.1–0.2 seconds. The slowest crosshead speeds were about two orders of magnitude slower (0.01 cm s^{-1}) and led to failure times of 1–10 seconds (Figure 7.1a). The crosshead speed used by *Sigrist* (2006) was 0.33 cm s^{-1} and likely resulted in failure times of around 1 second, so the subsequent analysis justifying the elastic approximation in this study qualifies for Sigrist's data as well.

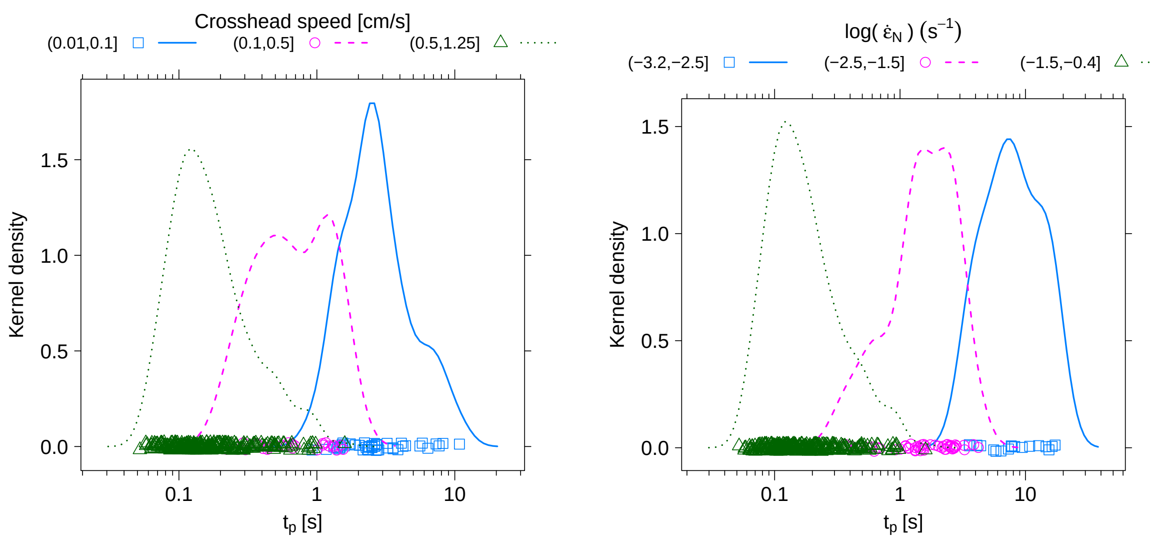

Figure 7.1: *Kernel density plots of the time to peak load t_p in bending experiments (n = 370), binned by crosshead speed (a) and the logarithm of the nominal strain rate (b). These data represent the full range of crosshead speeds used in the present study.*

7.1.1 Estimates of bulk creep strain at failure

Bažant and Gettu (1992) have suggested that an effective elastic analysis of fracture data is justified if the creep strain at failure is the same order of magnitude as the instantaneous elastic strain. This allows a self-consistent, if approximate, method of determining the rate-dependence of fracture parameters from tests over a range of times to failure. *Bažant and Gettu* analyzed a series of size effect tests at different rates, for which the creep strain at failure was in the range of 50–100% of the instantaneous elastic strain. The elastic solution was judged to be a good approximation of the full viscoelastic solution for this magnitude of creep strains, provided that an effective elastic modulus (creep compliance or secant modulus at peak load) was used in place of a fully-elastic modulus (see also *Bažant*, 2005).

For data from the present study, the creep strains at failure were estimated for the representative failure times in Figure 7.1. *Shinojima* (1966) determined numerical values for the parameters of a four-element Burgers' model (a Maxwell element in series with a Kelvin-Voigt element) from creep tests on snow in tension, compression, and torsion. Shinojima's derived model values for tensile creep tests were used for the following creep calculations. Table 7.1 contains results for the ratio of creep strain to the instantaneous elastic strain for different times to failure. See Appendix A for additional detail on the calculations.

Table 7.1: *Ratio of creep strain $\varepsilon(t)$ to instantaneous elastic strain $\varepsilon_\circ$ for different times, using the viscoelastic parameters measured in constant-load tensile tests by Shinojima (1966). Reference temperature for the Maxwell viscosity is $-5°C$.*

Time [s]	$\varepsilon(t)/\varepsilon_\circ$
0.1	0.0005
1	0.005
10	0.05
100	0.5

The creep strain magnitudes in Table 7.1 were calculated from constant-load creep tests. The experiments in the present study were conducted under displacement control, which does not correspond with the creep experiments. Creep strains in displacement-controlled loading are more difficult to measure, but this does not really matter here since the creep strain estimates are already quite low. The lower-bound estimate of the relaxation time for the tensile tests of *Shinojima* (1966) was about 300 seconds, which is more than an order of magnitude greater than the slowest failure times in the present study. For failure times corresponding to the slowest loading rates in the present study, the creep strains at failure were likely below 10% of the instantaneous elastic strain. These low values indicate that the analysis of even the slowest tests in the present study (as well as those of *Sigrist* (2006)) using an elastic framework should be an acceptable approximation to a fully viscoelastic solution, provided that the interest is in determining material parameters at different rates in a self-consistent manner. If stability calculations or other calculations which require an energy balance are being carried out, then viscous energy dissipation will need to be accounted for even over short timescales.

Representative nominal strain rates roughly corresponding to the bins of crosshead speed in Figure 7.1a are indicated in Figure 7.1b. Even the slowest crosshead speeds used in the present study led to nominal strain rates about an order of magnitude larger than the creep-to-fracture transition in tension (*Narita*, 1980, 1983). The transition strain rate, $\sim 10^{-4}$ s^{-1}, corresponds to failure times approaching 100 seconds for the scale and geometry of the beam bending tests in the present study. The calculations in Table 7.1 indicate that for this failure time the creep strain would be about 50% of the instantaneous elastic strain. This failure time at the transition strain rate is also near the lower-bound relaxation time observed by *Shinojima* (1966), a coincidence that deserves further attention. This may also suggest a rule of thumb for the limits of applicability of an effective elastic analysis of test data; namely, that the time to failure is short compared to the relaxation time.

The critical strain rates at the creep-to-fracture transition for different modes of loading have been used by many investigators to define the limits of linear elastic response for snow. This is an important conceptual difference from the interpretation given here to the limits of applicability of an effective elastic analysis as an approximation to an actual viscoelastic process. The transition strain rates represent a critical balance between creep and fracture (see e.g. *Schulson and Duval*, 2009), not a transition to fully elastic response. No studies to date have quantified strain rates, for different modes of static loading (below the dynamic range), that yield fully recoverable deformation in snow. The stance taken here is that an elastic framework for analysis is likely acceptable for any strain rate above the creep-to-fracture transition, provided that care is taken in defining appropriate rate-dependent parameters such as an effective elastic modulus using the secant modulus at peak load or creep compliance for the given time to failure. This is not to say that the material response can be considered fully elastic, since different material parameters are needed at different rates, but that rather an elastic solution is probably a reasonable approximation for simple calculations. Whether or not this approach is appropriate in a given scenario, it is crucial to recognize the prevalence of creep and rate effects within about two decades or more of the transition strain rate in designing experiments and interpreting test results. Rate effects must be systematically tested and accounted for to constrain the effects of creep on experimental data.

7.1.2 Creep effects within the fracture process zone

For assessing the total creep strains in fracture specimens, the effects of creep in the bulk of the specimen as well as rate-dependent creep and damage within the fracture process zone should be accounted for (*Cotterell and Mai*, 1996; *Bažant and Planas*, 1998). To date, no creep data for fracture specimens of snow have been reported. For concrete, greater rates of load relaxation in notched bending specimens than unnotched specimens of concrete was observed by *Bažant and Gettu* (1992), the difference being attributed to a greater rate of creep and damage accumulation in the fracture process zone of the notched specimens. Following these observations, the notched tests analyzed in Chapter 5 may have been affected by creep to a greater degree than the unnotched data used to calculate tensile or flexural strength in Chapter 4. This could also explain the weaker-than-expected rate effect in the paired notched-unnotched (zero-brittleness) data for the fracture toughness and effective process zone length in Section 5.4 compared to the strong rate effect observed for the process zone length in the notched size effect data of Section 5.2.

For the experiments in the present study, if the bulk creep and the creep in the FPZ are assumed to be of the same order of magnitude, then the total creep strain for a failure time of 1 second is still only about 1% of the instantaneous elastic strain. For the slowest tests of the present study ($t_p = 10$ s), the creep strain may reach levels on the order of 10% of the elastic strain. Even if the total creep strain estimates here are low by an order of magnitude, the ratio of creep strain to instantaneous elastic strain is still small enough for an effective elastic analysis to be justified. Therefore the elastic calculations in the present study of tensile strength, fracture toughness and effective process zone length are reasonable approximations to the full viscoelastic solutions, even for the slowest loading rates.

7.1.3 Failure times in slab avalanches

A final note on rate effects should be made regarding the range of actual strain rates in a snow slab prior to the tensile fracture which releases a slab avalanche. From typical dimensions of the length, width, and depth of slab avalanches (*McClung*, 2009a) and estimates of shear fracture speeds (*McClung*, 2007a), the total time of shear fracture propagation beneath the slab prior to tensile fracture is on the order of several seconds. This is about an order or magnitude longer than the time to failure of the majority of the experiments in the present study. However, a shorter timescale for the slab is appropriate for the region where the tensile fracture first initiates.

The clean, fast fractures observed at the crown lines of slab avalanches indicate that the tensile strain rate in the slab is above the creep-to-fracture transition, probably well above it. This implicitly suggests a rough correspondence between strain rates in slab avalanches and those used in the present study. If the rate-dependence of strength approaches an asymptotic limit with increasing strain rate above the creep-to-fracture transition (*Mellor and Smith*, 1966; *Narita*, 1983), then exact correspondence between the strain rates in the present study and those in slab avalanches is not necessary, provided that both are above the transition rate by at least a couple decades. The results of the present study are therefore applicable for relevant rates of deformation in slab avalanche tensile fractures.

7.2 Relation Between Beam Bending Tests and Tensile Fractures in Slab Avalanches

An appropriate and consistent scheme is necessary for determining the relationship between fracture parameters determined in the present study and those appropriate for analysis of slab avalanches—direct applicability of the lab-derived data may not be appropriate. Such a scheme should account for two fundamental differences between an actual slab and the experimental samples: first, the layered and heterogeneous structure of a typical snow slab compared to the homogeneous experimental specimens, and second, the difference between the stress and strain gradients in a bending beam and a snow slab. The first point is a question of the appropriate homogenization of the snow slab for the given analysis. The second is related to the link between length scales in the experiments and those in the snow slab.

7.2.1 Homogenization of a layered, orthotropic snow slab

In most fracture mechanical analyses of slab avalanche behaviour, the full-scale equivalent slab is taken as one with the same depth D as the actual slab, but characterized using the depth-averaged density of the slab. This is an appropriate homogenization for gravitational stress calculations, but a mean slab density is a crude index for selecting mechanical properties.

A more thorough and appropriate homogenization scheme might calculate, in addition to the mean density, some sort of mean structural index using penetration resistance measurements. Since the initial tensile fracture in a slab avalanche is assumed here to initiate in a boundary layer at the bottom of the slab, and since the cohesion of the slab in this boundary layer just above the weak layer is probably the most important for governing shear fracture initiation and propagation, more weight might be given to the properties of the slab toward the bottom in a homogenization scheme. Therefore the hardness of just the bottom of the slab or a weighted average hardness with more weight given to the properties at the bottom of the slab might be more appropriate for a single index by which to select appropriate fracture properties for the slab. This argument about giving more weight to the slab properties in the vicinity of where the tensile fracture initiates is fully generalizable, in the sense that some may argue that there are cases in which, for example, significant bending of the slab might cause the tensile fracture to initiate near the top of the slab (though the properties near the bottom would still be the most appropriate for the initial weak layer fracture). The determination of the equivalent homogeneous slab used for analysis should take into account the properties of the snow wherever the fracture is assumed or observed to initiate.

7.2.2 Length scales in avalanches and experiments

The characteristic length scale for the fracture mechanics of slab avalanches is the slope-normal slab thickness (*McClung*, 1979b, 1981, 1987). The characteristic length scale for the beam bending experiments in the present study was the beam depth. These length scales may not be directly comparable for determining appropriate parameters for analysis of slab avalanches. For example, the properties calculated from 10 cm deep beams may not be appropriate for a 10 cm thick slab.

Tensile fractures in slab avalanches are assumed to fail at crack initiation in a boundary layer at the base of the slab (*McClung and Schweizer*, 2006). The unnotched size effect law derived using the equivalent elastic crack approach (Chapter 5, Section 5.3.1) can also be derived by assuming that the fracture initiates when a boundary layer of length D_b attached to the tensile face of the beam reaches an average stress $f_{r\infty}$ (*Bažant*, 2005). This conceptualization is shown schematically in Figure 7.2a. Note that $f_{r\infty}$ is sometimes written as the tensile strength f_t (*Bažant and Li*, 1995), but in the equivalent elastic crack derivation $f_{r\infty}$ is understood as a combination of the fracture toughness and the effective fracture process zone length (Equation 5.36, page 190).

The size effect on the modulus of rupture (or unnotched size effect, Equation 5.38) is fully generalizable to any structure with a boundary-layer strain gradient as depicted in Figure 7.2a (*Bažant*, 2005). Therefore correspondence between the experimental data from beam tests can be directly translated to parameters

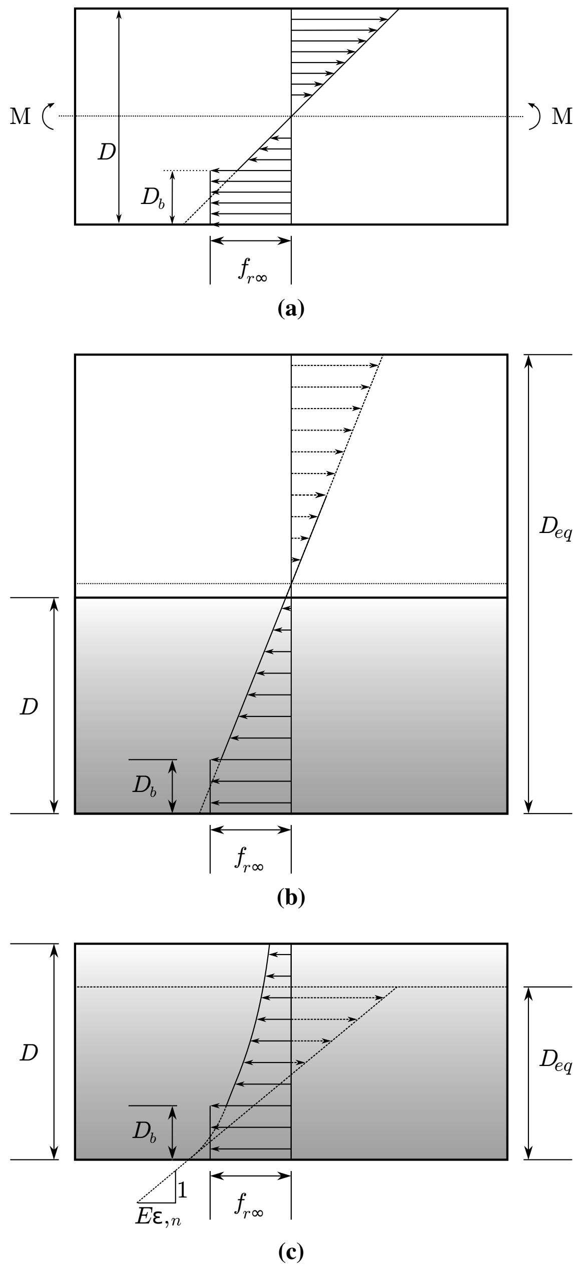

Figure 7.2: *Definition of the boundary layer of distributed cracking $D_b = f(c_f)$ as the region over which the average elastic stress in a bending beam is $f_{r\infty} = f(K_{Ic}, c_f)$, after Bažant (2005) (a); hypothetical stress distributions in an actual snow slab (shaded gray, slab thickness D), and definitions of equivalent beam depth D_{eq} that give the same structural response as the slab by matching the strain gradient at the tensile surface (b and c). The stress gradient at the bottom surface of the slab is $E\varepsilon_{,n}$, where $\varepsilon_{,n}$ is the tensile strain gradient normal to the surface. For a linear stress gradient (b), the correspondence is straightforward and leads to an equivalent beam depth more than twice the slab depth. For a nonlinear stress gradient which decreases sharply away from the base of the slab (c), the equivalent beam depth may be less than the slab depth.*

appropriate for a slab avalanche as long as (1) the strain gradient in the slab is known and (2) the strain gradient has a maximum at the base of the slab. If the snow slab is homogeneous, the strain-softening shear fracture in the weak layer beneath the slab will still cause a stress and strain gradient in the slab, with tensile stresses (and therefore strains) highest near the base of the slab (*McClung*, 1979b). Most snow slabs have a gradient in density and hardness with depth, so these stress and strain gradients caused by weak layer failure are likely to be magnified. If the maximum strain is located anywhere other than the bottom of the slab, the deterministic size effect will take a different form, as the initial tensile crack in such a case would be expected to initiate within the slab rather than at the base (unless the maximum strain is at the snow surface). In the absence of a strain gradient, there will be no deterministic strength size effect (*Bažant*, 2005), and the slab will fail when the tensile strength is reached over the full thickness of the slab.

If the strain gradient in the slab is known or can be approximated, the key to the equivalence problem relating beam data to the snow slab is to define an equivalent beam depth D_{eq} that gives the same strain gradient at the bottom of the beam as in the bottom of the slab. Since the values of $f_{r\infty}$ and D_b calculated in the lab were defined as material properties (or rather, for snow, *structural* properties) appropriate for the avalanche scale, they could then be used directly in the size effect law with the equivalent beam depth D_{eq}.

This correspondence requires knowledge of the strain gradient at the bottom of the snow slab, which is unknown. Numerical calculations of the sort carried out in Chapter 6 could aid in determining the strain gradient at the base of a layered slab under sufficient stresses for crack initiation (see also *Smith*, 1972). Some analytical solutions for layered beams are also available that may help to suggest the appropriate form of the strain gradient for different types of laminated slab structures. In the meantime the approach outlined here is purely conceptual.

Figures 7.2b and 7.2c show schematically the definition of an equivalent beam depth D_{eq} from two different assumed forms of the stress gradient (and implicitly the strain gradient) for a snow slab prior to failure. Depending on the nature of the gradient, the equivalent beam depth D_{eq} may be quite different than the slab depth D. If the stress gradient is linear in the slab and if the entire thickness of the slab is under tensile stress, the equivalent beam will be at least twice as large as the actual slab thickness (Figure 7.2b). For a nonlinear stress gradient in the slab, the picture may be quite different. If the gradient is strongly nonlinear with positive curvature, as in Figure 7.2c, the equivalent beam may be similar or even smaller in size than the actual slab. For negative curvature (not shown in the figure), the equivalent beam may be many times larger than the slab, as in the case for a linear gradient.

Provided that the strain gradient in a snow slab can be constrained for different scenarios, the equivalence calculations should be straightforward. The parameters K_{Ic} and c_f calculated from the lab experiments could be used to calculate $f_{r\infty}$ via Equation 5.36, or values of $f_{r\infty}$ reported in Section 5.3 and 5.4 could be used. The selection of appropriate mean parameter values for the snow slab would first be required given the structure of the actual snow slab (as discussed above with respect to homogenization). Given the strain gradient normal to the surface $\varepsilon_{,n}$ and Young's modulus E (or an effective modulus if viscoelastic effects are present), the equivalent beam depth (*Bažant*, 2005) is

$$D_{eq} = \frac{2f_{r\infty}}{E\varepsilon_{,n}}. \tag{7.1}$$

The size effect law for the modulus of rupture (Eq 5.36) is then written with D_{eq} in place of D, which in its simplest form results in the following equation for the nominal strength of a snow slab:

$$\sigma_N = f_{r\infty}\left(1 + \frac{D_b}{2f_{r\infty}}E\left\langle\varepsilon_{,n}\right\rangle\right) \tag{7.2}$$

where the Macaulay brackets $\langle X\rangle = max(X,0)$ have been introduced to limit the equation to situations where the strain decreases away from the surface (*Bažant*, 2005), as described above. This relation would allow the utilization of the experimental data collected and analyzed in the present study for the direct prediction of snow slab strength relevant for avalanche release.

7.3 Scale-Cohesion Classification Scheme

Much of the proposed scale-cohesion classification scheme introduced in Chapter 1 was quantified in the present study (Figure 7.3). The cohesive threshold distinguishes snow with sufficient internal cohesion to support the propagation of fractures. As with previous studies, cohesion was taken here as synonymous with tensile strength (*Bader and Kuriowa*, 1962; *Mellor*, 1968). The blade hardness gauge developed in the present study provided the first quantitative estimates of the cohesive threshold since the study of *Fukue* (1977), placing it in the range $0 < B < 1$ N. The blade hardness index B is also the only quantitative penetration resistance measurement that classifies snow at a length scale above the continuum limit, a distinction that makes B the most appropriate of the available hardness measures for correlation with continuum-scale fracture properties and applicability in continuum models of the deformation and fracture of snow.

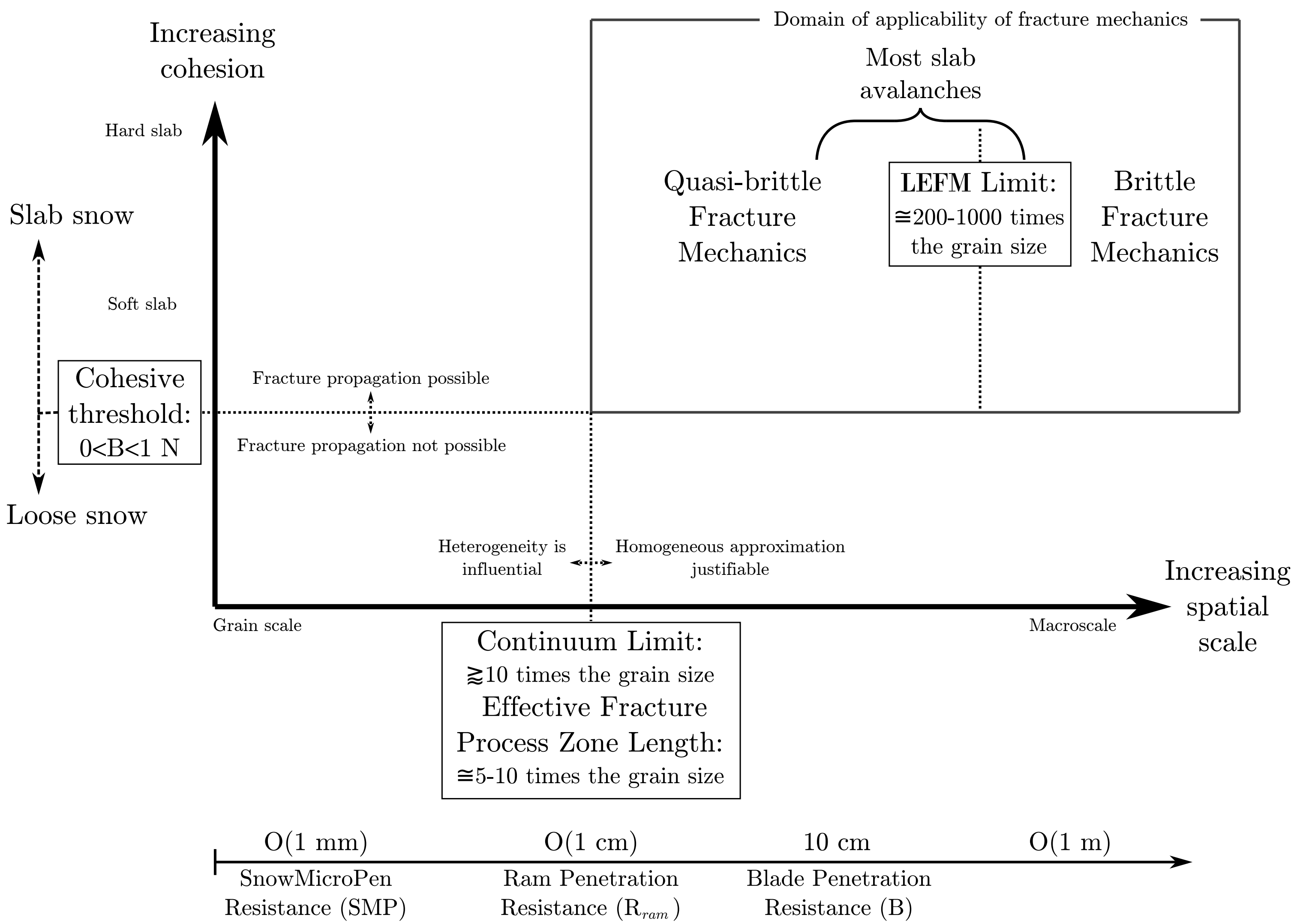

Figure 7.3: *Scale-Cohesion classification, revisited. The cohesive threshold has been narrowed to a small range in blade hardness index (B) values. The blade penetration resistance is the only existing hardness measure that characterizes snow above the continuum limit length scale, which has a lower bound of approximately 10 times the grain size. Based on the typical thickness of snow slabs, most slab avalanches fall within the range of length scales for which quasi-brittle fracture mechanics is necessary.*

The continuum limit length scale is an uncertain component of the scale-cohesion classification. This is primarily because systematic experiments were not conducted to directly address homogeneity relative to the grain size. This length scale is still fundamentally important to the application of continuum fracture mechanics to analyze slab avalanches. However, for the time being, reference to homogeneity requirements developed for other heterogeneous materials is necessary to suggest approximate bounds on this limit for snow. For polycrystalline ice, the lower bound on this length scale appears to be about 10 times the grain size (*Schulson and Duval*, 2009), though some studies place it around an order of magnitude larger (*Dempsey et al.*, 1999b; *Mulmule and Dempsey*, 2000). However, the applicability of these limits, which were developed for a solid crystalline material, for a highly porous material such as snow may not be appropriate. For the time being, the continuum limit is suggested to be at least 10 times the grain size. However, the practical difficulties experienced in extracting, handling and testing the smallest snow samples (D = 2.5 cm) indirectly suggests that a length scale closer to 50 times the grain size or more may be more appropriate for expecting homogeneous response. A lower bound slab thickness in avalanche statistics is around 10 cm (*Perla*, 1977), a length scale for which the continuum limit is most likely satisfied.

The upper bound specimen sizes used to fit the various size effect laws in Chapter 5 were in the range of D = 10–20 cm. The slab thickness in most avalanches is on the order of 10 cm to 1 m, not much greater than the lab scale (assuming approximate correspondence between the slab thickness and beam depth). The fracture parameters calculated from Bažant's size effect laws in Chapter 5 are defined as material properties at structural scales up to an order of magnitude greater than the lab scale (e.g. *Bažant and Kazemi*, 1990a). Therefore the fracture mechanical parameters calculated in the present study are applicable as material properties for the slab avalanche scale.

In most slab avalanches, therefore, the effective process zone length–the length appropriate for analysis using equivalent elastic fracture mechanics–is expected to be around 5–10 times the grain size. The relationship between the *actual* size of the process zone and the elastically-equivalent process zone remains uncertain, but might be reasonably estimated as about $2c_f$ as for concrete. However, for elastic continuum analysis of slab avalanche fractures, c_f is the fundamental length scale of importance.

As with the process zone length, the fracture toughness values reported in Chapter 5 are directly applicable for most analyses of tensile fractures in slab avalanches. For problems in which the slab thickness is comparable to the lab-scale specimens (i.e. $D \approx 10 - 20$ cm), a relation such as Equation 5.17 should be used to calculate an apparent fracture toughness K_{INu} for the given value of D and for an appropriate mean value of K_{Ic} for the structure of the snow. Once again, this requires the assumption that the slab thickness and beam depth have one-to-one correspondence, an assumption that is not likely to prove strictly correct.

7.3.1 Size requirements for LEFM applicability

The domains of applicability of LEFM and quasi-brittle fracture mechanics are indicated in the scale-cohesion classification of Figure 7.3. Quasi-brittle fracture mechanics accounts for the nonlinearity caused by a fracture process zone which is large *with respect to the specimen dimensions*. Therefore the quasi-brittle domain is a relative one, depending on the characteristic length scales in the problem. For both shear and tensile fracture propagation in slab avalanches, the characteristic length scale is the slope-normal slab thickness (*McClung*, 1979b, 1981, 1987), a distinction that allows the scale-cohesion classification to have applicability for both modes of fracture. Separate discussion for each mode is warranted, however.

Tensile fracture

The LEFM limit for tensile fracture, as indicated in Figure 7.3, was quantified using the brittleness number data calculated in Chapter 5. The mean brittleness number ($\beta = D/D_\circ$) was around 5 from the zero-brittleness (notched-unnotched) data, which indicates that LEFM is first applicable for a size range around 2-5 times the laboratory scale (for β = 10–25 as the approximate lower limit of applicability of LEFM). Given the typical grain size of the zero-brittleness data (0.5–1 mm), the LEFM limit is therefore around 200–1000 times the grain size (Figure 7.3).

Larger values of the brittleness number were calculated for the zero-brittleness data than the notched size effect data, thus the zero-brittleness data indicate closer proximity to LEFM. However, even though the notched size effect tests had more scatter and poorer fits to the corresponding size effect law, some weight should be given to the brittleness numbers from these data, which indicate further deviation from LEFM. Therefore the LEFM limit in Figure 7.3 should be viewed tentatively and preference should be given to the upper bound estimate (around 1000 times the grain size, or $\beta = 25$ as the rule of thumb) until more data are available.

The domain of applicability of quasi-brittle fracture mechanics for tensile fractures in slab avalanches therefore covers one to two orders of magnitude in multiples of the grain size above the continuum limit, assuming the continuum limit is 10 times the grain size. The conservative length-scale estimate for the LEFM limit is around 1 m (conservative in the sense of a null hypothesis of a large fracture process zone). This estimate was derived based on the assumption that the slab thickness correlates one-to-one with the beam depth in the experimental data. The proximity of slab avalanches to the LEFM limit may shift in either direction depending on the appropriate form of the strain gradient in the slab prior to tensile fracture (Figure 7.2). Therefore two sources of uncertainty are present with respect to judging the range of applicability of quasi-brittle fracture mechanics for slab avalanches, that of the appropriate definition of the LEFM limit and that of the equivalent beam depth given the strain gradient in the slab.

Shear fracture

Though the scale-cohesion classification scheme was developed here for tensile fractures, it may be generalizable to include shear fracture. *McClung* (2009b) estimated the size of the shear fracture process zone in the weak layer as around 100–200 times the grain size in the weak layer. If the length of the FPZ is about $2c_f$, then the elastically-equivalent process zone length in shear is about 50–100 times the grain size. This suggests that the scale-cohesion classification in Figure 7.3 may also be applicable for the initial shear instability in slab avalanches, provided that the estimates of the effective process zone length and the LEFM limit are increased by an order of magnitude. The continuum limit length scale may also need to be shifted by the same amount given the typically larger-sized grains in the weak layer in slab avalanches. The length scales shown in Figure 7.3 adjacent to the penetration resistance methods would also need to be shifted to the left, as the process zone length in the weak layer is probably on the order of 10 cm (*McClung*, 2009b).

7.4 Discussion

7.4.1 Experimental lessons

Natural snow sampling

It was difficult to incorporate low density snow into the current study. Testing newly fallen or relatively fresh snow, just as it gained cohesion, required that a uniform layer of storm snow was deposited thicker than 10 cm. New snow settles and densifies under the action of gravity, and the thickness of newly fallen snow layers observed during the field studies decreased substantially by the time that the snow gained enough cohesion to be extracted and handled. Furthermore, for sampling layers which were more or less homogeneous, the storm snow needed to be deposited in a fairly consistent manner, i.e. no substantial change in temperature, wind, or other environmental factors during the storm which would change the nature of the snow as it fell and deposited.

These factors ruled out many of the snow layers near the surface of the natural snowpack from investigation, as they were typically less than the 10 cm thickness required for sampling. Low-density and low-cohesion snow layers that were thicker than 10 cm typically had snow that was too fragile to allow extraction of large samples, so size effect testing was ruled out. The weakest snow that was tested in the present study was in the zero-brittleness (notched-unnotched) series, which only required a single specimen size. This is a clear advantage of the zero-brittleness method over the size effect methods, as it allowed a single specimen size and a size that was the most manageable for many kinds of snow. However, note that slab avalanches are observed in very soft and soft snow which is likely too fragile to extract, transport and test in a cold lab without storing the samples for extended periods of time. Therefore the snow sampled in the present study was biased toward stronger and stiffer snow, though a few soft and low density layers were successfully tested to partially anchor the parameter regressions as a function of density or blade hardness index. This allows the in situ estimation of properties such as tensile strength and fracture toughness for weakly cohesive snow layers that cannot be sampled and tested using the experimental methods developed and applied in the present study.

Beam bending tests for measuring snow properties

The four point bending size-effect test series NSE3 (Section 5.2, page 172) led to, by far, the best fit of the size effect law for all the notched size effect data. All other test series, conducted using three point bending and with shorter span-to-depth ratios, led to much more scatter and poorer fits for the same relative notch depth and loading rate. The better fit for the four point bending data can be explained by several likely factors. The first was that the horizontally-oriented bending tests allowed larger span to depth ratios than weight-compensated vertical tests. The second was related to the third-point loading of this test series (Figure 5.6b), which produces a constant bending moment (and no shear) in the central portion of the beam between the two load plates. In repeated experience using four-point bending, it appeared that the fractures were more consistent in terms of propagation in a straight line across the beam, which may have been a consequence of the loading geometry.

The horizontal testing method developed in the present study is a new and unique method for achieving two key objectives in bending tests for a fragile material such as snow, namely weight compensation and beam slenderness. The increased span to depth ratio (slenderness) in these tests is a consequence of the ability to place the support plates near the ends of the beam, which would not be possible in vertically-oriented tests without sacrificing weight compensation. The increased loading span possible in the horizontal orientation also allowed for third-point loading (four-point bending), which was not deemed possible for the shorter loading spans required in vertical tests. The small amount of friction between the sample and the support tables in the horizontal tests, rather than being a drawback, may have also played a stabilizing role near peak load in the experiments. This friction may have also contributed to the reduced scatter in the horizontally-oriented experiments.

Given the fragile nature of snow and the inability to handle the specimens in the same way as other materials which can be simply picked up and placed on supports, snow samples are very difficult to mount for bend tests. The snow samples were contacted only by pieces of styrofoam; no hand contact with the snow was permitted as a standard practice, a practice which made the mounting of the specimens on the supports a challenge. The snow could not be simply placed on rollers and then manipulated to square everything up. As a result, the rocker supports that were developed in the present study did not meet the original design specifications of approximating roller boundary conditions. Sliding of the specimens on the supports during bending, and associated friction, was unavoidable given the adopted design which did not allow any lateral translation of the support plates. The rocker supports did, for the most part, prevent localized crushing of snow during most tests, which was an additional design specification. Further development of a system for supporting snow samples which allows lateral translation of the support plates during bending, or otherwise prevents relative slip between the snow and the supports, should be pursued for any future experiments of the same sort.

Notch sensitivity was identified as the most likely source of the large scatter in the experiments of *Sigrist* (2006). A secondary contributing factor may have been creep effects in the vicinity of the notch prior to testing. All bend tests were conducted without weight compensation, and the bending moment due to self-weight of the samples contributed a large fraction of the ultimate bending moment. Enhanced stress relaxation in the vicinity of the notch, a characteristic observed in notched concrete tests (*Bažant and Gettu*, 1992), may have been a time-dependent source of scatter in Sigrist's tests if the snow specimens were mounted for different lengths of time prior to testing. For bend specimens, relative notch lengths of 0.3 or more would be most appropriate for reducing notch sensitivity and also for maximizing the possibility of stable crack growth initiation.

The post-peak strain softening behavior of snow in tension is still largely unknown. Stable crack growth initiation was not achieved in the experiments, as most tests were characterized by a loss of stability very near to the peak load. The apparent post-peak softening behavior measured by *Sigrist* (2006) was also likely an artifact of load cell rebound. The ability of a testing machine to perform the fast loading rates required in snow testing, combined with some sort of closed-loop servo control to achieve stable crack growth—all while operating at freezing temperatures—would likely require expensive customization of testing equipment. Different fracture geometries are likely the key to measuring stable crack growth and tensile strain softening in future studies. For example, in a fracture mechanical study of Antarctic shelf ice, *Rist et al.* (1999) abandoned three point bending tests in favor of an alternate test geometry because stable crack growth could not be achieved in three point bending. The lack of knowledge of post-peak softening was not altogether a failure of the present experimental study, however, as the fracture mechanical size effect laws used to analyze the experimental data only required the peak loads in the experiments. This is an advantage of Bažant's quasi-brittle formulations, and a primary reason they were applied here.

7.4.2 Applicability of results to avalanche operations

Mellor (1963) emphasized the convenience of hardness tests for providing simple, rapid and repeatable index measurements that can be correlated with properties of engineering interest such as strength. The blade penetration resistance gauge developed in the present study is the key to making a direct link between the results of the present research and operations involved in avalanche forecasting and control. The measure is easy to perform and closely analogous to the common hand hardness test which is used in nearly every avalanche forecasting operation, factors which have already promoted adoption of the gauge in several avalanche applications the United States.

The usefulness of the blade hardness index for tracking increases or decreases in cohesion and quantifying the vicinity of a snow layer to the cohesive threshold is one of the most advantageous characteristics of the blade hardness measure over other penetration resistance measures. In addition, the gauge can quantify the relative stiffness of a snow slab, an underlying weak layer (even a thin layer), and the basal layer and track them over time. Distinct relative differences in hand hardness between adjacent layers have been identified as a structural stability index which correlates strongly with slab avalanche occurrences (e.g. *McCammon and Schweizer*, 2002; *Schweizer and Jamieson*, 2003, 2007). The ability to more precisely quantify such a relative hardness difference using the blade gauge may lead to improved predictive capability using this type of structural stability index.

The ability to quantitatively correlate the blade hardness index and the mechanical properties of slab and weak layers such as strength and fracture toughness also has practical benefit. For example, the likelihood of triggering a slab avalanche and its release dimensions can be related to the ratio between fracture toughness in the slab to that in the weak layer (*McClung and Schweizer*, 2006). This fracture toughness ratio should be directly related to the ratio of blade hardness index in the slab to that in the weak layer. Since the blade gauge is easy to use and relatively inexpensive, it could prove to be an indispensable practical tool for avalanche forecasting operations.

The adoption of a quantitative and objective penetration resistance measure in avalanche operations would have direct benefit to the research community as well. Currently, the most widely used hardness measure is the hand test, a subjective technique that provides, at best, a self-consistent measure of resistance for an individual or an organization. The index values for the hand test are currently the only commonly reported hardness measures in avalanche data and are therefore useful in statistical correlations (e.g. *Schweizer and Jamieson*, 2003), but the index measurement is too coarse and subjective to use for predicting mechanical properties of snow, and different force standards have been applied in the test. If operations reported an objective and more precise measure such as the blade hardness index along with avalanche occurrence data, the data would be much more useful in developing and calibrating fracture mechanical models of slab avalanches. Ideally, this would then feed back to operations in the form of better forecasting techniques given better knowledge of the underlying physics of the phenomena at hand.

7.4.3 Future work

Experimental

Given the sensitivity of much of the experimental data to loading rate, more rate effect testing should be carried out in any future investigations of the fracture properties of cohesive snow related to avalanches. If possible, tests should be conducted over an even wider range of strain rates than in the present study. Ideally, the tests should be designed to cover strain rates below the creep-to-fracture transition to well above it. This will require a range of at least 4–5 orders of magnitude in loading rates. If instrumentation allows, measurements of recoverable deformation should be conducted to separate elastic from viscous deformation components as a function of rate.

Rate effects were also intertwined with size effects in the present study, since the constant loading rate in the size effect test series led to different nominal strain rates for differently sized beams. The smallest beams in the size effect experiments had the highest nominal strain rates, which, according to the rate-effect literature reviewed in this study, may have weakened the observed size effect on nominal strength. A stronger size effect may have been observed if the nominal strain rate, rather than the crosshead speed, been constant in these experiments. In future experiments using specimens of different size under displacement-controlled loading, the loading rate should be adjusted such that the nominal strain rate in the outer fiber of the beam is the same for each beam size. Even better, closed-loop servo control could be utilized to feed back a deflection measured on the beam itself (rather than the crosshead displacement or speed) for calculating a constant loading rate.

The combination of four point bending and horizontal weight compensation allowed increased span-to-depth ratios (more slender beams) and also produced tensile fractures which, in general, propagated in a straight line across the beam more consistently than using three point bending. Though it was more time consuming to set up experiments in this configuration, the higher quality data indicates that further work using a similar setup is worth the effort. If only vertical loading is possible, then the zero-brittleness method is recommended over size effect tests unless larger samples of snow can be collected or manufactured.

The experimental boundary conditions in future experiments should be improved from those used in the present study and those of *Sigrist* (2006). In bending experiments, some sort of roller mechanism should be devised for the supports to reduce the friction in the boundary conditions and reduce or eliminate slip between the snow and support plates that occurred in this study. The flat loading and support plates used in the present study were largely successful at minimizing, as much as possible for a material like snow, crushing at the load point and supports. Incorporating these flat plates, especially at the supports, with a roller mechanism would improve the quality of the experimental data and be especially helpful for calibrating numerical models.

Future experiments should also strive to achieve stable fracture behavior. Many of the experiments in this study became unstable upon fracture initiation. This could be addressed by investigating different fracture geometries or perhaps by using longer initial notch depths in beam bending tests—ensuring that weight compensation is also performed. Alternatively, testing under closed-loop servo control could provide longer periods of stable crack propagation prior to stability loss. Data from stable cracking experiments would be more useful for determining material fracture properties.

A technique for manufacturing snow in a consistent and repeatable manner would be extremely valuable for repeatability of experimental results. Comparing the results of experimental data arising from natural snow samples is difficult because natural snow varies so widely in structure depending on elevation and climate. That said, manufactured snow samples should not serve as a replacement for using natural snow samples, but rather as a complement to allow future investigators to calibrate, compare, and investigate equipment and procedures against the results of previous studies.

Investigating the transition in strength and fracture properties of snow as it reaches the melting temperature, transitioning from dry to moist to wet, would be a challenging but useful line of research. The difficulty of predicting wet slab avalanches can be attested by any avalanche forecaster, and it is not unreasonable to expect that in a warming climate there may be a greater number of wet slab avalanches compared to dry slab avalanches in many mountainous regions of the world. Addressing this problem experimentally would require a cold lab that has precise temperature and humidity control in order to hold snow samples stable sufficiently long to conduct experiments. Moist and wet snow would be difficult to maintain in a stable state for very long, but much remains to be learned about how snow fractures once liquid water is present in the ice matrix.

Using the blade penetration gauge, further field work to identify the penetration resistance at the cohesive threshold would be valuable, especially for practitioners. In January 2011 in the Selkirk Mountains, some preliminary data was obtained that addresses this question. A new digital force gauge with a 50 N capacity and a 0.005 N resolution was used (a Chatillon DFS-010). Storm snow had fallen on a well-developed surface hoar layer, but the initial storm snow was not cohesive enough to cause slab avalanches. After a period of about two days, over which the cohesion of the storm snow slowly increased, the first small slab avalanches began to occur. These avalanches were triggered remotely and released on small, unsupported features such as large boulders or roll-overs but did not propagate widely. In areas where these small avalanches could be safely reached, the blade gauge was used to penetrate the slab at the exposed crown fracture surface. The penetration resistance from these tests varied from being undetectable by the gauge (registering 0 N) to about 0.7 N, but was most commonly in the range of about 0.3–0.5 N. These results are preliminary and should be investigated further before practical guidance can be given to avalanche forecasters.

A further area of practical research using the blade gauge would be in exploring the penetration resistance in moist and wet snow. All of the data gathered with the gauge in this study was in dry snow. The blade penetration resistance is likely to increase in moist and wet snow for a given type of snow microstructure. Liquid water on the blade itself may pose problems during penetration.

Attaching the blade gauge to a testing machine and recording a high-frequency signal during penetration would allow for more precise interpretation of the resistance signal. This would facilitate comparison with other penetrometers such as the SMP and would allow analysis of the signal using micromechanical models. Furthermore, precise control over the penetration speed and distance from using a testing machine in a cold lab would assist in determining the dependence of the resistance on rate, temperature, and liquid water content.

Finally, in future experimental investigations of any mechanical properties of snow, much more information than simply the density is necessary to report for indexing against the properties of interest. Some objective measure of penetration resistance which indexes the structure of the snow should be carried out and reported. The loading rate and loading geometry should be described to facilitate comparison of data at different rates and from different types of tests. The snow temperature, grain size and grain type should also be reported as standard. In the present study, the analysis of data published in many previous papers was hampered by the lack of sufficient detail. A discussion around international standards for recording and reporting data in snow mechanics is warranted for the benefit of future investigations.

Analytical

Future refinements to the analytical framework of this study could improve upon the first-order approximations of a number of equations. First, higher-order beam theory is probably more appropriate than the simple beam theory that was used for much of the analysis here, especially given the small span to depth ratios used. Second, a viscoelastic beam theory might shed light on the rate dependence of properties such as flexural strength in the vicinity of the creep-to-fracture transition, and indicate whether the physical interpretation offered here of the toughening influence of viscous energy dissipation is indeed correct for explaining the decrease in strength with increasing rate. Finally, additional methods of fracture mechanics analysis ought to be applied to similar fracture data as obtained in this study. Only one type of effective crack or equivalent elastic crack analysis was applied in this study, of the type pioneered by Bažant and which requires only the peak loads from fracture tests. However, alternative effective crack models are available. Alternatively, cohesive crack models, which posit a closing pressure ahead of the crack tip to characterize fracture, might be explored. A further alternative is R-curve analysis, which, rather than using a single critical fracture parameter (fracture toughness or energy) to characterize fracture, uses a crack growth resistance curve to determine the conditions of fracture. In this approach, the entire R-curve itself is assumed to be a material property.

Numerical

There is ample room for further numerical model calibration and analysis. Much more experimental data from the present study is available which would be useful for model calibration. Of particular interest would be fitting of the size effect data, which might help to constrain the appropriate value of the fracture energy for the isotropic damage model. Additionally, experimental data on rate and temperature effects would be useful to simulate. Hundreds of additional experimental load-displacement curves could be "fit" with the numerical model to create spatial maps of model parameters for different types of snow and testing conditions. The construction of such parameter maps, or parameter spaces, would be tremendously beneficial for future investigation and application of the isotropic damage model related to slab avalanches.

Comparison of different numerical models, such as the rotating crack model (especially a nonlocal variant), against the isotropic damage model should be conducted to assess each model for strengths and weaknesses and determine the most appropriate model for avalanche applications. The model applied in the present study was judged to be adequate and promising, but no comparisons were made to assess whether the model choice, other than being physically motivated, was optimal.

7.5 Summary

An extensive experimental campaign was conducted to measure the strength and fracture mechanical properties of cohesive dry snow related to slab avalanches. The primary purpose of the research was to *understand* and *explain* the response of cohesive snow to tensile stresses and strain rates that cause fast fracture, as in slab avalanches. Numerical simulations of some experiments were conducted, and it was demonstrated that it is possible to *predict* many of the observed *nonlinear effects* in the tensile fracture of snow.

A new thin-blade penetration resistance gauge was developed that is easy to use and provides an objective index measure which is sensitive to the *structure* of cohesive snow. The blade gauge characterizes snow over a *length scale* for which snow—a highly porous and heterogeneous material—can be adequately approximated as a *continuum*. This allows the blade hardness index to have direct applicability in theories such as continuum mechanics and the various branches of fracture mechanics to analyze the deformation and fracture behavior of slab avalanches.

The blade hardness index was the single best indicator for the tensile strength and fracture toughness of cohesive snow. The cohesive threshold at which point snow can transmit sufficient tensile stress to support the propagation of fractures was quantitatively bounded within a narrow range of blade hardness index values. These results, combined with the low cost and ease of use of the blade gauge, ensure that the data collected here have direct applicability to field-based avalanche forecasting and control operations.

The tensile strength of snow was calculated from hundreds of unnotched bending tests in a cold lab. These data were synthesized with the published results of thousands of tensile strength tests from the literature. The new data agree well with the published data when expressed as a function of the snow density. The dependence of the tensile strength on hardness, grain size, loading rate, and specimen size was also demonstrated. The common use of density as the primary (and often only) index variable for strength was demonstrated as inferior to a *structural* index such as penetration resistance. This study highlights a need for more thorough and consistent reporting standards for cohesive snow properties in the field of snow mechanics.

Hundreds of additional laboratory fracture tests were conducted to determine fracture mechanical parameters for snow and their dependence on density, penetration resistance, and loading rate. Two different types of *size effect* methods were used as well as a paired notched-unnotched test method using a single specimen size. The data were analyzed using equivalent elastic (quasi-brittle) fracture mechanics to approximately account for the *nonlinearity in fracture* caused by a large fracture process zone. The fracture toughness, effective fracture process zone length, and several additional *length scales* associated with the tensile fracture of cohesive snow were calculated. *Rate effects* were observed in much of the data.

The data collected in the present study, combined with analysis of published data, resulted in the single largest collection of data on the tensile strength, fracture toughness, and fracture process zone length in the literature. These parameters can be expressed using density, penetration resistance, loading rate, and grain size as the most significant index variables.

Owing to the large effective process zone length compared to typical values of slab thickness, linear elastic fracture mechanics is not applicable to the analysis of most slab avalanches. Only for the very largest avalanches might the tensile fracture process zone have a negligible length compared to the slab thickness. Bažant's "universal" size effect law, a second-order equivalent elastic crack approximation, was determined to be the most appropriate relation for analyzing the experimental fracture data. The first-order notched and unnotched size effect laws had undesirable error levels associated with truncating various Taylor series expansions beyond the linear terms.

Using a nonlocal damage mechanics model implemented in an open-source finite element code, numerical simulations of a series of laboratory experiments were conducted. Model parameters were calculated from the experimentally-derived fracture parameters, and sensitivity analyses were conducted to constrain uncertain model parameters. The model was capable of simulating the propagation of a crack from a stress concentration as well as the initiation of a crack from a smooth boundary using similar parameters and boundary conditions. The simulated load-displacement curves showed fair agreement with the experimental curves and displayed quasi-brittle features, such as deviation from linearity prior to peak load and strain softening following peak load, that cannot be explained using a fully brittle failure model. Further work calibrating the model with other experimental data sets will help to constrain uncertain model parameters and establish parameter spaces for different types of snow and loading rates for future predictive modeling applications related to slab avalanches.

Creep and associated rate effects were present in some of the experimental data. However, for even the slowest rates of loading, the times to failure were short compared to the relaxation time for snow. Therefore, elastic theories (beam theory and quasi-brittle fracture mechanics) were deemed appropriate to analyze the data. Viscous energy dissipation would need to be accounted for in any calculations which involved an energy balance, but the relatively simple elastic analysis in the present study gave self-consistent results for the rate dependence of many fracture parameters.

An equivalence scheme was outlined for relating the experimental beam fracture data to actual snow slabs, which are quite different from beams. This scheme will allow the direct application of the extensive experimental results obtained in the present study to future analytical and numerical research into the fracture mechanics of slab avalanches.

Bibliography

Anderson, R. L. (1954), The problem of autocorrelation in regression analysis, *Journal of the American Statistical Association*, *49*(265), 113–129. Cited on page 321.

ASTM E399 - 05 (2005), Standard test method for linear-elastic plane-strain fracture toughness K_{Ic} of metallic materials, *Tech. rep.*, ASTM International. Cited on page 162.

Bader, H., and D. Kuriowa (1962), The physics and mechanics of snow as a material, *Tech. Rep. II-B*, Cold Regions Research and Engineering Laboratory, Hanover, New Hampshire. Cited on pages 1, 3, 4, 11, 16, 21, 22, 23, 108, and 262.

Bader, H., B. L. Hansen, J. A. Joseph, and M. A. Sandgren (1951), *Preliminary investigations of some physical properties of snow.*, SIPRE Report 7, U.S. Army Corps of Engineers Snow, Ice, and Permafrost Research Establishment, University of Minnesota. Cited on pages 11, 87, 89, 91, 92, and 100.

Bader, H., R. Haefeli, E. Bucher, J. Neher, O. Eckel, C. Thams, and P. Niggli (1954), *Snow and its metamorphism (Der Schnee und Seine Metamorphose)*, Snow Ice and Permafrost Research Establishment, U.S. Army Corps of Engineers, Wilmette Ill., SIPRE translation 14. Cited on pages 60, 85, 108, 129, and 238.

Ballard, G. E. H., and E. D. Feldt (1966), A theoretical consideration of the strength of snow, *Journal of Glaciology*, *6*, 159–170. Cited on pages 16 and 128.

Ballard, G. E. H., and R. W. McGaw (1966), A theory of snow failure, in *International Symposium on Scientific Aspects of Snow and Ice Avalanches, IAHS Publication No. 69*, pp. 160–169, Davos, Switzerland, Reports and Discussions. Cited on pages 16 and 128.

Banthia, N., and J. Sheng (1996), Fracture toughness of micro-fiber reinforced cement composites, *Cement and Concrete Composites*, *18*(4), 251–269, doi:10.1016/0958-9465(95)00030-5. Cited on pages 110 and 240.

Banthia, N., and J. Trottier (1995), Test methods for flexural toughness characterization of fiber reinforced concrete: Some concerns and a proposition, *ACI Materials Journal*, *92*(1), 1. Cited on page 233.

Bassis, J. N., H. A. Fricker, R. Coleman, Y. Bock, J. Behrens, D. Darnell, M. Okal, and J. B. Minster (2007), Seismicity and deformation associated with ice-shelf rift propagation, *Journal of Glaciology*, *53*(183), 523–536. Cited on page 222.

Bažant, Z. P. (1984), Size effect in blunt fracture - concrete, rock, metal, *Journal of Engineering Mechanics - ASCE*, *110*(4), 518–535. Cited on page 159.

Bažant, Z. P. (1991), Why continuum damage is nonlocal - micromechanics arguments, *Journal of Engineering Mechanics - ASCE*, *117*(5), 1070–1087. Cited on page 222.

Bažant, Z. P. (1994), Nonlocal damage theory based on micromechanics of crack interactions, *Journal of Engineering Mechanics - ASCE*, *120*(3), 593–617. Cited on page 222.

Bažant, Z. P. (1997), Scaling of quasibrittle fracture: Asymptotic analysis, *International Journal of Fracture*, *83*(1), 19–40. Cited on page 190.

Bažant, Z. P. (2005), *Scaling of structural strength*, 2nd ed., 336 pp., Butterworth-Heinemann, Oxford. Cited on pages 21, 23, 103, 159, 161, 188, 190, 197, 198, 200, 201, 202, 218, 237, 239, 255, 259, 260, 261, and 262.

Bažant, Z. P., and E. Becq-Giraudon (1999), Effects of size and slenderness on ductility of fracturing structures, *Journal of Engineering Mechanics*, *125*(3), 331–339. Cited on page 51.

Bažant, Z. P., and L. Cedolin (1991), *Stability of Structures*, Oxford University Press. Cited on page 234.

Bažant, Z. P., and R. Gettu (1992), Rate effects and load relaxation in static fracture of concrete, *ACI Materials Journal*, *89*(5), 456–468. Cited on pages 21, 22, 23, 125, 158, 178, 179, 210, 223, 232, 251, 254, 257, and 270.

Bažant, Z. P., and M. Jirásek (2002), Nonlocal integral formulations of plasticity and damage: Survey of progress, *J. Eng. Mech.*, *128*(11), 1119–1149, doi:10.1061/(ASCE)0733-9399(2002)128:11(1119). Cited on pages 17, 222, 223, 224, 225, 237, and 252.

Bažant, Z. P., and M. T. Kazemi (1990a), Determination of fracture energy, process zone length and brittleness number from size effect, with application to rock and concrete, *International Journal of Fracture*, *44*(2), 111–131. Cited on pages 14, 159, and 265.

Bažant, Z. P., and M. T. Kazemi (1990b), Size effect in fracture of ceramics and its use to determine fracture energy and effective process zone length, *Journal of the American Ceramic Society*, *73*(7), 1841–1853, doi:10.1111/j.1151-2916.1990.tb05233.x. Cited on pages 14, 21, 159, 172, 174, 177, 184, and 218.

Bažant, Z. P., and Y. Li (1997), Cohesive crack with rate-dependent opening and viscoelasticity: I. mathematical model and scaling, *International Journal of Fracture*, *86*(3), 247–265, doi:10.1023/A:1007486221395. Cited on page 23.

Bažant, Z. P., and Z. Li (1995), Modulus of rupture: Size effect due to fracture initiation in boundary layer, *Journal of Structural Engineering*, *121*(4), 739–746. Cited on pages 190 and 259.

Bažant, Z. P., and Z. Li (1996), Zero-brittleness size-effect method for one-size fracture test of concrete, *Journal of Engineering Mechanics - ASCE*, *122*(5), 458–468. Cited on pages 159, 190, 201, 202, 203, 204, and 242.

Bažant, Z. P., and S. Pang (2006), Mechanics-based statistics of failure risk of quasibrittle structures and size effect on safety factors, *Proceedings of the National Academy of Sciences of the United States of America*, *103*(25), 94349439, doi:10.1073/pnas.0602684103, PMC1480425. Cited on page 17.

Bažant, Z. P., and G. Pijaudier-Cabot (1988), Nonlocal continuum damage, localization instability and convergence, *Journal of Applied Mechanics - Transactions of the ASME*, *55*(2), 287–293. Cited on page 18.

Bažant, Z. P., and J. Planas (1998), *Fracture and size effect in concrete and other quasibrittle materials*, CRC Press, Boca Raton. Cited on pages 13, 14, 18, 21, 101, 113, 157, 159, 160, 161, 162, 163, 164, 167, 168, 169, 170, 171, 172, 173, 186, 188, 189, 190, 206, 209, 218, 222, 224, 233, 235, and 257.

Bažant, Z. P., G. Zi, and D. M. McClung (2003), Size effect law and fracture mechanics of the triggering of dry snow slab avalanches, *Journal of Geophysical Research*, *108*(B2), 2119, doi:10.1029/2002JB001884. Cited on pages 4, 5, 11, 18, 23, 57, and 158.

Bažant, Z. P., M. Vořechovský, and D. Novák (2007), Asymptotic prediction of energetic-statistical size effect from deterministic finite-element solutions, *Journal of Engineering Mechanics - ASCE*, *133*(2), 153–162. Cited on pages 196, 199, and 202.

Birkeland, K., K. Kronholm, M. Schneebeli, and C. Pielmeier (2004), Changes in the shear strength and micro-penetration hardness of a buried surface-hoar layer, *Annals of Glaciology*, *38*, 223–228. Cited on page 65.

Borstad, C. P., and D. M. McClung (2009), Size effect in dry snow slab tensile fracture, in *Proceedings of the 12th International Conference on Fracture*, Ottawa, Canada, 12-17 July, 2009, 10 pp. Cited on pages 57, 102, 103, and 157.

Borstad, C. P., and D. M. McClung (2011), Thin-blade penetration resistance and snow strength, *Journal of Glaciology*, *57*(202), 325–336. Cited on pages 34 and 56.

Bradley, C. C. (1966), The snow resistograph and slab avalanche investigations, in *International Symposium on Scientific Aspects of Snow and Ice Avalanches, IAHS Publication No. 69*, pp. 251–260, Davos, Switzerland, Reports and Discussions. Cited on pages 8 and 58.

Bradley, C. C. (1968), The resistograph and the compressive strength of snow, *Journal of Glaciology*, *7*(51), 499–506. Cited on pages 58 and 63.

Brown, R. L., and T. E. Lang (1975), On the fracture properties of snow, in *Proceedings of the International Symposium on Snow Mechanics, Grindelwald, IAHS Publication*, vol. 114, pp. 196—207. Cited on page 163.

Bucher, E. (1948), *Beitrag zu den Theoretischen Grundlagen des Lawinenverbaus*, German, Kommissionsverlag Kummerly & Frey, (Bern). Cited on pages 8, 9, 85, 87, and 99.

Butkovich, T. (1956), *Strength studies of high-density snow*, Snow Ice and Permafrost Research Establishment, U.S. Army Corps of Engineers, Research Report 18, Wilmette Ill. Cited on pages 4, 87, 100, and 129.

Camponovo, C., and J. Schweizer (2001), Rheological measurements of the viscoelastic properties of snow, *Annals of Glaciology*, *32*, 44–50. Cited on pages 56, 123, and 158.

Canadian Avalanche Association (CAA) (2007), Observational guidelines and recording standards for weather, snowpack and avalanches. Cited on pages 29, 33, 65, and 68.

Colbeck, S., E. Akitaya, R. Armstrong, H. Gubler, J. Lafeuille, K. Lied, D. McClung, and E. Morris (1990), The International Classification for Seasonal Snow on the Ground, *Tech. rep.*, The International Commission on Snow and Ice of the International Association of Scientific Hydrology. Cited on pages 33, 60, and 175.

Colbeck, S. C. (1982), An overview of seasonal snow metamorphism, *Reviews of Geophysics and Space Physics*, *20*(1), 45–61, doi:198210.1029/RG020i001p00045. Cited on page 4.

Conger, S. M., and D. M. McClung (2009), Comparison of density cutters for snow profile observations, *Journal of Glaciology*, *55*(189), 163–169. Cited on page 57.

Conway, H., and J. Abrahamson (1984), Snow stability index, *Journal of Glaciology*, *30*(106), 321–327. Cited on pages 4, 9, 104, and 105.

Conway, H., and J. Abrahamson (1988), Snow-slope stability - a probabilistic approach, *Journal of Glaciology*, *34*, 170–177. Cited on page 9.

Cotterell, B., and Y. W. Mai (1996), *Fracture Mechanics of Cementitious Materials*, Chapman & Hall, London. Cited on pages 18, 21, 23, 159, 164, 167, 186, 222, 233, 239, and 257.

de Quervain, M. (1951), *Die Festigkeitseigenschaften der Schneedecke und ihre Messung (Strength properties of a snow cover and its measurement)*, SIPRE Translation 9, Snow, Ice, and Permafrost Research Establishment, Wilmette, Illinois, translated by Charles M. Gottschalk of the SIPRE Project. Cited on pages 11, 60, 87, and 100.

Dempsey, J. P., and A. C. Palmer (1999), Non-universal scaling of arctic fractures, in *Proceedings of the 15th International Conference on Port and Ocean Engineering Under Arctic Conditions, August 1999, Helsinki, Finland*. Cited on pages 23 and 232.

Dempsey, J. P., R. M. Adamson, and S. V. Mulmule (1999a), Scale effects on the in-situ tensile strength and fracture of ice. part II: first-year sea ice at resolute, NWT, *International Journal of Fracture*, *95*(1-4), 347–366. Cited on page 17.

Dempsey, J. P., S. J. Defranco, R. M. Adamson, and S. V. Mulmule (1999b), Scale effects on the in-situ tensile strength and fracture of ice. part I: Large grained freshwater ice at Spray Lakes Reservoir, Alberta, *International Journal of Fracture*, *95*(1-4), 325–345. Cited on pages 13, 17, 22, 51, 224, and 265.

Fierz, C., R. Armstrong, Y. Durand, P. Etchevers, E. Greene, D. McClung, K. Nishimura, P. Satyawali, and S. Sokratov (2009), The International Classification for Seasonal Snow on the Ground, *IHP-VII Technical Documents in Hydrology 83*, UNESCO-IHP, Paris, IACS Contribution No. 1. Cited on pages 33, 56, 60, 61, 65, 67, 68, 112, 175, 192, 205, and 232.

Floyer, J. (2008), Layer detection and snowpack stratigraphy characterisation from digital penetrometer signals, Ph.D. thesis, University of Calgary, Calgary, Alberta Canada. Cited on pages 58, 61, 62, and 63.

Floyer, J., and J. Jamieson (2010), Rate-effect experiments on round-tipped penetrometer insertion into uniform snow, *Journal of Glaciology*, *56*(198), 664–672. Cited on page 61.

Föhn, P. M. B. (1987), The stability index and various triggering mechanisms, in *Avalanche Formation, Movement and Effects*, pp. 195—214, IAHS Publication No. 162, proceedings of the Davos Symposium. Cited on page 9.

Fukue, M. (1977), Mechanical performance of snow under loading, Ph.D. thesis, McGill University, Montreal, Quebec, Canada. Cited on pages 6, 11, 16, 57, 58, 59, 61, 62, 63, 68, 72, 78, 80, and 262.

Gettu, R., Z. P. Bažant, and M. E. Karr (1990), Fracture properties of high-strength concrete, *ACI Materials Journal*, *86*(6), 608–618. Cited on pages 194 and 232.

Geuzaine, C., and J. F. Remacle (2009), Gmsh: A 3-D finite element mesh generator with built-in pre- and post-processing facilities, *International Journal for Numerical Methods in Engineering*, *79*(11), 1309–1331, doi:10.1002/nme.2579. Cited on page 230.

Gibson, L. J., and M. F. Ashby (1988), *Cellular Solids: Structure & Properties*, Pergamon Press. Cited on page 214.

Glazovskaya, T. G. (1998), Global distribution of snow avalanches and changing activity in the northern hemisphere due to climate change, *Annals of Glaciology*, *26*, 337–342. Cited on page 2.

Gubler, H. (1978), An alternate statistical interpretation of the strength of snow, *Journal of Glaciology*, *20*(83), 343–357. Cited on pages 87 and 89.

Hadjab-Souag, H., J. F. Thimus, and M. Chabaat (2007), Detecting the fracture process zone in concrete using scanning electron microscopy and numerical modelling using the nonlocal isotropic damage model, *Can. J. Civ. Eng.*, *34*(4), 496–504, doi:10.1139/L06-132. Cited on page 227.

Haefeli, R. (1963), Stress transformations, tensile strengths, and rupture processes of the snow cover, in *Snow and Ice; Properties, Processes and Applications*, edited by W. D. Kingery, pp. 560–575, The M.I.T. Press, proceedings of a Conference held at the Massachusetts Institute of Technology, February 12-16, 1962. Cited on page 9.

Hertzberg, R. W. (1996), *Deformation and fracture mechanics of engineering materials*, 4th ed., Wiley, New York. Cited on pages 157 and 159.

Höller, P., and R. Fromm (2010), Quantification of the hand hardness test, *Annals of Glaciology*, *51*(54), 39–44. Cited on pages 60, 77, and 78.

IPCC (2007), Climate Change 2007, Synthesis Report, *Tech. rep.*, Contribution of Working Groups I, II and III to the Fourth Assessment Report of the Intergovernmental Panel on Climate Change. Cited on page 2.

Jaccard, C. (1966), Stabilité des plaques de neige, in *International Symposium on Scientific Aspects of Snow and Ice Avalanches, IAHS Publication No. 69*, pp. 170—181, Davos, Switzerland, Reports and Discussions. Cited on page 9.

Jamieson, J. B. (1988), In situ tensile strength of snow in relation to slab avalances, Master's thesis, University of Calgary. Cited on pages xi, 4, 11, 16, 77, 104, 105, 107, 121, 129, 138, 139, 140, 158, 194, 195, and 198.

Jamieson, J. B. (1995), Avalanche prediction for persistent snow slabs, Ph.D. thesis, University of Calgary. Cited on page 9.

Jamieson, J. B., and C. D. Johnston (1990), In situ tensile tests of snow-pack layers, *Journal of Glaciology*, *36*(122), 102–106. Cited on pages 16, 41, 104, 194, and 195.

Jamieson, J. B., and C. D. Johnston (1992), Snowpack characteristics associated with avalanche incidents, *Canadian Geotechnical Journal*, *29*(5), 862–866. Cited on pages 5 and 7.

Jamieson, J. B., and C. Stethem (2002), Snow avalanche hazards and management in Canada: challenges and progress, *Natural Hazards*, *26*, 35–53. Cited on page 1.

Jirásek, M., and P. Grassl (2008), Evaluation of directional mesh bias in concrete fracture simulations using continuum damage models, *Engineering Fracture Mechanics*, *75*, 1921–1943, doi:10.1016/j.engfracmech.2007.11.010. Cited on pages 225 and 252.

Jirásek, M., and B. Patzák (2002), Consistent tangent stiffness for nonlocal damage models, *Computers & Structures*, *80*(14-15), 1279–1293, doi:10.1016/S0045-7949(02)00078-0. Cited on pages 222, 225, 226, and 228.

Jirásek, M., and T. Zimmerman (1998), Rotating crack model with transition to scalar damage, *Journal of Engineering Mechanics*, *124*(3), 277–284. Cited on page 251.

Jirásek, M., S. Rolshoven, and P. Grassl (2004), Size effect on fracture energy induced by non-locality, *International Journal for Numerical and Analytical Methods in Geomechanics*, *28*, 653–670, doi:10.1002/nag.364. Cited on pages 227, 228, and 250.

Johnson, J. J., and M. Schneebeli (1999), Characterizing the microstructural and micromechanical properties of snow, *Cold Regions Science and Technology*, *30*, 91–100. Cited on page 61.

Keeler, C. M. (1969), Some physical properties of alpine snow, *Tech. rep.*, U.S. Army Corps of Engineers Cold Regions Research and Engineering Laboratory, Hanover N.H. Cited on pages 86, 87, 95, 98, 128, and 155.

Keeler, C. M., and W. F. Weeks (1968), Investigations into the mechanical properties of alpine snow-packs, *Journal of Glaciology*, *7*(50), 253–271. Cited on pages 77, 87, 89, 93, 95, 98, 128, 129, and 155.

Kirchner, H. O. K., G. Michot, and T. Suzuki (2000), Fracture toughness of snow in tension, *Philosophical Magazine A - Physics of Condensed Matter Structure Defects*, *80*(5), 1265–1272. Cited on pages 13 and 14.

Kirchner, H. O. K., G. Michot, H. Narita, and T. Suzuki (2001), Snow as a foam of ice: plasticity, fracture and the brittle-to-ductile transition, *Philosophical Magazine A - Physics of Condensed Matter Structure Defects*, *81*(9), 2161–2181. Cited on pages 13 and 214.

Kirchner, H. O. K., G. Michot, and J. Schweizer (2002a), Fracture toughness of snow in shear and tension, *Scripta Materialia*, *46*(6), 425–429. Cited on pages 13 and 14.

Kirchner, H. O. K., G. Michot, and J. Schweizer (2002b), Fracture toughness of snow in shear under friction, *Physical Review E*, *66*(2). Cited on page 14.

Kirchner, H. O. K., H. Peterlik, and G. Michot (2004), Size independence of the strength of snow, *Physical Review. E, Statistical, Nonlinear, and Soft Matter Physics*, *69*(1 Pt 1), 011,306, doi:14995613, PMID: 14995613. Cited on pages 195 and 198.

Lemaitre, J. (1996), *A Course on Damage Mechanics*, 2nd ed., Springer-Verlag, Berlin. Cited on page 223.

Lutz, E., K. Birkeland, and H. Marshall (2009), Quantifying changes in weak layer microstructure associated with artificial load changes, *Cold Regions Science and Technology*, *59*(2-3), 202–209, doi:10.1016/j.coldregions.2009.04.003. Cited on page 65.

Mackenzie, R., and W. Payten (2002), A portable, variable-speed, penetrometer for snow pit evaluation., in *Proceedings of the International Snow Science Workshop*, pp. 294–300, Penticton, B.C. Canada. Cited on page 61.

Malvern, L. E. (1969), *Introduction to the Mechanics of a Continuous Medium*, Series in Engineering of the Physical Sciences, Prentice-Hall, New Jersey. Cited on page 325.

Marshall, H. P., and J. B. Johnson (2009), Accurate inversion of high-resolution snow penetrometer signals for microstructural and micromechanical properties, *Journal of Geophysical Research - Earth Surface*, *114*(F04016), F04016, doi:10.1029/2009JF001269, doi:10.1029/2009JF001269. Cited on pages 56, 61, and 65.

Martin, E., G. Giraud, Y. Lejeune, and G. Boudart (2001), Impact of a climate change on avalanche hazard, *Annals of Glaciology*, *32*(1), 163–167, doi:10.3189/172756401781819292. Cited on page 2.

Martinelli, M. (1971), *Physical properties of alpine snow as related to weather and avalanche conditions*, USDA Forest Service Research Paper RM-64, Rocky Mountain Forest and Range Experiment Station, Fort Collins, Colorado. Cited on pages viii, xi, 4, 5, 63, 64, 77, 80, 86, 87, 95, 98, 100, 101, 102, 127, 129, 143, 144, 145, 152, 153, 154, and 155.

McCammon, I., and J. Schweizer (2002), A field method for identifying structural weaknesses in the snowpack, in *Proceedings of the International Snow Science Workshop, Penticton, British Columbia, Sept. 30 - Oct. 4, 2002*. Cited on page 271.

McClung, D., and P. Schaerer (2006), *The Avalanche Handbook*, 3rd ed., The Mountaineers, Seattle, WA. Cited on pages 1, 2, 3, 5, 7, 9, 10, 11, 38, 47, 60, 81, 121, and 172.

McClung, D. M. (1977), Direct simple shear tests on snow and their relation to slab avalanche formation, *J. Glaciol.*, *19*(81), 101–109. Cited on pages 4 and 10.

McClung, D. M. (1979a), In-situ estimates of the tensile strength of snow utilizing large sample sizes, *Journal of Glaciology*, *22*(87), 321–329. Cited on pages 4, 11, 104, and 129.

McClung, D. M. (1979b), Shear fracture precipitated by strain softening as a mechanism of dry slab avalanche release, *Journal of Geophysical Research*, *84*(B7), 3519–3526. Cited on pages 5, 10, 259, 261, and 266.

McClung, D. M. (1981), Fracture mechanical models of dry slab avalanche release, *Journal of Geophysical Research*, *86*(B11), 10,783–10,790. Cited on pages 4, 5, 10, 23, 251, 259, and 266.

McClung, D. M. (1987), Mechanics of snow slab failure from a geotechnical perspective, in *Avalanche Formation, Movement and Effects*, pp. 475–508, IAHS Publication No. 162, proceedings of the Davos Symposium. Cited on pages 5, 10, 158, 259, and 266.

McClung, D. M. (1996), Effects of temperature on fracture in dry slab avalanche release, *Journal of Geophysical Research - Solid Earth*, *101*(B10), 21,907–21,920. Cited on pages 5, 7, 23, and 158.

McClung, D. M. (2003), Size scaling for dry snow slab release, *Journal of Geophysical Research - Solid Earth*, *108*(B10). Cited on pages 4, 5, 7, and 9.

McClung, D. M. (2005), Dry slab avalanche shear fracture properties from field measurements, *Journal of Geophysical Research - Earth Surface*, *110*(F4). Cited on page 11.

McClung, D. M. (2007a), Dry snow slab shear fracture speeds, *Geophysical Research Letters*, *34*(10), L10,502. Cited on pages 56, 98, and 257.

McClung, D. M. (2007b), Fracture energy applicable to dry snow slab avalanche release, *Geophysical Research Letters*, *34*(2), L02,503. Cited on pages 13, 56, and 242.

McClung, D. M. (2009a), Dimensions of dry snow slab avalanches from field measurements, *Journal of Geophysical Research - Earth Surface*, *114*. Cited on pages 5, 12, 13, and 257.

McClung, D. M. (2009b), Dry snow slab quasi-brittle fracture initiation and verification from field tests, *Journal of Geophysical Research - Earth Surface*, *114*(F1), F01,022. Cited on pages 11, 158, and 267.

McClung, D. M., and J. Schweizer (1999), Skier triggering, snow temperatures and the stability index for dry-slab avalanche initiation, *Journal of Glaciology*, *45*(150), 190–200. Cited on page 9.

McClung, D. M., and J. Schweizer (2006), Fracture toughness of dry snow slab avalanches from field measurements, *Journal of Geophysical Research - Earth Surface*, *111*(F4), F04,008. Cited on pages 2, 12, 13, 14, 18, 157, 158, 187, 215, 259, and 271.

Mellor, M. (1963), Polar snow - a summary of engineering properties, in *Ice and Snow: Properties, Processes, and Applications*, edited by W. D. Kingery, pp. 528–559, M.I.T. Press, Proceedings of a Conference held at The Massachusetts Institute of Technology, February 12-16, 1962. Cited on page 270.

Mellor, M. (1968), Avalanches, *Tech. Rep. III-A3d*, Cold Regions Research and Engineering Laboratory, Hanover, New Hampshire. Cited on pages 2, 5, 8, 11, and 262.

Mellor, M. (1975), A review of basic snow mechanics, in *Proceedings of the International Symposium on Snow Mechanics, Grindelwald, IAHS Publication*, vol. 114, pp. 251–291. Cited on pages 4, 53, 93, and 123.

Mellor, M., and J. H. Smith (1966), Strength studies of snow, in *International Symposium on Scientific Aspects of Snow and Ice Avalanches, IAHS Publication No. 69*, pp. 100–113, Reports and Discussions. Cited on pages 4, 16, 21, 22, 122, 123, 128, 214, and 258.

Mindess, S. (1991), The fracture process zone in concrete, in *Toughening Mechanisms in Quasi-brittle Materials*, edited by S. P. Shah, Kluwer Academic Publishers. Cited on pages 21 and 167.

Mulmule, S., and J. Dempsey (2000), LEFM size requirements for the fracture testing of sea ice, *International Journal of Fracture*, *102*(1), 85–98. Cited on pages 17, 224, and 265.

Nakamura, T., O. Abe, R. Hashimoto, and T. Ohta (2010), A dynamic method to measure the shear strength of snow, *Journal of Glaciology*, *56*(196), 333–338. Cited on page 56.

Narita, H. (1980), Mechanical behavior and structure of snow under uniaxial tensile stress, *Journal of Glaciology*, *26*(94), 275–282. Cited on pages 4, 11, 21, 22, 23, 59, 78, 97, 108, 118, 122, 125, 232, and 256.

Narita, H. (1983), An experimental study on tensile fracture of snow, *Institute of Low Temperature Science, Hokkaido University*, *A32*, 1–37. Cited on pages 22, 23, 72, 97, 108, 118, 122, 123, 256, and 258.

Otsuka, K., and H. Date (2000), Fracture process zone in concrete tension specimen, *Engineering Fracture Mechanics*, *65*(2-3), 111–131, doi:10.1016/S0013-7944(99)00111-3. Cited on page 221.

Palmer, A. C., and J. R. Rice (1973), The growth of slip surfaces in the progressive failure of over-consolidated clay, *Proceedings of the Royal Society of London. Series A, Mathematical and Physical Sciences (1934-1990)*, *332*(1591), 527–548, doi:10.1098/rspa.1973.0040. Cited on page 10.

Patzák, B., and Z. Bittnar (2001), Design of object oriented finite element code, *Advances in Engineering Software*, *32*(10-11), 759–767. Cited on page 230.

Patzák, B., D. Rypl, and Z. Bittnar (2001), Parallel explicit finite element dynamics with nonlocal constitutive models, *Computers and Structures*, *79*(26-28), 2287–2297. Cited on page 230.

Perla, R. (1969), Strength tests on newly fallen snow, *Journal of Glaciology*, *8*(54), 427–441. Cited on pages 4, 106, 107, and 129.

Perla, R. (1975), Stress and fracture of snow slabs, in *Proceedings of the International Symposium on Snow Mechanics, Grindelwald, IAHS Publication*, vol. 114, pp. 208–221. Cited on page 10.

Perla, R. (1977), Slab avalanche measurements, *Canadian Geotechnical Journal*, *14*(2), 206–213. Cited on pages 3, 5, 9, 17, 158, 172, and 265.

Perla, R., and T. Beck (1983), Experience with shear frames, *Journal of Glaciology*, *29*(103), 485–491. Cited on pages 4 and 158.

Perla, R., and E. R. LaChapelle (1970), A theory of snow slab failure, *Journal of Geophysical Research*, *75*(36), 7619–7627. Cited on pages 5, 9, and 10.

Pielmeier, C., and M. Schneebeli (2003), Stratigraphy and changes in hardness of snow measured by hand, ramsonde and snow micro penetrometer: a comparison with planar sections, *Cold Regions Science and Technology*, *37*(3), 393–405, doi:10.1016/S0165-232X(03)00079-X. Cited on page 61.

Pijaudier-Cabot, G., and Z. P. Bažant (1987), Nonlocal damage theory, *Journal of Engineering Mechanics - ASCE*, *113*(10), 1512–1533. Cited on page 222.

Pilkey, W. D. (1997), *Peterson's Stress Concentration Factors*, 2nd ed., John Wiley & Sons. Cited on pages 91 and 92.

Planas, J., and M. Elices (1989), Size-effect in concrete structures: mathematical approximations and experimental validation, in *Cracking and Damage: Strain Localization and Size Effect*, edited by J. Mazars and Z. P. Bažant, pp. 462–476, Elsevier Applied Science, proceedings of the France-U.S. Workshop, Cachan, France, 6-9 Sept. 1988. Cited on page 21.

Pralong, A., and M. Funk (2005), Dynamic damage model of crevasse opening and application to glacier calving, *Journal of Geophysical Research*, *110*, doi:200510.1029/2004JB003104. Cited on page 224.

Pralong, A., K. Hutter, and M. Funk (2006), Anisotropic damage mechanics for viscoelastic ice, *Continuum Mechanics and Thermodynamics*, *17*(5), 387–408, doi:10.1007/s00161-005-0002-5. Cited on page 224.

Rawlings, J. O., S. G. Pantula, and D. A. Dickey (1998), *Applied Regression Analysis: A Research Tool*, Springer texts in statistics, 2nd ed., Springer, New York. Cited on pages 133, 181, 321, and 322.

Reiweger, I., and J. Schweizer (2010), Failure of a layer of buried surface hoar, *Geophysical Research Letters*, *37*, 5 PP., doi:201010.1029/2010GL045433. Cited on page 7.

Rist, M. A., P. R. Sammonds, S. A. F. Murrell, P. G. Meredith, C. S. M. Doake, H. Oerter, and K. Matsuki (1999), Experimental and theoretical fracture mechanics applied to Antarctic ice fracture and surface crevassing, *Journal of Geophysical Research - Solid Earth*, *104*(B2), 2973–2987. Cited on pages 51 and 270.

Ritz, C., and J. C. Streibig (2008), *Nonlinear Regression with R*, Use R! series, Springer, New York. Cited on pages 131, 173, 181, and 324.

Roch, A. (1966), Les variations de la rèsistance de la neige, in *International Symposium on Scientific Aspects of Snow and Ice Avalanches, IAHS Publication No. 69*, pp. 86–99, Davos, Switzerland, Reports and Discussions. Cited on pages 9, 11, 23, 87, 99, and 100.

Salm, B. (1971), On the rheological behavior of snow under high stresses, *Contributions from the Institute of Low Temperature Science*, *23*, 1–43. Cited on pages 17 and 222.

Schapery, R. A. (1997), Linear elastic and viscoelastic deformation behavior of ice, *Journal of Cold Regions Engineering*, *11*(4), 271—290. Cited on page 23.

Schneebeli, M., and J. Johnson (1998), A constant-speed penetrometer for high-resolution snow stratigraphy, *Annals of Glaciology*, *26*, 107–111. Cited on pages 61, 64, 87, and 93.

Schulson, E. M. (2001), Brittle failure of ice, *Engineering Fracture Mechanics*, *68*(17-18), 1839–1887, doi:10.1016/S0013-7944(01)00037-6. Cited on page 93.

Schulson, E. M., and P. Duval (2009), *Creep and fracture of ice*, Cambridge University Press, Cambridge UK. Cited on pages 4, 13, 17, 22, 23, 24, 100, 128, 224, 256, and 265.

Schulson, E. M., P. N. Lim, and R. W. Lee (1984), A brittle to ductile transition in ice under tension, *Philosophical Magazine A*, *49*(3), 353–363, doi:10.1080/01418618408233279. Cited on page 3.

Schweizer, J. (1998), Laboratory experiments on shear failure of snow, *Annals of Glaciology*, *26*, 97–102, Proceedings of the International Symposium on Snow and Avalanches, Chamonix Mont-Blanc, France, 26-30 May 1997. Cited on pages 4, 21, and 22.

Schweizer, J. (1999), Review of dry snow slab avalanche release, *Cold Regions Science and Technology*, *30*(1-3), 43–57, doi:10.1016/S0165-232X(99)00025-7. Cited on page 9.

Schweizer, J., and J. B. Jamieson (2001), Snow cover properties for skier triggering of avalanches, *Cold Regions Science and Technology*, *33*(2-3), 207–221. Cited on pages 60 and 82.

Schweizer, J., and J. B. Jamieson (2003), Snowpack properties for snow profile analysis, *Cold Regions Science and Technology*, *37*, 233–241. Cited on page 271.

Schweizer, J., and J. B. Jamieson (2007), A threshold sum approach to stability evaluation of manual snow profiles, *Cold Regions Science and Technology*, *47*(1-2), 50–59, doi:10.1016/j.coldregions.2006.08.011. Cited on pages 60, 82, and 271.

Schweizer, J., J. B. Jamieson, and M. Schneebeli (2003), Snow avalanche formation, *Reviews of Geophysics*, *41*(4), 1016, doi:10.1029/2002RG000123. Cited on pages 5, 7, 10, 11, 16, 56, 250, and 322.

Schweizer, J., G. Michot, and H. Kirchner (2004), On the fracture toughness of snow, *Annals of Glaciology*, *38*, 1–8. Cited on pages 13 and 14.

Schweizer, J., K. Kronholm, J. B. Jamieson, and K. W. Birkeland (2008), Review of spatial variability of snowpack properties and its importance for avalanche formation, *Cold Regions Science and Technology*, *51*(2-3), 253–272, doi:10.1016/j.coldregions.2007.04.009. Cited on page 4.

Shapiro, L. H., J. B. Johnson, M. Sturm, and G. L. Blaisdell (1997), Snow mechanics: Review of the state of knowledge and applications, *Tech. Rep. 97-3*, Cold Regions Research and Engineering Laboratory. Cited on pages 16, 56, 58, 63, and 238.

Shinojima, K. (1966), Study on the visco-elastic deformation of deposited snow, in *Physics of Snow and Ice: International Conference on Low Temperature Science*, vol. 1, part 2, edited by H. Oura, pp. 875–907, Institute of Low Temperature Science, Hokkaido University, Sapporo. Cited on pages 179, 232, 238, 255, 256, 325, and 326.

Sigrist, C. (2006), Measurement of fracture mechanical properties of snow and application to dry snow slab avalanche release, Ph.D. thesis, Swiss Federal Institute of Technology, Zurich. Cited on pages xi, 4, 14, 18, 28, 43, 98, 110, 114, 118, 141, 142, 158, 162, 163, 165, 171, 172, 173, 174, 175, 176, 177, 178, 180, 184, 185, 186, 195, 208, 215, 216, 233, 254, 255, 269, 270, and 272.

Sigrist, C., J. Schweizer, H. J. Schindler, and J. Dual (2005a), Fracture toughness of snow: size effects in a quasibrittle material, in *Proceedings of the 11th International Conference on Fracture - ICF XI*, Turin, Italy. Cited on pages 158 and 163.

Sigrist, C., J. Schweizer, H. J. Schindler, and J. Dual (2005b), On size and shape effects in snow fracture toughness measurements, *Cold Regions Science and Technology*, *43*(1-2), 24–35. Cited on pages 4, 14, 56, 158, 163, 183, and 195.

Smith, F. W. (1972), Elastic stresses in layered snow packs, *Journal of Glaciology*, *11*(63), 407—414. Cited on page 261.

Sommerfeld, R. A. (1969), The role of stress concentration in slab avalanche release, *Journal of Glaciology*, *8*, 451–462. Cited on pages 8 and 9.

Sommerfeld, R. A. (1974), Weibull prediction of tensile strength-volume relationship of snow, *Journal of Geophysical Research*, *79*(23), 3353–3356. Cited on pages 4, 11, 87, 88, 89, 91, 92, 96, 101, 102, 103, 129, 158, 188, 195, and 198.

Sommerfeld, R. A. (1980), Statistical-models of snow strength, *Journal of Glaciology*, *26*(94), 217–223. Cited on pages 104 and 158.

Sommerfeld, R. A., and R. M. King (1979), A recommendation for the application of the Roch index for slab avalanche release, *Journal of Glaciology*, *22*(88), 547–549. Cited on pages 9 and 158.

Sommerfeld, R. A., and F. Wolfe (1972), A centrifugal tensile tester for snow, *Research note RM-227*, Rocky Mountain Forest and Range Experiment Station, United States Department of Agriculture, Fort Collins, Colorado, U.S.A. Cited on pages 11, 86, 87, 91, and 103.

St. Lawrence, W., and C. C. Bradley (1975), The deformation of snow in terms of a structural mechanism, in *Proceedings of the International Symposium on Snow Mechanics, Grindelwald, IAHS Publication*, vol. 114, pp. 155–170. Cited on page 222.

St. Lawrence, W. F., T. E. Lang, R. L. Brown, and C. C. Bradley (1973), Acoustic emission in snow at constant rates of deformation, *Journal of Glaciology*, *12*(64), 144—146. Cited on page 222.

Stethem, C., J. B. Jamieson, P. Schaerer, D. Liverman, D. Germain, and S. Walker (2003), Snow avalanche hazard in Canada - a review, *Natural Hazards*, *28*(2/3), 487—515, doi:10.1023/A:1022998512227. Cited on page 2.

Szabo, D., and M. Schneebeli (2007), Subsecond sintering of ice, *Applied Physics Letters*, *90*(15), 151916, doi:10.1063/1.2721391. Cited on page 58.

Tada, H., P. C. Paris, and G. R. Irwin (2000), *The Stress Analysis of Cracks Handbook*, 3rd ed., The American Society of Mechanical Engineers (ASME) Press, New York. Cited on page 160.

Takeuchi, Y., Y. Nohguchi, K. Kawashima, and K. Izumi (1998), Measurement of snow-hardness distribution, *Annals of Glaciology*, *26*, 27–30, papers from the International Symposium on Snow and Avalanches, Chamonix Mont-Blanc, France, 26-30 May 1997. Cited on pages 77 and 78.

Tang, T., Z. P. Bažant, S. Yang, and D. Zollinger (1996), Variable-notch one-size test method for fracture energy and process zone length, *Engineering Fracture Mechanics*, *55*(3), 383–404. Cited on pages 184 and 200.

Tang, T., S. Yang, and D. G. Zollinger (1999), Determination of fracture energy and process zone length using variable-notch one-size specimens, *ACI Materials Journal*, *96*(1), 3–10. Cited on page 201.

Timoshenko, S. (1940), *Strength of materials.*, 2nd ed., D. Van Nostrand Co., N.Y. Cited on pages 69, 121, and 229.

Timoshenko, S., and J. Goodier (1951), *Theory of Elasticity*, 2nd ed., McGraw-Hill Book Co., New York. Cited on pages 110, 114, and 183.

Upadhyay, A., S. K. Joshi, and C. Chandel (2007), Tensile strength of snow using centrifugal technique, *Defence Science Journal*, *57*(6), 787795. Cited on pages 86, 87, 95, 96, 97, 98, 99, and 129.

Voight, B., et al. (1990), Snow avalanche hazards and mitigation in the United States, *Tech. rep.*, Panel on Snow Avalanches, Committee on Ground Failure Hazards Mitigation Research, Division of Natural Hazard Mitigation, Commission on Engineering and Technical Systems, National Research Council, Washington, D.C. Cited on pages 1 and 2.

Weibull, W. (1939), A statistical theory of the strength of materials, *Proceedings of the Royal Swedish Academy of Engineering Sciences*, *141*, 1–45. Cited on page 188.

Whiteley, G. M., and A. R. Dexter (1981), The dependence of soil penetrometer pressure on penetrometer size, *Journal of Agricultural Engineering Research*, *26*, 467–476. Cited on page 63.

Appendix A: Fracture Morphology From Bending Tests

This appendix contains a collection of images and analysis related to the fracture morphology from the bending experiments in the present study. The vast majority of the beam bending tests resulted in relatively straight and clean fractures that propagated across the sample in a direction perpendicular to the maximum applied tensile stress in the outer fiber of the beam, as in Figure A.1. The broken half of the sample remaining in the figure was from an unnotched, weight-compensated bending test on a beam sample of dimensions 10 cm by 30 cm by 10 cm, with a support span of 15 cm. Even for this very short span-to-depth ratio (1.5), the resulting fracture was tensile and originated at the outer fiber of the beam. This is in contrast to the rarely-observed shear failure across the beam shown in Figure 2.22 on page 50.

Figure A.2 shows the fracture surfaces from both halves of a notched beam sample after a test. The smooth surfaces are from the notch cutting, and the rough surfaces from the fracture. The fracture emanated from the notch tip and propagated across the sample in the same direction as the notch, normal to the direction of maximum tensile stress calculated from beam theory.

The typical roughness length scale of a fracture surface was approximated as about 10 times the grain size. This roughness length decreased with increasing slab stiffness or hardness, and vice-versa. The roughness length scales in Figures A.1 and A.2 were typical for most of the experiments in this study. For reference, the tensile fracture surface (crown) from a skier-triggered slab avalanche is shown in Figure A.3. This tensile fracture surface has a similar, if slightly greater, roughness length scale.

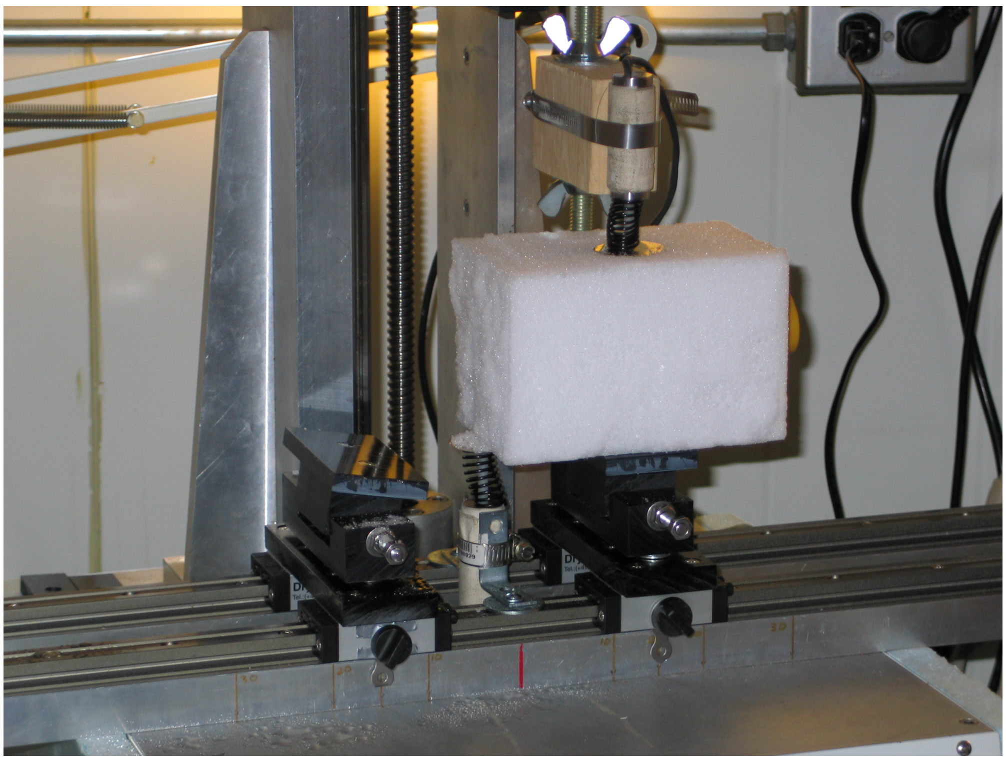

Figure A.1: *Broken half of a beam sample following an unnotched bending test.*

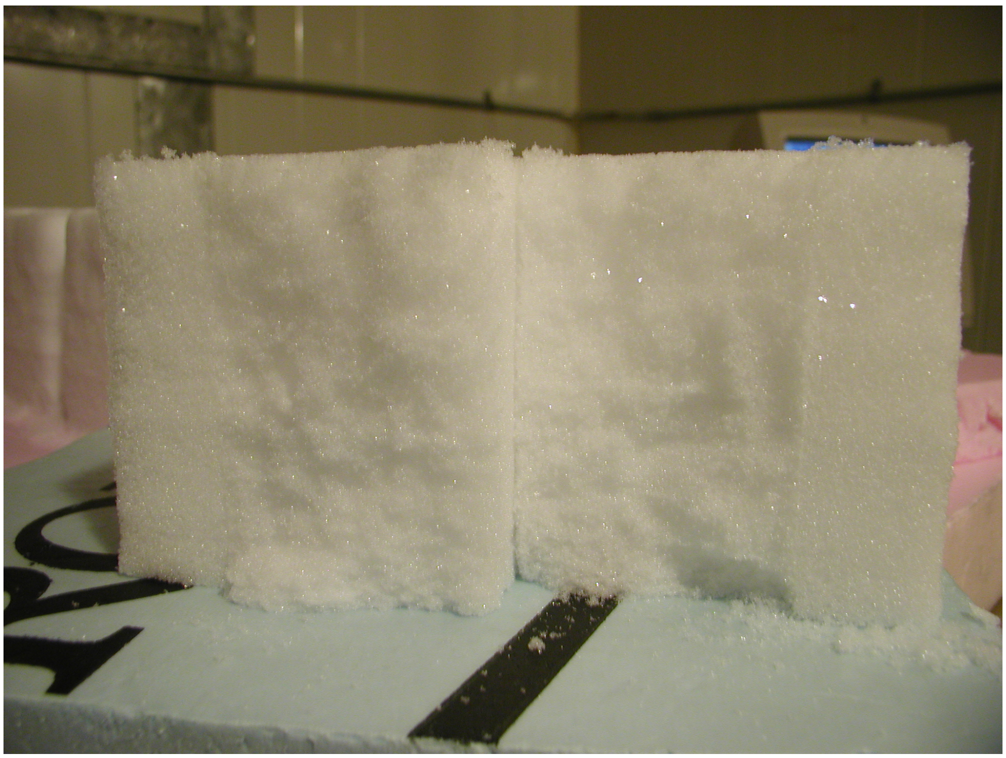

Figure A.2: *Broken halves of a beam sample following a notched bending test. The protrusion at the bottom center of the left half is a cluster of melted and refrozen grains. Apart from this protrusion, the roughness length scale of the fracture surfaces was typical of most of the experiments in this study.*

Figure A.3: *Tensile crown fracture surface from a soft slab avalanche.*

Fractured Sample Images: Before and After

The following images (Figures A.4-A.6) show slab samples mounted prior to a bending test followed by a photo taken immediately after the test. The tests were all from the same date and test series, and were conducted in weight compensated three point bending. The sample size and geometry as well as the loading geometry were the same as for the zero-brittleness (notched-unnotched) data in Chapter 5 (Section 5.4, page 200). In each case, the tensile crack originated at the bottom of the sample and propagated more or less in a straight line upward through the sample. Figures A.4 and A.5 show notched bending tests, and Figure A.6 shows an unnotched test. In both the notched and unnotched tests, the manner in which the crack propagated was similar: initiating near the tensile face of the beam and propagating normal to the direction of maximum principal stress according to beam theory. These observations hold in general for the bending tests conducted in this study. In some tests conducted in the same manner in this study, the crack deviated from propagating in a straight line when it neared the compressive face of the beam, in which case the crack sometimes curved toward one of the edges of the flat loading plate. However, this behavior would have occurred well after the peak load was reached.

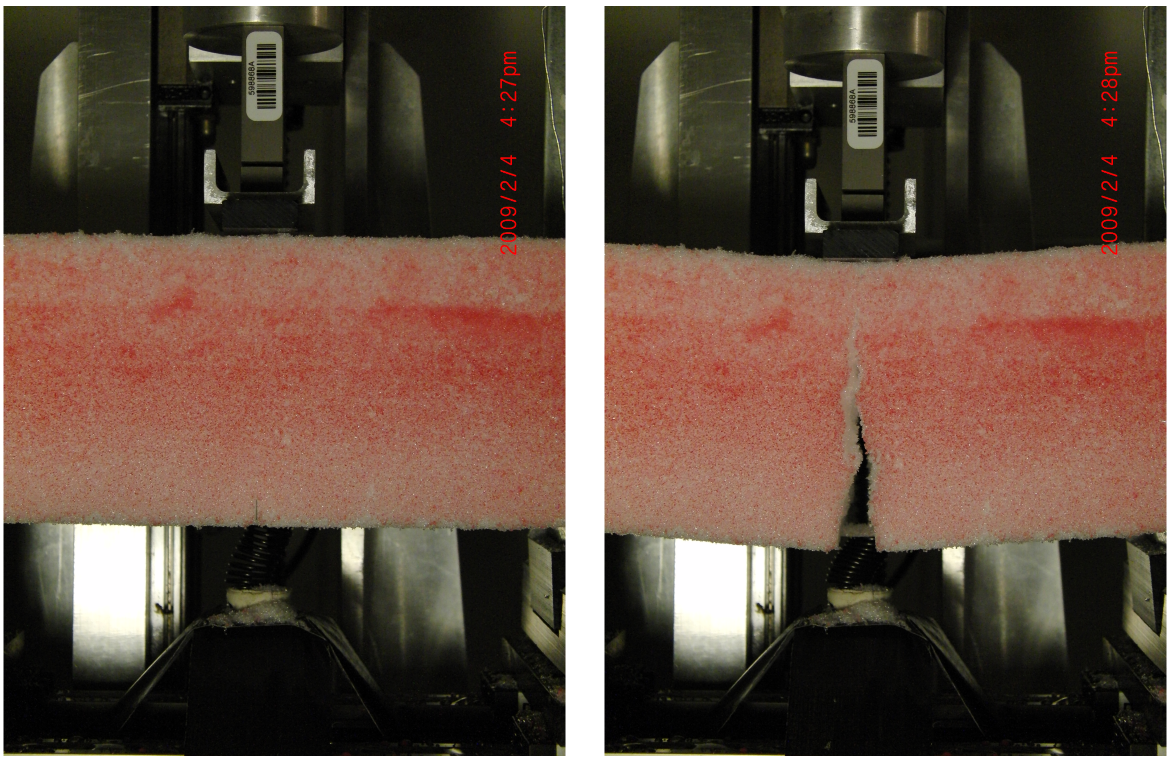

(a) **(b)**

Figure A.4: *Before and after images of an edge-notched three point bending test, vertically oriented and weight compensated. Beam depth* $D = 10$ *cm, length* $L = 50$ *cm, width 10 cm, support span* $S = 25$ *cm, crosshead loading rate 1.25 cm/s, bulk snow density 240 kg/m*^{3}*, blade hardness index 2.6 N, slab temperature* $-6.6\,^{\circ}C$*, notch depth 1 cm, snow composed of mixed rounded and faceted crystals 0.5–1 mm. Red spray paint applied to face of sample to improve contrast.*

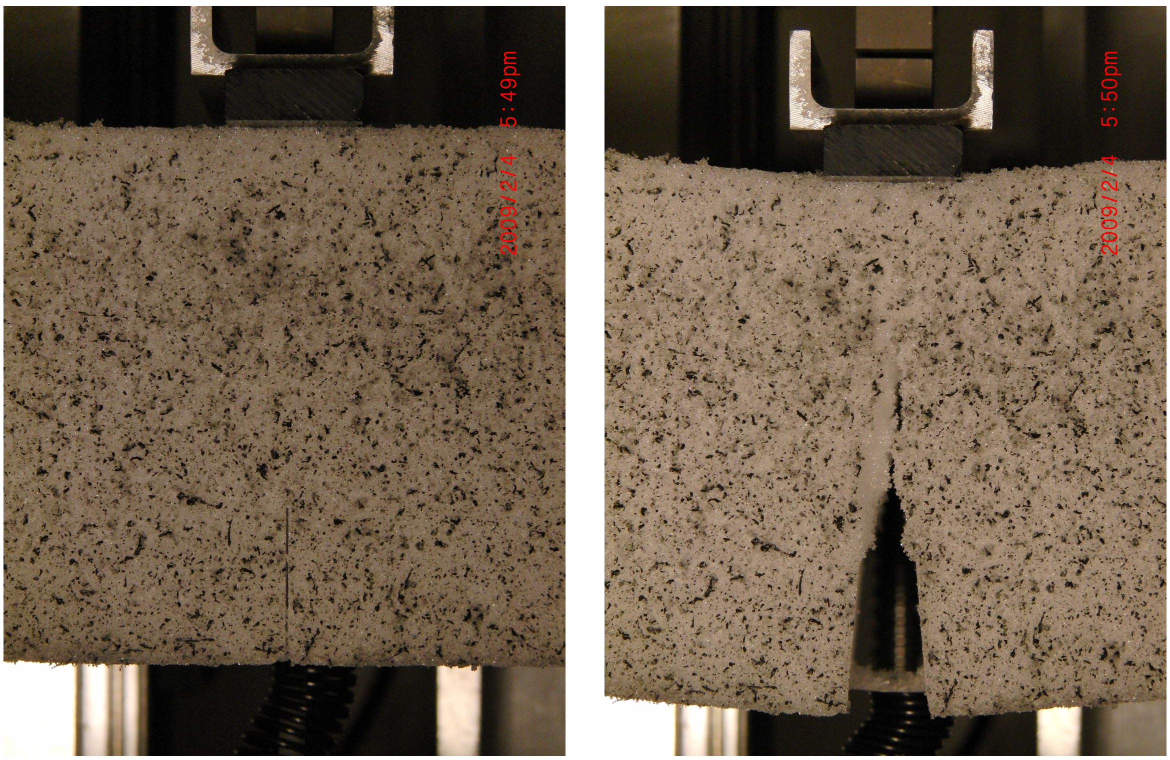

(a) **(b)**

Figure A.5: *Before and after images of an edge-notched three point bending test, vertically oriented and weight compensated. Beam depth* $D = 10$ *cm, length* $L = 50$ *cm, width 10 cm, support span* $S = 25$ *cm, crosshead loading rate 1.25 cm/s, bulk snow density 240 kg/m*^{3}*, blade hardness index 2.3 N, slab temperature* $-4.4\,^\circ C$*, notch depth 3 cm, snow composed of mixed rounded and faceted crystals 0.5–1 mm. Black speckle paint applied to face of sample to improve contrast.*

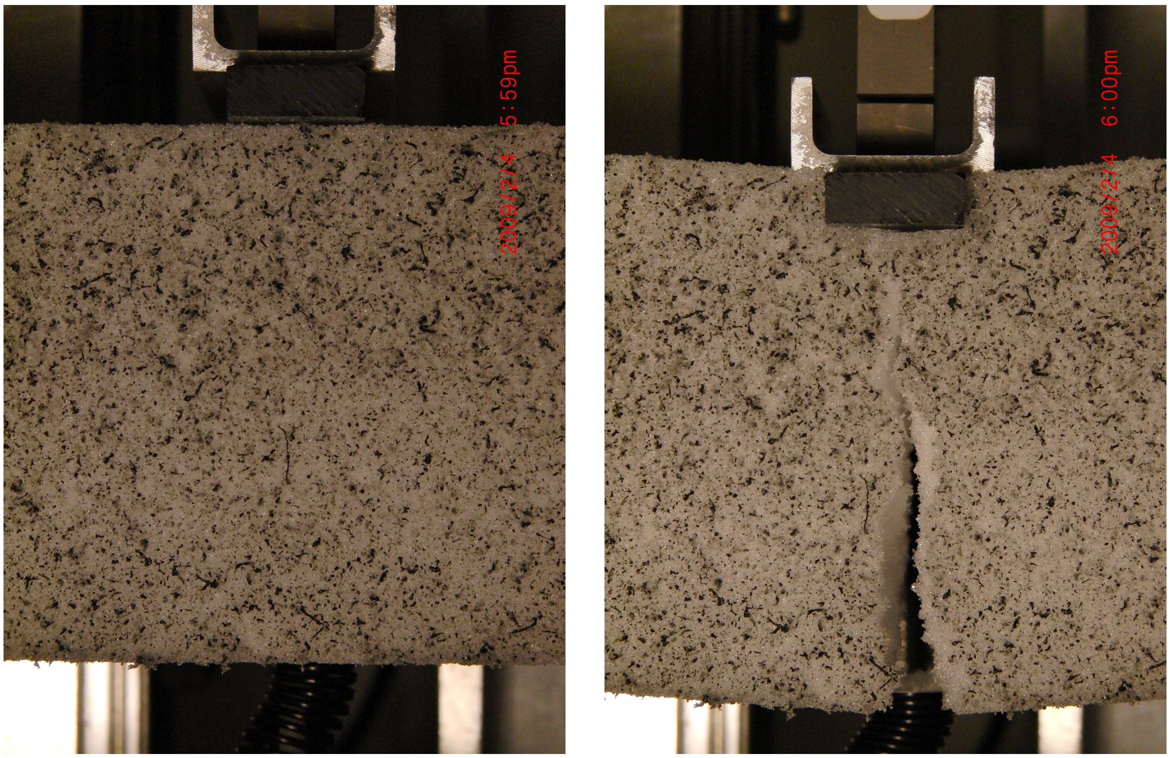

(a) **(b)**

Figure A.6: *Before and after images of an unnotched three point bending test, vertically oriented and weight compensated. Beam depth* $D = 10$ *cm, length* $L = 50$ *cm, width 10 cm, support span* $S = 25$ *cm, crosshead loading rate 1.25 cm/s, bulk snow density 242 kg/m*^{3}*, blade hardness index 2.3 N, slab temperature* $-4.3\,^{\circ}C$*, snow composed of mixed rounded and faceted crystals 0.5–1 mm. Black speckle paint applied to face of sample to improve contrast. Note the level of load plate crushing at the top of the sample, a feature that was more common in unnotched tests and in softer snow such as this.*

Fracture Sequence With Particle Tracking Analysis

The following sequence of images (Figures A.8–A.27) resulted from a high speed video of a fracture test. The test was conducted in four point bending in the horizontal weight-compensated orientation. The test was filmed from above, looking down on the sample. The movie captured an image of 512 by 512 pixels at a rate of 1900 frames per second. Only those frames just prior to and including the fracture are shown here. Figure A.7 indicates the field of view of the camera with respect to the rest of the sample and the loading geometry.

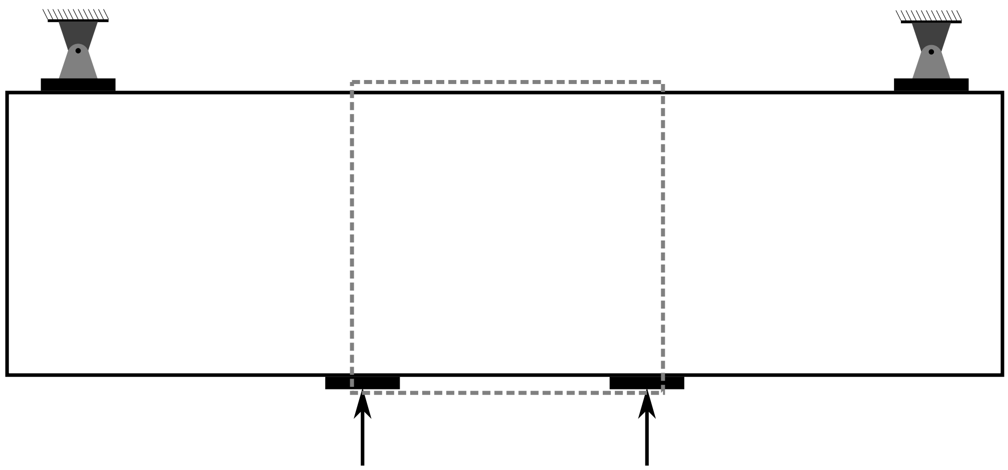

Figure A.7: *Schematic indicating field of view of high speed camera (dashed gray line) for subsequent fracture sequence, plan view. Test was conducted in four point bending on an unnotched sample in horizontal weight-compensated orientation. Sample had beam depth $D = 20$ cm, span to depth ratio $S/D = 3$, loaded at beam third points. Loading rate was 1.25 cm/s.*

In addition to showing sequential frames from the movie, graphs from a particle tracking analysis for each frame are shown for comparison. The surface of the sample was seeded with tracer particles (peppercorns) for tracking. The position, velocity, and acceleration of each tracer was calculated frame by frame and used to construct the accompanying quiver plots. The tail of each vector corresponds to the center of the corresponding tracer. The magnitude, direction, and color of the arrow indicate the results of the particle tracking in the indicated units for each figure.

The sequence of vector images for acceleration and velocity are more revealing than the actual movie frame or the displacement measurements. The acceleration and velocity signals indicate that the fracture initiates first near the tensile face of the beam. It then propagates more or less in a straight line across the

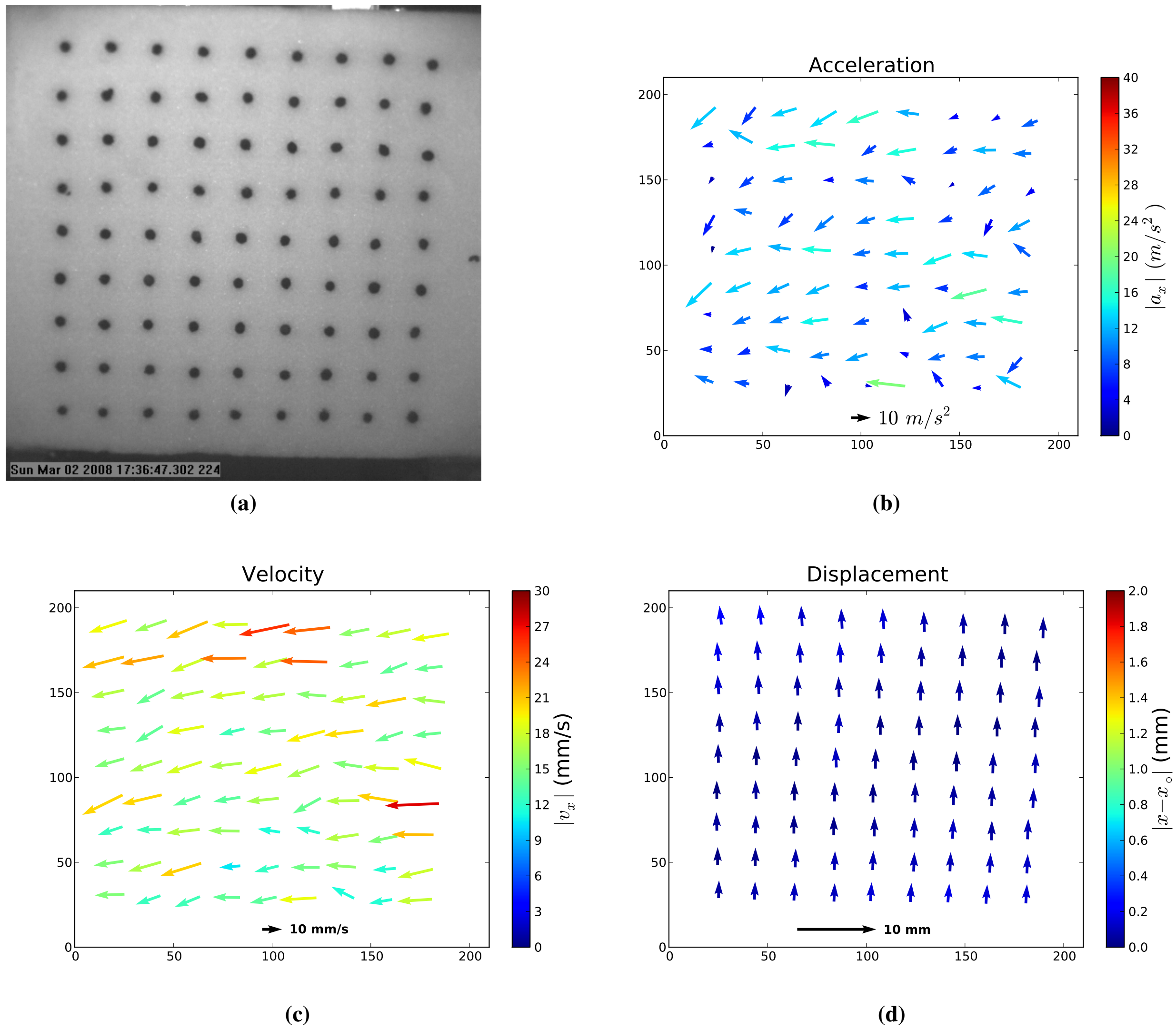

Figure A.8: *First image in a sequence showing tensile crack initiation and propagation in a bending test. Actual movie frame in (a), acceleration (b), velocity (c) and displacement (d) of black tracer particles calculated using particle tracking software.*

beam, again normal to the maximum applied tensile stress in the beam. The particle tracking indicates the formation of the crack well before visible crack formation can be seen in the actual movie frames.

This image sequence can best be visualized by appropriately sizing the electronic version of this document and then advancing ahead one page at a time.

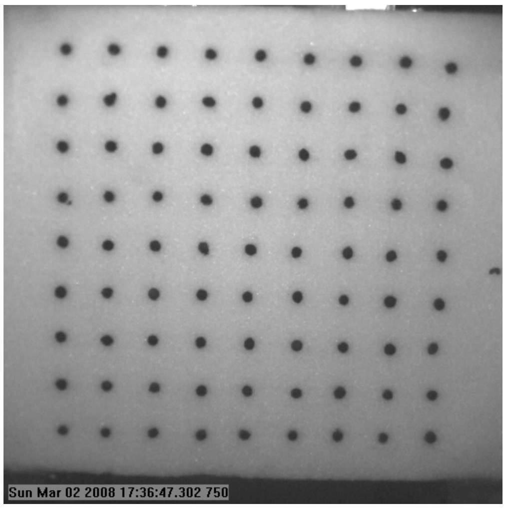

(a)

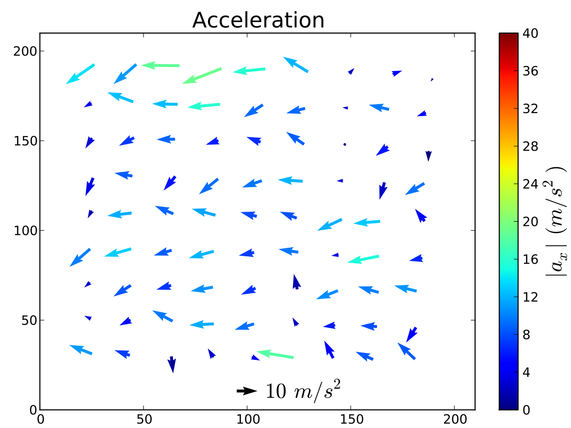

(b)

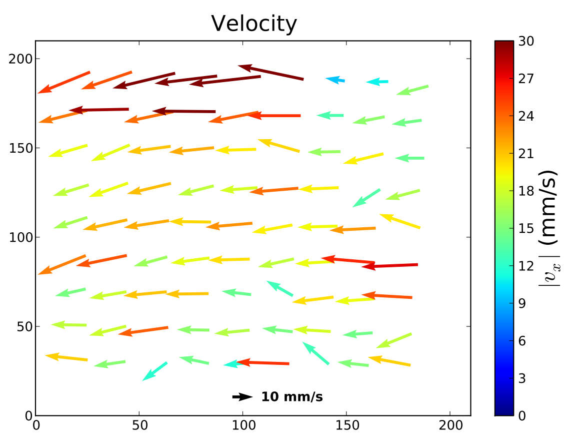

(c)

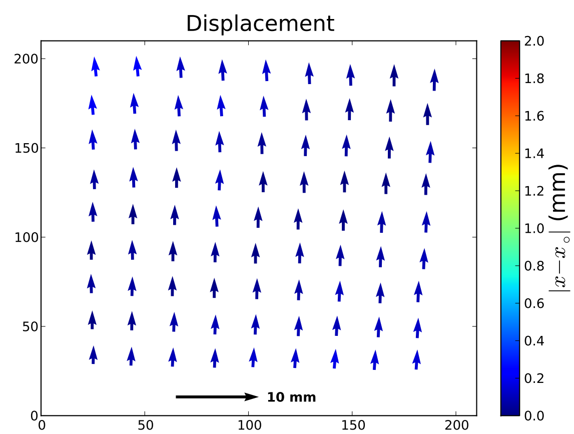

(d)

Figure A.9: *Crack sequence image 2.*

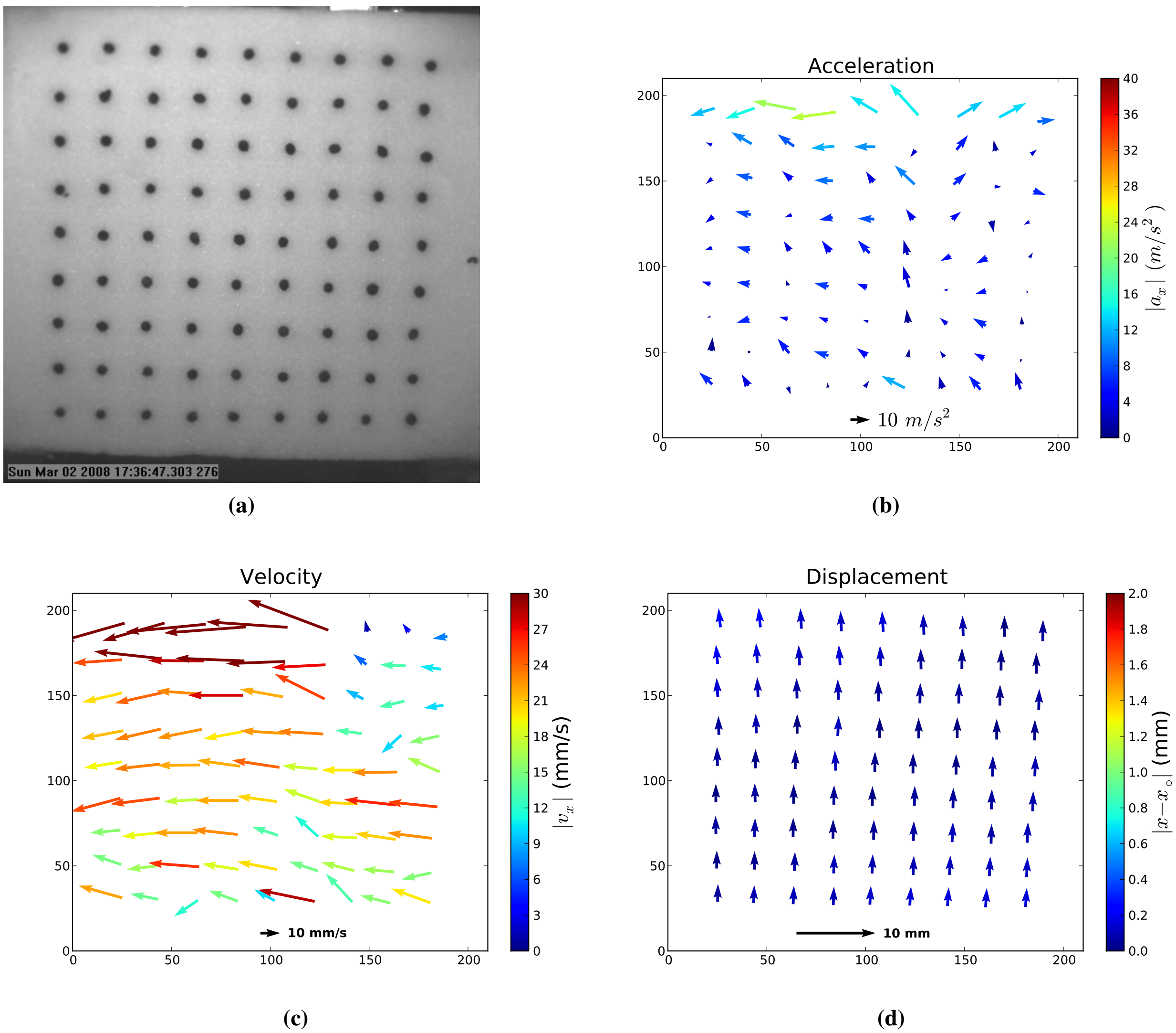

Figure A.10: *Crack sequence image 3. Initiation of tensile crack in the outer edge of the beam apparent in velocity and acceleration signals.*

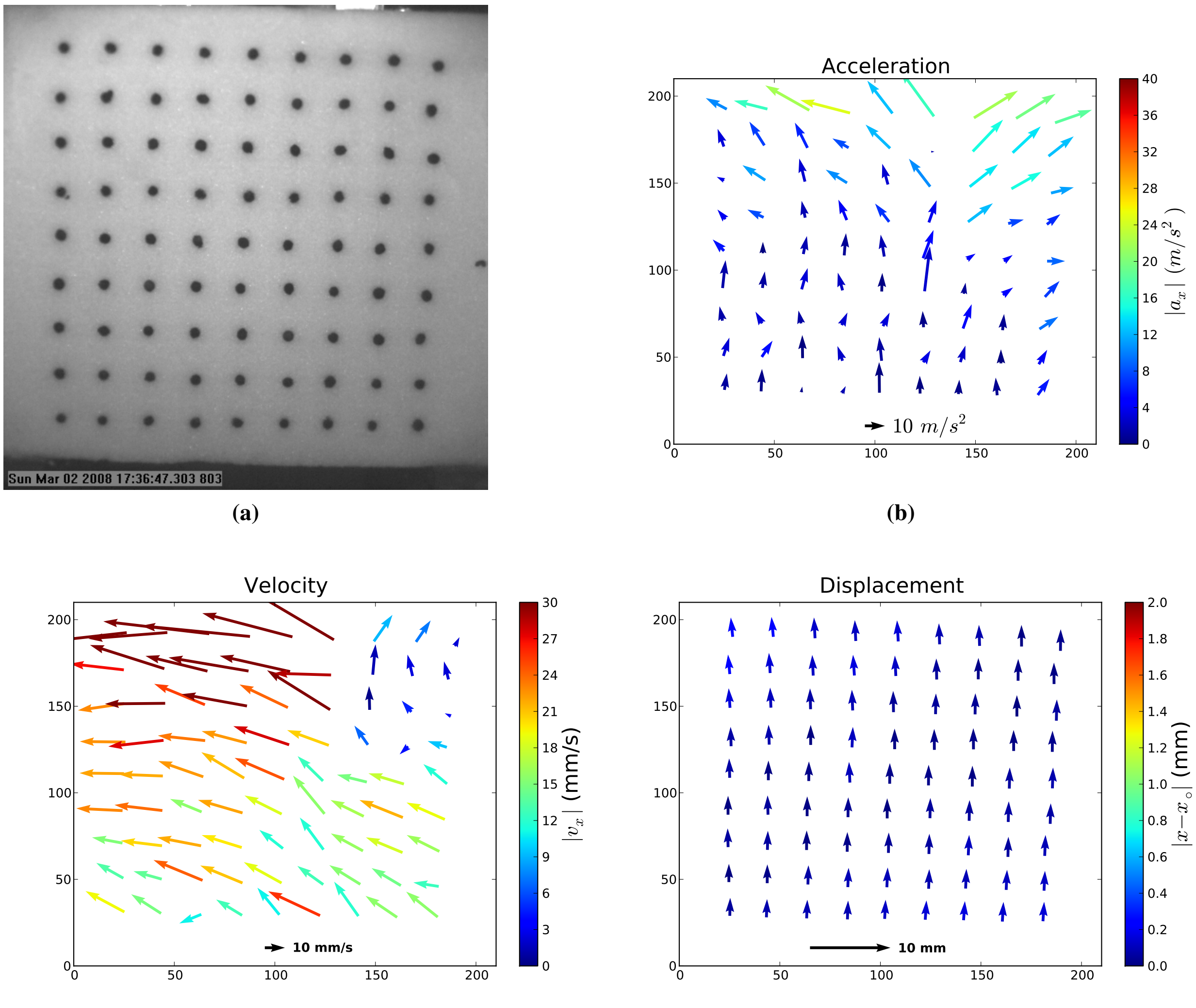

(a) (b) (c) (d)

Figure A.11: *Crack sequence image 4.*

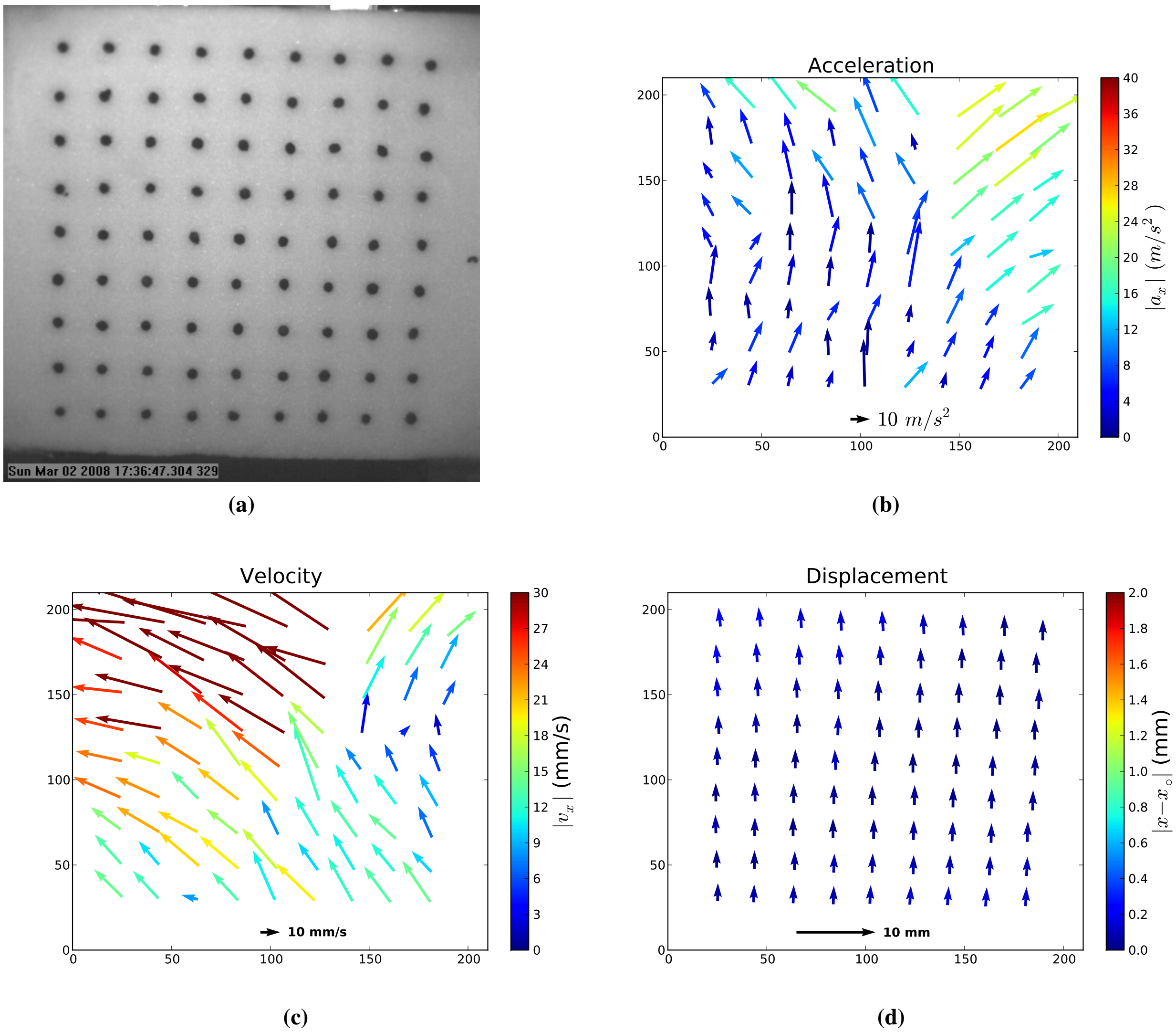

Figure A.12: *Crack sequence image 5.*

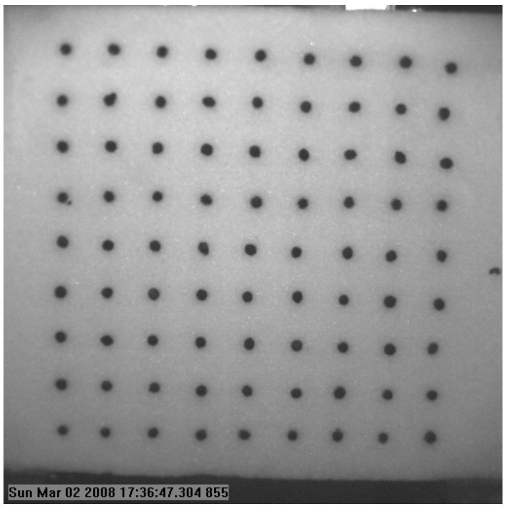

(a)

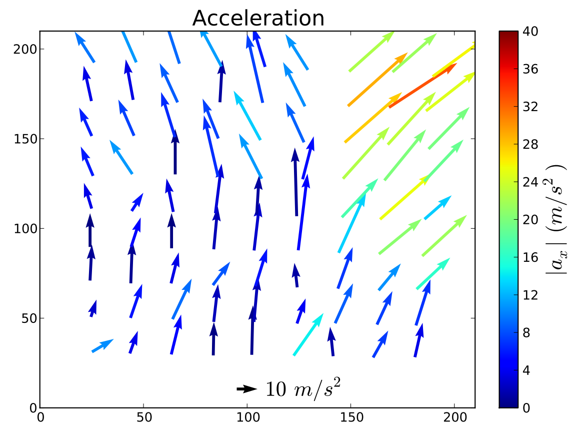

(b)

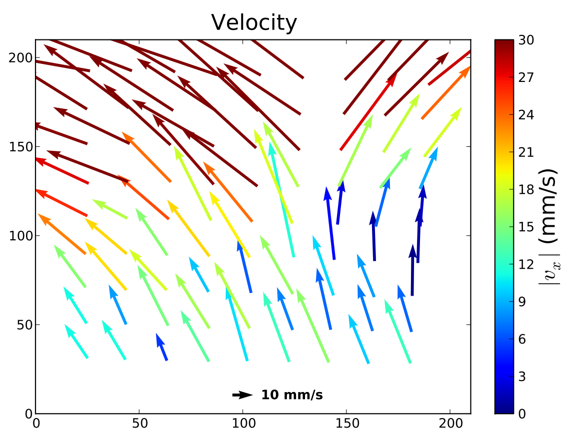

(c)

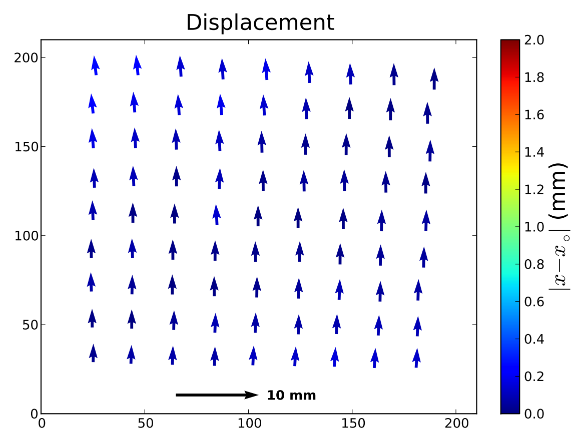

(d)

Figure A.13: *Crack sequence image 6.*

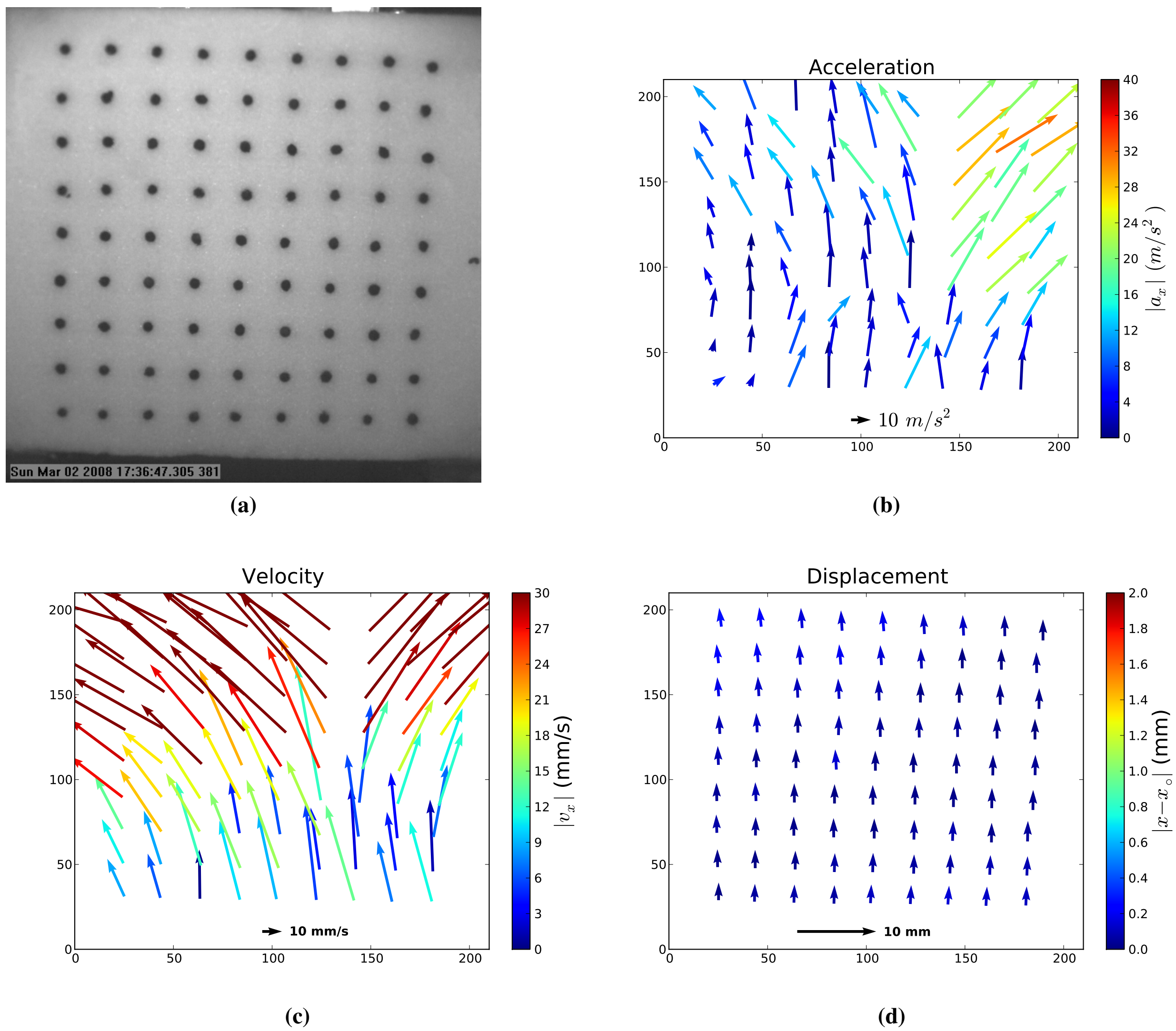

Figure A.14: *Crack sequence image 7.*

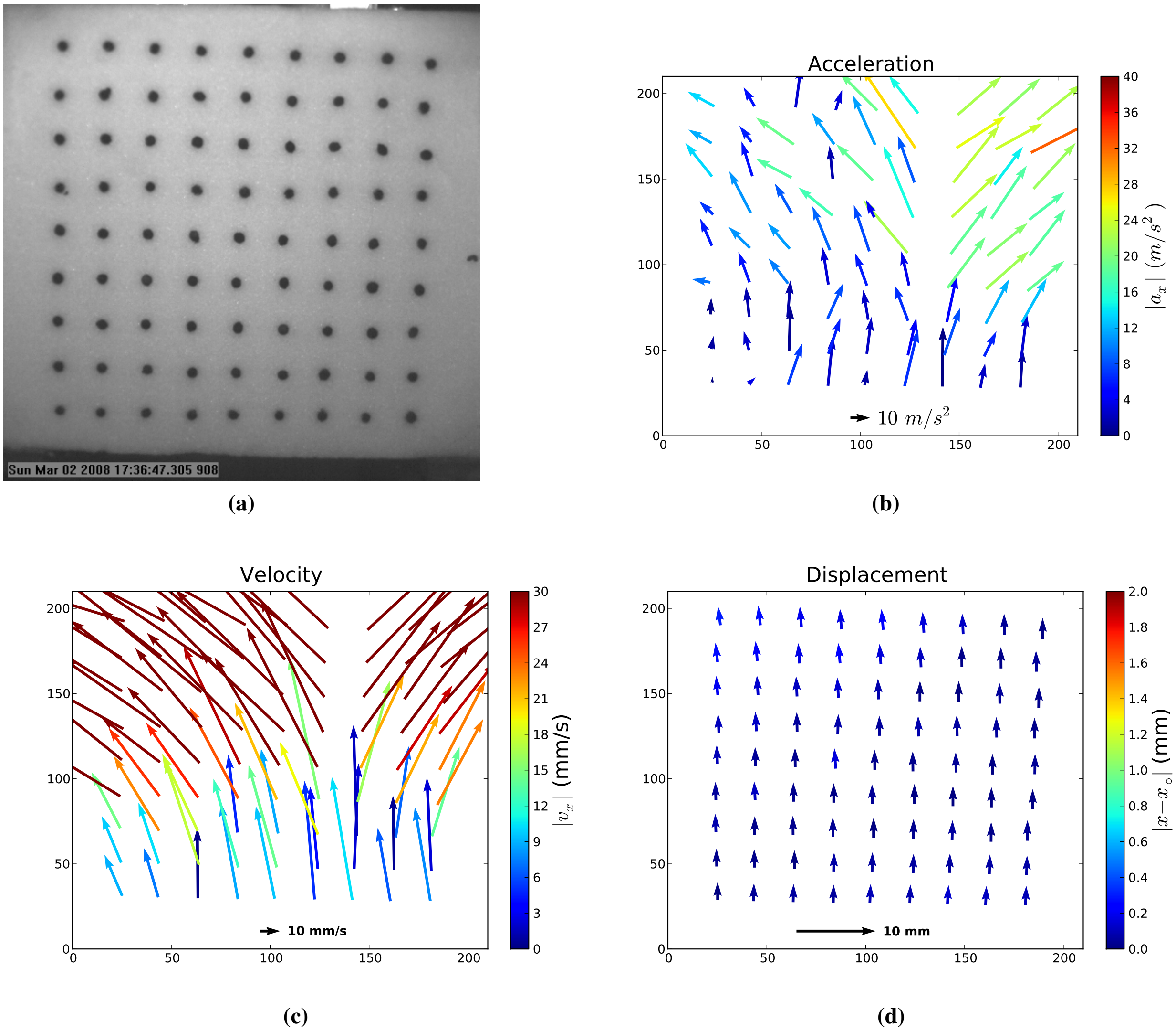

Figure A.15: *Crack sequence image 8. First* visible *indication of crack coalescence at top edge (tensile surface) of sample.*

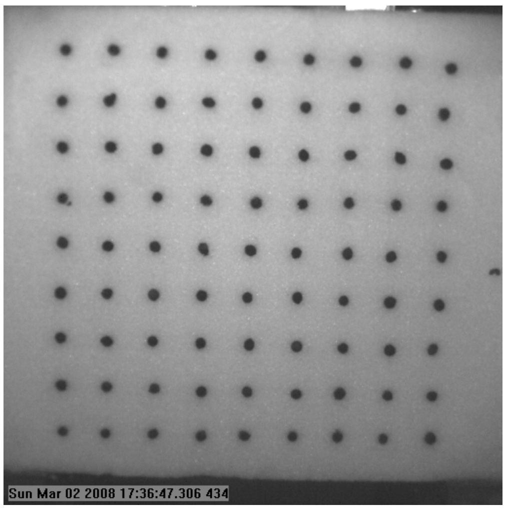

(a)

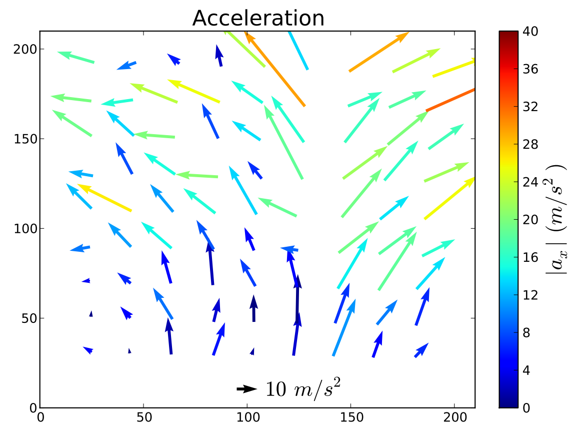

(b)

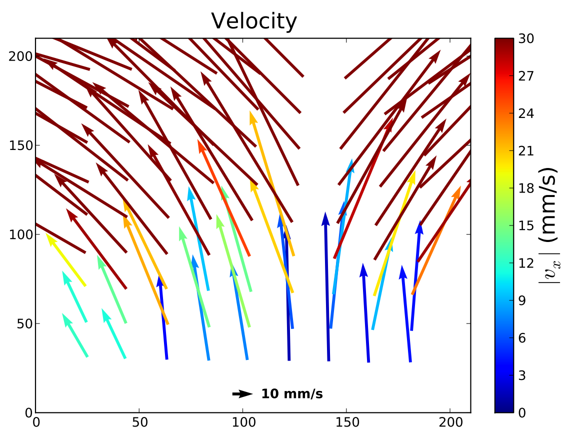

(c)

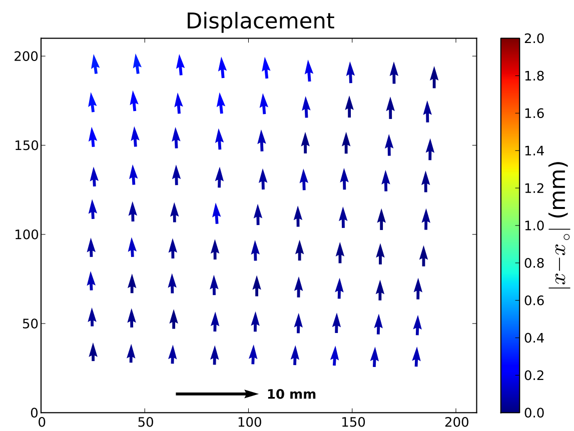

(d)

Figure A.16: *Crack sequence image 9.*

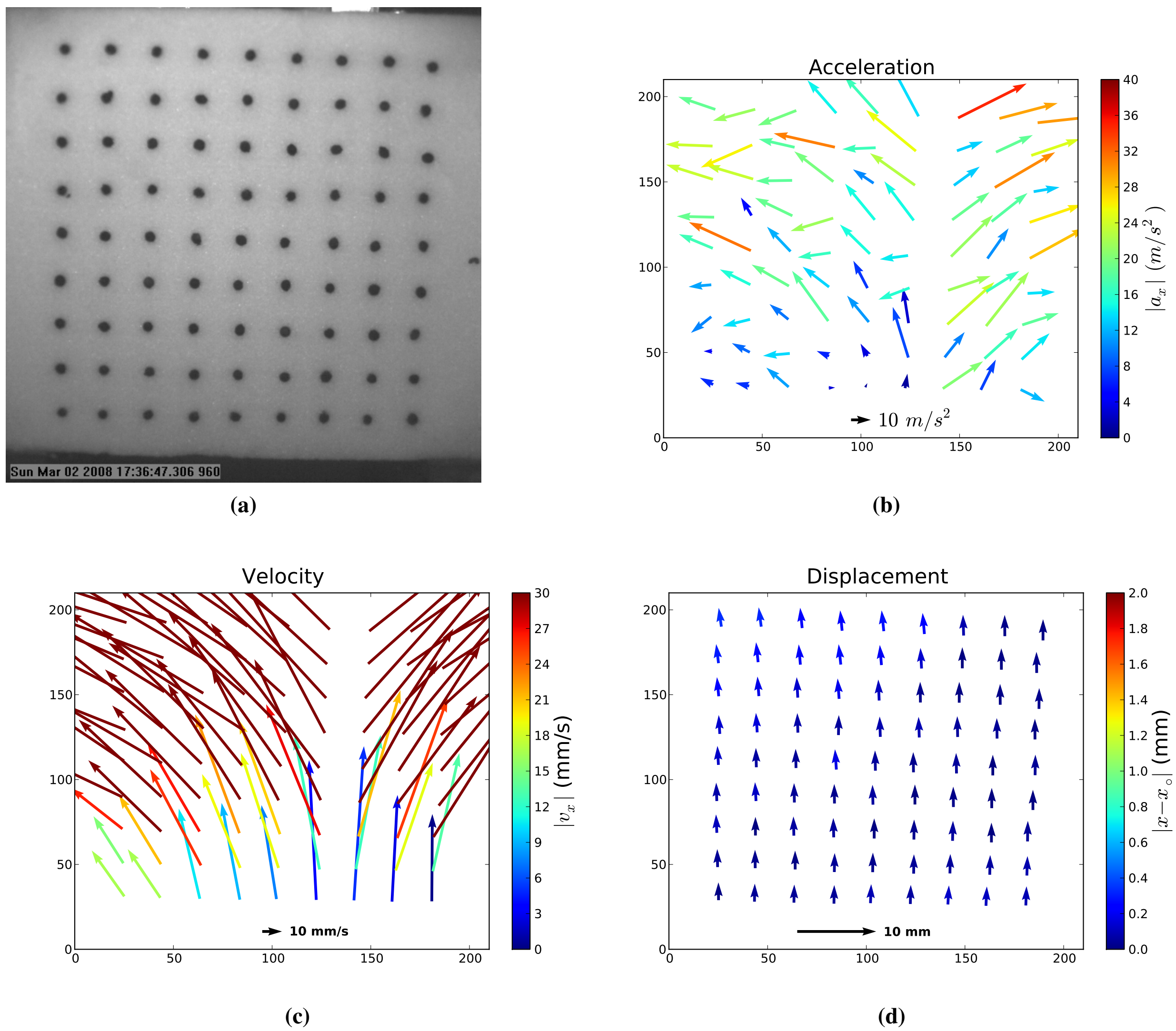

Figure A.17: *Crack sequence image 10.*

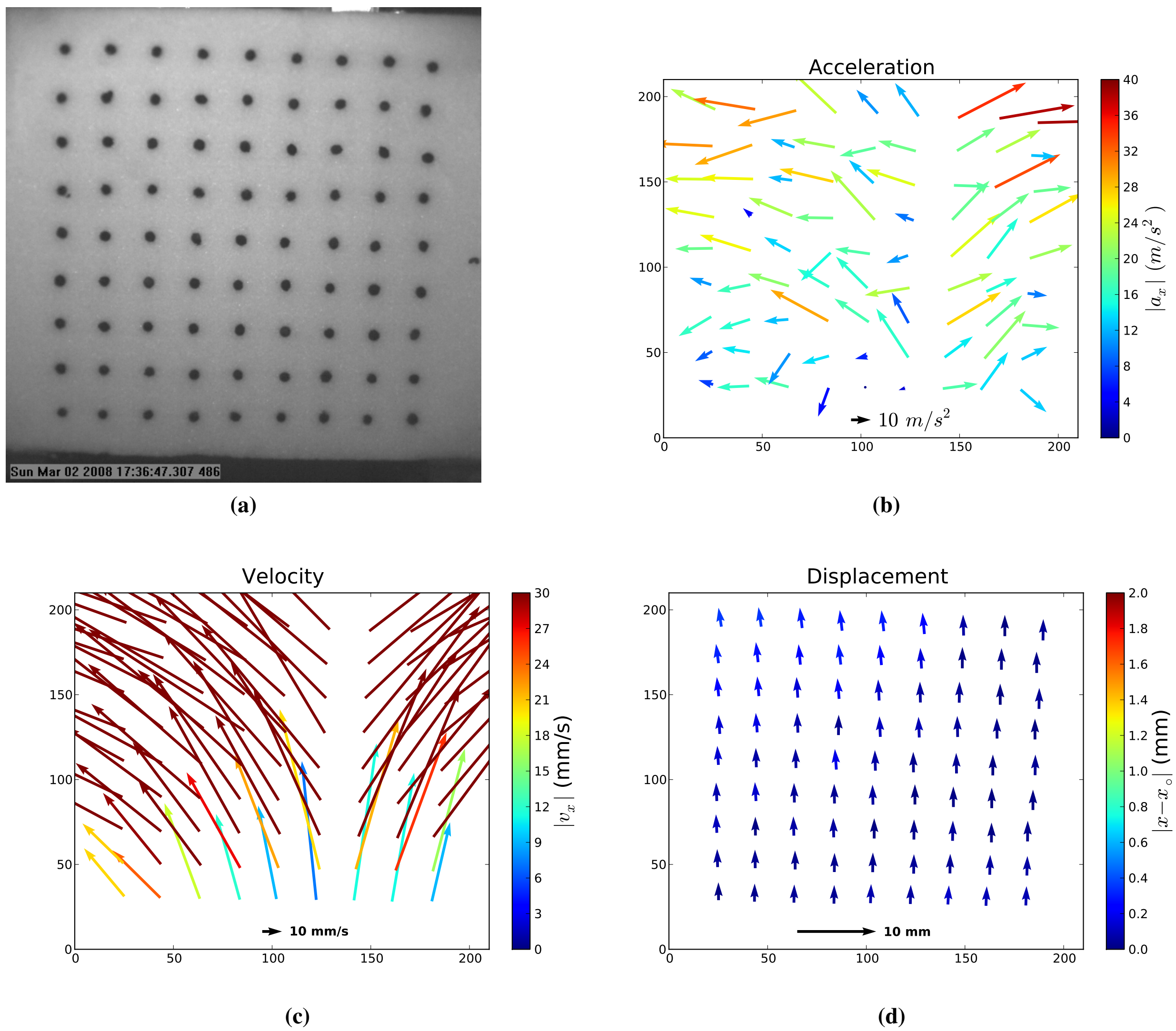

Figure A.18: *Crack sequence image 11.*

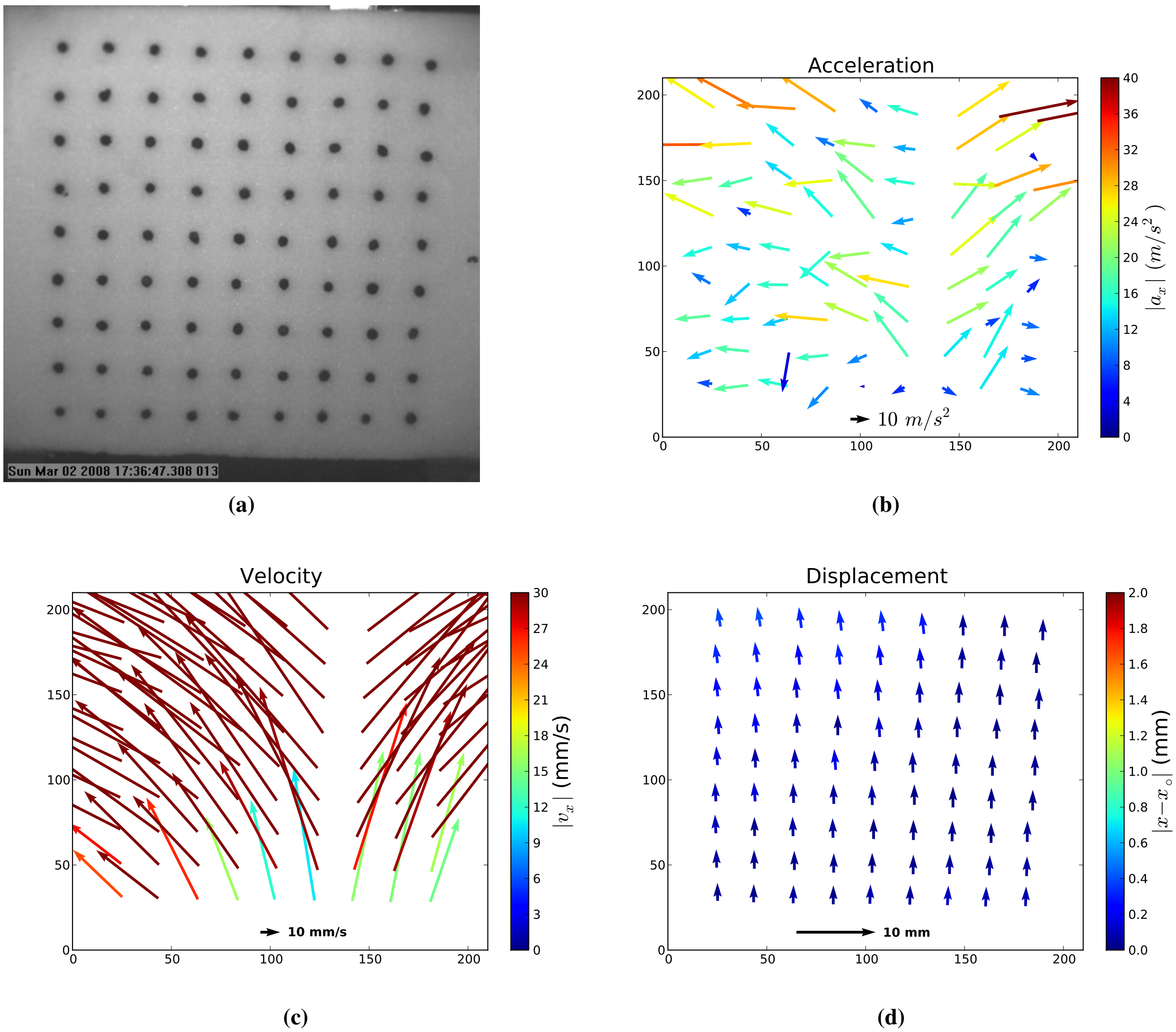

Figure A.19: *Crack sequence image 12.*

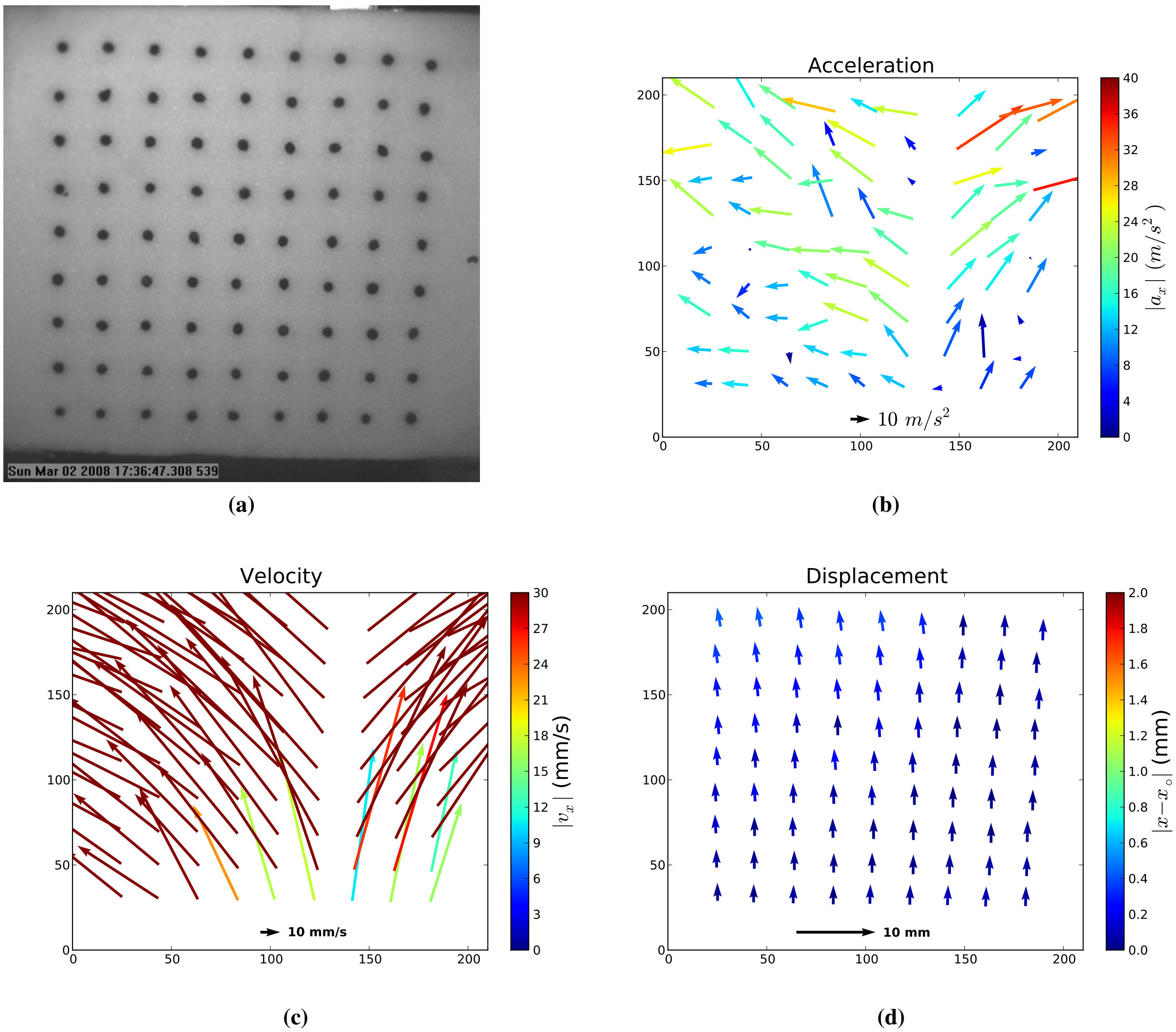

Figure A.20: *Crack sequence image 13.*

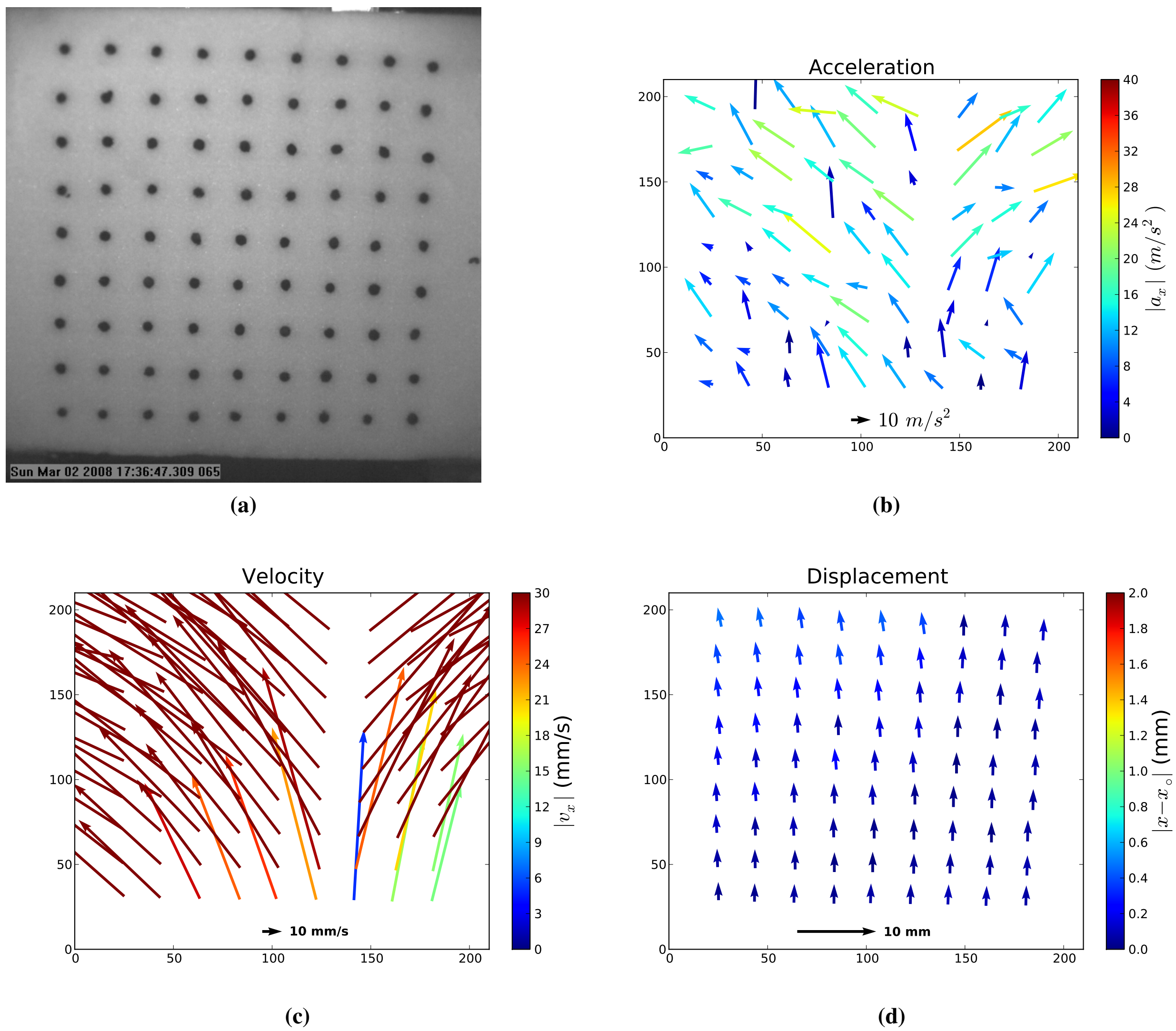

Figure A.21: *Crack sequence image 14.*

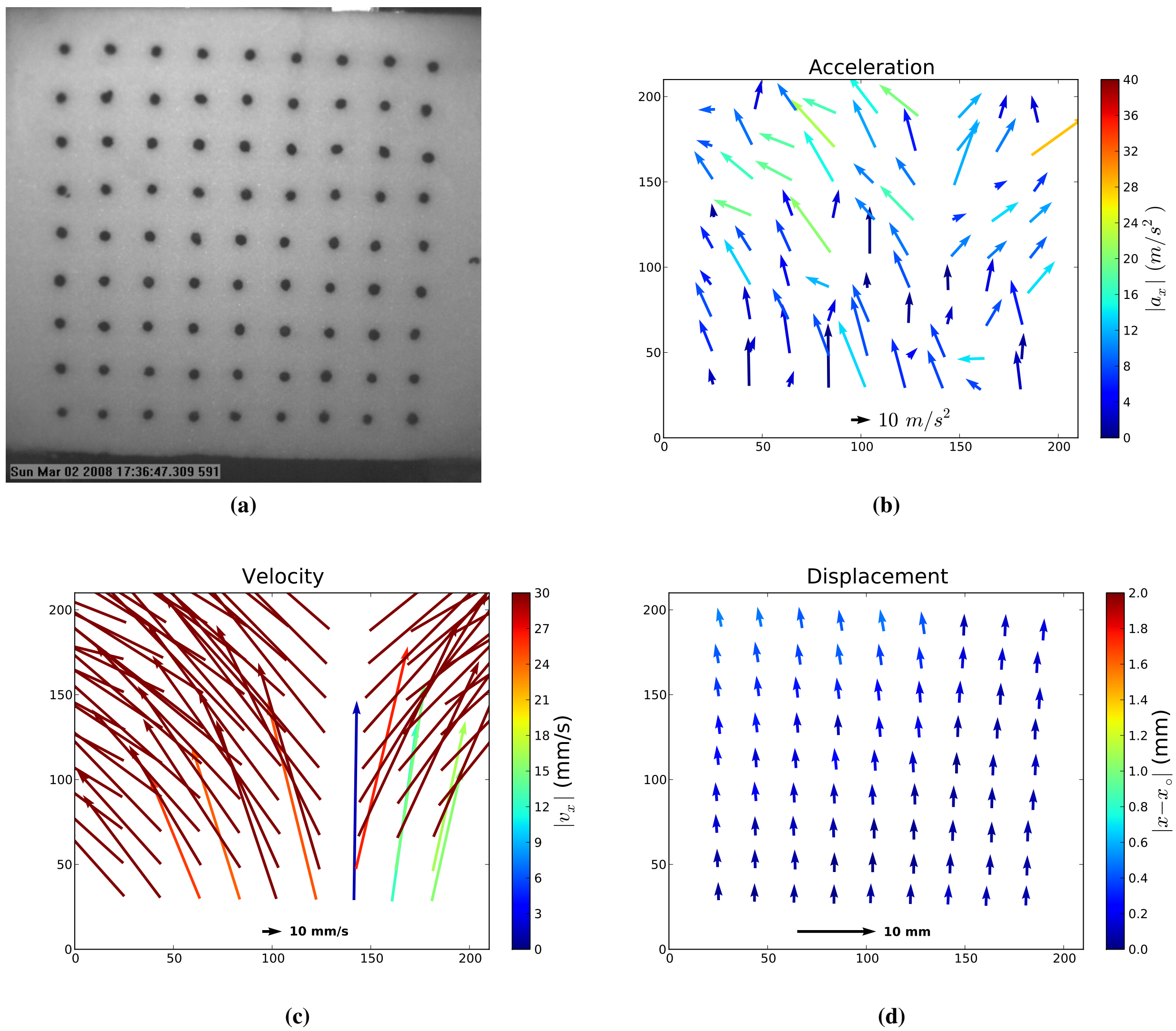

(a) **(b)**

(c) **(d)**

Figure A.22: *Crack sequence image 15.*

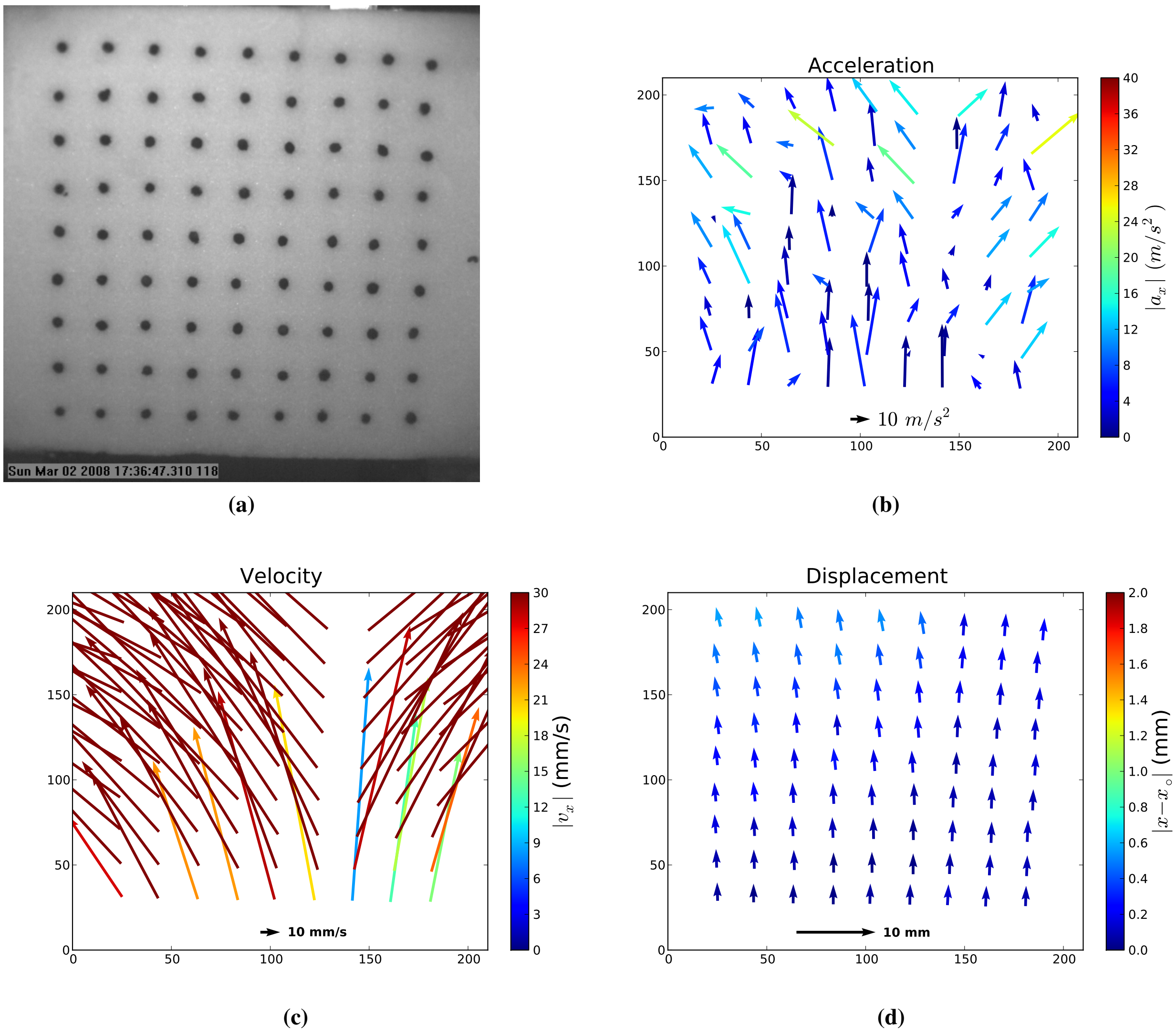

Figure A.23: *Crack sequence image 16.*

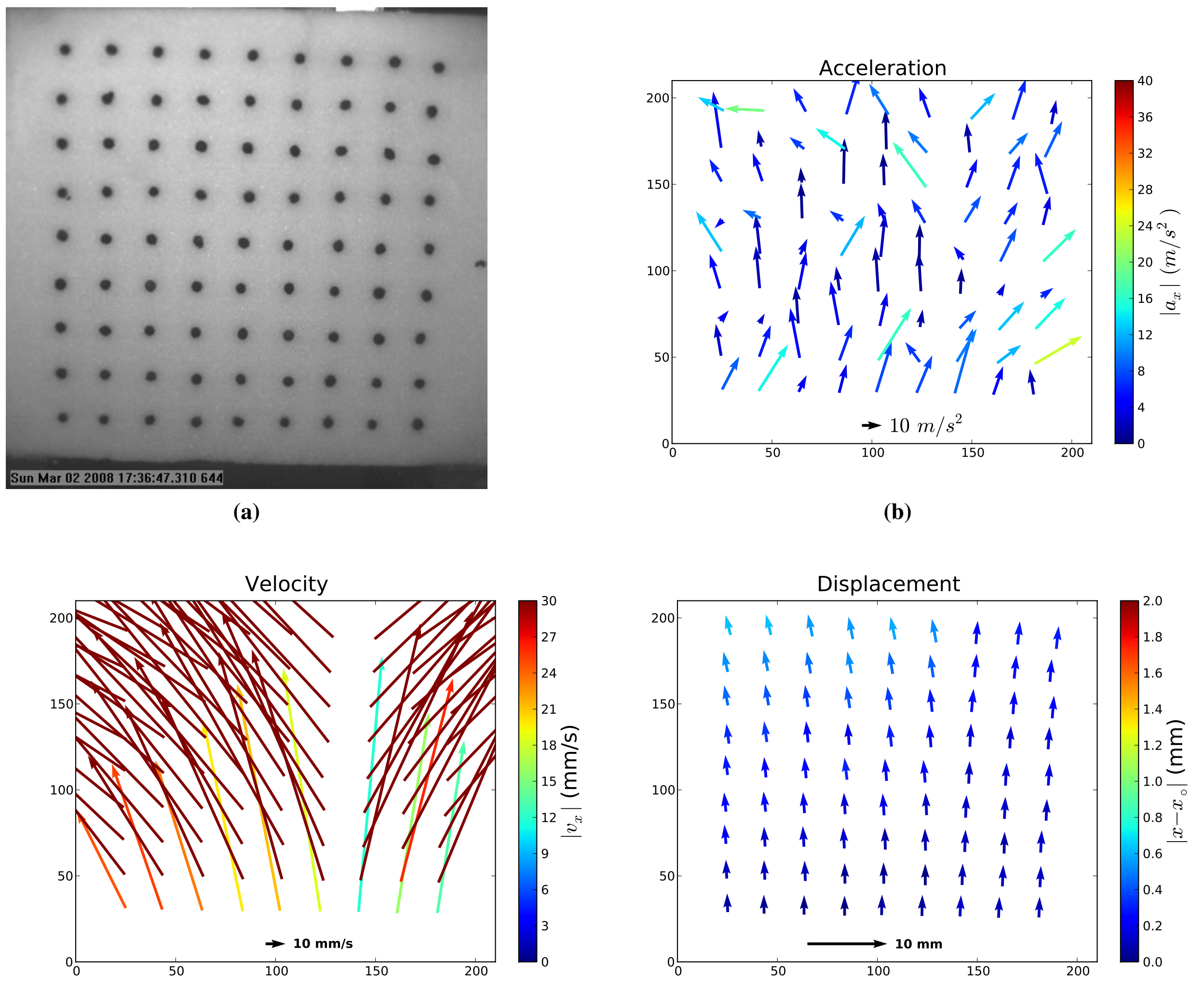

Figure A.24: *Crack sequence image 17.*

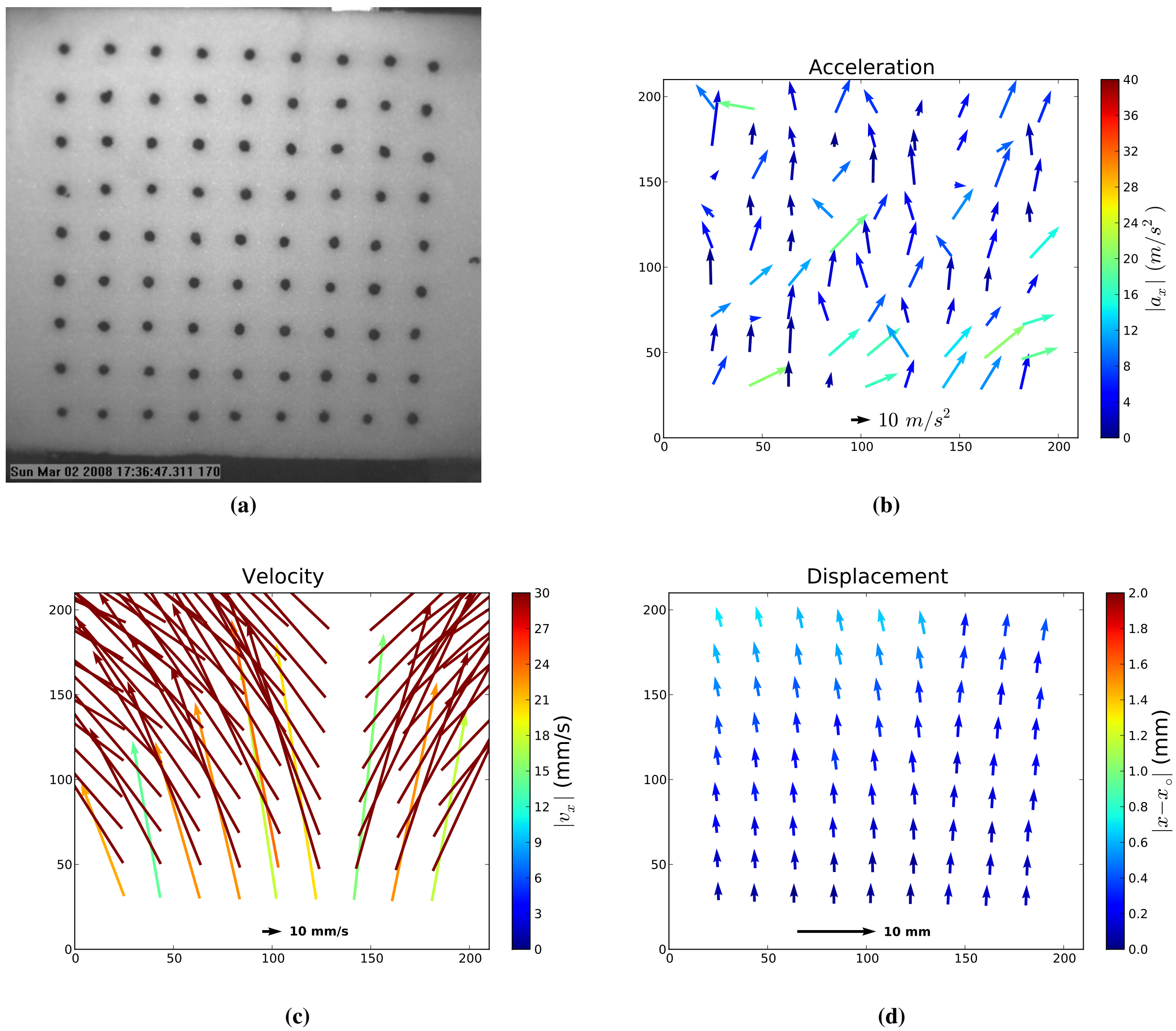

Figure A.25: *Crack sequence image 18.*

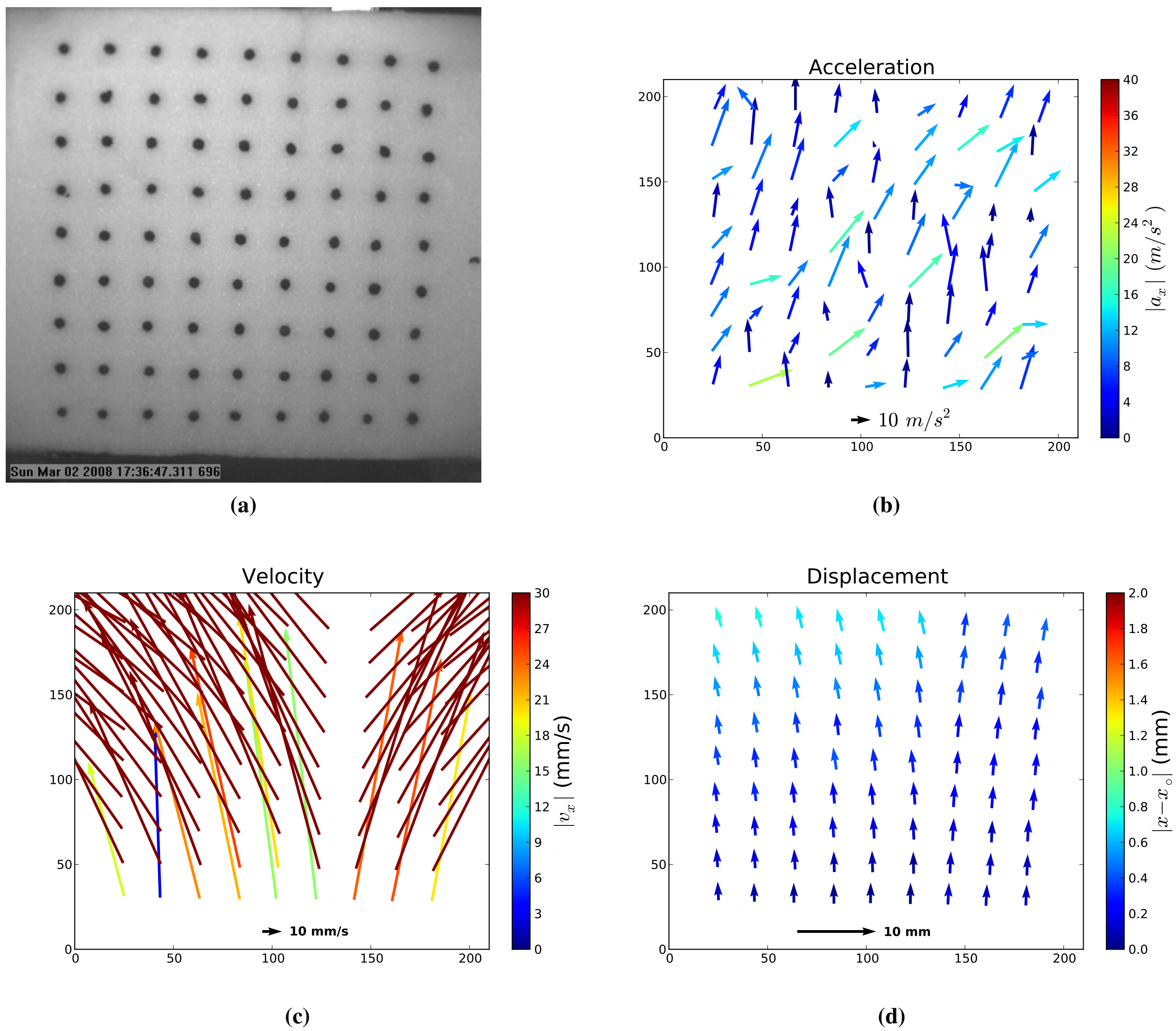

Figure A.26: *Crack sequence image 19.*

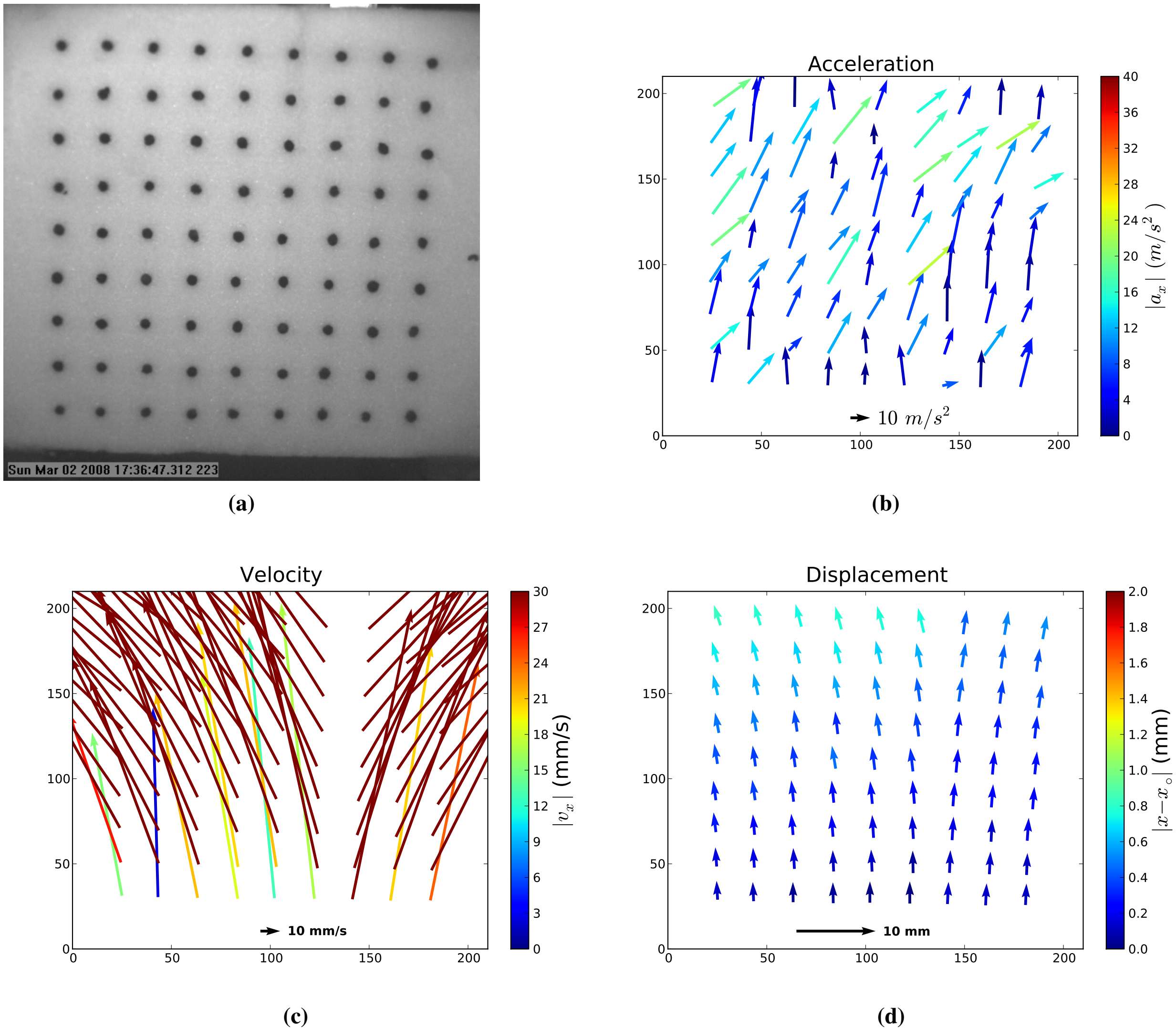

Figure A.27: *Crack sequence image 20. Visible crack, perhaps traction free, has propagated about 10 cm across the sample.*

Appendix B: Analysis of Regression Models

Assumptions in Least Squares Regression

In fitting a model of the form of Equation 4.24, or any other form, to experimental data using least squares, several fundamental assumptions are made (whether or not they are explicitly recognized). The model residuals, or random errors about the mean specified by the model, are assumed to be normally distributed, independent and have constant variance (the variance is independent of the mean in a normal distribution). The independent variable, or predictor is assumed to be measured without error.

The assumption of normally distributed errors is not essential for the estimation of model parameters themselves. Departure from normality does affect tests of significance and confidence intervals of model parameters, though (*Rawlings et al.*, 1998). In this study, the Shapiro-Wilk test (and normal quantile plots) have been used to test the null hypothesis that the residuals come from a normal distribution.

Ordinary least squares procedures give equal weighting to each data point. This requires that the variance structure of the residuals is homogeneous. If the residuals are heterogeneous (i.e. they display heteroscedasticity) then some data points contain relatively more or less information than others. In some cases weighted least squares can be used to make the variance structure homogeneous. If only normality or homoscedasticity could be achieved with a transformation or other procedure, addressing the heterogeneous variance structure to achieve homoscedasticity was chosen as preferable over normality of the residuals (*Rawlings et al.*, 1998).

Lack of independence in the errors is referred to as autocorrelation. Autocorrelated residuals can lead to biased estimates of the variance structure, imprecision in parameter confidence limits, and misleading hypothesis test results. Autocorrelation of the residuals is the result of any of the following (*Anderson*, 1954):

1. faulty choice of the form of the regression model
2. omission of important variables from the model
3. use of incorrect variables or poor data.

Generalized least squares, which takes into account the correlation structure in the data, can be used to remedy autocorrelated residuals. In models using the density as the lone predictor variable in this study, however, autocorrelation has been interpreted as a result of the variable selection. Variations in microstructure are usually used to explain scatter about mean functions of density (*Schweizer et al.*, 2003). The density is not an incorrect variable per se, but is an insufficient variable alone for scaling snow properties. No modeling procedure can make up for the failure of any model assumptions on this basis. The correlation structure of model residuals was assessed in this study graphically using residual plots and using the "runs test," a hypothesis test with the null hypothesis that the residuals are independent (not autocorrelated).

Autocorrelation can arise due to grouping in experimental design, which is typically the case when testing snow properties. For example, multiple snow samples are often taken from the same layer within the snowpack when effects of a variable other than the snow structure (such as temperature or loading rate) are to be tested. Such grouping typically produces positively correlated errors (*Rawlings et al.*, 1998).

Goodness of Fit of Nonlinear Regressions

The first indication of the goodness of fit of a nonlinear regression was visual inspection. If the model curve appeared to capture the mean structure of the data, only then were additional steps taken to assess other model assumptions and possible violations.

For comparing similar model forms applied to different data sets, visual inspection was not as useful. Relative comparisons could be made, in some cases, based on the conclusions of hypothesis tests such as the Shapiro-Wilk test for normality in the residuals or the runs test for independence of the residuals. Otherwise, a definition of R^2 for nonlinear regression was used.

The goodness of fit statistic R^2, analogous to the coefficient of determination in linear regression (represented by lower case r^2) was defined. If $\hat{y}_i$ is a modeled value, y_i is an observation of a dependent variable and $\bar{y}$ is the mean of all y_i, the following notation for sums of squares was used:

$$SS_{tot} = \sum i\,(y_i - \bar{y})^2 \tag{B.1}$$

$$SS_{reg} = \sum i\,(\hat{y}_i - \bar{y})^2 \tag{B.2}$$

$$SS_{err} = \sum i\,(y_i - \hat{y}_i)^2 \tag{B.3}$$

where SS_{tot} is the total sum of squares, SS_{reg} is the regression sum of squares and SS_{err} is the residual (error) sum of squares.

The coefficient of determination was then defined as

$$R^2 \equiv 1 - \frac{SS_{err}}{SS_{tot}}. \tag{B.4}$$

In ordinary linear regression, the total sum of squares is equal to the regression sum of squares plus the residual sum of squares,

$$SS_{tot} = SS_{reg} + SS_{err}. \tag{B.5}$$

Using Equation B.5 and B.4, the familiar coefficient of determination, written in terms of variance explained by the model, can be obtained:

$$r^2 = \frac{SS_{reg}}{SS_{tot}}. \tag{B.6}$$

However, the equivalency in Equation B.5 does not hold in general for nonlinear regression. It is only valid if a constant mean function is embedded in the nonlinear model, that is if there is some valid parameter combination that leads to a constant (nonzero) model prediction. When a constant mean function is embedded in the nonlinear model, the R^2 value in Equation B.4 represents the improvement of the nonlinear model over the constant mean function through the data. This is similar to the coefficient of determination r^2 in linear regression which represents the model improvement over a constant mean (intercept) function.

The common relative-density power law function used to express many snow properties (e.g. Equation 4.24) can be reduced to a constant mean function when the parameter b goes to zero, so the definition in Equation B.4 holds. If the model form cannot be reduced to a nonzero constant, then $\bar{y}$ in the total sum of squares in Equation B.1 must be eliminated to make the total sum of squares equal to the sum of squared deviations about zero.

Remedies for Model Violations

When model residuals were not normally distributed or had non-constant variance (both were generally present together if at all), the data were transformed in an attempt to remedy these violations. A transform-both-sides approach was applied, rather than transforming either the predictor or the response, to ensure that the original relationship between the response and predictor specified in the mean function was preserved (*Ritz and Streibig*, 2008). Transforming only one side (predictor or response, as in linear regression) distorts the relationship between the predictor and response in a nonlinear regression.

The form of the transformation was determined using the Box-Cox method, a profile likelihood approach that determines the optimal exponent of a power-law transformation for both response and predictor. The approach is implemented in the `boxcox` method in the `nlrwr` package in *R* (*Ritz and Streibig*, 2008). It should be noted that the Box-Cox method also indicates when a log transformation is more appropriate than a power-law transformation.

Following transformation and refitting, if model violations were still present, a weighted least squares regression was attempted. The variance structure could be modeled in a variety of ways. Since residuals most often increased with increasing values of the model mean, the variance structure was most commonly expressed as a power law function of the mean. The power law exponent was introduced as a free parameter, reducing the degrees of freedom of the model by 1 compared to the ordinary least squares. The `gnls` function in *R* was used to implement the variance model.

Appendix C: Viscoelastic Deformation of Snow over Short Timescales

In simple Kelvin or Maxwell models of viscoelasticity (e.g. *Malvern*, 1969), the material response depends on the ratio of t/τ, where t is the time of interest and τ is the relaxation or retardation time. *Shinojima* (1966) measured relaxation times in tensile tests of around 300-1000 seconds, depending on the type of test. The lower bound estimate is used here to err on the side of assuming more viscous deformation. These relaxation times are three orders of magnitude greater than the typical failure time in the fastest (and most common) bending tests in the present study. In the slowest tests, the beams failed in about 10 seconds or less, still an order of magnitude below the relaxation time.

If a constant strain $\varepsilon_\circ$ is applied to a Maxwell element (Figure C.1a) at $t = 0$ and held constant, the stress relaxation takes the form

$$\sigma(t) = E\varepsilon_\circ e^{-t/\tau}. \tag{C.1}$$

Assuming again $\tau = 300$ s, after 1 second the initial elastic stress $E\varepsilon_\circ$ will have relaxed to $0.997E\varepsilon_\circ$, falling to $0.97E\varepsilon_\circ$ after 10 seconds.

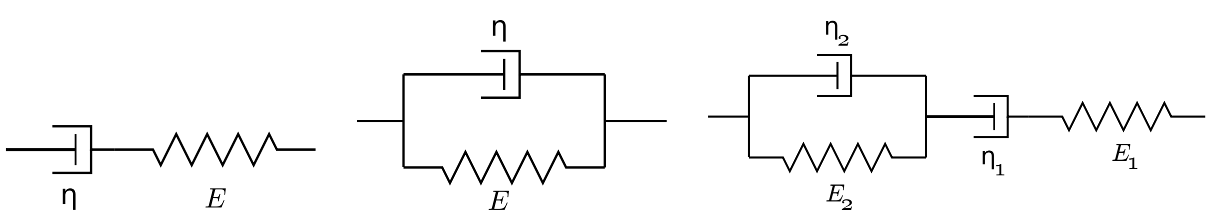

Figure C.1: *Viscoelastic elements as combinations of springs and dasphots.*

If a stress $\sigma_\circ$ is applied to a Kelvin-Voigt element (Figure C.1b) at $t = 0$ and held constant, the strain evolves over time as

$$\varepsilon(t) = \frac{\sigma_\circ}{E}\left(1 - e^{-t/\tau}\right) \tag{C.2}$$

where E is the spring constant and $\tau = \eta/E$ is the relaxation time, with η the viscous coefficient of the dashpot. For a relation time of 300 s, the strain after 1 second is $\varepsilon(t = 1s) = 0.003\sigma_\circ/E$. Thus the strain would be just a fraction of a percent of the elastic strain if the material were characterized by a linear elastic constitutive relation of the form $\sigma = E\varepsilon$, since there is no instantaneous elastic strain in a Kelvin-Voigt element. This strain would increase to 4% of the elastic value over a timescale of 10 s.

These simple models give an initial indication that creep effects are likely to be small in the beam experiments, given the small failure times relative to the relaxation time. However, a four-element Burgers' model (Figure C.1c) gives a better representation of the creep behavior of snow. *Shinojima* (1966) determined parameters for such a model from creep experiments at constant load. The creep curve for a Burgers' model takes the form

$$\varepsilon(t) = \sigma_\circ\left(\frac{1}{E_1} + \frac{t}{\eta_1} + \frac{1}{E_2}\left[1 - exp\left(\frac{-t}{\tau}\right)\right]\right) \tag{C.3}$$

where parameters correspond to the springs and dashpots in Figure C.1 and $\tau = \eta_2/E_2$ is the relaxation time. The values for E_1 and E_2 calculated by *Shinojima* were within about 4% of each other, and expressed as functions of density. The values of η_1 and η_2 nearly coincided for snow near the melting temperature, and had a similar density dependence as the elastic parameters. A relatively high reference temperature of -5° was chosen for calculating the Maxwell viscosity η_1. The creep strain values in Table 7.1 were calculated using Equation C.3. The stress term $\sigma_\circ$ and the density dependence in the model parameters dropped out after taking the ratio of creep strain to instantaneous elastic strain.

Index